MICRO-RAMP FLOW DYNAMICS

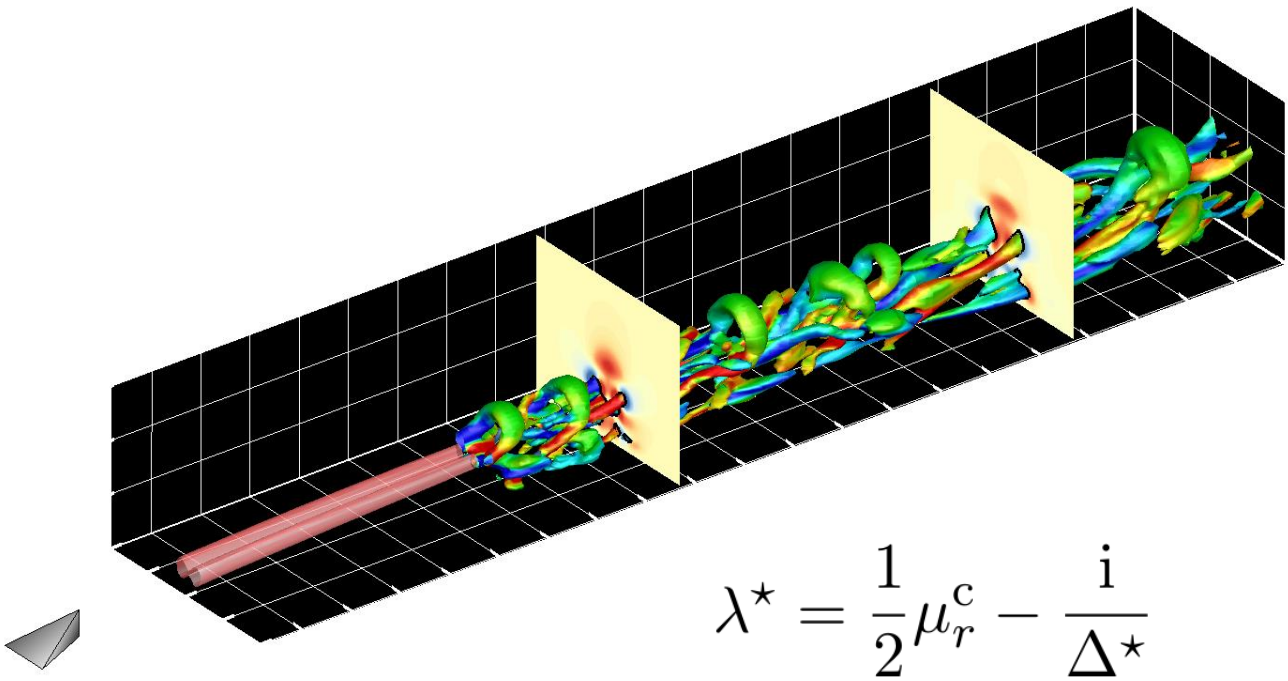

$$\lambda^\star = \frac{1}{2}\mu_r^{\mathrm{c}} - \frac{\mathrm{i}}{\Delta^\star}$$

JORDI CASACUBERTA PUIG

Aerodynamics

Faculty of Aerospace Engineering

TU Delft

Delft University of Technology

Master of Science Thesis

Micro-Ramp Flow Dynamics

Jordi Casacuberta Puig

July 10, 2018

Faculty of Aerospace Engineering

Delft University of Technology

Micro-Ramp Flow Dynamics

Master of Science Thesis

For obtaining the degree of Master of Science in Aerospace Engineering
at Delft University of Technology

Jordi Casacuberta Puig

July 10, 2018

Faculty of Aerospace Engineering · Delft University of Technology

Delft University of Technology

DELFT UNIVERSITY OF TECHNOLOGY
DEPARTMENT OF AERODYNAMICS

The undersigned hereby certify that they have read and recommend to the Faculty of Aerospace Engineering for acceptance the thesis entitled **"Micro-Ramp Flow Dynamics"** by **Jordi Casacuberta Puig** in fulfillment of the requirements for the degree of **Master of Science**.

Dated: July 10, 2018

Prof. Dr.-Ing habil. Stefan Hickel

Prof. Dr. Fulvio Scarano

Dr. Qingqing Ye

Ir. Koen J. Groot

Acknowledgement

Although the goal of this thesis project is formally to obtain the degree of Master of Science at the Delft University of Technology, the truth is that, during its realisation, I have gained much more than that. Besides an inherent personal growth, I have met a diversity of people with whom I have shared many experiences. And since life is what happens while you are trying to graduate, this brief section is an acknowledgement to those who helped me to carry out this work, but also to those who, in different ways, have made it a very special journey.

First and foremost, I may not be able to fully translate with words how thankful I am to my supervisors, Professor Stefan Hickel and PhD candidate Koen J. Groot for their guidance and support. Their teaching has allowed me to continuously learn and challenge myself. Professor Hickel has been an inspiration to me. He is an example of professionalism and devotion for teaching and engineering; his great deal of knowledge were constantly bringing new and interesting perspectives to my thoughts. And always with a smile on his face, something which is highly appreciated these days. Koen is what one obtains when passion, hard work and brilliance are combined together. He has *always* been there when a good discussion was required, helping me to understand and introduce to new conceptions within the fluid dynamics field. I am *very* grateful for the huge effort that he put in his supervision. We have shared many moments and I feel that he started as a supervisor and ended as a friend.

I would like to thank Dr. Henry J. Tol for providing the results of stability analysis used in this work, Dr. Qingqing Ye and Dr. Ferry Schrijer for having fruitful conversations about the micro-ramp, Tiago Pestana for helping me with INCA and Nico van Beek for his assistance in daily issues.

To all the Basement friends, my family during this time. The reader should know that the "Basement" is the place (a basement in fact) where the MSc students work during their thesis period and for which you end up having a special affection. First of all, Javier Fatou and Roberto Solana have been *the* friends during this journey. They have been there since the beginning and we rapidly created a group with Andrea Macarulla, Eduard Cabot and Mario Ruiz which made me enjoy the best experiences in Delft. With Lluís Laguarda we met later, but that did not stop us to see that we would get on really well (and enjoy the night life as it should be enjoyed). With Sofia Ribeiro, one of the nicest persons I have ever met, we have shared many special moments. She was part of my promotion class in TU Delft, together with Alberto Rius, Rajat Hebbare, Ankur Kislaya or Woosik Yoon amongst many others.

With Aman Jindal we started in the Basement and ended up drinking mojitos in Mallorca. Others came from outside Delft, as for instance Sébastien Niessen, with whom we fought against SFD and INCA together, or Álex del Estal, who still nowadays randomly sends me political memes. With Sumedh Jain we became the basement veterans and Ka Hin became

my neighbour for the majority of the time. Thanks Arun Kumar for the "scientific talks" ;). I also want to thank Nick Voogt&Yorin van Weersch for spicing up the Basement and my Rossinistraat house mates. Of course I do not want to forget about David Ordóñez; we went to the same high school, BSc and MSc universities and somehow we ended up in the same basement. With Ventsislav Pazhev we met dancing salsa (not together I mean, with Jaime Patterson we shared nice hipster moments, Corrado Corsetti and Deerek Risseeuw, thank you for your lasagna and keep pushing these bowling skills. Guillem Solivellas and Jordi Ávila, thanks for an *extra-ordinary* visit. And many others as Kitso Epema, Sumit Tambe, Nils Temme, Mart van Rijsingen, Marthin Bremm, Gonzalo González, or Andrea Rubino.

To my parents, Maria Teresa and Carles, for all the love and affection. And also, thank you for making me understand science the way I do nowadays. To my sister Sílvia, exceptional in so many senses. Although you now start an adventure very far from home, I feel you very close. And to my beloved Ainoa who, certainly, has been the best that happened to me during this thesis time.

Jordi Casacuberta Puig
10th of July, 2018, The Basement, Delft, The Netherlands

.

The formula of our happiness: a Yes, a No, a straight line, a goal...

Friedrich Nietzsche, The Antichrist

Abstract

Micro-ramps are passive flow control devices used to delay flow separation. Their use is widespread due to their reduced drag and structural robustness. We reproduce with Direct Numerical Simulations (DNS) recent Particle Image Velocimetry (PIV) experiments of the micro-ramp flow performed at TU Delft to study the wake of a micro-ramp immersed in a laminar and incompressible boundary layer. The micro-ramp is a vortex generator which induces a pair of streamwise counter-rotating vortices. The current literature identifies this structure as the main flow feature contributing to the increase of the near-wall momentum. The micro-ramp is also a surface roughness element which can trigger laminar-turbulent transition. The action of the induced vortices introduces a strong detached shear layer into the flow field, susceptible to Kelvin-Helmholtz (K-H) instability. We analyse the micro-ramp flow dynamics and the transitional mechanisms which develop in the micro-ramp wake. Furthermore, we intend to contribute to the discussion on the micro-ramp working principle, which has been put into question by other authors. We show the importance of the transitional perturbation development in the micro-ramp functionality.

Downstream-travelling streamwise vortices and transitional disturbances serve to the same purpose of increasing the momentum close to the surface. To examine their relative contribution in this regard, we numerically decompose the micro-ramp flow field into a laminar steady state and a time-dependant perturbation field. To achieve that, we apply Selective Frequency Damping (SFD), a numerical technique used to compute the steady solutions of globally unstable dynamical systems. SFD is a popular method nowadays and the preferred approach for aerospace applications. However, it has two case-dependant model parameters which are key to the method's effectivity and efficiency, and whose selection remains a challenge in the literature. Not every combination of the model parameters guarantees the success of SFD, and even if so, the required computational time may be so large that the approach is impractical. We provide the first rigorous analysis of the influence of these parameters to the functionality of SFD, leading to simple expressions and procedures for choosing them optimally. Furthermore, we prove that, under certain conditions, SFD is always able to stabilise a globally unstable flow configuration.

Table of Contents

List of Figures

List of Tables

Nomenclature

Abbreviations

CFD	Computational Fluid Dynamics
DNS	Direct Numerical Simulations
FTC	Flow Through Cycle
HL	Hairpin Leg
KH	Kelvin Helmholtz
LB	Leg Buffer
LBIV	Leg-Buffer-Induced Vortex
LHS	Left Hand Side
LoB	Lower Branch (of leg-buffer)
LST	Linear Stability Theory
PIV	Particle Image Velocimetry
POD	Proper Orthogonal Decomposition
RANS	Reynolds-Averaged Navier Stokes Equations
RHS	Right Hand Side
SFD	Selective Frequency Damping

Greek Symbols

$\boldsymbol{\omega}$	Vorticity	s^{-1}
χ	SFD control parameter	$rad\, s^{-1}$
Δ	SFD filter width	s
δ	Boundary layer height	m
δ_{un}	Undisturbed boundary layer height	m
ϵ_{R}	SFD residual	$-$
λ	Eigenvalues of the SFD-controlled system	$rad\, s^{-1}$
μ	Eigenvalues of the uncontrolled system (or dynamic viscosity)	$rad\, s^{-1}$ (or $Pa\, s$)
ν	Kinematic viscosity	$m^2\, s^{-1}$
ν_∞	Free-stream kinematic viscosity	$m^2\, s^{-1}$
ν_{w}	Wall kinematic viscosity	$m^2\, s^{-1}$
ρ	Density	$kg\, m^{-3}$

ρ_∞	Free-stream density	$kg\ m^{-3}$

Latin Symbols

$\boldsymbol{q}$	Instantaneous field	–
$\boldsymbol{q}'$	Perturbation field (with respect to the base flow)	–
$\boldsymbol{q}''$	Perturbation field (with respect to the mean flow)	–
$\boldsymbol{q}^{\mathrm{str}}$	Streaks field	–
$\boldsymbol{q}_{\mathrm{un}}$	Unperturbed field	–
$\boldsymbol{q}_s$	Base flow field	–
$\boldsymbol{v}$	Velocity field	$m\ s^{-1}$
$\langle \boldsymbol{q} \rangle$	Mean flow field	–
$\langle \boldsymbol{q} \rangle^{\mathrm{d}}$	Mean-flow distortion field	–
$\mathcal{R}e_{hh}$	Roughness Reynolds number	–
$\mathcal{R}e^{\star}_{hh}$	Roughness Reynolds number based on the wall kinematic viscosity	–
$\mathcal{R}e_h$	Reynolds number based on h	–
D	Cylinder diameter	m
h	Micro-ramp height	m
p	Pressure	Pa
p_∞	Free-stream pressure	Pa
s	Shear	s^{-1}
u	Streamwise velocity	$m\ s^{-1}$
u_∞	Free-stream velocity	$m\ s^{-1}$
u_h	Unperturbed streamwise velocity at $x/h = -1.25$, $y/h = 1$	$m\ s^{-1}$
v	Wall-normal velocity	$m\ s^{-1}$
w	Spanwise velocity	$m\ s^{-1}$
x	Streamwise coordinate	m
y	Wall-normal coordinate	m
z	Spanwise coordinate	m

Chapter 1

Introduction

1.1 Roughness-induced transition in boundary layer flows

1.1.1 Relevance for aerospace applications

Osborne Reynolds published in 1883 his famous investigations on hydrodynamic stability. He injected a thin stream of dye into a glass tube with water flow and observed the fluid motion. In Reynolds' words: "the internal motion of water assumes one or other of two broadly distinguishable forms, either the elements of the fluid follow one another along lines of motion which lead in the most direct manner to their destination, or they eddy about in sinuous paths the most indirect possible". Transition between these states, nowadays referred to as laminar and turbulent respectively, was observed to occur at approximately the same ratio of mean flow velocity times pipe diameter over kinematic viscosity. This combination of quantities forms a non-dimensional parameter, the Reynolds number $\mathcal{R}e$, which expresses the ratio of inertia force over viscous force governing this process. As a historical note, Sir George Stokes and Lord Rayleigh were the referees of Reynolds' paper. The latter wrote: "this paper records some well contrived experiments on a subject which has long needed investigation [...]. I am of opinion that the results are important, and that the paper should be published" (Zuck, 1971; Jackson and Launder, 2007).

In 1904 Ludwig Prandtl introduced the concept of boundary layer. When an object moves relative to a fluid, there exists a flow region in which velocity changes from zero at the wall to the free stream value away from it. This fluid layer, the boundary layer, can as well be laminar, turbulent or of transitional nature, i.e., switching from one state to the other. In the aerospace industry, controlling the state of the boundary layer is paramount for the aerodynamic design of aerospace vehicles. Features such as air resistance, vehicle manoeuvrability or surface heat transfer are strongly dependant on it (White, 2006). Nonetheless, the process through which a laminar flow transitions to a chaotic turbulent state is still far from being fully understood. The study of laminar-to-turbulent transition remains nowadays an active research topic within the aerodynamics community (Pinna, 2012).

Transition is affected by many parameters, among which wall imperfections occupy a central role and are the main focus of this work. Interest in the effect of roughness in the transition process comes, first of all, from the necessity to understand the interaction between fluid flow

and realistic surfaces (Ergin and White, 2006). Secondly, depending on the application, the effect of turbulence may be desirable or not; roughness elements can be used to either accelerate or delay transition (Fransson et al., 2006; Loiseau et al., 2014). A turbulent boundary layer contains more momentum close to the wall than a laminar one due to turbulent mixing. This results in larger velocity gradients and shear stresses on the body surface; skin friction of a turbulent boundary layer is roughly ten times larger than that of a laminar one (Fransson et al., 2006). Therefore, turbulence in boundary layers developing over streamlined bodies, whose dominant drag kind is skin-friction drag, is typically unwanted. On the other hand, a turbulent boundary layer is better able to resist adverse pressure gradients and thus it is less prone to separation. A reduction of the separated region results in less pressure drag, the dominant drag kind in bluff bodies and airfoils at high angle of attack. Thus, tripping the boundary layer, i.e., promoting early transition through the addition of tripping devices, may be of benefit in geometries with high curvature (Elsinga and Westerweel, 2012).

Improving the efficiency and reducing the drag of aircrafts remains nowadays of major priority due to environmental concerns involving noise contamination and air pollution (Jahanmiri, 2011). The goals of the European Statistical System (ESS) vision 2020 in aviation include a 50% reduction of perceived noise and 50% cut in fuel consumption. These goals appear almost impossible to achieve with the existing technology. Drag reduction in aerospace vehicles would also allow for larger flight ranges and higher vehicle speeds. According to Thibert et al. (1990) and Malik et al. (2013), skin friction drag in subsonic transport aircraft represents about 50% of total drag. Washburn (2011) estimates that for a 7400 km transport aircraft of 325 passengers, a 10% reduction in skin friction drag would result in 9% fuel saving. To maintain natural laminar flow over relevant aircraft parts and hence reduce skin-friction drag, shape design and hybrid laminar flow control are presented as main approaches (Blockley et al., 2016). An example of the latter is the usage of spanwise periodic discrete roughness elements to delay transition to turbulence; the introduction of a spanwise modulation of the boundary layer can act so as to stabilise Tollmien-Schlichting (TS) waves (Fransson et al., 2006). Despite promising numerical work, delay of transition in real flight conditions under this technique has not yet been possible (Blockley et al., 2016).

On the other hand, the aerodynamic performance of aircrafts operating at subsonic conditions and low Reynolds numbers may worsen if laminar separation occurs. This can be in terms of drag increase or maximum lift decrease. Structural damage, as a consequence of the instability of the process, is of concern as well (Delnero et al., 2007; Popelka et al., 2010). Sailplanes, Unmanned Aerial Vehicles (UAV), turbomachinery and wind turbines are examples of technology which may suffer from these unwanted effects. Promoting transition upstream the point of laminar separation remains the most effective way to prevent its occurrence (Aholt and Finaish, 2011). Surface roughness can be employed for this purpose (Lin, 2002).

1.1.2 Roughness-induced transition prediction

In this work, we deepen into the dynamics of boundary layer transition when it is promoted by an isolated three-dimensional roughness element. Transition predictions for this class of problems are traditionally based on correlations of the roughness Reynolds number, which is defined as

$$\mathcal{R}e_{hh} = \frac{u_h h}{\nu_\infty}, \tag{1.1}$$

with h being the height of the roughness element and u_h the streamwise velocity of the unperturbed boundary layer at this height (Tani, 1969; Sedney, 1973). For low $\mathcal{R}e_{hh}$, the flow downstream the roughness element remains laminar. When the so-called critical $\mathcal{R}e_{hh}$ is exceeded, the roughness element starts to affect transition. Increasing $\mathcal{R}e_{hh}$ moves upstream the transition location. At the so-called effective $\mathcal{R}e_{hh}$, transition occurs almost at the roughness element and further increments of $\mathcal{R}e_{hh}$ do not move the transition point (Schneider, 2008; Redford et al., 2010). Both critical and effective $\mathcal{R}e_{hh}$ depend on the roughness shape, disturbance environment and compressibility effects (Choudhari et al., 2009). Based on empirical work, Klebanoff et al. (1955) observe critical $\mathcal{R}e_{hh}$ to be contained in the range 600 to 900 for roughness elements with unity aspect ratio. If different from one, von Doenhoff and Braslow (1961) and Tani (1969) find the critical $\mathcal{R}e_{hh}$ to correlate with the aspect ratio of the element following a power law of exponent 2/5. Braslow and Horton (1958) throw the hypothesis that correlations using $\mathcal{R}e_{hh}$ only show good results for roughness elements well-contained within the boundary layer.

At high Mach numbers, surface roughness of small height (as compared to the boundary layer height) is not able to trigger transition; the $\mathcal{R}e_{hh}$ criterion appears to be invalid. This is assumed to be a consequence of the stabilising effect of compressibility (Braslow and Horton, 1958). For high-speed boundary layers, Redford et al. (2010) note the wall temperature and the Mach number, M, to play, together with $\mathcal{R}e_{hh}$, a central role for transition prediction. Bernardini et al. (2012) propose to condense all these effects into a modified version of the roughness Reynolds number, $\mathcal{R}e^{\star}_{hh}$, which evaluates the wall viscosity instead of the free-stream viscosity. From numerical experiments considering roughness elements with aspect ratios below the unity and a broad range of Mach numbers, $\mathcal{R}e^{\star}_{hh} = u_h h/\nu_{\mathrm{w}} = 460$ appears to serve as threshold value segregating the occurrence or not of transition.

1.1.3 Roughness-induced transition mechanisms and stability analysis

Despite being widely used for engineering applications, the correlations mentioned above are based on empirical work. There does not exist any global model describing the way a roughness element causes transition (Schneider, 2008). Nonetheless, in the low-speed regime there is generally consensus on the mechanisms underlying the transition process (Redford et al., 2010). Isolated roughness distorts the organisation of the laminar boundary layer and creates a wake dominated by streamwise vorticity (Landhal, 1980). Vortex filaments redistribute momentum within the boundary layer and introduce positive and negative streaks, which can be accompanied by an unstable detached shear layer. At this point it is important to clarify what does unstable mean in the current context. This term is linked to the concept of hydrodynamic stability, i.e., the response of fluid flow to small disturbances. The boundary layer is said to be stable if it returns to its original state after disturbances act on it. On the contrary, it is said to be unstable if the action of perturbations makes it evolve towards a new state. In the latter case, disturbances penetrating into the boundary layer (for instance sound waves) through receptivity mechanisms can get amplified and eventually lead to chaotic behaviour and turbulence (Pinna, 2012). Understanding fluid flow instabilities, i.e., the state when stability conditions are broken (Boiko et al., 2012), is hence of fundamental importance for the study of laminar-turbulent transition.

Flow instabilities of small amplitude can be characterised through linear stability analysis (Reed et al., 1996; Schmid and Henningson, 2001; Theofilis, 2003; Groot, 2013). Letting f

be the non-linear Navier-Stokes operator applied to a state variables $\boldsymbol{q}$ vector, with adequate boundary and initial conditions, the Navier-Stokes equations can be written as

$$\dot{\boldsymbol{q}} = f(\boldsymbol{q}), \tag{1.2}$$

where the dot expresses time derivative. The steady state of (1.2) satisfies $\dot{\boldsymbol{q}}_{\boldsymbol{s}} = f(\boldsymbol{q}_{\boldsymbol{s}}) = 0$. The stability approach relies on decomposing the instantaneous flow field into the base flow $\boldsymbol{q}_{\boldsymbol{s}}$ plus a time-dependent perturbation field $\boldsymbol{q}'$ such that

$$\boldsymbol{q}(\boldsymbol{x}, t) = \boldsymbol{q}_s(\boldsymbol{x}) + \epsilon_{\mathrm{A}} \boldsymbol{q}'(\boldsymbol{x}, t), \quad 0 < \epsilon_{\mathrm{A}} \ll 1, \tag{1.3}$$

where $\boldsymbol{x}$ represents the spatial coordinates and t the time. Linear stability analysis assumes perturbations to be infinitesimally small, i.e., to develop without distorting the base flow. Under this conditions, an analytical solution of the perturbation field can be obtained via linearisation of $f(\boldsymbol{q})$ around $\boldsymbol{q}_{\mathrm{s}}$, assuming the base flow to be known. The field $\boldsymbol{q}'$ is then obtained as a set of wave-like perturbations (eigenmodes) which develop independently. Each eigenmode can either die out (said to be stable) or get amplified (said to be unstable) in space and/or time. When disturbances acquire sufficiently large amplitudes, (1.3) is rendered invalid, linear stability stability breaks down, eigenmodes can interact with each other, and secondary instabilities may arise, ultimately triggering transition. Eigenmode growth is, however, one of the main paths to transition. Other scenarios involve transient disturbance growth or by-pass mechanisms (Reshotko, 2008). The boundary layer can be of unstable nature regardless of the presence or not of surface roughness; unstable detached shear layers may, however, introduce much stronger instabilities (Redford et al., 2010).

When analysing the wake of an array of cylindrical roughness elements, Ergin and White (2006) report the location of largest velocity fluctuations to be at the points of inflection of the velocity profile in wall-normal and spanwise directions. Accordingly, Kelvin-Helmholtz (K-H) is hypothesised to be the dominant instability kind. Ergin and White (2006) note the growth rate of perturbations to increase with the roughness height. At supercritical $\mathcal{R}e_{hh}$, transition is attributed to the fact that disturbances grow at a rate larger than that at which the base flow relaxes and tends to stabilise them. Growth of unstable eigenmodes sustained by the shear layer surrounding the element's wake is a common observation among many authors despite considering different roughness shapes and flow regimes. This is for instance the case of Choudhari et al. (2009) when analysing a micro-ramp array, Choudhari et al. (2010) for a diamond-shaped element, De Tullio et al. (2013) in the case of a rectangular prism or Loiseau et al. (2014) for a cylindrical element. In particular, these authors identify by means of linear stability analysis two unstable eigenmodes, the so-called sinuous and varicose instabilities. Kegerise et al. (2012) and De Tullio et al. (2013) observe the varicose one to be the dominant kind, i.e., to grow faster. According to Loiseau et al. (2014), however, it depends on the aspect ratio of the roughness element which one plays the central role.

Rizzeta and Visbal (2007) reproduce numerically the experiments of Ergin and White (2006). A train of hairpin vortices (Acarlar and Smith, 1986) is observed to originate due to an instability of the spanwise shear layer. These grow rapidly and lead to chaotic behaviour and breakdown of the unstable shear layer. Loiseau et al. (2014) identify hairpin vortex shedding close to the roughness element originated due to the varicose instability and to cause rapid transition. Ye et al. (2016), however, report that hairpin vortices incepted close to a micro-ramp roughness element lift up and do not play a role in the ultimate transition mechanisms.

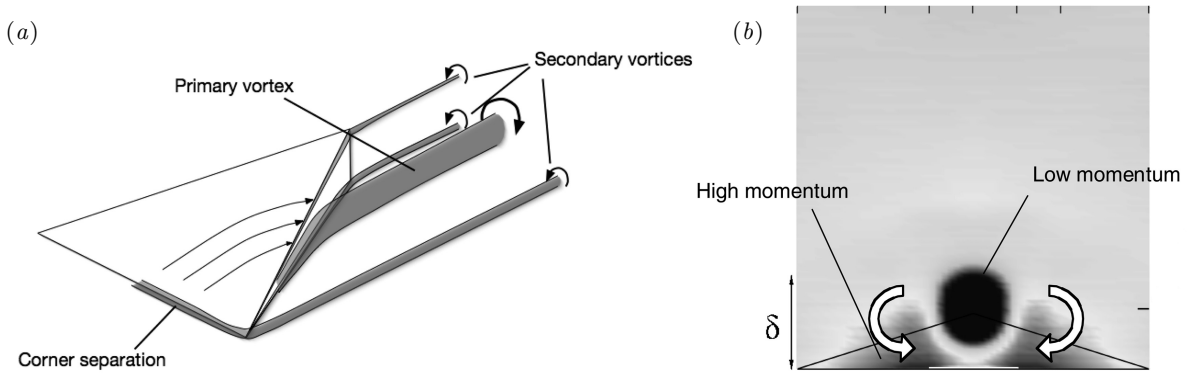

Figure 1.1: (*a*) micro-ramp geometry with vortex model as proposed by Babinsky et al. (2009). (*b*) illustration of the micro-ramp working principle according to Babinsky et al. (2009). Dark areas indicate momentum excess and deficit; arrows schematise the motion of the primary vortices; δ is the boundary layer height.

Instead, breakdown to turbulence is attributed to a second generation of hairpin vortices induced much downstream and near the wall.

Two different approaches are considered in this work to resolve flow physics, namely Linear Stability Theory (LST) and Direct Numerical Simulations (DNS). The first has already been introduced and aims to reveal the nature of flow instabilities developing close to the roughness element. When disturbances acquire sufficiently large amplitude, linear stability analysis loses its validity. Non-linear eigenmode evolution is then resolved via DNS. DNS computes the instantaneous flow field by numerically solving the Navier-Stokes equations without turbulence modelling. Since the computational grid has then to be fine enough to resolve all relevant flow structures, this method is computationally very expensive and is generally only used for simple geometries as for instance a single, isolated surface roughness element.

The main case analysed in this work considers a roughness element mounted on a flat plate and immersed in a nearly-incompressible boundary layer at Mach number $M = 0.2$. We have found little literature on roughness-induced transition in compressible boundary layers. This motivated the extension of the main analysis to a $M = 0.7$ boundary layer case (keeping fixed the roughness geometry and $\mathcal{R}e^{\star}_{hh}$) to additionally investigate the effects of compressibility.

1.2 The micro-ramp vortex generator

The roughness element used in this work is a micro-ramp vortex generator. The micro-ramp is a passive flow control device with potential for various aerodynamics applications (Lin, 2002). It is essentially a forward wedge; see figure 1.1(*a*). Fluid lifted at its leading edge falls from the slant edges and induces a pair of counter-rotating vortices, the primary vortex pair. This flow structure enhances the transport of momentum within the boundary layer. The term "micro" refers to the fact that, as opposed to conventional vortex generators, its height is lower than that of the undisturbed boundary layer. This results in less drag. Micro-ramps have furthermore gained interest due to their structural robustness. The choice of

this particular roughness shape for our analysis is motivated by the fact that bluff-fronted elements such as cylinders or hemispheres are standard geometries extensively investigated in the literature. A micro-ramp is wedge-shaped, for which less information is available.

An example of application of micro-ramp boundary layer trip is NASA's hypersonic vehicle X-43 (Hyper-X). An array of micro-ramps was proposed as tripping device in a $M = 7$ flight test. Turbulent engine inflow was desired due to better performance and robustness with respect to unstart of the propulsion system. Furthermore, transition to turbulence showed to reduce laminar separation at the compression ramps in the vehicle's forebody, which could have led to a reduction of mass captured by the engine (Berry and Auslender, 2001).

Anderson et al. (2006) report the wake of the micro-ramp to be dominated by counter-rotating vortices that alter the properties of the boundary layer and, in particular, reduce its shape factor. The boundary layer becomes better able to resist adverse pressure gradients. Babinsky et al. (2009) claim that the primary vortex pair produces an entrainment of high-momentum fluid towards the wall aside the centre plane, as schematised in figure 1.1(b). The boundary layer is made fuller and wall shear increases. This is the established consensus regarding the micro-ramp working principle. Babinsky et al. (2009) capture as well secondary vortices originated at the micro-ramp —see figure 1.1(a)— and strong momentum deficit at the centre plane. The latter, together with the primary vortex pair, are observed to gradually lift up due to vortex-induced upwash. Numerical experiments from Ghosh et al. (2010) and Lee et al. (2010) show agreement with flow topology presented by Babinsky et al. (2009). The primary vortex pair is confirmed responsible for producing momentum excess near the wall, and to persist far downstream (Ghosh et al., 2010). Li and Liu (2011) point out the central low-momentum dip to be generated by the action of primary vortices. Li and Liu (2010) discover a new structure in the micro-ramp wake: a train of arch-shaped vortices induced at the shear layer wrapping the central momentum deficit. Vortex shedding is attributed to K-H instability since the velocity profile has an inflection point.

Recent research efforts have focused on micro-ramps operating at turbulent and supersonic conditions due to the capability of the device in controlling shock-wave-boundary-layer interaction (Anderson et al., 2006; Babinsky et al., 2009; Blinde et al., 2009; Sun et al., 2012; Giepman et al., 2014). Tirtey et al. (2011), on a different scope, characterise the micro-ramp wake when it is immersed in a hypersonic and laminar boundary layer. Similar to previous references, a pair of counter-rotating vortices induced at the micro-ramp is identified as the main flow feature. They also detect secondary vortical structures aside the primary vortices, which rotate in an opposite sense. The overall wake shows to expand in spanwise direction. The occurrence of transition is attributed to the fact that the primary vortices amplify part of the disturbance field. Ye et al. (2016) and Ye (2017) recently assessed, for the first time, the transitional wake of a micro-ramp immersed in a laminar and incompressible boundary layer. One of the aims of this work is to numerically reproduce experimental results from Ye (2017) considering $\mathcal{R}e_{hh} = 460$. The time-averaged flow organisations presented by Ye et al. (2016) and Ye (2017) depict the primary vortex pair, as well as further pairs of secondary and tertiary vortices developing aside; see figure 1.2. Widely reported and common to all flow regimes is the fact that the primary vortices are observed to persist until far downstream, to induce central upwash and lateral downwash, and to gradually lift off from the surface. In the instantaneous flow field, Ye (2017) detects a train of vortices similar to that reported by Li and Liu (2010); secondary vortical structures growing in between are as well identified. The spanwise expansion of wake contamination is attributed to the latter. This is in line with

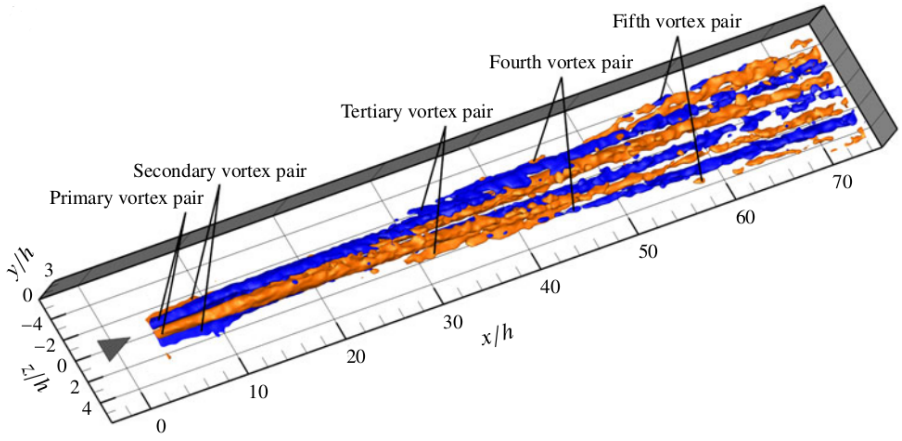

Figure 1.2: Streamwise vortices downstream the micro-ramp in the time-averaged configuration detected by streamwise vorticity (Ye et al., 2016).

observations from Tirtey et al. (2011).

The micro-ramp has been object of study for many researchers. There is generally consensus regarding the micro-ramp flow topology and on the fact that this device is capable of re-energising the lower part of the boundary layer and make it better able to resist adverse pressure gradients. Nonetheless, some authors have recently questioned the micro-ramp working principle. This is for instance the case of Wang et al. (2013), who claim that the primary vortices are not capable of entraining high-momentum fluid from the free-stream near the wall while developing downstream the micro-ramp. Instead, the mechanism which makes the boundary layer fuller relies on the exchange of fluid between low and mid portions of the boundary layer along the micro-ramp chord. Li and Liu (2011) assess the performance of the micro-ramp for shock-induced separation control. A reduction of the separation bubble is not attributed to increased wall shear due to primary vortex motion, but to the fact that arch-shaped vortices induced at the shear layer destroy the shock. Accordingly, Li and Liu (2011) suggest the micro-ramp to work differently from traditional vortex generators. Blinde et al. (2009) find no evidence of the primary vortices in the instantaneous flow field sufficiently far from the micro-ramp. Bo et al. (2012) point in a similar direction and hypothesise that the basic flow pattern is first consequence of the motion of the primary vortices and thereafter maintained by hairpin vortex dynamics.

Based on the above survey, the micro-ramp appears to play a double role with regard to boundary-layer-momentum enhancement. On the one hand, it generates a counter-rotating vortex pair which induces strong upwash and downwash. At the same time, however, this introduces a strong instability into the flow field which can lead to generation of large-scale hairpin vortices. In this work, we therefore put an extra focus on the role played by the primary vortices on the one hand and the transitional perturbation structures on the other hand in the transport of momentum near the wall. To segregate mechanisms, we decompose the flow field as $\boldsymbol{q} = \boldsymbol{q}_\mathrm{s} + \boldsymbol{q}'$, i.e., the steady laminar base flow and the time-dependant perturbation field following the LST approach. First, we compute DNS of the micro-ramp base flow, $\boldsymbol{q}_\mathrm{s}$, at supercritical $\mathcal{R}e_{hh}$. This allows for isolation of flow structures intrinsically contained in the system's steady state and a better understanding of their momentum-transport

capabilities. The particular interest of this decomposition for the current case is the fact that the primary vortex pair is an element of the base flow. Thereafter, we compute DNS of $\boldsymbol{q} = \boldsymbol{q}_s + \boldsymbol{q}'$. Upon comparison between $\boldsymbol{q}_s$ and time-averaged $\boldsymbol{q}$, differences can be attributed to the effect of perturbation development.

All in all, we aim to better understand relevant flow structures and transitional mechanisms present in the micro-ramp wake, as well as to shed light on the aforementioned controversy regarding the micro-ramp working principle. To our knowledge, this is the first attempt to perform DNS of the micro-ramp flow. This work may serve for future studies in which micro-ramps would be used for laminar flow control applications. Furthermore, the fact that we consider laminar and incompressible flow conditions may help to better characterise mechanisms which could be partially masked in more complex flow environments.

1.3 Unstable steady-state solutions to Navier-Stokes equations via Selective Frequency Damping

Previously, we have pointed out the interest in obtaining an accurate representation of the micro-ramp base flow. Steady-state solutions of the Navier-Stokes equations are also of interest in other flow applications. In Computational Fluid Dynamics (CFD), accurate base flow solutions may also serve as initial conditions, reducing the computational cost, and/or as boundary conditions, for absorbing layers or sponge zones (Teixeira and Alves, 2017). On a different scope, turbulent flows approached with the Reynolds-Averaged Navier-Stokes (RANS) equations may not accurately predict a flow phenomenon if time-independent solutions cannot be determined; an example for RANS of leading-edge stall is presented by Richez et al. (2016).

The difficulty in computing time-independent Navier-Stokes solutions arises for globally unstable flow fields, inasmuch as the instantaneous flow naturally diverges from the steady state (Åkervik et al., 2006). To overcome this obstacle, mainly two numerical methods are employed in the literature: Newton iteration methods (Knoll and Keyes, 2004) are the classical approach; however, these methods may have severe practical limitations due to the sensitivity to the initial guess and the required computational cost for large and strongly nonlinear systems (Cunha et al., 2015; Teixeira and Alves, 2017). In the past years, the Selective Frequency Damping (SFD) method developed by Åkervik et al. (2006) has arisen as a solid alternative. Its robustness and ease of implementation into existing time-stepping methods have made it increasingly popular to the point that it is generally the preferred method for aeronautical applications (Richez et al., 2016).

Based on control theory, SFD adds a linear forcing term to (1.2), which drives the flow field $\boldsymbol{q}$ towards $\boldsymbol{q}_s$ (Åkervik et al., 2006). As this target solution is not known beforehand, $\boldsymbol{q}_s$ is substituted by a low-pass filtered version of $\boldsymbol{q}$, denoted by $\bar{\boldsymbol{q}}$. The evolution equation for $\boldsymbol{q}$ is then rewritten as

$$\dot{\boldsymbol{q}} = f(\boldsymbol{q}) - \chi(\boldsymbol{q} - \bar{\boldsymbol{q}}), \qquad \chi \in \mathbb{R}^+. \tag{1.4}$$

The forcing is a linear reaction term proportional to the high-frequency content of the flow. Its effectiveness in quenching unstable frequencies and hence suppressing the associated instabilities depends on the feedback control coefficient χ. Åkervik et al. (2006) suggest an

exponential kernel filter to compute $\bar{\boldsymbol{q}}$. Since the implementation of the integral formulation of the filter would generally imply infeasible memory requirements in practice, its differential formulation is considered instead:

$$\dot{\bar{\boldsymbol{q}}} = \frac{\boldsymbol{q} - \bar{\boldsymbol{q}}}{\Delta}, \qquad \Delta \in \mathbb{R}^{+}. \tag{1.5}$$

The time constant Δ is related to the cut-off frequency (ω_c) of the low-pass filter through $\Delta = 1/\omega_c$. The performance of SFD depends on the two aforementioned parameters of the model, χ and Δ, which must be chosen as inputs of the simulation. Appropriate values depend on the flow problem and hence their selection is key to the method's effectiveness and efficiency as they determine the stability and convergence rate (Åkervik et al., 2006; Jordi et al., 2014, 2015; Cunha et al., 2015). Not every combination of χ and Δ guarantees that the flow field is driven towards the steady state, and even if so, the required computational time may be so large that the approach is impractical. Hence, how to select adequate χ and Δ is a common predicament in the literature.

SFD has nonetheless been very successfully applied to two- and three-dimensional flow configurations: Åkervik et al. (2006) first apply the method for stabilising a separation bubble with success and the steady solution of a confined separated flow is obtained by Åkervik et al. (2007). Pier (2008) compute the base flow around a sphere to analyse local and global instabilities developing in the wake. Schmid (2008) analyse the stability of the flow in a square cavity by using a reference solution computed with SFD. Bagheri et al. (2009) successfully apply SFD to stabilise a jet in crossflow and Fani et al. (2014) find the base flow for a three-dimensional T-mixer. Loiseau et al. (2014) study roughness-induced transition by performing stability analyses using base-flow solutions computed with SFD. More recently, Richez et al. (2016) apply SFD to stabilise RANS simulations of the turbulent separated flow around an airfoil at stall and Kurz and Kloker (2016) computed with SFD the steady state of a three-dimensional boundary layer over a swept wing with roughness elements. Significant contributions to the advancement of the methodology where published by Jordi et al. (2014), who develop an alternative SFD formulation, and Cunha et al. (2015), who develop an optimisation method for SFD simulations based on Dynamic Mode Decomposition (DMD).

The model parameters χ and Δ are commonly based on rough estimations introduced by Åkervik et al. (2006) or on parametric studies of simplified models. Jordi et al. (2014, 2015) used a scalar model problem to infer the behaviour of SFD when applied to a real flow problem. By using this model, Jordi et al. (2014) generate stability curves identifying the influence of χ and Δ and indicate that SFD is incapable of stabilising steady unstable eigenmodes, corroborating the results of Vyazmina (2010). It is observed that increasing χ may not always guarantee convergence, contrary to the consensus introduced by Åkervik et al. (2006). Jordi et al. (2015) hypothesise that the parameter values that optimise the scalar model problem also optimise the full flow problem and developed a coupled approach, which combines the computation of partially converged flow fields, stability analyses and parameter optimisation for the model problem. Cunha et al. (2015) use DMD of the controlled flow field to determine parameters that minimise the growth rate of the least stable DMD mode.

There are cases in which SFD reportedly failed (Vyazmina, 2010; Jones and Sandberg, 2011). It is claimed that cases in which the flow field presents steady unstable eigenmodes, SFD is unable to drive the simulation towards the steady state. Several authors indicate that too large χ yield infeasible simulation times (Cunha et al., 2015; Jones and Sandberg, 2011;

Åkervik et al., 2006). Massa (2014) and Teixeira and Alves (2017) report that stabilising a flow field that is unstable to more than one eigenmode can be a challenging task. In particular, Massa (2014) claim that SFD fails to converge towards the base flow if unstable eigenvalues with high amplification rates and low-frequency weakly unstable eigenvalues are both present in the flow field. In conclusion, a better understanding of χ and Δ is required to establish the feasibility of the method in the first place. In this work, we provide the first rigorous analysis of the effectivity and efficiency of SFD, leading to simple expressions and procedures for finding optimal χ and Δ values.

1.4 Research questions and objectives

Based on this literature review, we identify four relevant research questions, each of which is broken down into further sub-questions. First, in §3 we analyse the dynamics of SFD systems and scrutinise the role played by the SFD model parameters. We aim to answer the following questions:

Which values of χ and Δ are effective and most efficient to compute with SFD the steady state of a globally unstable flow field?

1. Does SFD fail to stabilise systems with unstable steady eigenmodes?
2. Does the feasibility of the method depend on specific eigenvalue properties?
3. Given an adequate Δ, does increasing χ always yield a stabilised system?
4. How can multiple discrete unsteady eigenmodes be accounted for?

In §4, we analyse the micro-ramp flow dynamics. First, in §4.2 we examine the base flow topology and try to provide answers to the following questions:

How is the base flow organisation of a micro-ramp immersed in a laminar and incompressible boundary layer at low supercritical $\mathcal{R}e_{hh}$ conditions?

1. Which are the main flow features?
2. Can the laminar primary vortex pair keep a sustained entrainment of high-momentum fluid towards the wall?
3. Do secondary vortical structures arise?
4. What is the origin of the regions of momentum excess and momentum deficit (measured with respect to the unperturbed boundary layer)?

Finally, in §4.3 and in §4.4 we analyse the topology of the instantaneous and mean flow fields and intend to answer the following questions:

What are the stability characteristics of the micro-ramp wake?

1. What flow regions are susceptible to instability growth?

2. Can stability analysis accurately represent the dynamics of small-amplitude perturbations and match results from DNS in the linear perturbation regime?

How are the instantaneous and mean flow organisations downstream of a micro-ramp immersed in a laminar and incompressible boundary layer at low supercritical $\mathcal{R}e_{hh}$ conditions?

1. Which are the main instantaneous flow structures?
2. How is the organisation of the base flow altered by the presence of transitional perturbations? Are there major differences between base and mean flow fields?
3. Is the primary vortex pair sustained in the instantaneous flow field?
4. Which flow features contribute most significantly to the enhancement of momentum transport and, in particular, to the transport of high-momentum fluid near the wall?
5. What is the main working principle of the micro-ramp?

Accordingly, the main goals of the present work are to:

- Implement Selective Frequency Damping (SFD) into TU Delft's in-house code INCA.
- Investigate how the SFD input parameters χ and Δ ought to be chosen to effectively and efficiently stabilise globally unstable flow configurations.
- Test the SFD implementation by computing the steady state of a two-dimensional incompressible cylinder flow at $\mathcal{R}e = 100$.
- Compute using Direct Numerical Simulations (DNS) and analyse the base flow of a micro-ramp immersed in a laminar $M = 0.2$ boundary layer at low supercritical $\mathcal{R}e_{hh}$ conditions.
- Compute using Direct Numerical Simulations (DNS) and analyse the instantaneous transitional $M = 0.2$ micro-ramp flow at low supercritical $\mathcal{R}e_{hh}$ conditions. Identify differences with base flow results.
- Compare the results of micro-ramp DNS with tomographic PIV experiments carried out for the same set-up and with results from linear stability analysis applied to the SFD-computed base flow.
- Extend the analysis to a micro-ramp flow problem considering a laminar $M = 0.7$ boundary layer.

Chapter 2

Methodology

2.1 Formulation of problems

2.1.1 Governing equations and state variables

The non-linear equations ruling the dynamics of a fluid system are of the form $\dot{\boldsymbol{q}} = f(\boldsymbol{q})$ (1.2). For an incompressible two-dimensional flow field, the case of the cylinder flow problem analysed in this work, the vector of state variables $\boldsymbol{q}$ reads

$$\boldsymbol{q}(x, y, t) = [u(x, y, t)\ v(x, y, t)]^{\mathrm{T}}. \tag{2.1}$$

For a compressible three-dimensional flow field, the case of our micro-ramp flow problem, the vector of state variables is then of the form

$$\boldsymbol{q}(x, y, z, t) = [\rho(x, y, z, t)\ \rho u(x, y, z, t)\ \rho v(x, y, z, t)\ \rho w(x, y, z, t)\ \rho e_{\mathrm{t}}(x, y, z, t)]^{\mathrm{T}}. \tag{2.2}$$

For the cylinder case, u represents the streamwise velocity component and v the velocity component perpendicular to it. For the micro-ramp case, u is kept as streamwise velocity, v is taken as wall-normal velocity and w represents the spanwise velocity. These variables together form the velocity vector field, denoted by $\boldsymbol{v}$. The density field is denoted by ρ and e_{t} represents total energy. Concerning the coordinate system, x is defined as streamwise direction, y is the direction orthogonal to it in the cylinder case and the wall-normal direction in the micro-ramp case, z is the span-wise direction; see figures 2.2 and 2.4.

In the incompressible regime, the motion of a Newtonian fluid flow with viscosity μ is described by a system of non-linear partial differential equations which impose conservation of mass and momentum. This system reads

$$\nabla \cdot \boldsymbol{v} = 0, \tag{2.3}$$

$$\rho \frac{\partial \boldsymbol{v}}{\partial t} + \rho\,(\boldsymbol{v} \cdot \nabla)\,\boldsymbol{v} = -\nabla p + \mu \nabla^2 \boldsymbol{v}. \tag{2.4}$$

After taking the divergence of (2.4) and combining it with divergence-free condition (2.3), one obtains a coupling between pressure, p, and velocity:

$$\nabla^2 p = -\nabla \cdot (\boldsymbol{v} \cdot \nabla \boldsymbol{v}) \,. \tag{2.5}$$

In incompressible fluid systems, $f(\boldsymbol{q}) = -(\boldsymbol{v} \cdot \nabla)\,\boldsymbol{v} - (1/\rho)\,\nabla p + \nu \nabla^2 \boldsymbol{v}$, $\nu = \mu/\rho$.

In the compressible regime, the system of partial differential equations which describes the motion of a Newtonian fluid flow adds an extra equation, the energy conservation equation, and reads

$$\frac{\partial \rho}{\partial t} + \nabla \cdot (\rho \boldsymbol{v}) = 0, \tag{2.6}$$

$$\frac{\partial (\rho \boldsymbol{v})}{\partial t} + \nabla \cdot (\rho \boldsymbol{v}\boldsymbol{v}) = -\nabla p + \nabla \cdot (\boldsymbol{\tau}_{\mathrm{v}}) \,, \tag{2.7}$$

$$\frac{\partial (\rho e_{\mathrm{t}})}{\partial t} + \nabla \cdot (\rho e_{\mathrm{t}} \boldsymbol{v}) = -\nabla \cdot (p \boldsymbol{v}) - \nabla \cdot \boldsymbol{q}_{\mathrm{h}} + \nabla \cdot (\boldsymbol{v} \boldsymbol{\tau}_{\mathrm{v}}) \,, \tag{2.8}$$

with the stress tensor, $\boldsymbol{\tau}_{\mathrm{v}}$, and heat flux, $\boldsymbol{q}_{\mathrm{h}}$, computed as

$$\boldsymbol{\tau}_{\mathrm{v}} = \mu \left(\nabla \boldsymbol{v} + (\nabla \boldsymbol{v})^{\mathrm{T}} - \frac{2}{3} \nabla \cdot \boldsymbol{v} \boldsymbol{I} \right), \tag{2.9}$$

$$\boldsymbol{q}_{\mathrm{h}} = -\kappa \nabla T, \tag{2.10}$$

considering Stokes' hypothesis and Fourier's law. T is temperature, κ denotes thermal conductivity, $\boldsymbol{I}$ is the identity matrix. In compressible fluid systems, $f(\boldsymbol{q})$ is then taken as the RHS of (2.6), (2.7), (2.8) when operators of the form $\partial/\partial t$ are isolated on the LHS.

For compressible flows, an extra equation is required to close the system, the equation of state. Assuming a calorically perfect gas,

$$p = (\gamma - 1) \left(\rho e_{\mathrm{t}} - \frac{1}{2} \rho ||\boldsymbol{v}||^2 \right), \tag{2.11}$$

with γ being the ratio of specific heats. Finally, viscosity is related to the temperature following a power law,

$$\mu = \mu_\infty \left(\frac{T}{T_\infty} \right)^{0.75} . \tag{2.12}$$

Thermal conductivity is related to the Prandtl number,

$$\kappa = \frac{c_p \mu}{Pr}, \qquad c_p = \frac{\gamma R}{\gamma - 1}. \tag{2.13}$$

Assuming the fluid to be air, $Pr = 0.72$, $R = 287\ m^2/(s^2 K)$, $\gamma = 1.4$.

2.1.2 Formal definition of relevant flow quantities

We next define relevant flow variables used in the analysis of results presented in this work, and which have not been introduced previously. Vorticity, $\boldsymbol{\omega}(x, y, z, t)$, and shear, $s(x, y, z, t)$, are computed by numerically differentiating the velocity field using finite differences. Vorticity is obtained as the curl of the velocity field,

$$\boldsymbol{\omega} = \nabla \times \boldsymbol{v}. \tag{2.14}$$

Shear is a scalar field defined as the Frobenius norm of the strain-rate tensor, i.e.,

$$s = ||\frac{1}{2}\left(\nabla \boldsymbol{v} + (\nabla \boldsymbol{v})^{\mathrm{T}}\right)||_{\mathrm{F}}. \tag{2.15}$$

In the micro-ramp case, for large $|z/h|$ (h represents the micro-ramp height) denoted by z_{un}/h, the velocity field behaves as a two-dimensional boundary layer without flow distortions introduced by the micro-ramp. The state variables vector in this so-called unperturbed region is denoted by

$$\boldsymbol{q}_{\mathrm{un}}(x, y) = \boldsymbol{q}(x, y, z_{\mathrm{un}}). \tag{2.16}$$

Let the streaks field, $\boldsymbol{q}^{\mathrm{str}}(x, y, z, t)$, then be defined as

$$\boldsymbol{q}^{\mathrm{str}} = \boldsymbol{q} - \boldsymbol{q}_{\mathrm{un}}. \tag{2.17}$$

Instantaneous state variables are obtained as the instantaneous solution of $f(\boldsymbol{q})$. Steady-state solutions computed via SFD are taken as the instantaneous converged $\bar{\boldsymbol{q}}$. Time-averaged state variables, $\langle \boldsymbol{q} \rangle$, are computed as follows:

$$\langle \boldsymbol{q} \rangle = \frac{1}{t_1 - t_0} \int_{t_0}^{t_1} \boldsymbol{q}\, dt, \tag{2.18}$$

with t_0 and t_1 being the initial and final time instants over which a variable is time-averaged. By subtracting the base flow to the mean flow we obtain the so-called mean-flow distortion:

$$\langle \boldsymbol{q} \rangle^{\mathrm{d}} = \langle \boldsymbol{q} \rangle - \boldsymbol{q}_s. \tag{2.19}$$

In the present work, we differentiate between the instantaneous perturbation field measured with respect to the base flow (1.3) or with respect to the mean flow. The latter, denoted by $\boldsymbol{q''}$, is obtained as

$$\boldsymbol{q''} = \boldsymbol{q} - \langle \boldsymbol{q} \rangle\,. \tag{2.20}$$

The shape factor of the boundary layer, in its incompressible form, is defined as

$$H = \frac{\delta^\star}{\theta}, \tag{2.21}$$

with

$$\delta^\star = \int_0^\infty \left(1 - \frac{u}{u_\infty}\right) dy \tag{2.22}$$

and

$$\theta = \int_0^\infty \frac{u}{u_\infty}\left(1 - \frac{u}{u_\infty}\right) dy. \tag{2.23}$$

2.2 The SFD Framework

2.2.1 Original SFD formulation

We now introduce the theoretical background of SFD dynamics. The mathematical and numerical tools described next will be used to model, predict and optimise the behaviour of SFD simulations. SFD equations (1.4) and (1.5) can be discretised using any time-marching scheme. In case of convergence, $\boldsymbol{q}$ and $\bar{\boldsymbol{q}}$ have the same steady state, $\dot{\boldsymbol{q}}_s = \dot{\bar{\boldsymbol{q}}}_s = 0$ and $\boldsymbol{q}_s = \bar{\boldsymbol{q}}_s$. We therefore can use the difference between them as convergence criterion $\epsilon_{\mathrm{R}} = ||\boldsymbol{q} - \bar{\boldsymbol{q}}||_{L_2}$, with ϵ_{R} representing the so-called SFD residual of the simulation. As time progresses and $\epsilon_{\mathrm{R}} \to 0$, the linear forcing term in (1.4) approaches zero and the steady solution of (1.4) becomes identical to that of (1.2). This guarantees that no artificial base flow solutions are created in spite of the fact that the system is changed. The (linear) dynamics of the modified system can be addressed through the linearisation of (1.4) and (1.5) yielding:

$$\begin{bmatrix} \dot{\boldsymbol{q}}' \\ \dot{\bar{\boldsymbol{q}}}' \end{bmatrix} = \underbrace{\begin{bmatrix} \boldsymbol{J} - \chi \boldsymbol{I} & \chi \boldsymbol{I} \\ \frac{\boldsymbol{I}}{\Delta} & -\frac{\boldsymbol{I}}{\Delta} \end{bmatrix}}_{\boldsymbol{G}} \begin{bmatrix} \boldsymbol{q}' \\ \bar{\boldsymbol{q}}' \end{bmatrix}, \tag{2.24}$$

where $\bar{\boldsymbol{q}}'$ indicates the perturbation of the $\bar{\boldsymbol{q}}$ field, $\boldsymbol{J}$ denotes the Jacobian of $f(\boldsymbol{q})$ around $\boldsymbol{q}_s$. The relation between the eigenvalues $\mu = \mu_r + \mathrm{i}\mu_i$ of the original system, $-\mathrm{i}\boldsymbol{J}$, with the eigenvalues $\lambda = \lambda_r + \mathrm{i}\lambda_i$ of the modified system, $-\mathrm{i}\boldsymbol{G}$, was derived by Åkervik et al. (2006) and is here rewritten as

$$\lambda_{1,2} = \frac{1}{2}\left(\mu - \mathrm{i}\chi - \frac{\mathrm{i}}{\Delta} \pm \frac{\mathrm{i}}{\Delta}\sqrt{(1 - \Delta[\mathrm{i}\mu + \chi])^2 + 4\chi\Delta}\right), \qquad \mu, \lambda \in \mathbb{C}. \tag{2.25}$$

The subindices of $\lambda_{1,2}$ express that every original eigenvalue μ is mapped onto two λ eigenvalues. This is a consequence of doubling the dimension of the system by introducing $\bar{\boldsymbol{q}}$. Garnaud et al. (2012) derived an expression for the inverse mapping, which maps the λ's back onto the μ's:

$$\mu = \lambda + \mathrm{i}\chi\left(1 - \frac{1}{1 - \mathrm{i}\lambda\Delta}\right). \tag{2.26}$$

The time independence of the linearised system permits prescribing the following ansatz for the perturbation field

$$\boldsymbol{q}'(\boldsymbol{x}, t) = \sum_{j=-\infty}^{\infty} A_j \underbrace{\tilde{\boldsymbol{q}}_j(\boldsymbol{x})\mathrm{e}^{-\mathrm{i}\mu^j t}}_{\boldsymbol{p}'_j(\boldsymbol{x},t)}, \quad A_j \in \mathbb{C}, \tag{2.27}$$

where A_j is the amplitude coefficient, and $\tilde{\boldsymbol{q}}_j(\boldsymbol{x})$ is the complex valued shape function corresponding to the j^{th} eigenvalue μ^j (Schmid and Henningson, 2001; Theofilis, 2003) and $\mu^{-j} = -\overline{\mu^j}$. Accordingly, an eigenmode with associated eigenvalue μ is stable if $\mu_i < 0$, neutral if $\mu_i = 0$, and unstable if $\mu_i > 0$. The variable $\boldsymbol{p}'_j = \tilde{\boldsymbol{q}}_j(\boldsymbol{x})\mathrm{e}^{-\mathrm{i}\mu^j t}$ is introduced to include the temporal behaviour of the eigenmode.

The same exponential dichotomy applies to λ when considering the controlled SFD eigenspectrum. In that case $\tilde{\tilde{\boldsymbol{q}}}$ represents the shape function corresponding to the eigenvalue λ. Åkervik et al. (2006) observe that the controlled eigenvalues $\lambda_{1,2}$ have associated eigenvectors $\tilde{\tilde{\boldsymbol{q}}}_{1,2}$ which are a phase-shifted version of $\tilde{\boldsymbol{q}}$. In fact $\tilde{\tilde{\boldsymbol{q}}}_{1,2} = \beta_{1,2}\tilde{\boldsymbol{q}}$, where

$$\beta_{1,2} = 1 + \frac{\lambda_{1,2} - \mu}{\mathrm{i}\chi}. \tag{2.28}$$

This illustrates that the SFD eigenvalue problem does not introduce new eigenfunction shapes. The exponential temporal behaviour associated to $\tilde{\tilde{\boldsymbol{q}}}_j$ will be expressed as $\bar{\boldsymbol{p}}'_j$.

2.2.2 *Encapsulated* formulation of SFD

The encapsulated formulation of SFD (hereafter referred to as ESFD) described by Jordi et al. (2014) allows the application of SFD without modifying the core of CFD solvers. ESFD separates the linear and non-linear parts of (1.4) and (1.5):

$$\begin{bmatrix} \dot{\boldsymbol{q}} \\ \dot{\bar{\boldsymbol{q}}} \end{bmatrix} = \begin{bmatrix} f(\boldsymbol{q}) \\ \boldsymbol{0} \end{bmatrix} + \begin{bmatrix} -\chi\boldsymbol{I} & \chi\boldsymbol{I} \\ \dfrac{\boldsymbol{I}}{\Delta} & -\dfrac{\boldsymbol{I}}{\Delta} \end{bmatrix} \begin{bmatrix} \boldsymbol{q} \\ \bar{\boldsymbol{q}} \end{bmatrix} = \begin{bmatrix} f(\boldsymbol{q}) \\ \boldsymbol{0} \end{bmatrix} + \boldsymbol{T}\boldsymbol{D}\boldsymbol{T}^{-1} \begin{bmatrix} \boldsymbol{q} \\ \bar{\boldsymbol{q}} \end{bmatrix} \tag{2.29}$$

with

$$\boldsymbol{D} = \begin{bmatrix} \boldsymbol{0} & \boldsymbol{0} \\ \boldsymbol{0} & -\left(\chi + \dfrac{1}{\Delta}\right)\boldsymbol{I} \end{bmatrix} \qquad \text{and} \qquad \boldsymbol{T} = \begin{bmatrix} \boldsymbol{I} & -\chi\Delta\boldsymbol{I} \\ \boldsymbol{I} & \boldsymbol{I} \end{bmatrix}. \tag{2.30}$$

The non-linear subsystem contains the Navier-Stokes operator f, whose implementation in a CFD solver is represented by the functional Φ, that maps the discrete solution from a temporal state t^n to $t^{n+1} = t^n + \tau$. The linear subsystem is integrated analytically over the time step τ:

$$\begin{bmatrix} (\boldsymbol{q}^\star)^{n+1} \\ (\bar{\boldsymbol{q}}^\star)^{n+1} \end{bmatrix} = \begin{bmatrix} \Phi(\boldsymbol{q}^n) \\ \bar{\boldsymbol{q}}^n \end{bmatrix}; \quad \begin{bmatrix} \boldsymbol{q}^{n+1} \\ \bar{\boldsymbol{q}}^{n+1} \end{bmatrix} = \underbrace{\boldsymbol{T}\mathrm{e}^{\boldsymbol{D}\tau}\boldsymbol{T}^{-1}}_{\boldsymbol{H}} \begin{bmatrix} (\boldsymbol{q}^\star)^{n+1} \\ (\bar{\boldsymbol{q}}^\star)^{n+1} \end{bmatrix}, \tag{2.31}$$

where $\boldsymbol{q}^\star$ and $\bar{\boldsymbol{q}}^\star$ represent intermediate solutions of (1.4) and (1.5) when applying the splitting method and

$$\boldsymbol{H} = \frac{1}{1+\chi\Delta} \begin{bmatrix} \boldsymbol{I} + \chi\Delta\boldsymbol{I}\mathrm{e}^{-\left(\chi+\frac{1}{\Delta}\right)\tau} & \chi\Delta\boldsymbol{I}\left(1 - \mathrm{e}^{-\left(\chi+\frac{1}{\Delta}\right)\tau}\right) \\ \boldsymbol{I} - \boldsymbol{I}\mathrm{e}^{-\left(\chi+\frac{1}{\Delta}\right)\tau} & \chi\Delta\boldsymbol{I} + \boldsymbol{I}\mathrm{e}^{-\left(\chi+\frac{1}{\Delta}\right)\tau} \end{bmatrix} = \begin{bmatrix} h_{11}\boldsymbol{I} & h_{21}\boldsymbol{I} \\ h_{12}\boldsymbol{I} & h_{22}\boldsymbol{I} \end{bmatrix}. \tag{2.32}$$

2.2.3 Parametrisation of the behaviour of SFD

Equation (2.25) links the linearised dynamics of the original system and that of the controlled system. For a complete characterisation of the functionality of SFD, it is necessary to establish another link between the exact linearised system dynamics and the discrete numerical solutions. First and foremost, a main objective is to find χ and Δ that stabilise the

numerically represented system. However, the inverse approach is also of interest. When a simulation performed using SFD does not converge towards the base flow, it may be because the flow's inherent unsteady nature is not completely quenched (physical instability), due to the numerical methods used to integrate the controlled system (numerical instability), or a combination of both.

Cunha et al. (2015) state that, under certain conditions, the spectral properties of (2.24) can be represented as superposition of mono-modal problems, for which (2.24) is assumed equivalent to

$$\begin{bmatrix} \dot{\boldsymbol{p}}'_j \\ \dot{\bar{\boldsymbol{p}}}'_j \end{bmatrix} = \underbrace{\begin{bmatrix} (-\mathrm{i}\mu^j - \chi)\boldsymbol{I} & \chi\boldsymbol{I} \\ \dfrac{\boldsymbol{I}}{\Delta} & -\dfrac{\boldsymbol{I}}{\Delta} \end{bmatrix}}_{\boldsymbol{G}_j} \begin{bmatrix} \boldsymbol{p}'_j \\ \bar{\boldsymbol{p}}'_j \end{bmatrix}, \qquad j = 1, 2, \ldots, \infty. \tag{2.33}$$

Two main approaches are presented next to characterise the eigenvalues α associated to an SFD simulation. By integrating (2.33) between two temporal states t^n and t^{n+1}, one obtains

$$\begin{bmatrix} (\boldsymbol{p}'_j)^{n+1} \\ (\bar{\boldsymbol{p}}'_j)^{n+1} \end{bmatrix} = \mathrm{e}^{\boldsymbol{G}_j\tau} \begin{bmatrix} (\boldsymbol{p}'_j)^{n} \\ (\bar{\boldsymbol{p}}'_j)^{n} \end{bmatrix} = \boldsymbol{B}_j \begin{bmatrix} (\boldsymbol{p}'_j)^{n} \\ (\bar{\boldsymbol{p}}'_j)^{n} \end{bmatrix}, \qquad j = 1, 2, \ldots, m. \tag{2.34}$$

The exact eigenvalues of $\boldsymbol{B}_j = \mathrm{e}^{\boldsymbol{G}_j\tau}$ are

$$\alpha^j_{\mathrm{ex}_{1,2}} = \mathrm{e}^{-\mathrm{i}\lambda^j_{1,2}\tau}. \tag{2.35}$$

We see that only pairs of χ and Δ values which locate all $\lambda_{1,2}$ in the lower half-plane lead to convergence.

The ESFD formulation applied to (2.33) can be written as

$$\begin{bmatrix} (\boldsymbol{p}'_j)^{n+1} \\ (\bar{\boldsymbol{p}}'_j)^{n+1} \end{bmatrix} = \underbrace{\begin{bmatrix} h_{11}\boldsymbol{I} & h_{21}\boldsymbol{I} \\ h_{12}\boldsymbol{I} & h_{22}\boldsymbol{I} \end{bmatrix} \begin{bmatrix} \sigma^j\boldsymbol{I} & \boldsymbol{0} \\ \boldsymbol{0} & \boldsymbol{I} \end{bmatrix}}_{\boldsymbol{C}_j} \begin{bmatrix} (\boldsymbol{p}'_j)^{n} \\ (\bar{\boldsymbol{p}}'_j)^{n} \end{bmatrix} \quad j = 1, 2, \ldots, m. \tag{2.36}$$

Accordingly, $\sigma^j \in \mathbb{C}$ takes the role of Φ and represents the operator that numerically integrates the subsystem defined by $\dot{\boldsymbol{p}}'_j = -\mathrm{i}\mu^j \boldsymbol{p}'_j$, such that $(\boldsymbol{p}'^{\star}_j)^{n+1} = \sigma^j (\boldsymbol{p}'_j)^n$ in the intermediate step of ESFD. Examples of possible expressions for σ^j are:

$$\begin{aligned} \sigma^j &= \mathrm{e}^{-\mathrm{i}\mu^j\tau} && \text{(exact solver)}, \\ \sigma^j &= 1 - \mathrm{i}\mu^j\tau && \text{(explicit Euler)}, \\ \sigma^j &= 1 - \mathrm{i}\mu^j\tau - \tfrac{1}{2}(\mu^j\tau)^2 + \tfrac{1}{6}\mathrm{i}(\mu^j\tau)^3 && \text{(3rd-order explicit Runge-Kutta)}. \end{aligned}$$

The coefficients h_{11}, h_{12}, h_{21} and h_{22} are linked to the action of the filter and the proportional controller in (1.4) and (1.5) and σ^j condenses the information of the numerical time marching scheme. Therefore, the combined physical and numerical stability is characterised through the eigenvalues of $\boldsymbol{C}_j$, which read

$$\alpha^j_{\mathrm{num}_{1,2}} = \frac{1}{2}\left(h_{11}\sigma^j + h_{22} \pm \sqrt{(h_{11}\sigma^j - h_{22})^2 + 4h_{12}h_{21}\sigma^j} \right). \tag{2.37}$$

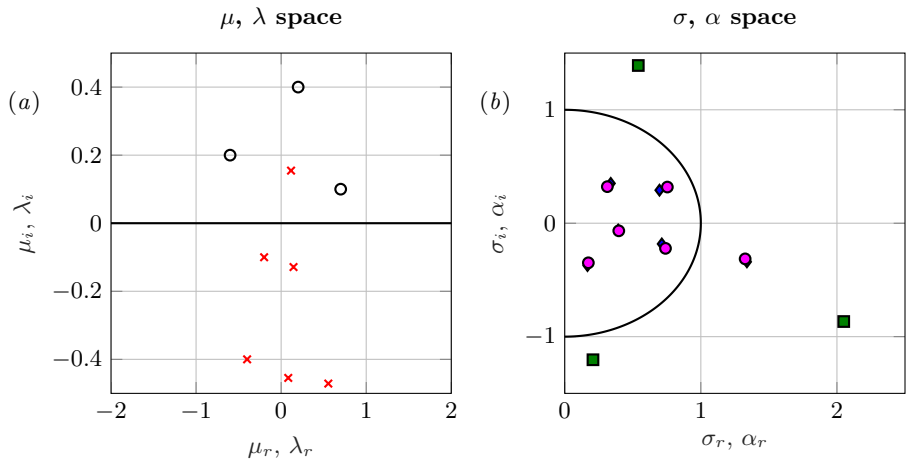

Figure 2.1: Eigenvalue spaces relevant in SFD: μ (empty circles), λ (red crosses), σ (green squares), α_{ex} (purple circles) and α_{num} (blue diamonds). $\mu^j = 0.2+0.4\text{i};\ -0.6+0.2\text{i};\ 0.7+0.1\text{i}$, $\sigma^j = \mathrm{e}^{-\text{i}\mu^j\tau}$, $\chi = 0.5$, $\Delta = 5$ and $\tau = 2$.

The numerical solution of (1.4) and (1.5) can only converge towards the steady state if all $\alpha^j_{\text{num}_{1,2}}$ satisfy $|\alpha^j_{\text{num}_{1,2}}| < 1$.

The different eigenvalue spaces are summarised in figure 2.1. The original formulation of SFD, in which the coupled problem is solved without discretisation and splitting error, is represented by a $\mu \mapsto \lambda \mapsto \alpha_{\text{ex}}$ mapping. ESFD corresponds to a $\mu \mapsto \sigma \mapsto \alpha_{\text{num}}$ mapping. Even with an exact time marching method, $\sigma^j = \mathrm{e}^{-\text{i}\mu^j\tau}$, $\alpha_{\text{num}} \neq \alpha_{\text{ex}}$ due to the fact that

$$\begin{bmatrix} -\text{i}\mu^j & 0 \\ 0 & 0 \end{bmatrix} \text{ and } \begin{bmatrix} -\chi & \chi \\ 1/\Delta & -1/\Delta \end{bmatrix}$$

do not commute and thus $\boldsymbol{B}_j \neq \boldsymbol{C}_j$; see (Jordi, 2015). However, $\alpha_{\text{num}} \to \alpha_{\text{ex}}$ as $\tau \to 0$ and accordingly α_{ex} is considered representative for α_{num} if conditionally stable time marching methods are used.

The characterisation of the eigenvalues α and the structure of the discretised system presented above allows to parametrise the evolution of the residual of an SFD simulation. After an initial transient, $\epsilon_R(t)$ follows an exponential trend proportional to the growth rate of the least stable eigenvalue of the controlled eigenspectrum, which we denote by λ^{s}.

2.3 Set-up of the cylinder DNS

The DNS of the cylinder flow presented in this work have been performed using the Finite-Volume (FV) Immersed Boundary Method (IBM) (Meyer et al., 2010) TU Delft in-house code INCA (Hickel et al., 2014). A diameter-based Reynolds number $\mathcal{R}e = u_\infty D/\nu_\infty = 100$ is considered. The cylinder has unit diameter, $D = 1$. The two-dimensional fluid domain extent is $-16D \leq x \leq 25D$ in the streamwise direction and $-22D \leq y \leq 22D$ in the transverse direction, which matches the domain used by Barkley (2006); the centre of the cylinder is located at $(0, 0)$. The structured mesh contains 5.1×10^5 hexahedral cells, with smooth hyperbolic refinement towards the cylinder in x and y directions. A uniform inflow of

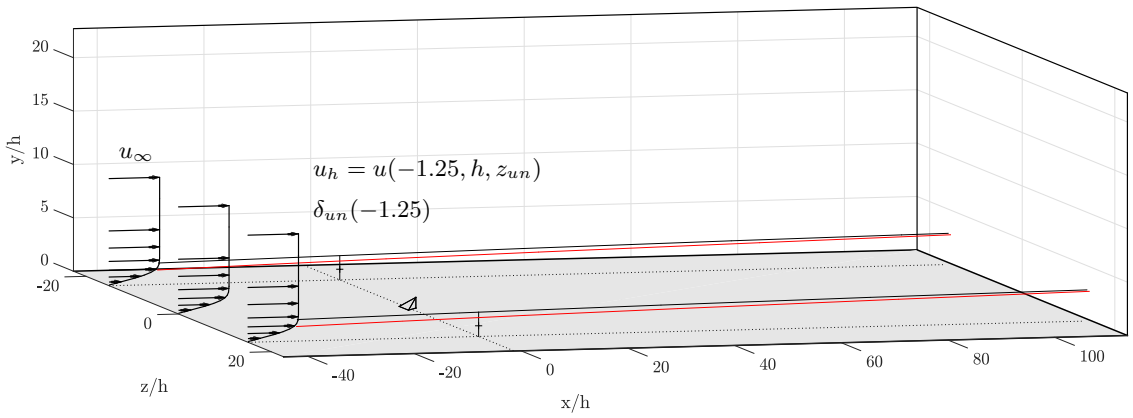

Figure 2.2: Sketch of the micro-ramp flow problem containing the micro-ramp geometry, inlet $M = 0.2$ laminar boundary layer profiles (computed at $x/h = -45.44$ and plotted at $z/h = 0$ and $z/h = \pm 15$) and height of the undisturbed boundary layer developing in streamwise direction for $M = 0.2$ (black) and $M = 0.7$ (red) configurations. Ticks indicating the micro-ramp height at $z = z_{\text{un}}$. Domain size matches the computational box.

$u_\infty = 1$ is imposed at the inlet, the total pressure is fixed at the outlet, no-slip conditions are applied at the surface of the cylinder, and symmetry conditions are imposed at the transverse boundaries. The Navier-Stokes equations are discretised in time using an explicit third-order Runge-Kutta (RK) method (Gottlieb et al., 2001) with CFL = 1; the flow field is initialised at a uniform streamwise velocity. A global time-stepping approach is used, since we are interested in studying the global properties of the flow field in time. ESFD is used to compute the base solution.

2.4 Set-up of the micro-ramp DNS

2.4.1 Micro-ramp geometry and problem definition

Figure 2.2 schematises the micro-ramp flow problem simulated in this work. The three-dimensional fluid domain extent is $-45h \leq x \leq 114h$ in streamwise direction, $0h \leq y \leq 23h$ in wall-normal direction, and $-23h \leq z \leq 23h$ in spanwise direction. The micro-ramp tip is located at $(0, 0, 0)$. The domain size is chosen such that boundaries are sufficiently far from the micro-ramp and we are conservative enough to capture all relevant physical phenomena.

Case	$\mathcal{R}e_h$	$\mathcal{R}e_{hh}$	$\mathcal{R}e^\star_{hh}$	h/δ_{un}	u_h/u_∞
Incompressible (Ye, 2017)	700	468	468	0.44	0.67
$M = 0.2$ DNS	700	463	461	0.44	0.67
$M = 0.7$ DNS	700	506	469	0.54	0.77

Table 2.1: Comparison of boundary layer parameters between Ye (2017) and the current work.

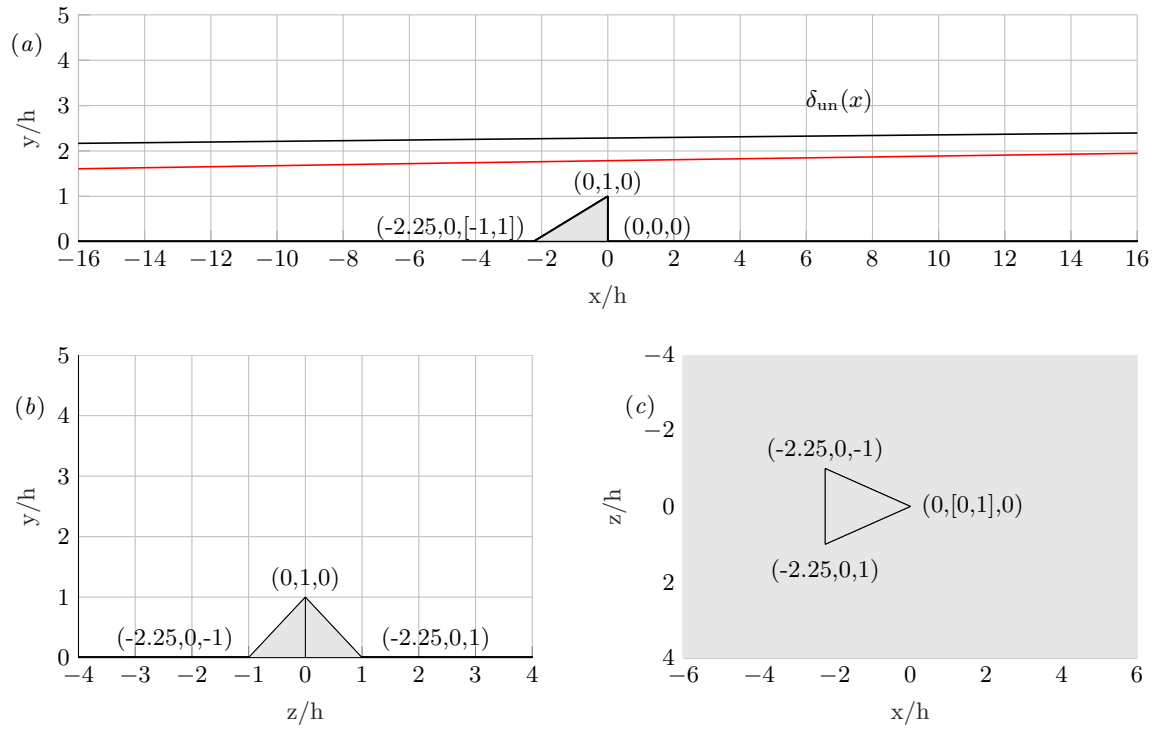

Figure 2.3: Micro-ramp geometry with coordinates of the vertices and projected edges. (*a*) lateral view and height of the undisturbed boundary layer for $M = 0.2$ (black) and $M = 0.7$ (red) configurations, (*b*) back view, (*c*) top view.

Based on the literature survey, especial concerns are the upward shift of the micro-ramp wake and the fact that Ye (2017) reports first inception of turbulent spots at $x/h \approx 70$.

The micro-ramp is mounted on a flat plate. A laminar compressible two-dimensional boundary layer develops along the surface. It is obtained as solution of the self-similar compressible Blasius boundary layer (White, 2006) and imposed as initial condition in SFD simulations. Unsteady micro-ramp simulations running without SFD use the converged steady-state solution $\bar{\boldsymbol{q}}$ as initial condition. We highlight the fact that even though we consider the physics of the $M = 0.2$ case to be of quasi-incompressible nature, all micro-ramp simulations presented in this work are solved using the compressible Navier-Stokes equations.

We impose the boundary layer height at the inlet to be such that we match values of $\mathcal{R}e_{hh}$ reported by Ye (2017); that is $\delta = 1.92h$ and $\delta = 1.57h$ at $x/h = -45$ for $M = 0.2$ and $M = 0.7$ cases respectively. Boundary layer parameters extracted from current DNS are summarised in table 2.1 and compared with those reported by Ye (2017). It ought to be emphasised that Ye (2017) computes the roughness Reynolds number based on flow properties evaluated at $x/h = -1.25$, $y/h = 1$, thus slightly upstream the micro-ramp tip. For the sake of consistency we follow this convention. The micro-ramp height is denoted by h, δ_{un} is the boundary layer height at $z = z_{un}$ and $u_h = u(-1.25h, h, z_{un})$. The parameter $\mathcal{R}e_h$ follows a more conventional definition of the Reynolds number and reads $\mathcal{R}e_h = u_\infty h/\nu_\infty$. There is 1% difference between $\mathcal{R}e_{hh}$ reported by Ye (2017) and $\mathcal{R}e_{hh}$ considered in this work. There is 1.7% difference in $\mathcal{R}e^\star_{hh}$ between current $M = 0.2$ and $M = 0.7$ configurations. The micro-ramp is, for all cases, well-immersed within the boundary layer. We note the boundary layer in the $M = 0.2$ case

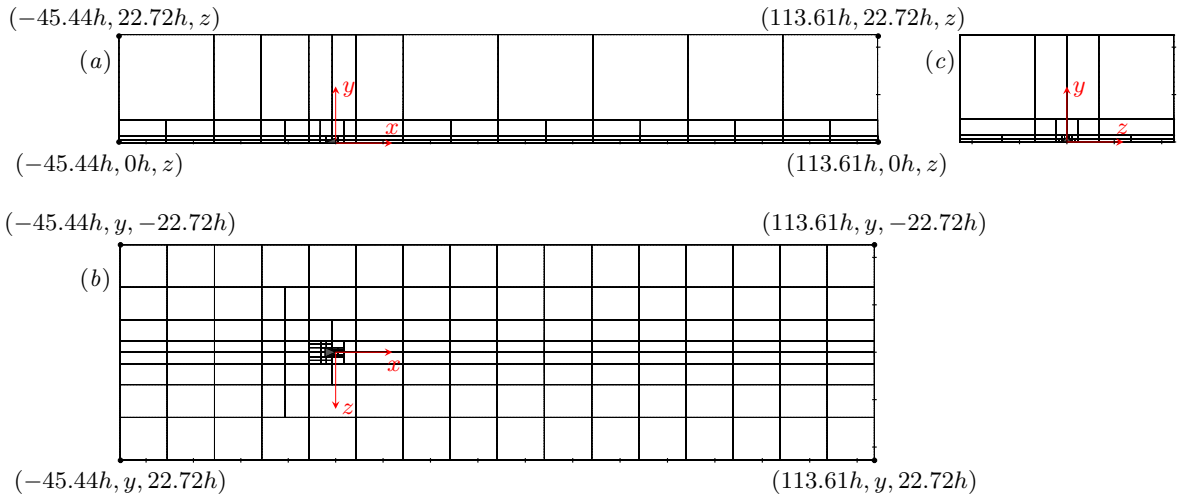

Figure 2.4: Computational domain with the micro-ramp geometry, axis orientation, coordinates of the external vertices, and grid blocks. Edge ticks with $10h$ spacing starting from the origin. (a) lateral view, (b) top view, (c) front view.

to be thicker than that of the $M = 0.7$ case at the micro-ramp tip for a fixed $\mathcal{R}e^{\star}_{hh}$; see figure 2.3($a$). This is supposedly consequence of the stabilising effect of compressibility.

Figure 2.3 shows the micro-ramp geometry. It has the same dimensions as that used by Ye (2017), which is one of the most reported in the literature (Anderson et al., 2006; Giepman et al., 2014). The micro-ramp span and chord are $2h$ and $2.25h$ respectively. The aspect ratio of the element is then 0.5. Following empirical correlations of Klebanoff et al. (1955) and von Doenhoff and Braslow (1961), the approximate lower and upper limits of critical $\mathcal{R}e_{hh}$ are 455 and 682 respectively. This implies that our analysis considers a supercritical Reynolds roughness number, just above the critical value. Therefore we expect transition to occur.

2.4.2 Grid topology and numerical set-up

Figure 2.4 illustrates the computational domain. It is divided in 430 blocks defined via Adaptative Mesh Refinement (AMR) and contains 5.66×10^6 hexahedral cells. The structured grid is highly refined around the micro-ramp and near the wall, as detailed in figure 2.5. We obtain $y^+ < 1$ in these regions. Besides in the near-wall and near-ramp regions, it is important to include a sufficiently large number of grid points in flow regions featuring large shear. A poor resolution of shear layers may lead to underestimation of their strength and thus inaccurate computation of instability growth. We find, *a posteriori*, a too steep grid coarsening in spanwise direction at $x/h = 4.25$. Based on post-processing results, this is observed to yield inaccuracies in the computed flow variables around this streamwise coordinate. It remains unclear whether this has a significant impact on the resolved instabilities.

Alike the cylinder case, DNS of the micro-ramp flow have been performed using the Finite-Volume approach and the Immersed Boundary Method to model the blockage of the micro-

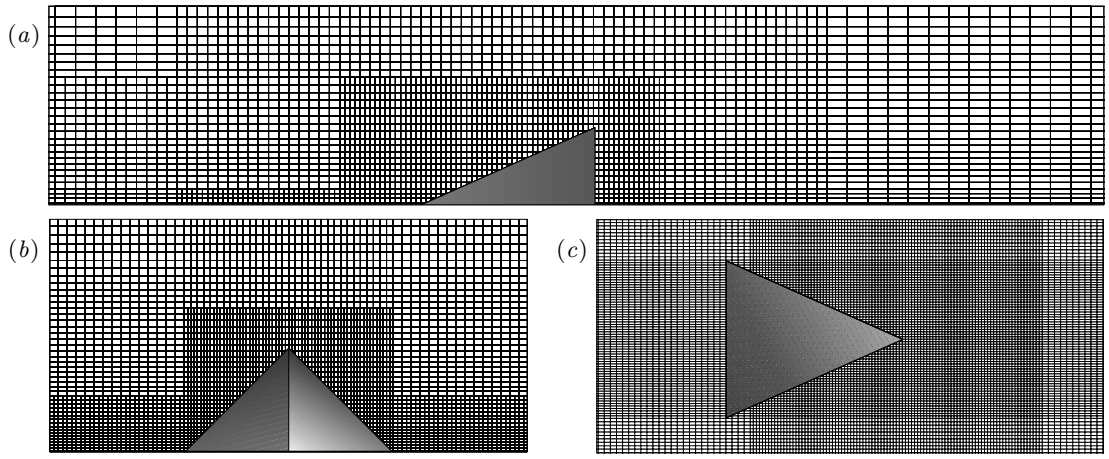

Figure 2.5: Grid refinement around the micro-ramp geometry. (*a*) lateral view, (*b*) back view, (*c*) top view.

ramp. Regarding the boundary conditions, we specify a Riemann inflow condition with a Blasius boundary layer for target at the inlet. A Riemann inflow condition is imposed at the top boundary as well, targeted to $u_\infty = 1$. We prescribe outflow at the outlet, i.e., $\partial^2 \boldsymbol{v}/\partial x^2 = 0$ and $\partial p/\partial x = 0$, while symmetric conditions are applied at the transverse boundaries. We impose non-slip conditions at the wall and at the micro-ramp surface. The flat plate is set to be adiabatic. As a consequence, we expect different wall temperatures in the $M = 0.2$ and $M = 0.7$ configurations. According to Redford et al. (2010), wall temperature plays an important role in the transition process. This effect aims to be condensed by fixing $\mathcal{R}e^{\star}_{hh}$, as proposed by Bernardini et al. (2012). We use a 5th-order Weighted Essentially Non-Oscillatory (WENO) (Liu et al., 1994) with an HLLC flux function (Toro et al., 1994). The aforementioned is summarised in table 2.2. The compressible Navier-Stokes equations are marched in time using a third order explicit RK method with CFL = 1. We use a global time-stepping approach for the same reason as for the cylinder case and ESFD to compute the micro-ramp base flow. We choose the SFD residual to serve as stopping criterion for steady-state simulations.

Case	Inlet	Top	Outlet	Wall	Spatial discretisation
$M = 0.2$	Blasius ($\delta = 1.92h$)	$u_\infty = 1$	outflow	adiabatic non-slip	5th-order WENO HLLC
$M = 0.7$	Blasius ($\delta = 1.57h$)	$u_\infty = 1$	outflow	adiabatic non-slip	5th-order WENO HLLC

Table 2.2: Boundary conditions and spatial discretisation schemes.

2.5 Linear Stability Analysis

For validation purposes, the system's transient behaviour and stability obtained from the DNS is compared with the results from linear stability analyses (Schmid and Henningson, 2001; Theofilis, 2011; Groot, 2013) for both the the cylinder and the micro-ramp cases. The author wants to especially thank Henry J. Tol and Koen J. Groot for providing the results of the linear stability analyses presented in this work.

In the cylinder case, we apply global stability analysis assuming the perturbation field to behave as specified in (2.27). The stability analysis is performed for the base flow obtained from the instantaneous converged solution of the ESFD simulation. A Galerkin projection of the linearised incompressible Navier-Stokes equations is performed to obtain an explicit discrete expression for the Jacobian $\boldsymbol{J}$ and to form the eigenvalue problem. The global eigenspectrum for the uncontrolled and controlled flow is respectively obtained as the eigenvalues of the matrices $-\mathrm{i}\boldsymbol{J}$ and $-\mathrm{i}\boldsymbol{G}$. The stability analysis is performed on the domain $-5D \leq x \leq 20D$, $-12.5D \leq y \leq 12.5D$. An unperturbed flow is assumed at both the cylinder, the inflow boundary and the transverse boundaries. A stress-free condition is prescribed at the outflow boundary. For the spatial discretisation, third-order C^0 multivariate spline elements (de Boor, 1987; Lai and Schumaker, 2007) are used to represent the velocity field. The pressure is eliminated from the equations by using a space of velocity fields that are divergence free and a suitable choice of the variational formulation. Details regarding the numerical method are provided in Tol et al. (2016).

In the micro-ramp case, we apply spanwise BiGlobal stability analysis (Groot, 2013). In spite of the rather simple formulation of the three-dimensional perturbation problem (2.27), the numerical resolution of the associated large matrix system for the three-dimensional micro-ramp case is very expensive. Assumptions can be introduced to alleviate its computational cost. In spanwise BiGlobal stability analysis, the base flow is assumed to be homogeneous in streamwise direction, i.e., $\partial \boldsymbol{q}_s/\partial x = 0$, and the stability problem is solved in a fluid plane. Under this hypothesis (which is questionable close to the micro-ramp), eigenmode amplitude in this direction is treated as a modal wave. The perturbation ansatz then reads

$$\boldsymbol{q'}(\boldsymbol{x},t) = \sum_{j=-\infty}^{\infty} A_j \tilde{\boldsymbol{q}}_j(y,z) \mathrm{e}^{\mathrm{i}\left(\xi^j x - \mu^j t\right)}, \quad A_j \in \mathbb{C}, \quad \xi_j \in \mathbb{C}, \quad \mu_j \in \mathbb{C}, \tag{2.38}$$

with ξ^j being the streamwise wavenumber and μ^j the eigenvalues of the Jacobian matrix linearised around a spanwise fluid plane. Introducing ansatz (2.38) into the linearised form of $f(\boldsymbol{q})$, with adequate boundary conditions, leads to an eigenvalue problem. The Arnoldi algorithm is then used to compute the 100 most unstable eigenmodes. Incompressible BiGlobal stability analysis is applied to full y-z planes of the instantaneous ESFD converged $M = 0.2$ micro-ramp solution. The stability problem is discretised using a Chebyshev spectral collocation method. Further details regarding the current numerical set-up can be found in Groot (2013) and Groot et al. (2016).

Chapter 3

Steady-State Solutions to Navier-Stokes Equations via SFD

3.1 Analysis overview

In this chapter, we aim to answer the following question: how should the input parameters χ and Δ be chosen to effectively and efficiently stabilise an unstable flow problem with SFD? This is addressed by analysing the influence of χ and Δ to the functionality of SFD. First, in §3.2 we mathematically describe the behaviour of SFD systems, derive useful properties, and present analytical expressions of χ and Δ which virtually always stabilise a flow problem ruled by one unstable eigenmode. This analysis is extended to flow systems supporting multiple unstable eigenmodes. In §3.3 we introduce a new technique, named as *flow unleash*, which serves to characterise the properties of the unstable eingenmode of the flow. In §3.4 we present a parameter optimisation method. We derive analytical expressions for χ and Δ which minimise the spectral radius of an SFD simulation under certain conditions. This is tested by stabilising the wake of the $\mathcal{R}e = 100$ cylinder flow problem described in §2.3.

3.2 Role of χ and Δ

3.2.1 Effective stabilisation of isolated unstable eigenmodes

We analyse the role played by χ and Δ in the performance of SFD by studying the $\mu \mapsto \lambda$ mapping (2.25). It relates the eigenvalues of an uncontrolled system $f(\boldsymbol{q})$, with the eigenvalues of its controlled SFD version. In §2.2 we have shown that SFD convergence can only be achieved if χ and Δ yield λ with $\lambda_i < 0$ for all μ. For the sake of simplicity, we first assume that only one instability mode is present in the flow field. The stabilisation of flow configurations with more than one unstable eigenmode is tackled in §3.2.2.

The eigenvalues of the controlled system, $\lambda_{1,2}$, are the solutions of the quadratic equation

$$\lambda^2 + \left(\mathrm{i}\left(\chi + \frac{1}{\Delta}\right) - \mu\right)\lambda - \frac{1}{\Delta}\mathrm{i}\mu = 0, \tag{3.1}$$

from which the two useful expressions

$$\lambda_1 + \lambda_2 = \mu - \mathrm{i}\left(\chi + \frac{1}{\Delta}\right) \quad \text{and} \quad \lambda_1\lambda_2 = -\frac{1}{\Delta}\mathrm{i}\mu \tag{3.2}$$

can be immediately derived by using Vieta's formulas.

Åkervik et al. (2006) indicate that χ should be larger than the growth rate of the unstable modes present in the flow field and that $1/\Delta$ ought to be smaller than the frequency of these modes. Following ansatz (2.27), modal growth rate and frequency are respectively identified with the imaginary and the real part of the system's eigenvalues. We denote with μ^{c} the most unstable eigenvalue associated to a flow configuration. As $\mu_i^{\mathrm{c}} > 0$, the parameters are expected to scale with μ^{c}, in such a way that $\chi \sim \mu_i^{\mathrm{c}}$ and $1/\Delta \sim \mu_r^{\mathrm{c}}$. Accordingly, 3.2 can be rewritten in non-dimensional form considering the following change of variables:

$$\hat{\chi} = \frac{\chi}{\mu_i^{\mathrm{c}}}, \qquad \hat{\Delta} = \Delta\mu_r^{\mathrm{c}}, \qquad \hat{\lambda}_r = \frac{\lambda_r}{\mu_r^{\mathrm{c}}}, \qquad \hat{\lambda}_i = \frac{\lambda_i}{\mu_i^{\mathrm{c}}}, \tag{3.3}$$

such that

$$\hat{\lambda}_{1,r} + \hat{\lambda}_{2,r} = 1, \quad \hat{\lambda}_{1,r}\hat{\lambda}_{2,r} - \left(\frac{\mu_i^{\mathrm{c}}}{\mu_r^{\mathrm{c}}}\right)^2 \hat{\lambda}_{1,i}\hat{\lambda}_{2,i} = \frac{\mu_i^{\mathrm{c}}}{\mu_r^{\mathrm{c}}}\frac{1}{\hat{\Delta}}, \tag{3.4}$$

$$\hat{\lambda}_{1,i} + \hat{\lambda}_{2,i} = 1 - \hat{\chi} - \left(\frac{\mu_i^{\mathrm{c}}}{\mu_r^{\mathrm{c}}}\right)^{-1}\frac{1}{\hat{\Delta}}, \quad \hat{\lambda}_{1,i}\hat{\lambda}_{2,r} + \hat{\lambda}_{1,r}\hat{\lambda}_{2,i} = -\left(\frac{\mu_i^{\mathrm{c}}}{\mu_r^{\mathrm{c}}}\right)^{-1}\frac{1}{\hat{\Delta}}. \tag{3.5}$$

It becomes obvious that the non-dimensional expressions that define the $\mu \mapsto \lambda$ mapping depend only on the single non-dimensional parameter $(\mu_i^{\mathrm{c}}/\mu_r^{\mathrm{c}})$; the equations are self-similar when $\mu_i^{\mathrm{c}}/\mu_r^{\mathrm{c}}$ is kept constant.

By operating on (2.25) and (3.2), the following asymptotic behaviour can be derived:

$$\left.\begin{array}{l} \lim\limits_{\chi\to 0} \lambda_{\mathrm{n}} = \mu \\ \lim\limits_{\chi\to 0} \lambda_{\mathrm{a}} = -\dfrac{\mathrm{i}}{\Delta} \end{array}\right\} \qquad \left\{\begin{array}{l} \lim\limits_{\chi\to\infty} \lambda_1 = 0 \\ \lim\limits_{\chi\to\infty} \lambda_2 = \mu_r - \mathrm{i}\infty \end{array}\right. \tag{3.6}$$

which reveal the structure of the two λ branches resulting from the complex square root in (2.25). In the limit when $\chi \to 0$ (linear forcing vanishes), one class of λ solutions corresponds to each of the natural μ eigenvalues, hence denoted by λ_{n}. The complementary λ_{a} eigenvalues are artificial solutions associated to the filter and degenerate to a point located at $-\mathrm{i}/\Delta$ if $\chi \to 0$. When $\chi \to \infty$, one set of λ solutions tends to minus infinity in their imaginary part and μ_r in their real part, while there is another group that moves towards the origin. The notation λ_1 and λ_2 in (3.6) shall indicate that it is generally not possible to continuously track the natural branch (i.e., the one associated to μ when $\chi \to 0$) or the artificial branch (i.e., the one associated to $-\mathrm{i}/\Delta$ when $\chi \to 0$) when $\chi \to \infty$. This is illustrated in figure 3.1(b). A major part of the analysis presented in this section relies on this asymptotic behaviour. The complementary limiting behaviour in terms of Δ is

$$\left.\begin{array}{l} \lim\limits_{\Delta\to\infty} \lambda_1 = 0 \\ \lim\limits_{\Delta\to\infty} \lambda_2 = \mu - \mathrm{i}\chi \end{array}\right\} \qquad \left\{\begin{array}{l} \lim\limits_{\Delta\to 0} \lambda_{\mathrm{n}} = \mu \\ \lim\limits_{\Delta\to 0} \lambda_{\mathrm{a}} = 0 - \mathrm{i}\infty \end{array}\right. \tag{3.7}$$

The present approach is limited to flow fields ruled by instabilities with $\mu_r \neq 0$, which is conform with the low-pass filter nature of the stabilisation term. Many authors conclude that SFD is unable to stabilise steady eigenmodes (Vyazmina, 2010; Jordi et al., 2014; Cunha et al., 2015). This is confirmed by analysing the $\mu \mapsto \lambda$ mapping, when imposing $\mu = \mathrm{i}\mu_i$. For this particular case, the $\lambda_{1,2}$ solutions are always purely imaginary and never intersect with each other. Recalling (3.2), $\lambda_{1,i}\lambda_{2,i} = -\mu_i/\Delta$ and if $\mu_i > 0$, regardless of χ and Δ, it is impossible to place both $\lambda_{1,2}$ solutions within the stable region.

Another fundamental property of SFD is that a stable μ will never be mapped towards the upper semi-plane. By manipulating the expression of the inverse mapping, (2.26), a criterion can be derived relating the real parts of μ and the associated $\lambda_{1,2}$ solutions:

$$\frac{\mu_r}{\lambda_r} = 1 + \frac{\chi\Delta}{(1+\lambda_i\Delta)^2 + (\lambda_r\Delta)^2} \geq 1, \tag{3.8}$$

which proves that μ_r, $\lambda_{1,r}$ and $\lambda_{2,r}$ share signs and that $|\lambda_r| \leq |\mu_r|$. By using this result and imposing $\mu_i < 0$, the real part of (3.2) requires that $\lambda_{1,i}\lambda_{2,i} > 0$. The imaginary part of (3.2) conclusively requires $\lambda_{1,i} < 0$ and $\lambda_{2,i} < 0$, proving the statement of Åkervik et al. (2006), that stable μ eigenvalues cannot yield unstable $\lambda_{1,2}$ solutions. Based on the problem symmetry illustrated by (3.8), we generalise the analyses considering μ^{c} with $\mu_r^{\mathrm{c}} > 0$ and hence $\mu_i^{\mathrm{c}}/\mu_r^{\mathrm{c}} > 0$. However, all results are equally valid if $\mu_r^{\mathrm{c}} < 0$.

Next, it is analysed how each $\lambda_{1,2}$ solution evolves by fixing Δ at different discrete positive values, taking χ as a real continuous variable with $\chi \in [0, \infty)$ and assuming $\mu_r^{\mathrm{c}} \neq 0$; see figure 3.1($a$). Figure 3.1($b$) contains four pairs of branches representative of the whole λ solution space. Figure 3.1(c) complements the results with the gradients with respect to χ of the $\lambda_{1,2}$ solution branches, i.e.,

$$\frac{\partial\lambda_{1,2}}{\partial\chi} = \frac{1}{2}\mathrm{i}\left(-1 \pm \frac{\Delta(\mathrm{i}\mu+\chi)+1}{\sqrt{(1-\Delta[\mathrm{i}\mu+\chi])^2 + 4\chi\Delta}}\right). \tag{3.9}$$

For every μ with $\mu_r \neq 0$, there exists a unique pair of real and positive χ and Δ values for which $\lambda_1 = \lambda_2 = \lambda^\star$. These special SFD parameters are hereafter denoted by $\chi^\star$ and $\Delta^\star$. The case $\Delta = \Delta^\star$, represented by the solid black line in figure 3.1, establishes a threshold separating two main trends of the solution branches. Considering $\Delta < \Delta^\star$, the natural branch approaches the origin as χ grows, whereas the artificial branch tends to $-\mathrm{i}\infty$. The dash-dotted line and the dotted line in figure 3.1 correspond to subcritical cases following the aforementioned trend. The dash-dotted natural branch never crosses the real axis; the associated eigenvalues never become stable. On the other hand, there is a specific χ-range for which the dotted branch of natural λ solutions are located within the stable region. For sufficiently large χ values, the dotted natural branch solution crosses the real axis a second time. The real axis is not crossed for larger χ, so increasing the control coefficient further will be counterproductive. For $\Delta > \Delta^\star$, the overall trend is inverse; the artificial branch approaches 0 from the upper semi-plane when $\chi \to \infty$, whereas the natural branch tends to $-\mathrm{i}\infty$. The dashed line in figure 3.1 is representative of this supercritical behaviour. Besides the structure of the branches, another relevant difference exists between subcritical and supercritical cases. For $\Delta < \Delta^\star$ the dominant eigenvalue is always associated with the natural branch, thus changing continuously with χ. Contrarily, for $\Delta > \Delta^\star$ this role switches

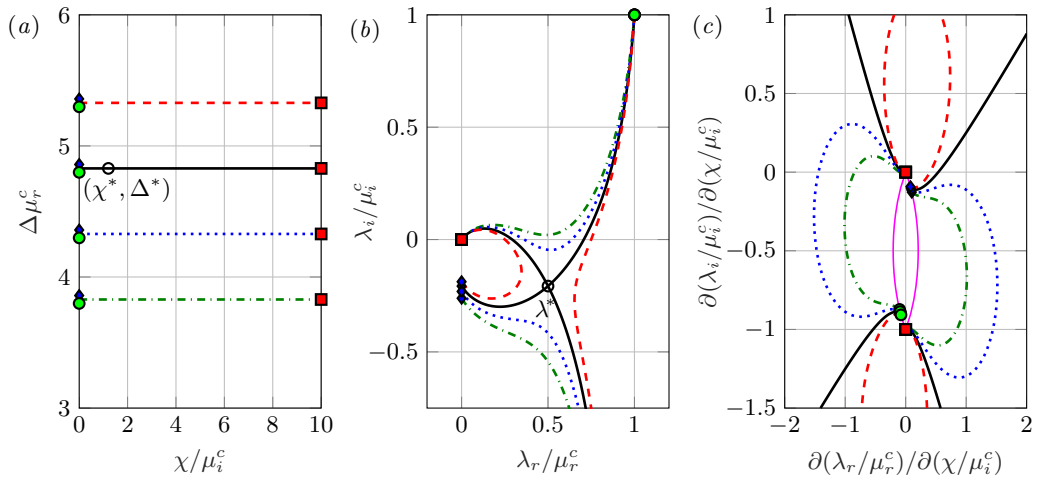

Figure 3.1: (*a*) χ and Δ, (*b*) solution branches in the λ space and (*c*) solution branches in the $\partial\lambda/\partial\chi$ space. Start of the natural branches (green circles), start of the artificial branches (blue diamonds), end points of all solutions (red squares), coordinates of $\chi^\star$ and $\Delta^\star$ in (*a*) and $\lambda^\star$ in (*b*) (empty circles). $\Delta\mu^c = 3.83$ (dash-dotted green), 4.33 (dotted blue), 4.83 (solid black), 5.33 (dashed red). Curve encompassing all start and end points of the $\partial\lambda_{1,2}/\partial\chi$ branches in (*c*) (magenta).

from one branch to the other; as χ is increased, the artificial branch claims dominance over the natural branch as the imaginary parts of the eigenvalues intersect.

Åkervik et al. (2006) claim that very large χ will always drive the system towards the base solution, but possibly at a low convergence rate. The present results prove that this is not the case. Regardless of whether the case is subcritical or supercritical, there is always a branch that for large χ approaches the origin from above, yielding unstable eigenvalues. In figure 3.1(*c*), the branches of the gradient field approaching 0 for growing χ cross the real axis close to the origin, and thereafter always yield $\partial\lambda_i/\partial\chi < 0$. This may, at a first glance, seem surprising as we just proved that no stable μ can be mapped onto the unstable region; however, a λ solution associated to an *unstable* μ eigenvalue may switch from one region to another depending on the selected values of χ and Δ.

These results, which are graphically observed in figure 3.1, can also be proven by considering the complex argument of $\lambda_1\lambda_2 = -\frac{1}{\Delta}\mathrm{i}\mu$ (3.2),

$$\varphi_1 + \varphi_2 = \arg\left(-\frac{1}{\Delta}\mathrm{i}\mu\right) = -\arctan\left(\frac{\mu_r}{\mu_i}\right) = \arctan\left(\frac{\mu_i}{\mu_r}\right) - \frac{\pi}{2} = \varphi_\mu - \frac{\pi}{2} \tag{3.10}$$

with φ_1 and φ_2 denoting the arguments of λ_1 and λ_2 respectively; φ_μ represents the argument associated to the eigenvalue μ. Equation (3.10) shows that for a given μ, the sum of the arguments of the $\lambda_{1,2}$ solutions is constant and independent of χ and Δ. In particular, (3.10) implies that the constant value must correspond to $\varphi_1+\varphi_2$, and can be conveniently evaluated for $\chi \to 0$, where the angle associated to the natural solution is φ_μ and the angle associated to the artificial solution is $\arg(-\mathrm{i}/\Delta) = -\pi/2$. Evaluating the $\lambda_{1,2}$ solutions for $\chi \to \infty$,

(3.10) becomes

$$\lim_{\chi\to\infty}\varphi_1+\lim_{\chi\to\infty}\varphi_2=\lim_{\chi\to\infty}\varphi_1+\underbrace{\lim_{\lambda_{2,i}\to-\infty}\left(\arctan\left(\frac{\lambda_{2,i}}{\mu_r}\right)\right)}_{-\pi/2}=\varphi_\mu-\frac{\pi}{2}, \tag{3.11}$$

assuming, without loss of generality, that $\mu_r^{\mathrm{c}}>0$. This conclusively implies:

$$\lim_{\chi\to\infty}\varphi_1=\varphi_\mu=\arctan\left(\frac{\mu_i}{\mu_r}\right). \tag{3.12}$$

That is, the solution branch that approaches the origin follows an asymptote having the same argument as μ. If $\mu_i>0$, $\varphi_\mu>0$ and the least stable branch always approaches 0 from the upper semi-plane. Thus, choosing large χ yields unstable behaviour of the system.

With all, the key ingredient to find adequate SFD parameters is that the critical point

$$\lambda^\star=\frac{1}{2}\mu_r^{\mathrm{c}}-\frac{\mathrm{i}}{\Delta^\star} \tag{3.13}$$

is always located within the stable region, regardless of μ^{c}. When applying

$$\chi^\star=\frac{|\mu^{\mathrm{c}}|+\mu_i^{\mathrm{c}}}{2}, \tag{3.14}$$

$$\Delta^\star=\frac{2}{|\mu^{\mathrm{c}}|-\mu_i^{\mathrm{c}}} \tag{3.15}$$

as parameters of the model, the associated $\lambda_{1,2}$ solutions are both mapped towards $\lambda^\star$ and hence they are always located in the real direction at half of the real part of μ^{c} and at an imaginary coordinate coinciding with the origin of the artificial branch; see figure 3.1(b). Due to the fact that $\lambda^\star$ is located in the lower half-plane for any unstable μ^{c}, the parameter choice $\chi=\chi^\star$ and $\Delta=\Delta^\star$ will always stabilise the linear flow problem in an exponential sense, asymptotically in time.

3.2.2 Stabilisation of systems with more than one unstable eigenmode

The parameters $\chi^\star$ and $\Delta^\star$ always stabilise a flow field ruled by one unstable eigenvalue μ^{c}, under the condition $\mu_r^{\mathrm{c}}\neq 0$. The present section extends the analysis to cases ruled by more than one unstable eigenmode. It is initially assumed that N unstable μ eigenvalues associated to the uncontrolled system are located in the upper half-plane. The most unstable eigenvalue, i.e., the one with the highest growth rate μ_i, is denoted by μ^{c}, while the other unstable eigenvalues are denoted by μ^{k}, $\mathrm{k}\in\{1,2,\ldots,\mathrm{N}-1\}$, and satisfy $\mu_i^{\mathrm{c}}\geq\mu_i^{\mathrm{k}}>0$. The proposed methodology relies on applying $\chi^\star$ and $\Delta^\star$ as parameters of the model using μ^{c} in (3.14) and (3.15), due to the fact that μ^{c} is by definition the most critical eigenvalue to be stabilised. Thereafter, the part of the μ space that is mapped into the stable region is analytically determined.

For that purpose, (3.2) is used in combination with two restrictive conditions: the model parameters are determined as $\chi=\chi^\star(\mu^{\mathrm{c}})$ and $\Delta=\Delta^\star(\mu^{\mathrm{c}})$ and the bounding curve of the stability domain (loci of neutral stability) is determined by imposing that either $\lambda_{1,i}=0$ or $\lambda_{2,i}=0$. The results are independent of the latter choice due to the symmetry of the problem. Two intermediate results can be immediately derived:

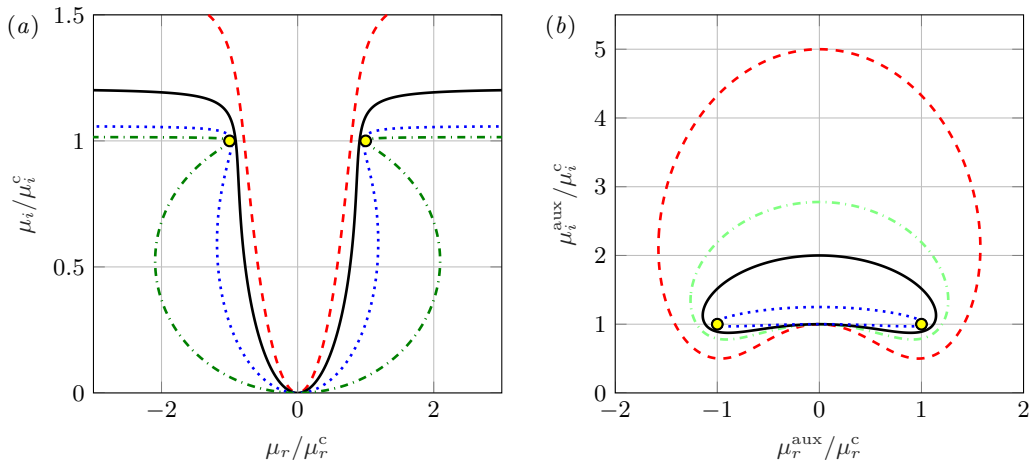

Figure 3.2: Stability curves in the μ space using (3.17). (*a*) μ eigenvalues mapped towards neutral λ_1 or λ_2 with $\chi = \chi^\star(\mu^c)$ and $\Delta = \Delta^\star(\mu^c)$. (*b*) regions encompassing μ^{aux} for which $\chi = \chi^\star(\mu^{aux})$ and $\Delta = \Delta^\star(\mu^{aux})$ will stabilise μ^c. μ_i^c/μ_r^c: 0.5 (dashed red); 0.75 (dash-dotted light green); 1 (solid black); 2 (dotted blue) and 4 (dashed-dotted dark green). μ^c (yellow circles).

1. For a generic unstable μ, when one of its associated λ solutions lies on the real axis, the complementary λ solution is stable. This validates the usage of the condition $\lambda_{1,i} = 0$ or $\lambda_{2,i} = 0$ to define stability regions in the μ space.

2. The complementary λ solution satisfies

$$\lambda_r \mu_r = -\lambda_i \mu_i, \tag{3.16}$$

   meaning that the lines connecting the origin of the complex plane with a generic unstable μ and its associated stable λ are orthogonal.

The geometrical curve encompassing the μ eigenvalues for which one λ solution is neutral satisfies

$$\left(\frac{\mu_i}{\mu_r}\right)^3 - 2\left(\frac{\mu_i}{\mu_r}\right)^2 \frac{|\mu^c|}{\mu_r} + \left(\frac{\mu_i}{\mu_r}\right)\left(1 + \frac{|\mu^c|^2}{\mu_r^2}\right) - \frac{1}{2\mu_r}\left(|\mu^c| + \mu_i^c\right) = 0. \tag{3.17}$$

Figure 3.2(*a*) shows four examples of curves plotted following (3.17). As stated earlier, the SFD mapping is self-similar with respect to the parameter μ_i^c/μ_r^c. Thus the curves maintain their shape for constant μ_i^c/μ_r^c. All μ^k below the curves will be stabilised, while those located above will remain unstable in the λ space.

The cases in which one or more μ^k have large μ_i^k/μ_r^k (relative to μ_i^c/μ_r^c), are potential candidates to remain unstable, as can be inferred from figure 3.2(*a*). A possible solution to this is to define an auxiliary value, $\mu^{aux} \in \mathbb{C}$, which may not correspond to any physical eigenmode of the flow, but $\chi^\star(\mu^{aux})$ and $\Delta^\star(\mu^{aux})$ could lead to a global stabilisation. For that purpose, equation (3.17) can be used inversely. Another approach is to determine the values $\mu^{aux} = \mu_r^{aux} + \mathrm{i}\mu_i^{aux}$ for which the corresponding $\chi^\star$ and $\Delta^\star$ imply neutral $\lambda_{1,i}(\mu^c)$ or $\lambda_{2,i}(\mu^c)$. Figure 3.2(*b*) plots limiting curves computed following this second approach.

When aiming to stabilise μ^c and all μ^k, the intersection of all regions encompassed by the μ^{aux} boundaries has to be found, if it is not empty. Figure 3.3(*b*) shows that the parameter

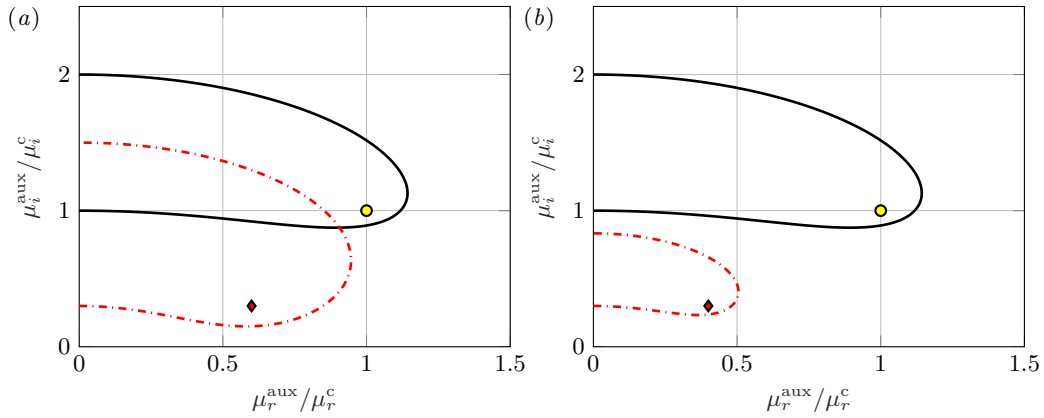

Figure 3.3: Limiting curves defining the sets of μ^{aux} values stabilising μ^{c} or μ^{k} if $\chi = \chi^{\star}(\mu^{\mathrm{aux}})$ and $\Delta = \Delta^{\star}(\mu^{\mathrm{aux}})$ are chosen. $\mu^{\mathrm{c}} = 1 + 1\mathrm{i}$ (yellow circles, solid black), $\mu^{\mathrm{k}} = 0.6 + 0.3\mathrm{i}$ (*a*), $\mu^{\mathrm{k}} = 0.4 + 0.3\mathrm{i}$ (*b*) (red diamonds, dash-dotted red).

choice $\chi = \chi^{\star}(\mu^{\mathrm{c}})$ and $\Delta = \Delta^{\star}(\mu^{\mathrm{c}})$ or $\chi = \chi^{\star}(\mu^{\mathrm{k}})$ and $\Delta = \Delta^{\star}(\mu^{\mathrm{k}})$ cannot lead to a global stabilisation of the system. However, for the case in figure 3.3(a) there exists a complementary finite range of χ and Δ for which SFD stabilises the system.

Particularly relevant are the μ^{aux} when curves of figure 3.2(b) cross the imaginary axis. Denoting l_{u} and l_{l} as the upper and lower limits respectively, and operating on (3.17) using the second approach described above, it is possible to show that

$$l_{\mathrm{u}}(\mu^{\mathrm{c}}) = \frac{|\mu^{\mathrm{c}}|^2}{\mu_i^{\mathrm{c}}}, \quad l_{\mathrm{l}}(\mu^{\mathrm{c}}) = \mu_i^{\mathrm{c}}, \tag{3.18}$$

such that the non-dimensional distance between l_{u} and l_{l} is:

$$\frac{l_{\mathrm{u}}(\mu^{\mathrm{c}}) - l_{\mathrm{l}}(\mu^{\mathrm{c}})}{\mu_i^{\mathrm{c}}} = \left(\frac{\mu_i^{\mathrm{c}}}{\mu_r^{\mathrm{c}}}\right)^{-2}. \tag{3.19}$$

This result highlights the relevance of the non-dimensional parameter $\mu_i^{\mathrm{c}}/\mu_r^{\mathrm{c}}$ once again. As shown in figure 3.2(b), the length defined by $l_{\mathrm{u}}(\mu^{\mathrm{c}}) - l_{\mathrm{l}}(\mu^{\mathrm{c}})$ can be considered indicative of the broadness of the range of χ and Δ values that drive the system towards the base flow. If μ^{c} is unknown initially and χ and Δ ought to be tested by trial-and-error, the stabilisation of flow fields ruled by a μ^{c} with a large complex argument will be difficult. Furthermore, from the topology of the limiting curves in figure 3.2(b), it follows that SFD will only stabilise a flow field ruled by more than one unstable eigenmode if

$$l_{\mathrm{l}}(\mu^{\mathrm{c}}) \leq l_{\mathrm{u}}(\mu^{\mathrm{k}}), \tag{3.20}$$

which implies

$$\mu_i^{\mathrm{c}} \leq \frac{|\mu^{\mathrm{k}}|^2}{\mu_i^{\mathrm{k}}} = \frac{|\mu^{\mathrm{k}}|}{\sin\varphi_{\mathrm{k}}} = |\mu^{\mathrm{k}}|\sqrt{1 + \left(\frac{\mu_i^{\mathrm{k}}}{\mu_r^{\mathrm{k}}}\right)^{-2}}, \tag{3.21}$$

with φ_{k} being the argument of a given μ^{k}. This result confirms the trend observed in figure 3.2(a). For SFD to be able to drive the system towards the base flow when several unstable

eigenvalues are present, all μ^{k} are required to have a small $\mu_i^{\mathrm{k}}/\mu_r^{\mathrm{k}}$ ratio and a large modulus relative to μ_i^{c}. Equation (3.21) indicates under which conditions the statement given by Massa (2014), claiming that SFD fails to stabilise flow fields ruled by large growth rates and low-frequency low-energy eigenmodes, holds. We see that the difficulty does not strictly come from a growth rate difference, but from the presence of μ^{k} with large $\mu_i^{\mathrm{k}}/\mu_r^{\mathrm{k}}$ value located close to the origin.

3.2.3 Feasibility and required accuracy

Refocussing the attention on flow problems ruled by one unstable μ^{c} with $\mu_r^{\mathrm{c}} \neq 0$, the parameters $\chi^\star$ and $\Delta^\star$ always effectively stabilise the problem. In practice, however, the effectiveness depends on the accuracy of the available estimate for μ^{c}. Accordingly, the sensitivity of $\chi^\star$ and $\Delta^\star$ with respect to the input parameter μ^{c} for a flow problem unstable to a single discrete eigenmode is of high relevance.

We consider the perturbed eigenvalue:

$$\mu^\epsilon = \mu(1+\epsilon) = \mu_r(1+\epsilon) + \mathrm{i}\mu_i(1+\epsilon), \quad |\epsilon| \ll 1. \tag{3.22}$$

Evaluating $\chi_\epsilon^\star = \chi^\star(\mu^\epsilon)$ and $\Delta_\epsilon^\star = \Delta^\star(\mu^\epsilon)$ for different values of the error parameter ϵ, the regions of the μ eigenspectrum having one of their associated λ solutions on the real axis (neutral stability) are determined. This approach resembles that presented in §3.2.2; the condition $\lambda_{1,i} = 0$ or $\lambda_{2,i} = 0$ to generate stability curves is also valid under the present analysis, since (3.16) applies here as well. By operating on (3.2), applying $\chi = \chi_\epsilon^\star$ and $\Delta = \Delta_\epsilon^\star$ and setting $\lambda_{1,i} = 0$ or $\lambda_{2,i} = 0$, the following condition is derived:

$$(1+\epsilon_{\max})^2 - \frac{\frac{\mu_i}{\mu_r} + \left(1 + 4\left(\frac{\mu_i}{\mu_r}\right)^2\right)\sqrt{1+\left(\frac{\mu_i}{\mu_r}\right)^2}}{2\frac{\mu_i}{\mu_r}\left(1+4\left(\frac{\mu_i}{\mu_r}\right)^2\right)}(1+\epsilon_{\max}) + 1 = 0. \tag{3.23}$$

The solutions of the quadratic equation (3.23) indicate the maximum allowed relative error $\epsilon_{\max}$ for a given eigenvalue μ that is aimed to be stabilised. Fundamental for the present analysis is the fact that (3.23) only depends on the non-dimensional parameter μ_i/μ_r. Accordingly, all μ eigenvalues with an equal argument have a common tolerance and, as a consequence, share the same difficulty to be stabilised when using SFD. The higher μ_i/μ_r, the smaller $\epsilon_{\max}$ and the higher the required relative digital precision of μ^{c}, $\chi^\star$ and $1/\Delta^\star$. Small relative perturbations around the required true values of $\chi^\star$ and $\Delta^\star$ may lead to ineffectiveness for cases ruled by an instability with a large $\mu_i^{\mathrm{c}}/\mu_r^{\mathrm{c}}$. These results are linked to the behaviour of

Eigenvalue argument	Affordable error	Stabilisation difficulty
$\mu_i^{\mathrm{c}}/\mu_r^{\mathrm{c}} < 1.12$	$\epsilon_{\max} > 10\%$	easy
$2.82 > \mu_i^{\mathrm{c}}/\mu_r^{\mathrm{c}} > 1.12$	$10\% > \epsilon_{\max} > 1\%$	
$\mu_i^{\mathrm{c}}/\mu_r^{\mathrm{c}} > 2.82$	$\epsilon_{\max} < 1\%$	hard

Table 3.1: Classification of flow instabilities based on the required accuracy in the computation of $\chi^\star$ and $\Delta^\star$ to guarantee convergence towards the steady state.

the limiting curves shown in figure 3.2(b); the higher μ_i^c/μ_r^c, the closer the curves to μ^c. A classification of instabilities based on the feasibility of SFD is presented in table 3.1.

3.3 The flow unleash technique

3.3.1 Methodology

Accurately determining the parameter μ^c requires a stability analysis, in turn requiring the base flow. We present a new technique, here referred to as *flow unleash*, through which we can accurately estimate μ^c with only one SFD or ESFD simulation. The unleash technique relies on driving the controlled simulation to a low enough residual level $\epsilon_R = ||\boldsymbol{q} - \bar{\boldsymbol{q}}||_{L_2}$ at time $t = t_u$. Then we continue the simulation for $t \geq t_u$ with $\chi = 0$ and maintain $\bar{\boldsymbol{q}}$ constant and equal to the last converged value, i.e., $\bar{\boldsymbol{q}}(\boldsymbol{x}, t) = \bar{\boldsymbol{q}}(\boldsymbol{x}, t_u)$ for $t \geq t_u$. By setting the control coefficient to $\chi = 0$, residual disturbances can grow and the unstable system will depart from the converged base state. To that end, the computed base flow is perturbed at $t = t_u$ by adding random white noise with amplitude ϵ_R to the solution. When the small perturbation dynamics is dominated by the most unstable eigenmode of the flow, the residual curve $\epsilon_R(t)$ is linear and corresponds to the exponential growth rate μ_i^c and $\ln(\epsilon_R)$ should therefore show a linear trend whose slope matches μ_i^c until non-linear saturation sets in.

3.3.2 Application to the cylinder flow

The results of applying the flow unleash technique to a $\mathcal{R}e = 100$ cylinder flow problem are shown in figure 3.4(a). Four unleash cases are represented, using $\epsilon_R(t_u) = 10^{-3}$, 10^{-4}, 10^{-5}, and 10^{-6}. The first main observation is that the expected linear growing trend of the residual curves starts developing after a significant number of time steps from the unleash. There is an initial transient after which the global mode develops. The exponential growth can be observed after all stable modes have died out. Regarding the range over which $\ln(\epsilon_R)$ grows linearly, two noteworthy considerations must be done. First of all, the point at which the linear growth starts developing depends on the amplitude of the noise imposed at $t = t_u$. However, the slope of the residual curves is independent of the initial disturbances, as expected. Secondly, the residual curves' slopes for the cylinder flow case are observed to increase asymptotically as ϵ_R decreases. From a physical point of view, throughout the controlled SFD simulation, the stabilised shear field must develop in time. Thus, for the present simulations, initialised with a uniform flow field, the growth rate of the associated K-H instability changes as the wake approaches the steady state. At a low enough residual level, the shear field can be assumed to be fully developed and μ^c approaches a limiting value. Following the same physical interpretation, the growth rate of the least stable eigenvalue of the controlled eigenspectrum, λ_i^s, changes throughout the controlled simulation. This may explain the slight bending of the residual curve of the SFD-stabilised simulation with respect to the expected linear behaviour for large ϵ_R, see figure 3.4(a).

The characterisation of μ^c requires to estimate the real part of μ^c. For that purpose, we suggest to compute the frequency from the time-signal measured with strategically placed probes. The probes are placed in areas where the eigenmode develops. This eigenmode associated to μ^c is represented in figure 3.5(b,d). The total measurement time is restricted to

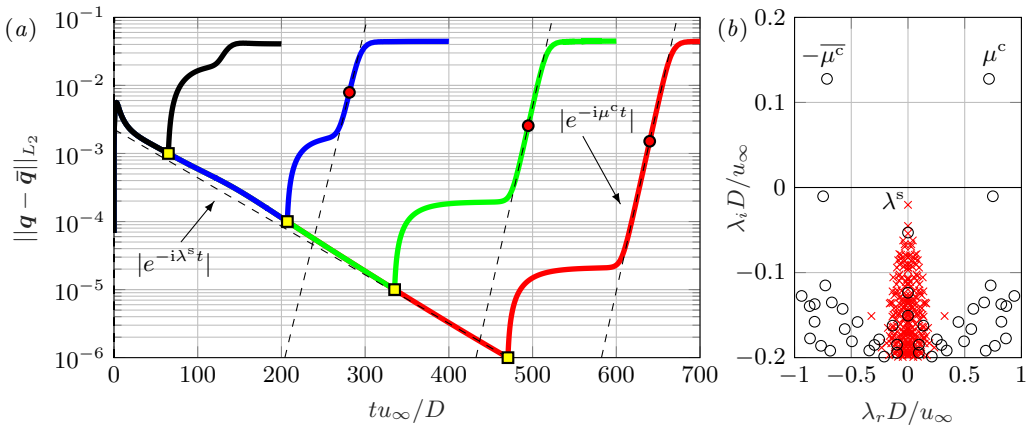

Figure 3.4: (*a*) SFD residual $\epsilon_{\mathrm{R}} = ||\boldsymbol{q} - \bar{\boldsymbol{q}}||_{L_2}$ (solid lines) using $\chi = 0.5$ and $\Delta = 3$. Fits to exponential parts (dashed lines). Unleash times (yellow squares) at $\epsilon_{\mathrm{R}} = 10^{-3}$ (black), 10^{-4} (blue), 10^{-5} (green), 10^{-6} (red). Location of null curvature in the linear range of the unleashed curves (red circles). (*b*) μ- (empty circles) and λ- (crosses) eigenspectrum from stability analysis computed with $\epsilon_{\mathrm{R}} = 10^{-6}$ base flow.

the linear growth phase. As pointed out by Barkley (2006), the frequency of the eigenmode and the nonlinear limit cycle defer for non-critical Reynolds numbers. Therefore, the approach adopted by some authors, as for instance Richez et al. (2016), to select Δ based on the frequencies captured in the fully developed non-linear flow is generally inadequate. When applying the flow unleash technique, the dominant frequency measured in the linear flow regime matches with the natural frequency of the unstable eigenmode developing in the flow, as shown in table 3.2.

To illustrate the accuracy of the flow unleash technique, table 3.2 compares μ^{c} obtained with this method, from stability analysis (using the $\boldsymbol{q}$ and $\bar{\boldsymbol{q}}$ fields as base flows) and with the value reported by Barkley (2006). One of the main advantages of the flow unleash technique is that the perturbation characterisation is carried out using the same numerical set-up as the flow simulation. Thus, the captured modal behaviour does correspond to the true perturbation dynamics in the simulation. On the other hand, when applying the flow unleash technique, the accuracy of the user-inferred eigenmode stability properties is subject to measurement errors. To minimise ambiguity, we propose to compute the value of $\mu_i^{\mathrm{c}} = \partial \ln(\epsilon_{\mathrm{R}})/\partial t$ from the residual curves at the point of null curvature. The uncertainty of these measurements of μ_i^{c} for the present cylinder simulations is approximately $\pm 0.002\, U_\infty/D$. Here μ_r^{c} is determined as the average of the dominant frequency computed at probes placed at $(2,-1)$; $(2,1)$; $(6,-1)$;

ϵ_{R}	**Flow unleash**	**Stability analysis ($\boldsymbol{q}$)**	**Stability analysis ($\bar{\boldsymbol{q}}$)**
10^{-3}	–	$\pm 0.7826 + 0.1426\mathrm{i}$	$\pm 0.7873 + 0.1431\mathrm{i}$
10^{-4}	$0.7240 + 0.1164\mathrm{i}$	$\pm 0.7181 + 0.1287\mathrm{i}$	$\pm 0.7183 + 0.1287\mathrm{i}$
10^{-5}	$0.7139 + 0.1257\mathrm{i}$	$\pm 0.7145 + 0.1278\mathrm{i}$	$\pm 0.7145 + 0.1278\mathrm{i}$
10^{-6}	$0.7135 + 0.1271\mathrm{i}$	$\pm 0.7142 + 0.1277\mathrm{i}$	$\pm 0.7142 + 0.1277\mathrm{i}$

Table 3.2: $\mu^{\mathrm{c}} D/u_\infty$ inferred using the flow unleash technique, global stability analysis using $\boldsymbol{q}$ or $\bar{\boldsymbol{q}}$ as the base flow at ϵ_{R}. Barkley (2006) presents the value $\pm 0.7395 + 0.1298\mathrm{i}$.

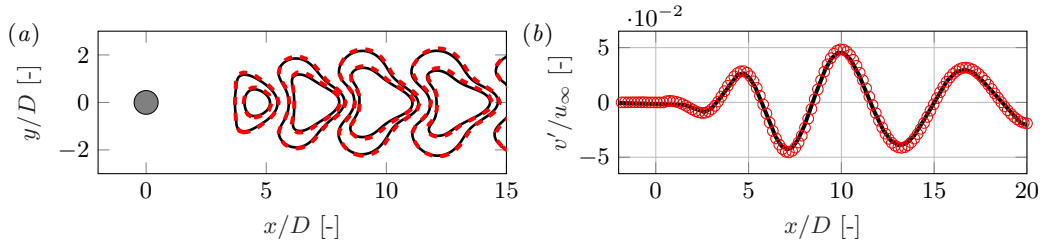

Figure 3.5: Dominant eigenmode (v') when the base flow is unleashed, associated to μ^c. (*a*) shows the xy-field, while (*b*) shows the profile along $y = 0$. Solid black lines: $\boldsymbol{q} - \bar{\boldsymbol{q}}$ from DNS, dashed red lines and red symbols: real part of global eigenfunctions from linear stability analysis.

$(6, 1)$. Table 3.2 also shows the convergence of μ^c with respect to ϵ_R when performing both stability analyses and DNS simulations, both methods match up to the measurement precision at $\epsilon_R = 10^{-6}$.

By keeping $\bar{\boldsymbol{q}}$ constant after the flow is unleashed, the field $\boldsymbol{q} - \bar{\boldsymbol{q}}$ becomes representative of the perturbation, $\boldsymbol{q'}$, developing in the unleashed flow field. This is valid under the assumption that $\bar{\boldsymbol{q}}(\boldsymbol{x}, t_u)$ sufficiently approximates $\boldsymbol{q}_s(\boldsymbol{x})$, which sets a requirement in the convergence level. Hence, the variable $\boldsymbol{q} - \bar{\boldsymbol{q}}$ can be compared to the eigenfunction of the unstable eigenmode developing in the unleashed flow field. Figure 3.5 shows that the mode ruling the flow unleash DNS matches the eigenmode of the stability analysis.

3.4 Optimisation

3.4.1 The role of stable eigenmodes

Jordi et al. (2015) claim that the pair of χ and Δ that optimises the scalar problem (2.33) for μ^c also optimises the full flow problem. One result of §3.2.1 was that $\chi^\star$ and $\Delta^\star$ minimise the spectral radius of the scalar problem, since $\lambda^\star$ represents the configuration for which $\max\{\lambda_i(\mu^c)\}$ is located at the furthest possible distance from the real axis. Therefore, the application of the optimisation routine presented by Jordi et al. (2015) and the expressions for $\chi^\star$ and $\Delta^\star$ are expected to yield the same convergence rate. To optimise the SFD set-up, however, the role played by the stable eigenvalues has to be considered as well, because the ultimate convergence rate of an SFD simulation is determined by the least stable eigenvalue λ^s, which does not necessarily correspond to $\lambda^c_{1,2} = \lambda_{1,2}(\mu^c)$. This philosophy also underlies the recently proposed Newton-Krylov method by Citro et al. (2017), taking advantage of accounting for the slower decaying modes. The location of the least stable eigenvalue λ^s of the controlled eigenspectrum depends on the associated μ^s eigenvalue and the choice of parameters of the model χ and Δ.

When the stable eigenvalues are considered in the optimisation process, the choice $\chi^\star$ and $\Delta^\star$ leads to a suboptimal convergence rate, shown as follows. By combining the real part of the first expression with the imaginary part of second expression in 3.2, we obtain

$$\lambda_{2,r}\left(\lambda_{1,i} + \frac{1}{\Delta}\right) + \lambda_{1,r}\left(\lambda_{2,i} + \frac{1}{\Delta}\right) = 0. \tag{3.24}$$

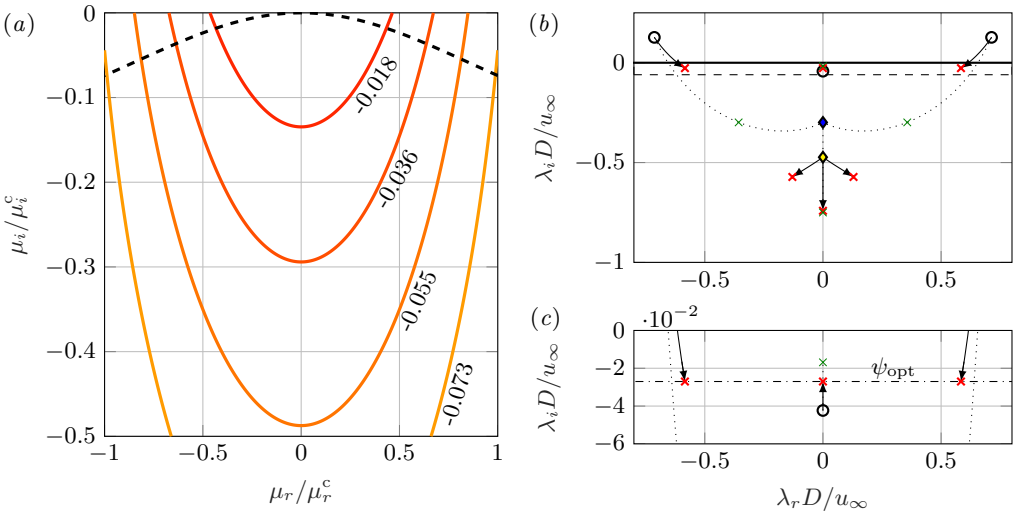

Figure 3.6: (*a*) Least stable λ_i isocontours (solid lines) in the μ space with $\chi = \chi^\star(\mu^c)$ and $\Delta = \Delta^\star(\mu^c)$ considering $\mu^c = 1 + 1\mathrm{i}$. Boundary for which $\max\{\lambda_{1,i}, \lambda_{2,i}\} \lesseqgtr \mu_i$ (dashed line). (*b*) Path of λ-solutions varying χ in the range $[0, \chi_{\text{opt}}]$ with $\Delta = \Delta_{\text{opt}}$ (solid black arrows) and χ in the range $[0, \chi^\star]$ with $\Delta = \Delta^\star$ (dotted lines). (*c*) Zoom. μ (empty circles), $-\mathrm{i}/\Delta_{\text{opt}}$ (yellow diamond), $-\mathrm{i}/\Delta^\star$ (blue diamond), λ for $(\chi, \Delta) = (\chi_{\text{opt}}, \Delta_{\text{opt}})$ (red thick crosses), and λ for $(\chi, \Delta) = (\chi^\star, \Delta^\star)$ (green thin crosses).

Hence, for a fixed μ and variable χ and Δ, either one λ solution is located above $-\mathrm{i}/\Delta$ and the complementary solution is located below $-\mathrm{i}/\Delta$, or both solutions cross in imaginary part at $\lambda_{1,i} = \lambda_{2,i} = -1/\Delta$. The latter can only occur if (Åkervik et al., 2006)

$$\mu_i - \chi + \frac{1}{\Delta} = 0. \tag{3.25}$$

For a general eigenspectrum with many $\mu \neq \mu^c$, (3.24) implies that the choice $\chi = \chi^\star(\mu^c)$ and $\Delta = \Delta^\star(\mu^c)$ places the solutions of each pair $\lambda_{1,2} \neq \lambda_{1,2}^c$ above and below $\lambda^\star(\mu^c)$ respectively. For this particular parameter choice, (3.25) yields $\mu_i^c - \chi^\star(\mu^c) + 1/\Delta^\star(\mu^c) = 0$; thus all eigenvalues with $\mu_i \neq \mu_i^c$ have $\lambda_{1,2}$ located above and below $\lambda_i = -1/\Delta$. The implication for the optimisation of the SFD set-up is that the choice $\chi^\star$ and $\Delta^\star$ entails the existence of λ solutions with $\lambda_i > \lambda_i^\star$. The optimisation of the scalar problem thus generally implies suboptimal convergence of the full flow problem, since its application does not guarantee the minimisation of $\lambda_i^s > \lambda_i^\star$.

Next, a new hypothetical optimal configuration is proposed. To illustrate the role of χ and Δ in the $\mu \mapsto \lambda$ mapping, Åkervik et al. (2006, figure 2) consider μ on the horizontal straight line, i.e., $\mu = \mu_r + b\mathrm{i}$, $b \in \mathbb{R}$. Here, the analysis is restricted to $b < 0$, characterising stable eigenvalues. All μ are mapped onto two solution branches, one of them giving the least stable λ eigenvalue depending on the relation between b, χ and Δ. The μ's located close to the imaginary axis will be shifted upwards the most, the maximum being attained at $\mu_r = 0$. For a given full μ spectrum, the least stable λ^s may be associated to either the steady eigenvalue with the largest growth rate or less stable unsteady eigenvalues depending on their relative location on the complex plane and the parameters χ and Δ. Figure 3.6(*a*) is representative of this, illustrating that the largest λ_i correspond to μ located close to the imaginary axis.

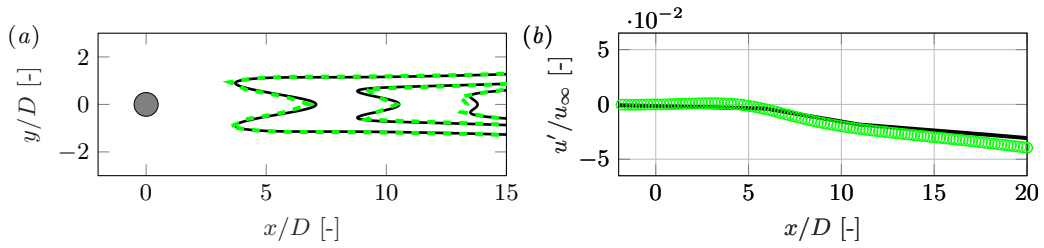

Figure 3.7: Dominant eigenmode of the flow (u') when applying SFD, associated to λ^{s}. (*a*) shows the xy-field, while (*b*) shows the profile along $y = 0$. Solid black lines: $\boldsymbol{q} - \bar{\boldsymbol{q}}$ from DNS, dashed green lines and green symbols: real part of global eigenfunctions from linear stability analysis.

When the previous analysis is extended to a general flow problem with discrete μ, the candidates to take the role of λ^{s} are stable, steady (or low-frequency) eigenmodes.It is unlikely for μ^{c} to take the role of λ^{s}, because the steady and low-frequency stable eigenvalues will be shifted upwards, while μ^{c} shifts downwards. The spectral radius is hypothetically minimised when the least stable λ solutions intersect $\max\left\{\lambda^{\mathrm{c}}_{1,i}, \lambda^{\mathrm{c}}_{2,i}\right\}$ in the imaginary coordinate at the furthest possible downwards distance from $\lambda_i = 0$. The μ value corresponding to λ^{s} is denoted by μ^{s} and can be characterised by measuring the slope of the controlled SFD residual curve. This slope is proportional to λ^{s}_i and the frequency of the dominant wave-like perturbations in the controlled flow field corresponds to λ^{s}_r. Using the inverse mapping 2.26, the value of μ^{s} can be determined.

For the cylinder flow case, the least stable μ that rules effective SFD simulations corresponds to a steady mode. That is, in the range of χ and Δ values that stabilises μ^{c}. For this reason, we assume μ^{s} to be purely imaginary in the analysis in the following section. By evaluating the slope of the SFD residual curve at $\epsilon_{\mathrm{R}} = 10^{-6}$, it is obtained that $\mu^{\mathrm{s}} D/u_\infty = -0.0423\mathrm{i}$. The optimal configuration of the λ eigenvalues is illustrated in figures 3.6(*b*) and (*c*). The arrows indicate the path followed by the selected μ when χ is increased from 0 at a fixed Δ. The final χ and Δ ($\chi_{\mathrm{opt}}, \Delta_{\mathrm{opt}}$), have been computed by using the method that we describe in §3.4.2. The artificial λ solutions emanating from the point located at $-\mathrm{i}/\Delta_{\mathrm{opt}}$ are far from becoming the least stable eigenvalues of the controlled eigenspectrum in this case. The natural λ solutions corresponding to μ^{c} and μ^{s} define the minimal spectral radius and cross in their imaginary part when $\chi = \chi_{\mathrm{opt}}$ and $\Delta = \Delta_{\mathrm{opt}}$. Note that the crossing in the imaginary part can take place for different combinations of χ and Δ. Within this set, χ_{opt} and Δ_{opt} correspond to the absolute minimum spectral radius. In the linear controlled perturbation regime, the field $\boldsymbol{q} - \bar{\boldsymbol{q}}$ closely resembles the eigenfunction associated to λ^{s} obtained through an independent stability analysis, see figure 3.7, which yields $\mu^{\mathrm{s}} D/u_\infty = -0.0529\mathrm{i}$. Although the eigenvalue deviates from the growth measured from the slope of the SFD residual curve, the shape of the fields yield a convincing match. The main difference is observed close to the outflow boundary, and steady modes are indeed sensitively affected by boundary conditions.

3.4.2 Computation of optimal χ and Δ

The optimisation method presented next relies on running a controlled SFD or ESFD simulation and unleashing the flow afterwards. From the residual curves of the unleashed and

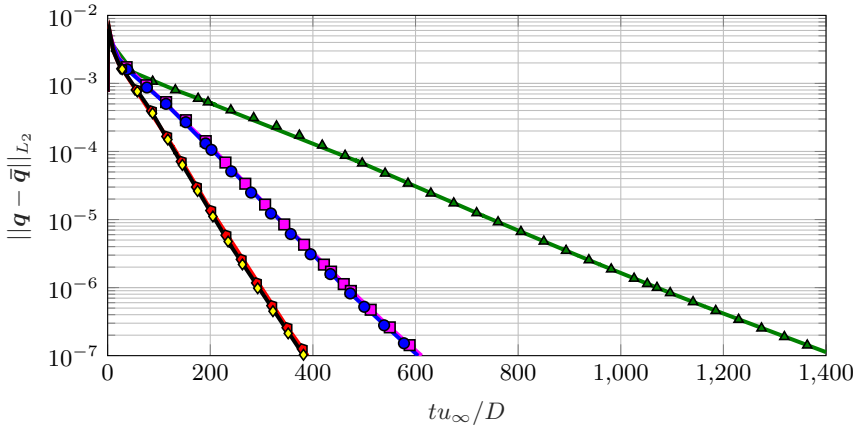

Figure 3.8: Comparison of the L_2 norm of $\boldsymbol{q}-\bar{\boldsymbol{q}}$ along ESFD simulations performed using different SFD parameters. The values of χ and Δ considered for each simulation are: $\chi_{\text{opt}} = 0.2524$ and $\Delta_{\text{opt}} = 2.1173$, optimal values computed by inferring μ^{c} and μ^{s} through the application of the technique of flow unleash (solid black line and yellow diamonds); $\chi_{\text{sp}} = 0.2608$ and $\Delta_{\text{sp}} = 2.1524$, optimal values computed with a previous knowledge of uncontrolled eigenspectrum (solid red line and red pentagons); $\chi^\star = 0.4259$ and $\Delta^\star = 3.3465$ (solid magenta line and magenta squares); $\chi = 0.4510$ and $\Delta = 3.1440$, reported by Jordi et al. (2015) (solid blue line and blue circles); $\chi = 1$ and $\Delta = 5$ (solid green line and green triangles). All values of χ and $1/\Delta$ are given in units of u_∞/D.

controlled flow simulations, μ^{c} and μ^{s} can be inferred following the approaches described in §3.3.1 and §3.4.1, respectively. We define $\psi \in \mathbb{R}$ as the imaginary coordinate at which the vertical crossing of the λ's corresponding to μ^{c} and μ^{s} occurs. By operating on (3.2), the minimal ψ,

$$\psi_{\text{opt}} = \frac{\mu_i^{\text{s}}}{2 - \frac{(\mu_r^{\text{c}})^2}{2\mu_i^{\text{s}}\left(\mu_i^{\text{s}} - \mu_i^{\text{c}}\right)}} \left(\frac{\mu_i^{\text{c}}}{\mu_i^{\text{s}}} - \frac{(\mu_r^{\text{c}})^2}{2\mu_i^{\text{s}}\left(\mu_i^{\text{s}} - \mu_i^{\text{c}}\right)} + \frac{|\mu^{\text{c}}|}{|\mu^{\text{s}}|} \right), \tag{3.26}$$

is obtained for

$$\Delta_{\text{opt}} = \frac{\mu_i^{\text{s}}}{\psi_{\text{opt}} \left(\frac{(\mu_r^{\text{c}})^2}{2\left(\mu_i^{\text{s}} - \mu_i^{\text{c}}\right)} \left(\frac{\psi_{\text{opt}}}{\mu_i^{\text{s}}} - 1 \right) - \psi_{\text{opt}} - \mu_i^{\text{s}} + \mu_i^{\text{c}} \right)}, \tag{3.27}$$

$$\chi_{\text{opt}} = -\frac{1}{\Delta_{\text{opt}}} - \psi_{\text{opt}} + \mu_i^{\text{s}} \left(1 + \frac{1}{\psi_{\text{opt}} \Delta_{\text{opt}}} \right). \tag{3.28}$$

In deriving these formulas, it is assumed that $\mu^{\text{s}} = \text{i}\mu_i^{\text{s}}$, i.e., the controlled simulation is ruled by the critical steady eigenmode.

The residual curves corresponding to different model parameters are compared in figure 3.8. The spectral radius obtained with χ_{opt} and Δ_{opt} is 0.9734. This value closely resembles the optimal one of 0.979 reported by Cunha et al. (2015), obtained through DMD. Following (2.35), the optimal spectral radius presented in this article corresponds to $\lambda_i^{\text{s}} D/u_\infty = -0.0270$; the spectral radius obtained by Cunha et al. (2015) is given by $\lambda_i^{\text{s}} D/u_\infty = -0.021$. A similar convergence rate is obtained using the analytical expressions with μ^{c} and μ^{s} either

inferred from the controlled and unleashed residual curves or those obtained with the stability analysis. The first case appears to yield a slightly lower computational time, which means that the eigenvalues inferred through the application of the flow unleash technique are more representative for the dynamics in the simulation than the stability analysis. This may be related to the sensitivity of the stable steady mode to the outflow boundary conditions, as mentioned before. The stability analysis provides the full spectrum. We can thus verify that the found control parameters yield the optimal spectral radius accounting for the full eigenspectrum. No other eigenmode becomes dominant in this particular case. The usage of $\chi^\star(\mu^c)$ and $\Delta^\star(\mu^c)$, which is suboptimal, yields the same performance as the parameters used by Jordi et al. (2015), a result which is in agreement with the analysis exposed in §3.4.1. The optimised configuration reduces the computational time by 35%. A much larger reduction by 75% is observed when comparing χ_{opt} and Δ_{opt} and general SFD parameters, $\chi = 1$ and $\Delta = 5$. At $t \approx 400 u_\infty / D$, the usage of χ_{opt} and Δ_{opt} has converged the base flow to a residual level one order of magnitude lower than with the values presented by Jordi et al. (2015) and three orders of magnitude lower than the usage of $\chi = 1$ and $\Delta = 5$.

Chapter 4

The Micro-Ramp Working Principle

4.1 Analysis overview

In the introduction of this work, we have pointed out divergences in the literature regarding the working principle of the micro-ramp. The current state of the art identifies a pair of streamwise counter-rotating vortices induced at the micro-ramp, the primary vortex pair, responsible for lifting up low momentum fluid at the centre plane and entraining high-momentum fluid towards the wall aside (Babinsky et al., 2009; Ghosh et al., 2010; Lee et al., 2010). This redistribution of momentum leads to enhanced wall shear and a decrease of the boundary layer shape factor (Anderson et al., 2006). A fuller velocity profile results in better resistance against adverse pressure gradients (Lin, 2002; Verma and Hadjadj, 2015). There is consensus on the fact that the micro-ramp is capable of re-energising the lower portion of the boundary layer. Nonetheless, discrepancies arise regarding what mechanisms cause this effect.

Wang et al. (2013) question the capability of the primary vortex pair to transport high-momentum fluid from the free stream towards the surface. According to Wang et al. (2013), the mechanism of the micro-ramp is the exchange of high- and low-momentum fluid from different portions of the boundary layer triggered at the micro-ramp rather than by downstream-travelling vortices. Li and Liu (2011) test the performance of the micro-ramp to control shock-induced separation. A reduction of the separation bubble is achieved. However, this is not attributed to increased wall shear under the action of the primary vortex pair but to the fact that vortex rings induced by K-H instability at the micro-ramp wake destroy the shock. Blinde et al. (2009) find no sign of the primary vortex pair in the instantaneous flow field sufficiently downstream the micro-ramp. Eventual breakdown of the primary vortices is reported by Lu et al. (2010). According to Bo et al. (2012), excess and deficit of momentum in the micro-ramp wake is first produced by the action of the primary vortex pair and thereafter sustained by the dynamics of hairpin vortices.

In this chapter, we analyse transitional flow dynamics behind a micro-ramp and the capability of this device to promote transition. DNS results are compared with tomo-PIV experiments of Ye (2017) and with results from linear stability analysis. The micro-ramp geometry and boundary layer properties considered for the analysis, as well as the set-up of the DNS simulations, are detailed in §2.4. At the same time, this study aims to further contribute to the

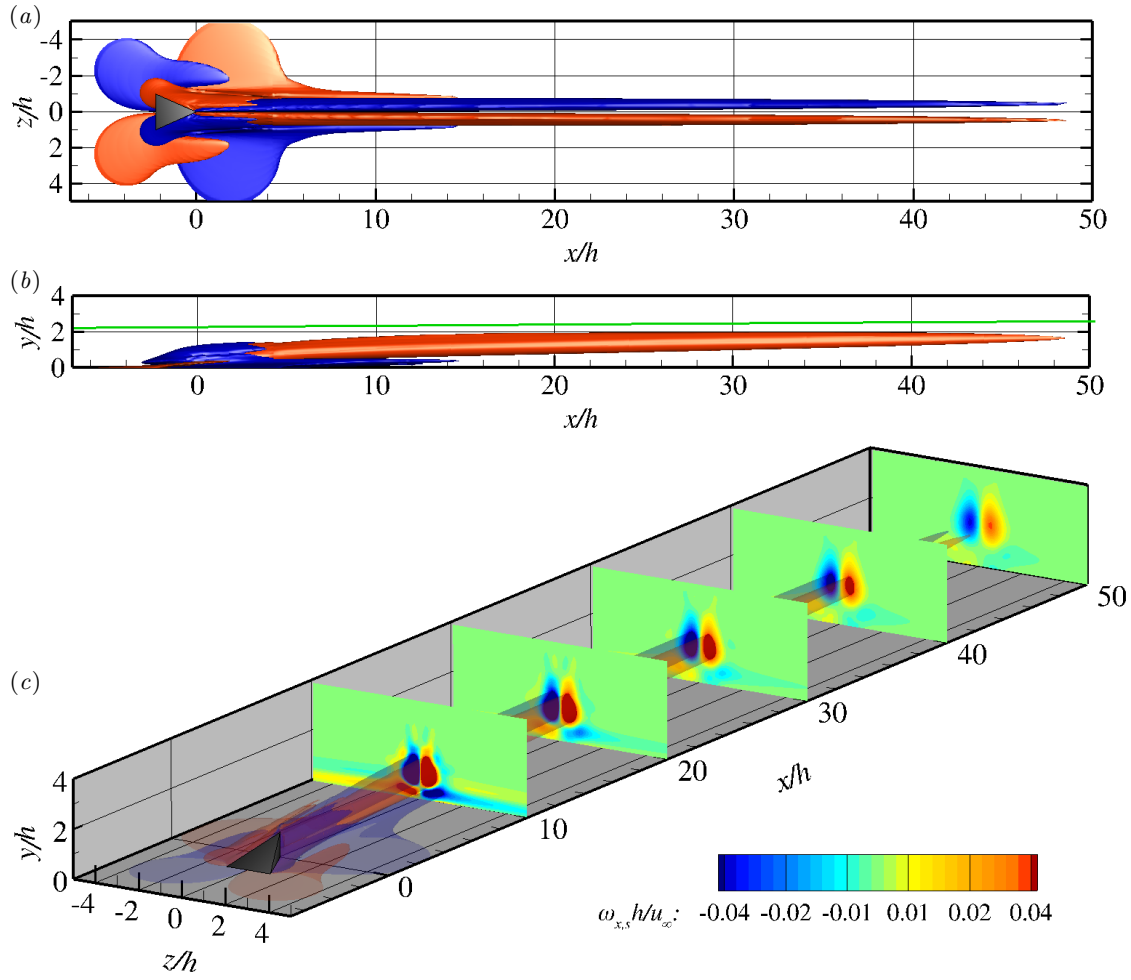

Figure 4.1: Streamwise vorticity in the base flow. (*a*) top and (*b*) side views of iso-surfaces of $\omega_{x,s}h/u_\infty = \pm 0.04$, unperturbed boundary layer edge (solid green line). The micro-ramp geometry is superimposed onto the iso-surfaces. (*c*) perspective of translucent iso-surface and y-z planes at $x/h = 10;\ 20;\ 30;\ 40;\ 50$.

aforementioned discussion regarding the micro-ramp working principle. Although previous work devoted to this topic generally considers turbulent and supersonic flow conditions, recent investigations from Ye (2017) of the incompressible and transitional micro-ramp wake reveal the existence of flow structures of nature similar to those captured in a turbulent boundary layer. These were previously described in §1.2. In particular, the time-averaged organisation of the micro-ramp wake presented by Ye (2017) depicts the primary vortex pair and further pairs of secondary vortices developing aside. In the instantaneous flow field, a train of hair-pin vortices induced by K-H instability is reported as major feature. Accordingly, we expect the current analysis to serve for future studies in which micro-ramps would be employed for laminar flow control applications, as well as to provide better understanding of mechanisms which may be partially convoluted in more complex flow environments.

The literature shows the micro-ramp to play a dual role: it is a vortex generator and a surface roughness element with potential to promote transition. Initially, the micro-ramp induces a

counter-rotating vortex pair which generates central upwash and lateral downwash. At the same time, the action of these vortices distorts the organisation of the laminar boundary layer and introduces velocity streaks and a possibly unstable detached shear layer. If $\mathcal{R}e_{hh}$ is large enough, unstable disturbance growth can lead to the formation of large-scale hairpin vortices and trigger transition. The evolution of transitional flow structures downstream the micro-ramp may distort the structure of the primary vortex pair, introduce a new instantaneous flow organisation, and alter the properties of the near-wall flow region. Accordingly, we are interested in characterising the role played by the primary vortices on the one hand and the transitional perturbations on the other hand in the micro-ramp functionality as they serve the same purpose. To that end, we propose to segregate mechanisms by decomposing the instantaneous micro-ramp flow field as $\boldsymbol{q}(\boldsymbol{x},t) = \boldsymbol{q}_{\mathrm{s}}(\boldsymbol{x}) + \boldsymbol{q'}(\boldsymbol{x},t)$, i.e., the steady laminar base flow and a time-dependant perturbation field following the approach of linear stability theory.

The first part of the analysis presented in this chapter addresses the base flow organisation (§4.2). We compute DNS of $\boldsymbol{q}_{\mathrm{s}}$ by applying SFD since the micro-ramp wake is unstable for the currently considered supercritical $\mathcal{R}e_{hh}$. The subscript "s" is hereafter used to denote base flow quantities, which are obtained as the instantaneous converged $\bar{\boldsymbol{q}}$ solution (§2.2). Since the primary vortex pair is an element intrinsically contained in the system's steady solution, by computing $\boldsymbol{q}_{\mathrm{s}}$ we can isolate the structure of the primary vortices and analyse their momentum-transport capabilities in absence of perturbation development. In figure 4.1, we show iso-contours of streamwise vorticity in the base flow; the primary vortices are identified as the elongated structures featuring large (absolute) values of streamwise vorticity.

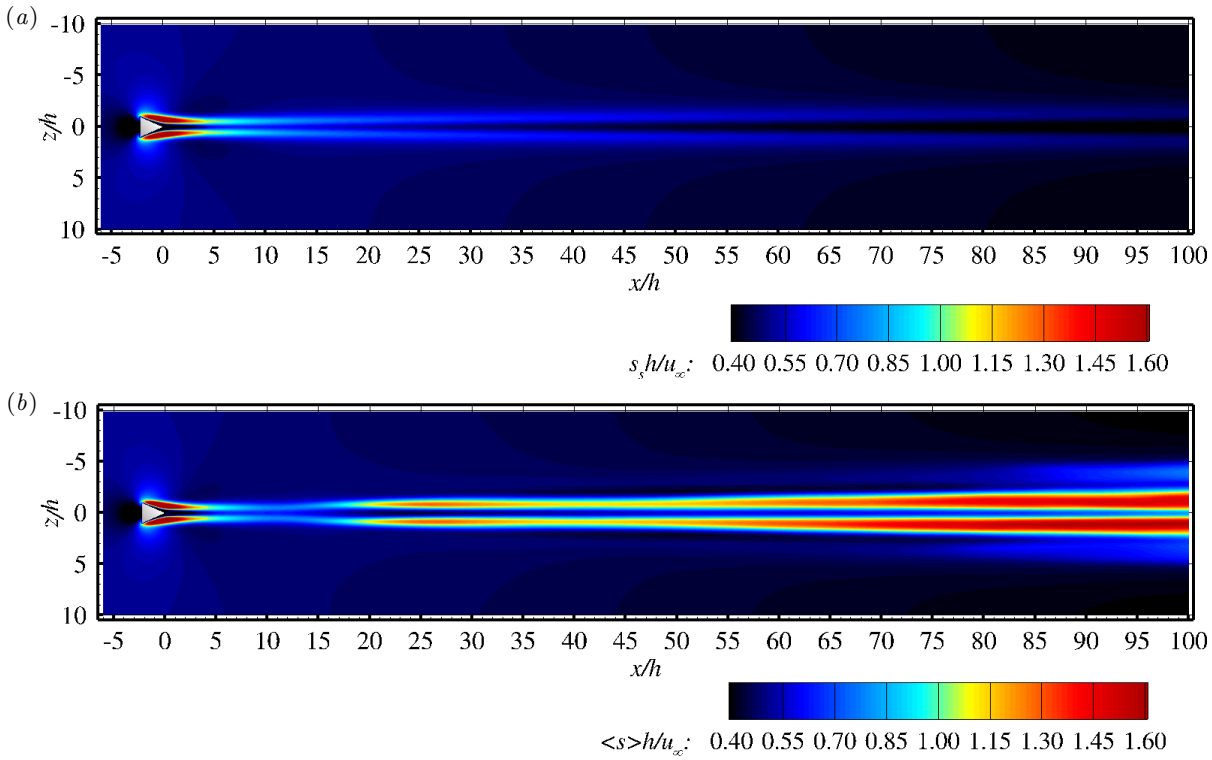

Figure 4.2: Wall shear in (*a*) the base and (*b*) the time-averaged flow fields.

These have an associated persisting rotational motion (as shown later on). We detect a region of high streamwise vorticity close to the micro-ramp; upon examination of the solution $\boldsymbol{q}_\mathrm{s}$, we inquire as well on whether other base flow structures —for instance secondary vortices— coexist with the primary vortex pair. Figure 4.2(a) portrays wall shear in the base flow, a quantity which is used in this work to characterise the "health" of the boundary layer and, in turn, the performance of the micro-ramp. The imprint of the primary vortices in figure 4.2(a) appears evident. Symmetric regions of enhanced wall shear arise aside the micro-ramp and are prolonged until the end of the domain. In line with observations of Wang et al. (2013), largest wall velocity gradients are captured near the micro-ramp. When moving downstream, wall shear exhibits a rapid decay. Results of figures 4.2(a) thus suggest the model of near-wall flow re-energisation under the action of downstream-travelling vortex filaments to be insufficient.

After analysing the base flow solution, in the third section of this chapter we focus the attention on the behaviour of the instantaneous transitional flow (§4.3). We first apply linear stability analysis (§2.5) and the flow unleash technique (§3.3.1) to characterise the behaviour of *small*-amplitude perturbations (1.3). Assessing linear dynamics of the disturbance field $\boldsymbol{q'}$ provides useful knowledge regarding the onset and nature of flow instabilities in the micro-ramp wake. Thereafter, we compute DNS of $\boldsymbol{q}$ and characterise *large*-amplitude perturbation development. We examine the instantaneous behaviour of the micro-ramp wake, with emphasis put on the evolution of perturbation-induced vortical structures.

In the fourth section of this chapter, we discuss the time-averaged organisation of $\boldsymbol{q}$ (§4.4). Mean flow quantities are hereafter denoted by angle brackets. It should be noted that base flow variables may also be time-averaged. We introduce the convention that "base flow" refers to the solution $\boldsymbol{q}_\mathrm{s}$ and "mean flow" refers to the solution $\langle \boldsymbol{q}_\mathrm{s} + \boldsymbol{q'} \rangle$. Upon comparison between $\boldsymbol{q}_\mathrm{s}$ and $\langle \boldsymbol{q} \rangle$, differences can be exclusively attributed to the effect of disturbance growth. Figures 4.2(b) and A.9(b) of the appendix respectively depict wall shear and boundary layer shape factor in the mean flow. At first glance, we observe major differences between base and mean representations sufficiently downstream the micro-ramp. In the mean flow, wall shear is enhanced in the range $10 \leq x/h \leq 20$ and, far downstream the micro-ramp, the central strips of increased wall shear display much larger values than in the base flow. Moreover, the wake of the micro-ramp expands in spanwise direction; at the end of the computational domain, the region of enhanced wall shear covers a spanwise extent much larger than the micro-ramp span. These results highlight the importance of the perturbation development to improve the performance of the micro-ramp in the current conditions. Accordingly, in §4.4, we describe differences between base and mean flow topology and inquire on the role of perturbations in the enhancement of momentum transport near the wall.

The analysis presented in this chapter considers a micro-ramp immersed in a quasi-incompressible $M = 0.2$ boundary layer. In §A.5 in the appendix, we extend some of the most relevant results to a $M = 0.7$ flow case. We show that compressibility acts stabilising; we capture a perturbation activity much weaker than in the $M = 0.2$ case. As a consequence, the distributions of wall shear in the base flow and in the mean flow resemble qualitatively.

4.2 Base flow

We commence the analysis of the micro-ramp flow by identifying and describing the main characteristics of the $M = 0.2$ base flow. This flow field is a steady-state solution of the Navier-Stokes equations computed via ESFD. DNS simulations are performed with $\chi = 0.96$ and $\Delta = 1.86$ until a convergence bound of $\epsilon_R = 10^{-6}$ is reached. These SFD parameters are based on the stability results of Groot et al. (2016).

4.2.1 Primary elements of the base flow topology

The primary vortex pair emanating from the slant edges of the micro-ramp is reported in the literature as the main feature in micro-ramp flows. It is a structure captured in flow regimes ranging from incompressible to hypersonic (Babinsky et al., 2009; Lee et al., 2010; Tirtey et al., 2011; Ye et al., 2016). As mentioned previously, our results indicate that the primary vortex pair is an element contained in the $\boldsymbol{q}_s$ solution. The structure and evolution in space of the primary vortices in the base flow is characterised through iso-surfaces of streamwise vorticity and planes of projected streamlines with streamwise velocity in figures 4.1 and 4.3. The vortices are counter-rotating; inherent to their nature is the fact that they induce upwash at the centre plane and a lateral downwash. The induced positive wall-normal velocity causes them to rapidly lift off from the surface (Babinsky et al., 2009). However, we observe the primary vortex pair to remain within the boundary layer at all streamwise stations. Already at $x/h \approx 30$, the lifting motion of the vortices has become much less pronounced, as compared to the micro-ramp vicinity; see figure 4.1(b). Generally in this work, the terms "micro-ramp vicinity" and "close/far to/from the micro-ramp" refer to the x-direction. Along x/h, the primary vortices show to move away from the centre plane; at $x/h = 100$ the vortex cores are separated in spanwise direction by a distance of approximately $2h$. This explains the spanwise expansion of the lateral strips of increased wall shear in figure 4.2(a). Even though the intensity of the vortices decays with x/h, they are observed to persist far downstream the micro-ramp.

Along the micro-ramp and at its downstream vicinity, the action of the primary vortices highly distorts the structure of the boundary layer at the micro-ramp span. High-momentum fluid from intermediate portions of the boundary layer penetrates into the low-momentum region under the action of downwash. In parallel, the upwash moves low momentum fluid from the lower portion of the boundary layer upward. Consequently, a region in which the streamwise momentum is larger than in the unperturbed boundary layer (momentum excess region) is initially generated aside the centre plane and near the surface, together with a central region in which the streamwise momentum is lower than in the unperturbed boundary layer (momentum deficit region); see figure 4.3(a). The region of reduced momentum, regarded as a unique flow phenomenon (Li and Liu, 2010), has centred the attention of many researchers. It was initially detected by Babinsky et al. (2009). Sun et al. (2012) and Ye et al. (2016) tackle the streamwise evolution and recovery process, Li and Liu (2011) and Wang et al. (2013) inquire into the origin. Especially the origin has been a subject of great controversy in the literature. Babinsky et al. (2009) identify the deficit region as the "remnant of the device wake that has moved slightly away from the surface as a result of upwash". Lee et al. (2010) ascribe the deficit to the pairing of the primary vortex tubes. Wang et al. (2013) claim that the low-momentum fluid from the lower part of the boundary layer upstream the micro-ramp

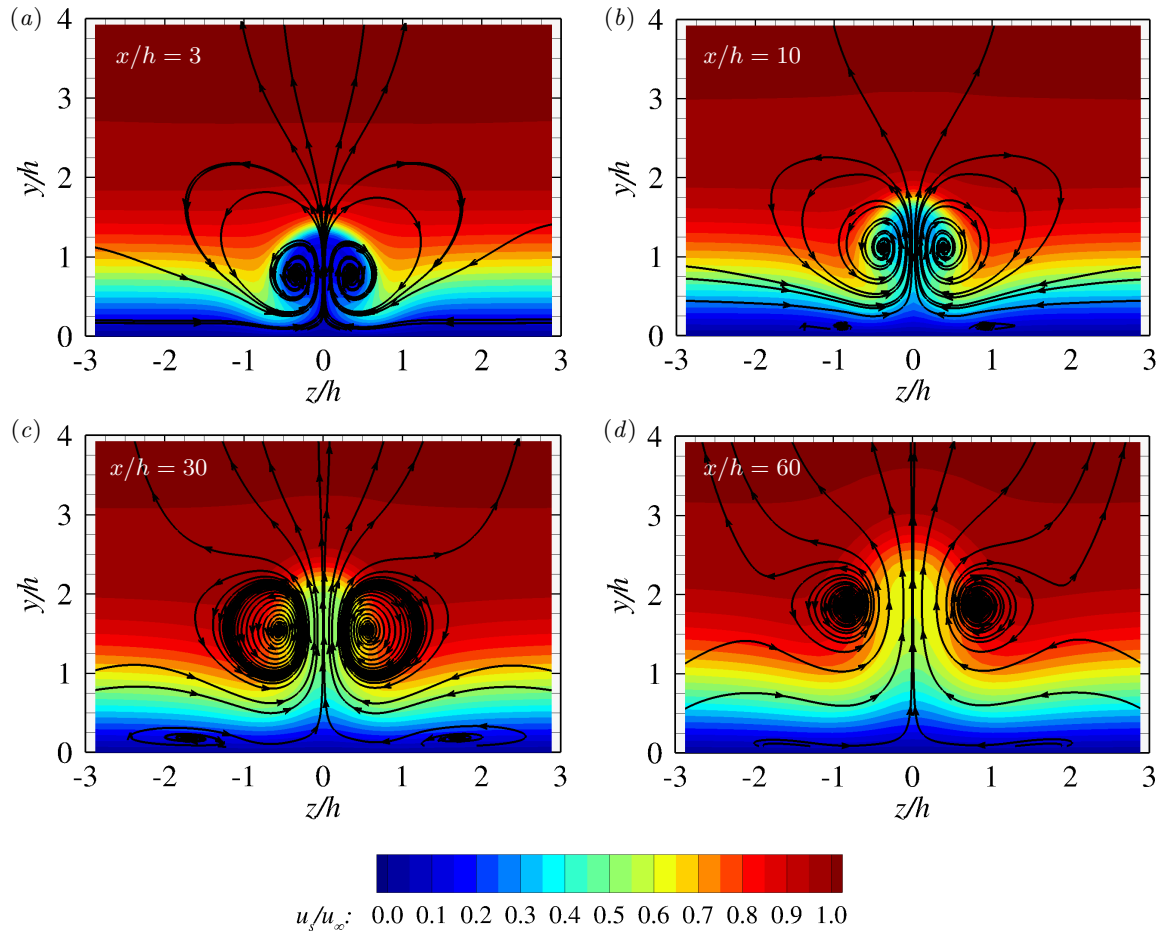

Figure 4.3: y-z planes of streamwise velocity with selected projected streamlines at (*a*) $x/h = 3$, (*b*) $x/h = 10$, (*c*) $x/h = 30$, (*d*) $x/h = 60$.

is the origin of the deficit, lifted-up under the action of the primary vortices. To shed light into this matter, the nature and evolution of the momentum deficit region is scrutinised in further sections of this work.

Downstream the micro-ramp, the action of the primary vortices initially keeps redistributing momentum within the distorted boundary layer. The central low-momentum dip shows to reduce its strength and to move upward for increasing x/h at a rate similar to that of the primary vortices; see figure 4.3. We notice a rapid recovery of the lower portion of the boundary layer in streamwise direction. From significantly close to the micro-ramp in x/h, and while moving downstream, the near-wall fluid layers start to reorganise towards a configuration resembling that of the unperturbed boundary layer; see figure 4.3(b,c). The primary vortex pair rapidly becomes incapable of maintaining effective the entrainment of high-momentum fluid close to the surface. It is assumed to be mainly consequence of the initial strong lift-up of the primary vortices, together with the steep decrease in magnitude of lateral downwash in x/h ($|v_s^{\min}|$ is less than 1% of u_∞ for $x/h > 22$). Ghosh et al. (2010) and Li and Liu (2010) report as well that downwash induced by the primary vortices in the turbulent wake of the micro-ramp weakens rapidly. The current results are conform with the significant decrease of

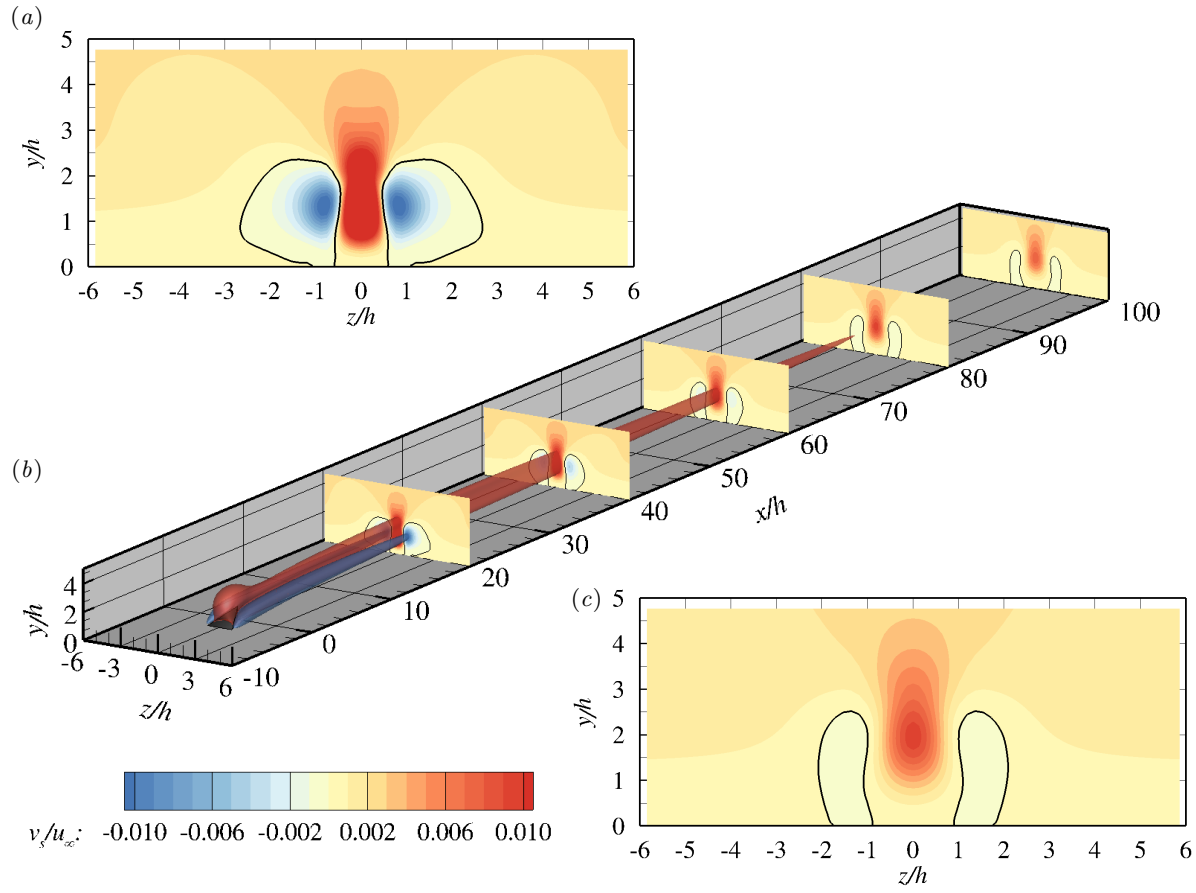

Figure 4.4: Wall-normal velocity. y-z planes at (*a*) $x/h = 20$, (*c*) 80, (*b*) perspective of y-z planes at $x/h = 20$; 40; 60; 80; 100 with iso-contour of $v_s/u_\infty = 0$ (black line) and iso-surfaces of $v_s/u_\infty = 0.01$ (red), -0.01 (blue).

the wall shear in the base flow for $x/h > 10$ illustrated in figure 4.2(a).

The rapid decay of downwash intensity along the streamwise direction contrasts with the endurance of central upwash, which is kept significant until far downstream; see figure 4.4. As a matter of illustration, and highlighting that $\delta_{un}(-1.25h)/h = 2.27$: for $x/h = 1$, $v_s^{max}/u_\infty = 0.14$ at $y/h \approx 0.6$; for $x/h = 30$, $v_s^{max}/u_\infty = 0.02$ at $y/h \approx 1.5$; for $x/h = 100$, $v_s^{max}/u_\infty = 0.008$ at $y/h \approx 2.1$. At $x/h = 20$, $|v_s^{max}| \approx 2|v_s^{min}|$; at $x/h = 80$, $|v_s^{min}|$ is one order of magnitude smaller than $|v_s^{max}|$.

Far downstream the micro-ramp, the lowest-level fluid aside the centre plane is practically fully recovered. The remnant of the primary vortices is only capable of inducing a weak rotational motion; the layers of streamwise velocity located underneath the vortex cores display little curvature; see figure 4.3(d). The wall shear aside the centre plane features values much lower than at the micro-ramp downstream vicinity, but larger than in the unperturbed region; see figure 4.2(a). The latter is not the case at $z/h = 0$; on the one hand, close to the micro-ramp, the addition of high-momentum fluid towards the centre plane is rather weak, as illustrated in figures A.3 and A.4 of the appendix. On the other hand, for large x/h, the persisting upwash maintains significant its influence close to the surface and progressively lifts the layers of

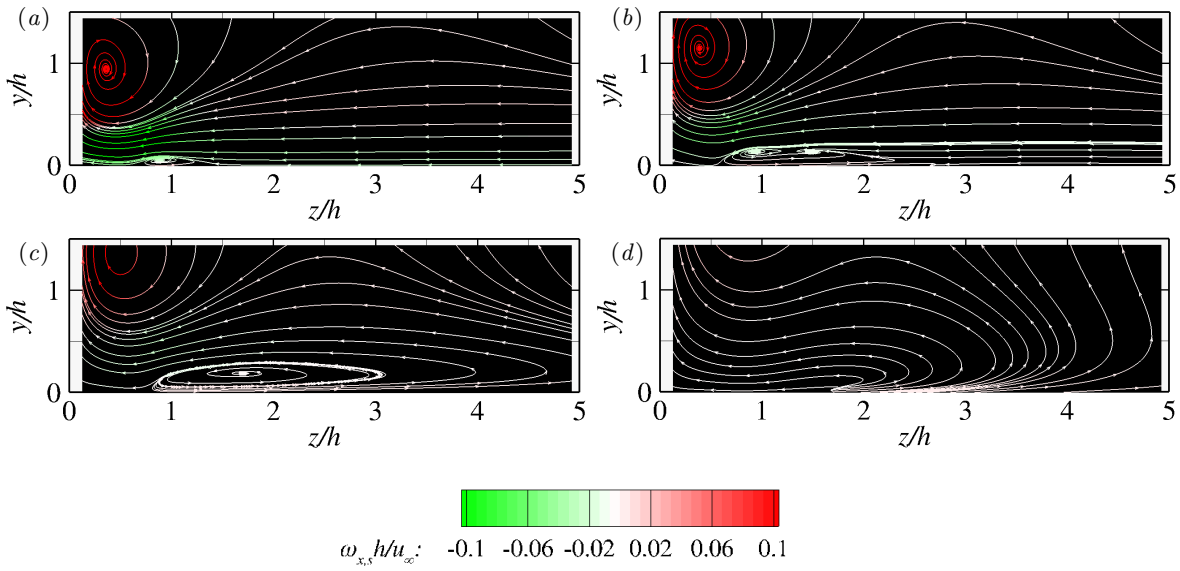

Figure 4.5: y-z planes of projected streamlines colour-coded by streamwise vorticity at (*a*) $x/h = 6$, (*b*) 11, (*c*) 20, (*d*) 60.

low-momentum fluid at the centre plane for increasing x/h. The boundary layer at $z/h = 0$ gradually becomes emptier and the central-upper layers of streamwise velocity are shaped in a sharp-pointed fashion (figure 4.3(d)). This is a detrimental effect, inasmuch as wall shear around the centre plane attains values similar or even lower than in the unperturbed region; see figure 4.2(a).

So far, we have identified one vortical structure in the base flow, the primary vortex pair, which shows to play a central role. We next inquire on whether other vortical systems are contained in the $\boldsymbol{q}_\mathrm{s}$ solution. Ghosh et al. (2010) and Li and Liu (2011) detect secondary vortical structures developing in streamwise direction beneath the primary vortex pair. In the experiments conducted by Ye (2017), secondary streamwise vortices are captured in the time-averaged field aside the primary vortices. However, these structures are hypothesised to be an artefact of time-averaging not present in the instantaneous flow field. Upon first glance, figure 4.1 shows a region of high $|\omega_{s,x}|$ underneath the primary vortices. At the vicinity of the micro-ramp this is not directly identified as secondary vortices, but a near-wall region of high shearing motion due to the generation of momentum excess.

The onset and growth of secondary vortices in the base flow is investigated in more detail by plotting the streamlines of the flow. Figure 4.5 displays y-z planes of projected streamlines at four representative streamwise positions. At $x/h = 6$, a weak streamwise rotational motion is captured near the wall; see figure 4.5(a). It is assumed to be the onset of secondary vortices induced by the action of the primary vortex pair. They appear to grow in between the surface and the near-wall regions of enhanced shear and to rotate with a sense opposite to that of the primary vortices. At $x/h = 11$, each secondary vortex bifurcates into two branches (figure 4.5(b)). These branches then re-connect at $x/h = 13$. While bifurcated, the secondary structures spread in spanwise direction, a trend which is accentuated downstream the re-connection point. As a consequence, already at $x/h = 20$, the influence of the secondary

vortex pair covers a large spanwise extent; see figure 4.5(c). No further pairs of secondary streamwise vortices are captured in the current base flow. Far downstream the micro-ramp, only the remnant of the secondary vortex pair in the near wall region (figure 4.5(d)) and the primary vortices are observed. Based on this qualitative inspection, the rather weak secondary vortices do not show evidence to have a significant impact onto the transport of high- and low-momentum fluid across the boundary layer. The reliability of the previous analysis is subjected to the grid resolution. The steep spanwise coarsening of the grid at $x/h = 4.25$ has been observed to slightly affect the accuracy of the computation of flow features around this streamwise position. The fact that this occurs close to the onset of the secondary vortices may impact on their inception. At $x/h = 6$, three grid points cover the wall-normal extent of the vortices. The λ_2 and Q-criterion detection methods did not show conclusive results.

4.2.2 Flow around the micro-ramp

In the previous section, we have qualitatively shown that entrainment of high-momentum fluid close to the wall is significant only for a limited range of x/h values downstream the micro-ramp. Accordingly, we now focus on the behaviour of the flow around the micro-ramp and at its direct downstream vicinity, with special emphasis put on the origin and initial development of the primary vortex pair and its role in the generation of momentum excess and deficit. The latter remains controversial in the literature.

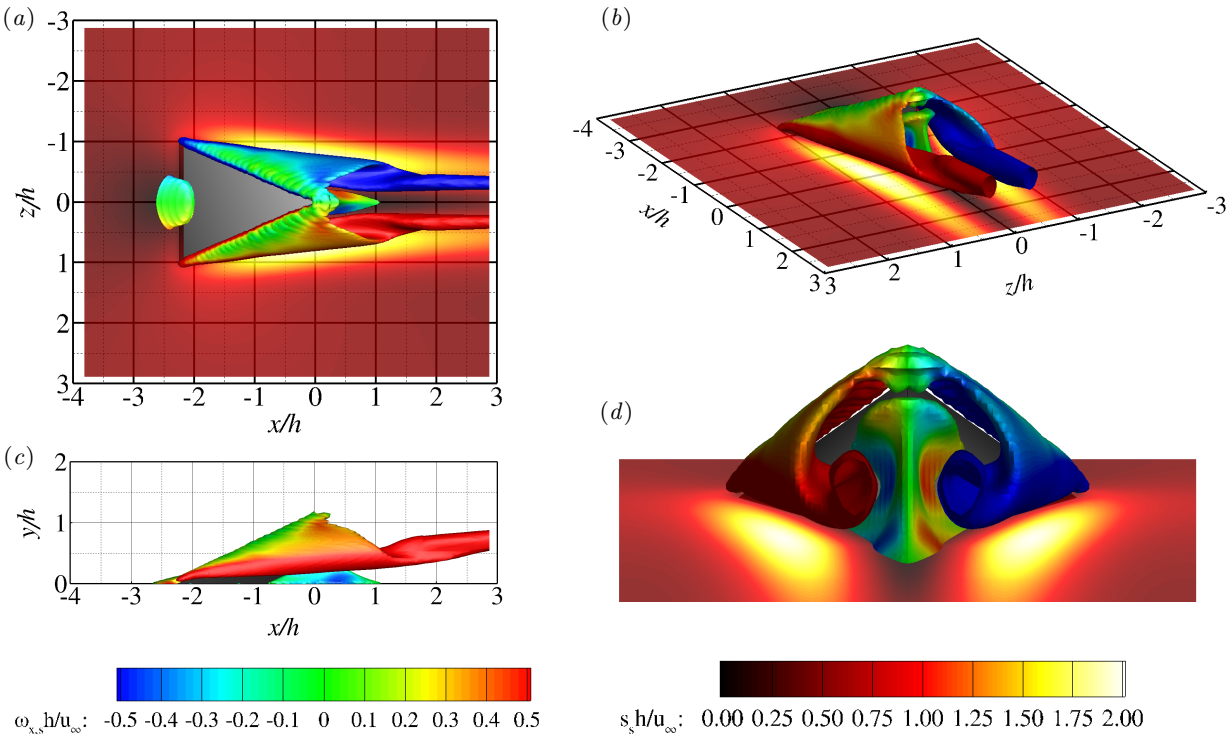

Figure 4.6: Flow separation represented by $u_s/u_\infty = 0$ isosurfaces, primary vortices detected by Q-criterion ($Qh/u_\infty = 0.1$), colour-coded by streamwise vorticity. Wall shear at $y/h = 0$. (a) top view. (b) perspective. (c) side view. (d) inclined back view.

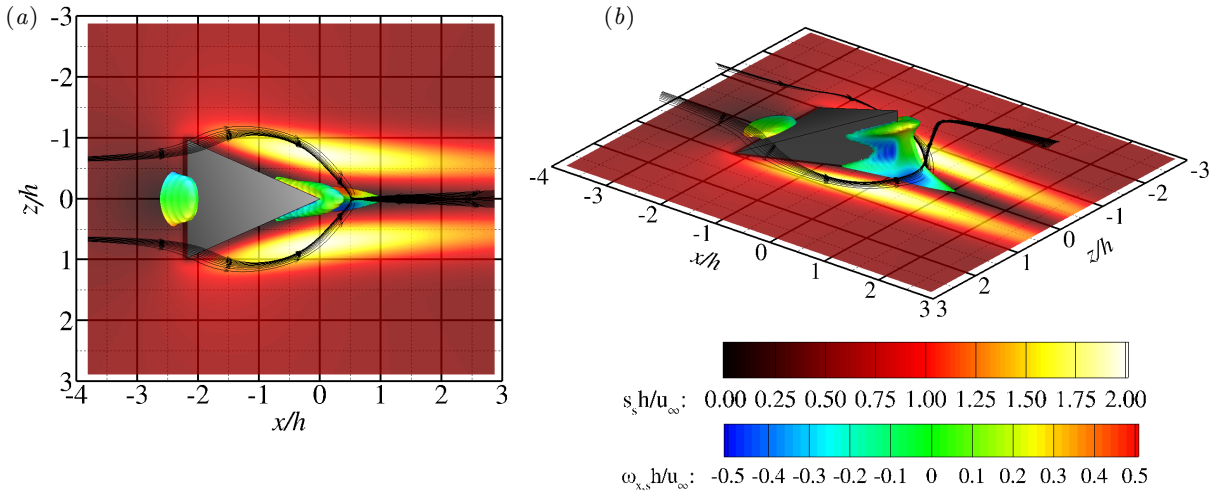

Figure 4.7: Flow separation represented by $u_s/u_\infty = 0$ isosurfaces colour-coded by streamwise vorticity similar to figure 4.6. Slice of shear at $y/h = 0$. Rake of streamlines generated with seeds placed at $(x, y, z)/h = (0.5, 0.3, [-0.05, 0.05])$. (*a*) top view. (*b*) perspective.

Flow recirculation is detected at the leading and trailing edges of the micro-ramp. Leading edge separation is also reported by Babinsky et al. (2009) and Li et al. (2011). These authors point out that leading edge separation creates a horseshoe vortex in front of the micro-ramp which propagates downstream. We do not find evidence of the existence of this structure in our results. The flow reversal region at the trailing edge extends up to $x/h = 1$, as illustrated in figures 4.6 and 4.7. A similar rear separation region is reported by Wang et al. (2014) in the instantaneous supersonic and turbulent wake of the micro-ramp. However, flow reversal in (Wang et al., 2014) appears to be weaker and featuring three disconnected regions. Around the edges of the micro-ramp, separated vortices are captured by Q-criterion (Haller, 2004); see figure 4.6. The element in this work referred to as primary vortex pair is recognised as these separated vortices travelling downstream in the form of streamwise-developing structures. Similar observations are performed by Wang et al. (2013). The action of the primary vortices is observed to delay trailing edge separation at the central part of the micro-ramp's side walls. In figure 4.6(d), the middle portion of the $u_s/u_\infty = 0$ isosurface indicating separation features large values of streamwise vorticity with a rotational sense opposite to that of the primary vortex structure developing aside.

According to Wang et al. (2013), the lowest level fluid is strongly lifted up under the influence of the primary vortices along the chord of the micro-ramp. This gives rise to the origin of the momentum deficit. At the same time, the high-momentum fluid from outer portions of the boundary layer upstream the micro-ramp is entrained in the near-wall region. In view of their results, Wang et al. (2013) claim that the main working principle of the micro-ramp is the —what they refer to as— mechanism of position alternation of low- and high-momentum fluid along the micro-ramp. This mechanism is revealed in figure 4.8 and in agreement with the results presented by Wang et al. (2013). Fluid moving over the slant edges of the micro-ramp generates strong downwash which causes a large-scale transport of streamwise momentum along the micro-ramp chord. The large acceleration of the fluid due to the steep change in geometry in conjunction with the fact that wall-normal gradients of streamwise momentum

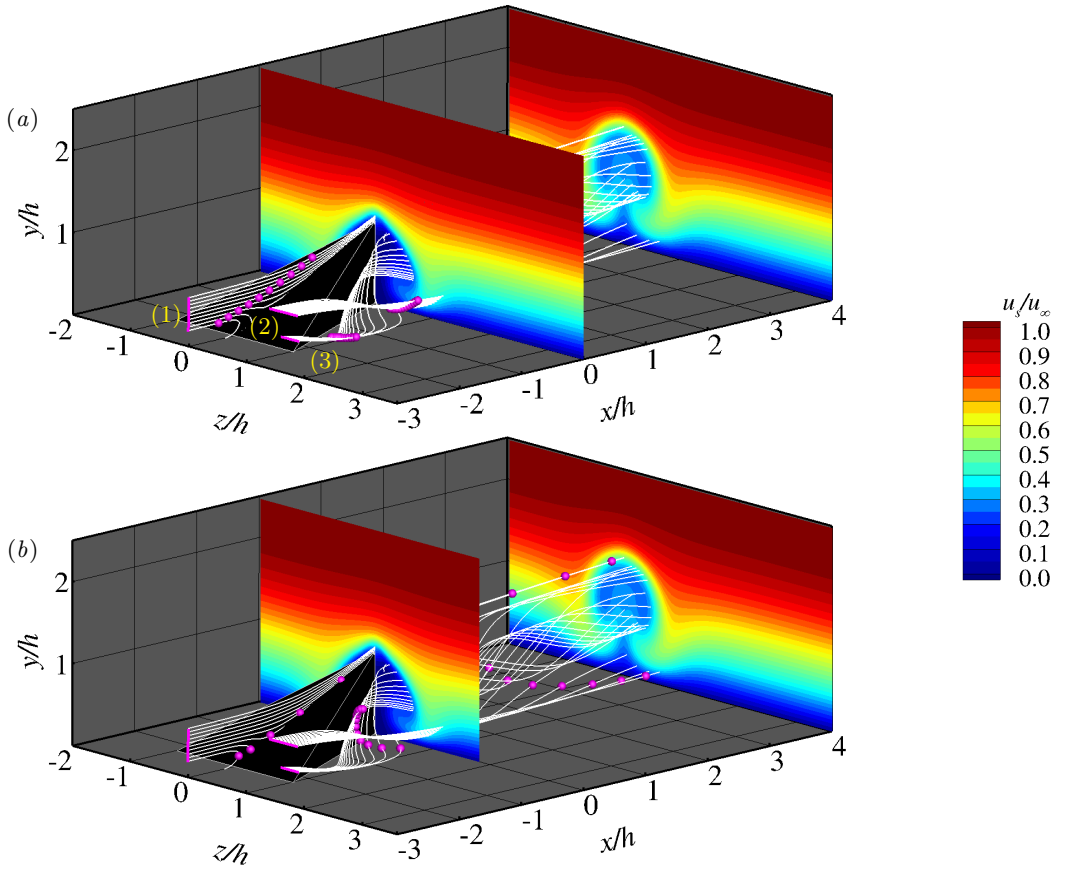

Figure 4.8: y-z planes of streamwise velocity at $x/h = 0$ and 4. Rake of streamlines generated with seeds placed at (1) $(x, y, z)/h = (-3, [0.2, 0.6], 0)$, (2) $(-2.25, 0.45, [0.6, 1.1])$, (3) $(-2.25, 0.15, [0.6, 1.1])$. Particles following the streamlines in time (magenta spheres), initially located at the origin of the rakes (magenta lines). (*a*) represents a time instant prior to (*b*).

are strong in the range $0 \leq y/h \leq 1$, effectively generate momentum excess and deficit already at $x/h = 0$.

The origin and nature of the deficit region is an open question in the literature. We agree with part of the current consensus (Li and Liu, 2011; Wang et al., 2013) in that the central deficit is caused by the action of the primary vortices and its source is the low-momentum fluid upstream the micro-ramp placed along its span (figure 4.8). The behaviour of the streamlines of the flow with seeds placed in the region indicated with a yellow (3) in figure 4.8 illustrates the latter. However, we propose to add to this model the contribution of flow reversal. As portrayed in figure A.3(a) of the appendix, at $x/h = 0$, the separation region features a central bone-shaped contour and initially defines the core of the deficit region. The primary vortices place low-momentum fluid at its sides, under the mechanism described above. This combination of effects gives birth to the structure of the central momentum deficit, which is initially spade-shaped. Immediately downstream, flow recovers from separation and the rotational motion of the vortices gives the low-momentum dip its characteristic circular shape, widely reported in the literature (Babinsky et al., 2009; Ghosh et al., 2010; Sun et al., 2012; Ye et al., 2016).

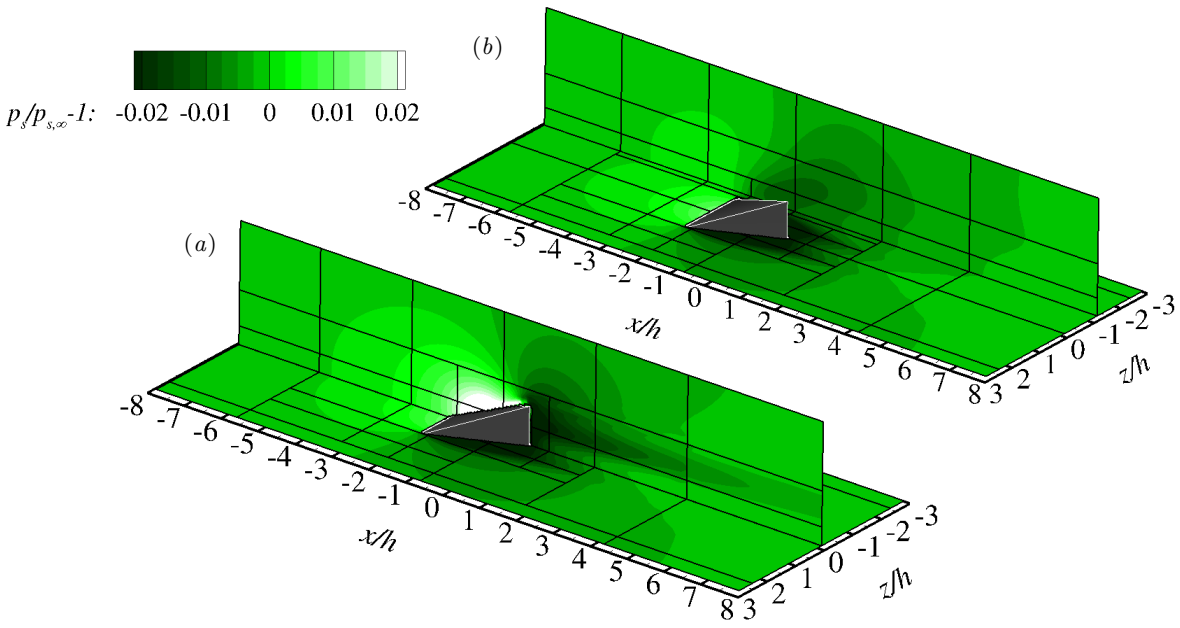

Figure 4.9: Pressure difference around the micro-ramp. x-z planes at $y/h = 0$ and y-x planes at (*a*) $z/h = 0$, (*b*) $z/h = -1.2$. Interface of mesh blocks (solid black lines).

Figure 4.8 furthermore shows a clear-cut visualisation of some of the characteristic effects described in the previous section. In particular, once position alternation has taken place, the vortices move part of the high-momentum fluid that was entrained near the wall back towards upper portions mostly within the deficit region. The streamlines of the flow with seeds placed in the region indicated with a yellow (2) in figure 4.8 show a divergent pattern; a number of particles remain within the momentum excess region, whereas the others are lifted by the upwash into the momentum deficit region (illustrated in figure 4.7(b) as well). This may be an explanation for the efficient recovery of the core of the low-momentum dip in x/h in the base flow. In parallel, we observe the system of entrained high-momentum fluid and the low-momentum dip to move upward.

The presence of the micro-ramp in the boundary layer alters the pressure distribution, as illustrated in figure 4.7. On the one hand, $p_s - p_{s,\infty}$ is positive upstream the micro-ramp and on its upper face, where the pressure difference attains its maximum positive values. This is ascribed to the effect of velocity deceleration upstream the micro-ramp and flow recirculation at its leading edge. On the other hand, at the sides of the micro-ramp and at its downstream vicinity, $p_s - p_{s,\infty}$ acquires negative values. The low pressure region aside the micro-ramp is assumed to be caused by the influence of the cores of the primary vortices. Near the micro-ramp tip, this vortex-induced low pressure contributes to the decrease of the pressure due to trailing edge flow separation. Figure 4.9 displays streamwise planes of pressure difference at $z/h = 0$ and $z/h = -1.2$, two spanwise coordinates which serve to characterise the behaviour of pressure in the deficit and excess regions respectively. Around these spanwise coordinates, at $x/h = 0$, $p_s - p_{s,\infty}$ has attained low values. Further downstream, pressure recovery yields $\partial p_s/\partial x > 0$. The current pressure distribution is in qualitative agreement with that presented by Yan et al. (2016) for a supersonic micro-ramp flow.

4.2.3 Streamwise-momentum-streak and shear fields

As reported above, the interaction of the micro-ramp with the incoming boundary layer significantly alters its structure already at $x/h = 0$. Downstream the micro-ramp, the regions of added and reduced momentum show to move away from the surface for increasing x/h and to reduce their strength. These observations are made upon inspection of the streamwise velocity field. We next aim to more thoroughly characterise the evolution in space of the regions of added and reduced momentum because it is of relevance to assess the micro-ramp performance. To that end, we compute the streamwise-velocity-streak field (2.17) of the $\boldsymbol{q}_s$ solution. This field, denoted by u_s^{str}, is the difference between the streamwise velocity and the unperturbed boundary layer, i.e., $u_s^{str} = u_s - u_{un}$. Accordingly, the momentum excess region is hereafter formally defined as the portion of the flow field at which $u_s^{str} > 0$, whilst the momentum deficit region is defined as the portion with $u_s^{str} < 0$. The streamwise-velocity-streak field of the micro-ramp base flow is depicted in figure 4.10.

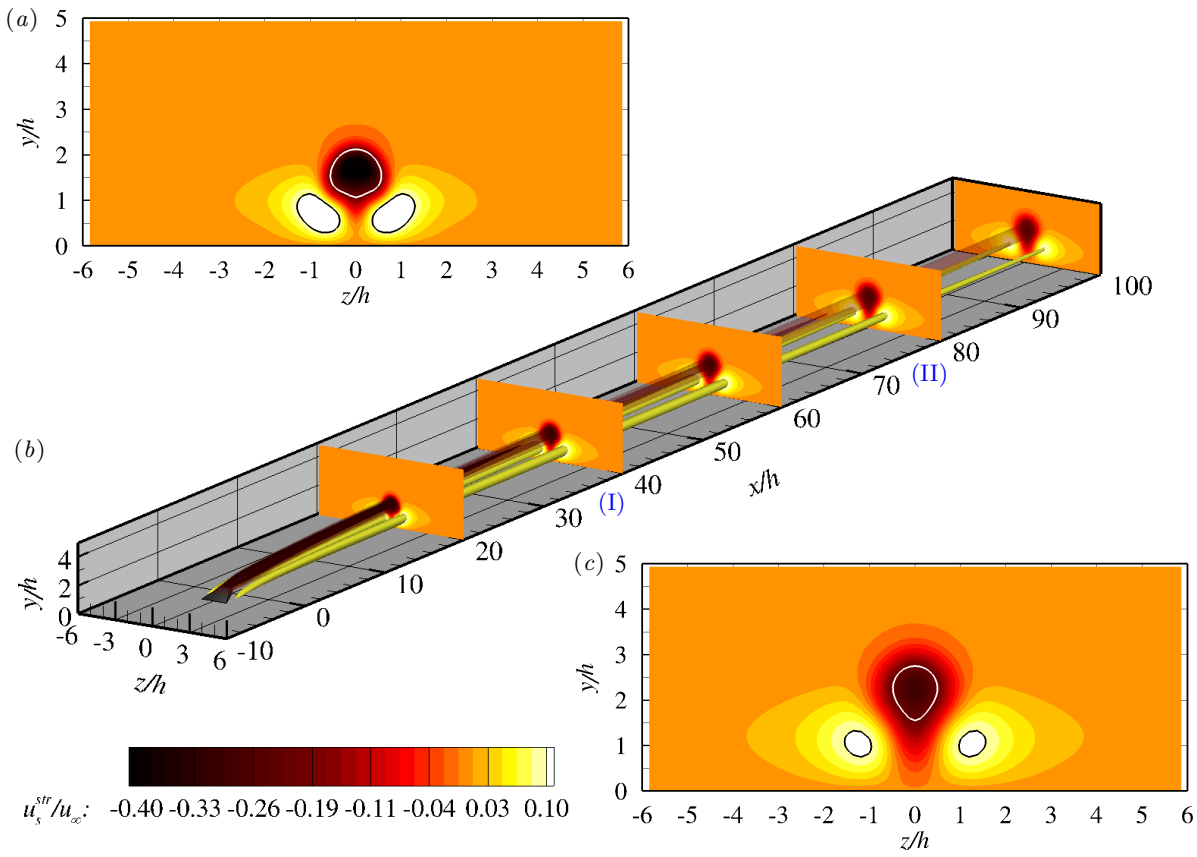

Figure 4.10: Streamwise velocity streaks. y-z planes at (*a*) $x/h = 20$, (*c*) 80 with iso-contours of $u_s^{str}/u_\infty = -0.2$ (white line), 0.1 (black). (*b*) perspective of y-z planes at $x/h = 20$; 40; 60; 80; 100 with iso-surfaces of -0.4 (black opaque); -0.3 (brown moderately translucent); -0.2 (red highly translucent); 0.1 (yellow opaque). Ending positions of the iso-surfaces defined by $u_s^{str}/u_\infty = -0.4$ and -0.3 at $x/h = 36$ (I) and 74 (II).

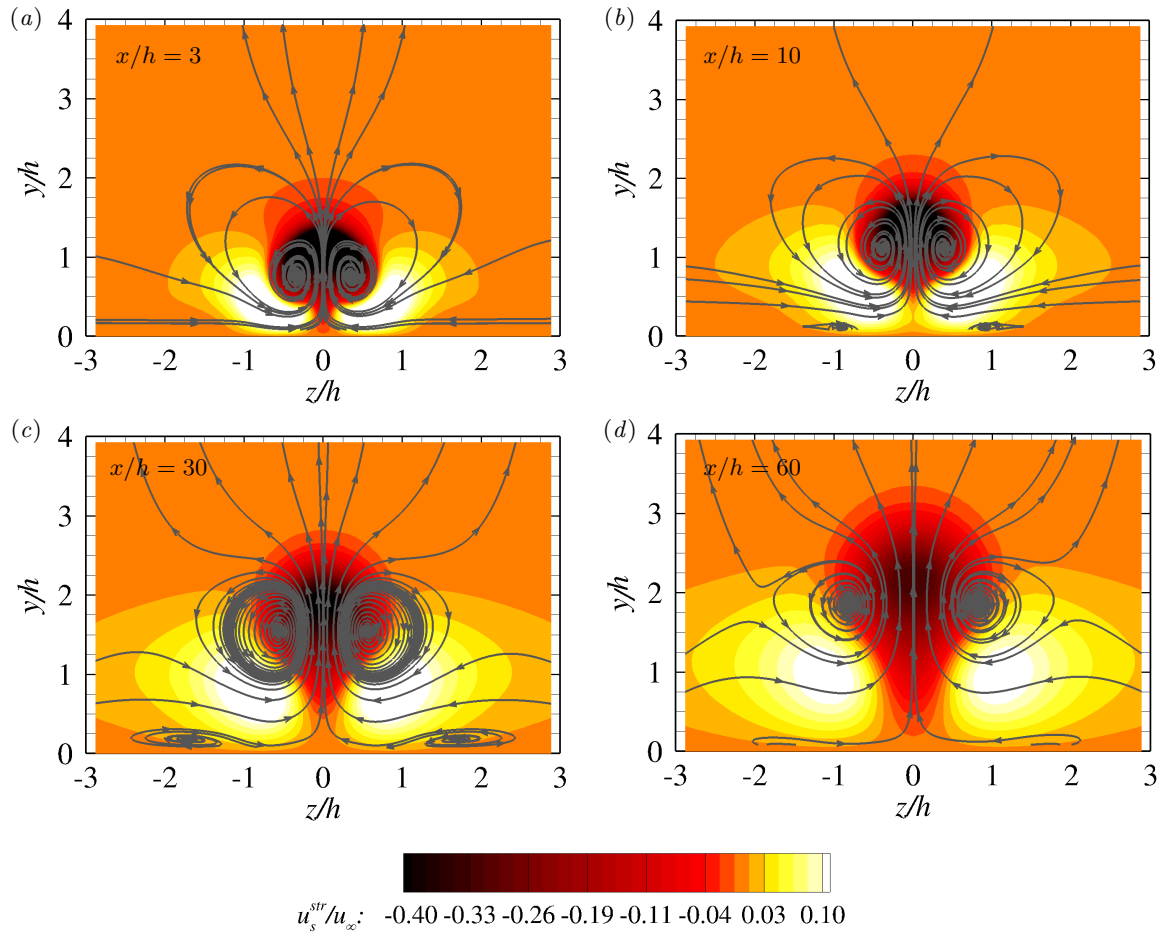

Figure 4.11: y-z planes of streamwise velocity streaks with selected projected streamlines at (a) $x/h = 3$, (b) 10, (c) 30, (d) 90.

In figure 4.11, we reproduce figure 4.3 and show a representation of the streamwise-velocity-streak field at four representative x/h stations together with the projected streamlines of the flow. The spatial evolution of the regions of momentum excess and deficit in the range $0 \leq x/h \leq 10$ is illustrated in figures A.3 and A.4 of the appendix.

At $x/h = 0$, the excess region is made up of two symmetric lobes attached to the wall; see figure A.3(c) of the appendix. The deficit region is initially spade-shaped, due to the combination of flow reversal at the centre plane and the placement of low-momentum fluid at its sides, as described in §4.2.2. Immediately downstream, the rotational motion of the vortices expands the excess lobes towards the centre plane, hence reducing the initial momentum deficit at $z/h = 0$ close to the wall. This is illustrated in figure A.4(c) of the appendix. At $x/h = 10$, the excess lobes are practically connected at the centre plane. Nonetheless, the streamwise-momentum-streak field features small values at $z/h = 0$ (figure 4.11(b)). This is conform with the reduced wall shear at the centre plane for small x/h. As the primary vortices move away from the surface, so do the excess lobes and the low-momentum dip. The excess of momentum at the wall gradually becomes less strong.

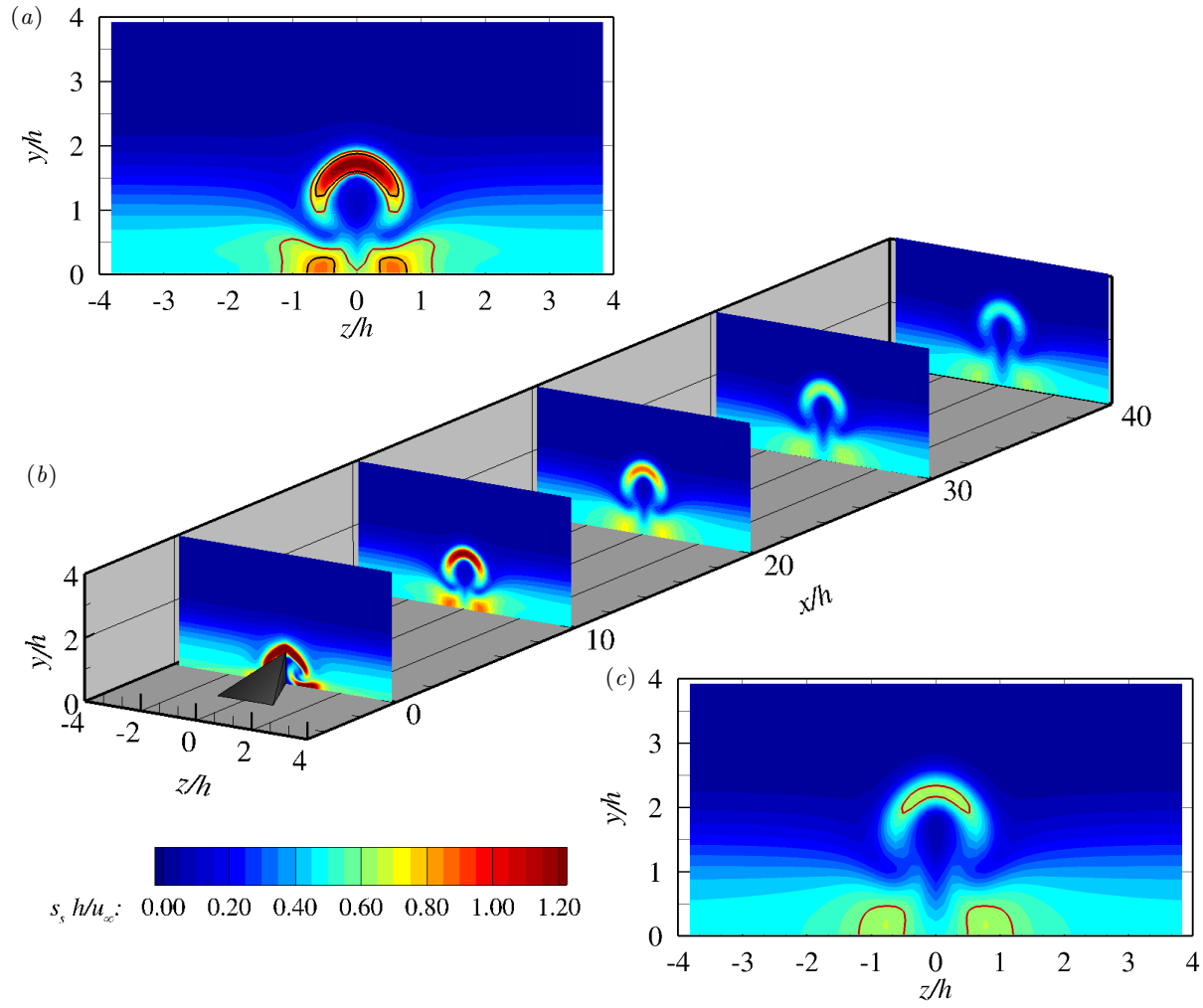

Figure 4.12: Shear. y-z planes at (*a*) $x/h = 10$, (*c*) 30 with iso-contours of $s_s h/u_\infty$ attaining $1/2$ and $2/3$ of the peak value (red and black lines). (*b*) perspective of y-z planes at $x/h = 0$; 10; 20; 30; 40.

Along $0 \leq x/h \leq 10$, the excess lobes move from aside the centre plane towards $z/h = 0$. For $x/h \geq 10$ this trend is reverted, which is ascribed to the gradual spanwise shift of the primary vortex pair for increasing x/h. This effect, in conjunction with the previously reported sustained action of central upwash, cause the deficit region to propagate downward towards the wall; see figure 4.11(c,d). In parallel, its upper boundary expands radially. Far downstream the micro-ramp, the excess lobes have increased their area by expanding in y- and z-directions and the deficit region has become bulb-shaped. The near-wall fluid layers feature small values of u_s^{str}. Both the deficit and the excess regions have become more homogeneous and their core values have significantly decreased, as compared to near-ramp streamwise positions.

The regions of reduced and added momentum are accompanied by strong shear layers. The shear field of the micro-ramp base flow, defined as the norm of the strain-rate tensor (2.15), is portrayed in figure 4.12. The low-momentum dip is partially bounded by an arch-shaped

shear layer since it features large gradients of streamwise velocity in the wall-normal and spanwise directions at its upper boundary. This structure is hence linked to the momentum deficit. The wall-normal shear layer appears to be stronger than the spanwise shear layer. When moving downstream, the overall structure lifts up and decreases in strength due to the rapid recovery of the central momentum deficit. Further regions of high shearing motion are captured aside the centre plane near the wall, as a consequence of the entrainment of high-momentum fluid close to the surface. These high-shear patches are related to the strips of enhanced wall shear in figure 4.2(a). Downstream the micro-ramp, they show to decrease in strength due to the recovery of the flow near the wall and to progressively shift towards larger $|z/h|$. The development of shear layers in the near-ramp field is portrayed in figures A.3(i,j) and A.4(i,j) of the appendix.

4.2.4 Derivation and evaluation of a streamwise-momentum-streak transport equation for incompressible steady flow fields

Previous qualitative observations have suggested that the laminar primary vortices are unable to maintain a significant generation of momentum excess sufficiently downstream the micro-ramp. In an attempt to assess this fact quantitatively, we next derive a streamwise-momentum-streak transport equation for incompressible steady flow fields. With it, we intend to identify which flow mechanisms play a dominant role in the generation of streamwise-velocity streaks, evaluate their relative contribution as a function of x/h and further understand how the momentum excess and deficit evolve downstream the micro-ramp.

The following derivation assumes steady incompressible flow with constant viscosity, which is a reasonable approximation for $M < 0.3$. Furthermore, in the unperturbed flow region (2.16), $w_{\mathrm{un}} = 0$, $\partial u_{\mathrm{un}}/\partial z = 0$ and $\partial v_{\mathrm{un}}/\partial z = 0$. Since we are interested in mathematically characterising the behaviour of the momentum excess and deficit in the base flow, we propose to decompose the base flow velocity field, $\boldsymbol{v}_{\mathrm{s}}$, as

$$\boldsymbol{v}_{\mathrm{s}} = \boldsymbol{v}_{\mathrm{un}} + \boldsymbol{v}_{\mathrm{s}}^{\mathrm{str}}, \tag{4.1}$$

i.e., the sum of the velocity field of the unperturbed boundary layer, $\boldsymbol{v}_{\mathrm{un}}$, and the velocity-streak field, $\boldsymbol{v}_{\mathrm{s}}^{\mathrm{str}}$. The pressure field is decomposed similarly. For incompressible flows,

$$\nabla \cdot \boldsymbol{v}_{\mathrm{un}} = 0, \tag{4.2}$$

and

$$\nabla \cdot \boldsymbol{v}_{\mathrm{s}}^{\mathrm{str}} = 0. \tag{4.3}$$

By introducing the velocity and pressure decompositions into the streamwise component of the momentum conservation equation (2.4), we obtain

$$\rho \left(\boldsymbol{v}_{\mathrm{un}} + \boldsymbol{v}_{\mathrm{s}}^{\mathrm{str}}\right) \cdot \left(\nabla u_{\mathrm{un}} + \nabla u_{\mathrm{s}}^{\mathrm{str}}\right) = -\frac{\partial p_{\mathrm{un}}}{\partial x} - \frac{\partial p_{\mathrm{s}}^{\mathrm{str}}}{\partial x} + \mu \nabla^2 u_{\mathrm{un}} + \mu \nabla^2 u_{\mathrm{s}}^{\mathrm{str}}. \tag{4.4}$$

The steady streamwise momentum conservation equation for the unperturbed flow reads

$$\rho \left(\boldsymbol{v}_{\mathrm{un}} \cdot \nabla\right) u_{\mathrm{un}} = -\frac{\partial p_{\mathrm{un}}}{\partial x} + \mu \nabla^2 u_{\mathrm{un}}, \tag{4.5}$$

and hence combining (4.4) with (4.5) and (4.3) yields

$$\rho(\boldsymbol{v}_{\mathrm{un}} \cdot \nabla) u_{\mathrm{s}}^{\mathrm{str}} = -\frac{\partial p_{\mathrm{s}}^{\mathrm{str}}}{\partial x} + \mu \nabla^2 u_{\mathrm{s}}^{\mathrm{str}} + \nabla \cdot (-\rho u_{\mathrm{un}} \boldsymbol{v}_{\mathrm{s}}^{\mathrm{str}}) + \nabla \cdot (-\rho u_{\mathrm{s}}^{\mathrm{str}} \boldsymbol{v}_{\mathrm{s}}^{\mathrm{str}}), \tag{4.6}$$

or, by using (4.1) to combine the last two terms,

$$\underbrace{\rho(\boldsymbol{v}_{\mathrm{un}} \cdot \nabla) u_{\mathrm{s}}^{\mathrm{str}}}_{\textbf{streak advection}} = \underbrace{-\frac{\partial p_{\mathrm{s}}^{\mathrm{str}}}{\partial x}}_{\textbf{pressure}} + \underbrace{\mu \nabla^2 u_{\mathrm{s}}^{\mathrm{str}}}_{\textbf{diffusion}} + \underbrace{\nabla \cdot \overbrace{(-\rho u_{\mathrm{s}} \boldsymbol{v}_{\mathrm{s}}^{\mathrm{str}})}^{\textbf{streak stress}}}_{\textbf{streak-shear-correlation}} . \tag{4.7}$$

This equation resembles the streamwise component of the momentum conservation equation, with advection, pressure and viscous diffusion. However, we additionally obtain an extra term, the so-called streak-shear-correlation. It is interpreted as the divergence of an apparent stress, $-\rho u_{\mathrm{s}} \boldsymbol{v}_{\mathrm{s}}^{\mathrm{str}}$, hereafter referred to as streak stress, in an analogous fashion to the treatment of the Reynolds stresses in the RANS equations (White, 2006). The streak-shear-correlation term, as its name suggests, requires large velocity streaks in presence of strong velocity gradients to effectively contribute to the generation of $\rho u_{\mathrm{s}}^{\mathrm{str}}$. The relative contribution of each component is further revealed when the term is expanded:

$$-\rho \left(u_{\mathrm{s}}^{\mathrm{str}} \frac{\partial u_{\mathrm{s}}}{\partial x} + v_{\mathrm{s}}^{\mathrm{str}} \frac{\partial u_{\mathrm{s}}}{\partial y} \right), \tag{4.8}$$

using $\nabla \cdot \boldsymbol{v}_{\mathrm{s}}^{\mathrm{str}}$.

We have identified three main mechanisms contributing to the generation of $\rho u_{\mathrm{s}}^{\mathrm{str}}$ and we aim to characterise their role in the micro-ramp base flow. To that end, expression (4.7) is evaluated using a control volume approach; we denote by Ω^{E} the domain of the flow field with $u_{\mathrm{s}}^{\mathrm{str}} > 0$ (momentum excess region), and by Ω^{D} the domain of the flow field with $u_{\mathrm{s}}^{\mathrm{str}} < 0$ (momentum deficit region). Both Ω^{E} and Ω^{D} are continuous three-dimensional domains, as exemplified in figure 4.10. The approach presented next relies on computing the relative contribution of pressure, diffusion and streak stresses to the flux of $\rho u_{\mathrm{s}}^{\mathrm{str}}$ across the boundary of Ω^{E} and Ω^{D} (denoted by $\partial\Omega^{\mathrm{E}}$ and $\partial\Omega^{\mathrm{D}}$) as function of the streamwise coordinate.

We split the streamwise extent of the domain into segments defined by points x_i and x_{i+1}, $i = 1, 2, 3...$ The cross-sectional areas of Ω^{E} and Ω^{D} at x_i are respectively denoted by A_i^{E} and A_i^{D}. We integrate (4.7) over A_i^{E} and A_i^{D} (superscripts E and D are next omitted) at a streamwise position x_i:

$$\int_{A_i} \rho(\boldsymbol{v}_{\mathrm{un}} \cdot \nabla) u_{\mathrm{s}}^{\mathrm{str}} \, dA_i = \int_{A_i} -\frac{\partial p_{\mathrm{s}}^{\mathrm{str}}}{\partial x} \, dA_i + \int_{A_i} \mu \nabla^2 u_{\mathrm{s}}^{\mathrm{str}} \, dA_i + \int_{A_i} \nabla \cdot \left(-\rho u_{\mathrm{s}} \boldsymbol{v}_{\mathrm{s}}^{\mathrm{str}}\right) \, dA_i. \tag{4.9}$$

The term on the LHS of (4.9), the flux of $\rho u_{\mathrm{s}}^{\mathrm{str}}$ across $\partial\Omega^{\mathrm{E}}$ or $\partial\Omega^{\mathrm{D}}$ at x_i, expresses whether locally streamwise-momentum streaks are generated, destructed or maintained. When the analysis is applied to Ω^{E}, positive and negative contributions of the terms on the RHS of (4.9) are respectively associated to local generation and destruction of (positive) streamwise momentum streaks. On the contrary, when considering Ω^{D}, positive and negative contributions of the terms on the RHS are respectively associated to local destruction and generation

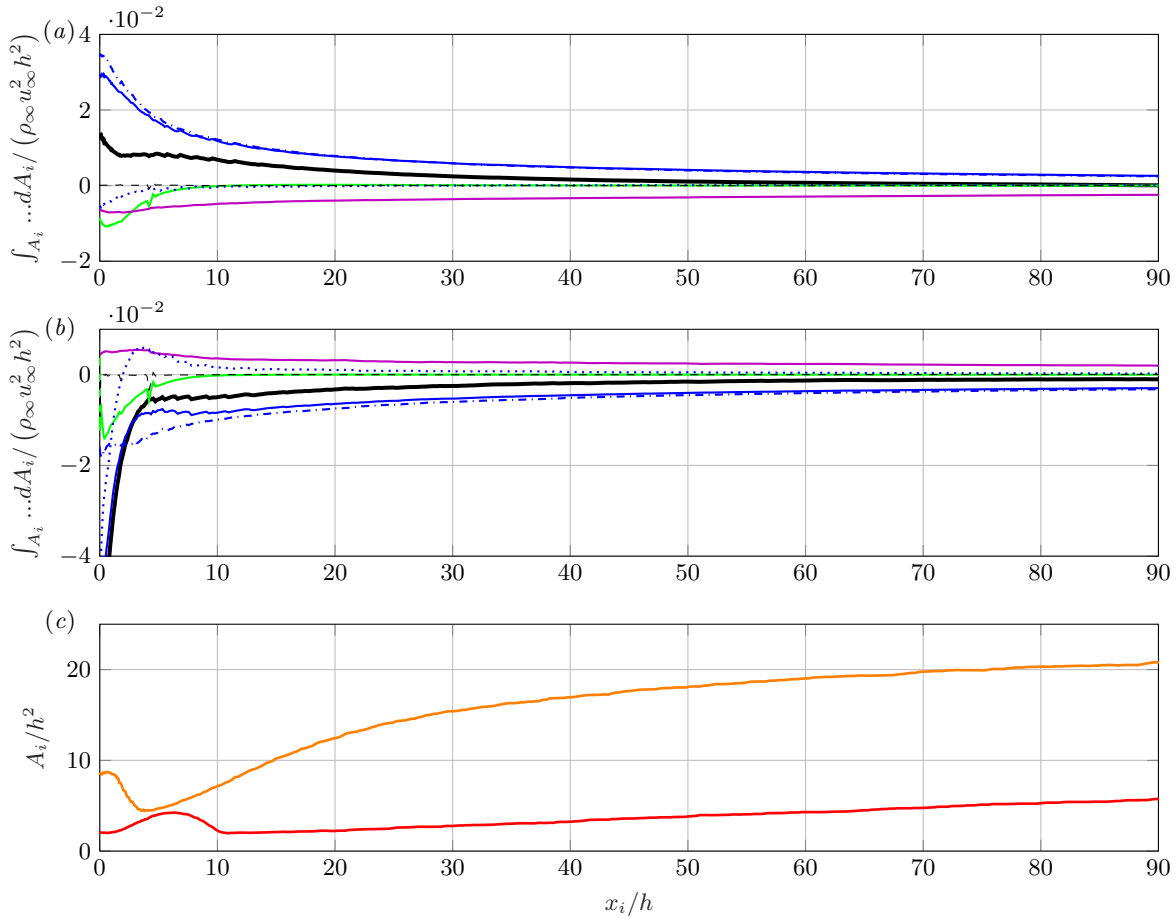

Figure 4.13: Integral terms of (4.9) as function of the streamwise coordinate evaluated in (*a*) Ω^{E}, (*b*) Ω^{D}: $\rho(\boldsymbol{v}_{\mathrm{un}} \cdot \nabla) u_{\mathrm{s}}^{\mathrm{str}}$ (solid black), $-\partial p_{\mathrm{s}}^{\mathrm{str}}/\partial x$ (solid green), $\mu \nabla^2 u_{\mathrm{s}}^{\mathrm{str}}$ (solid magenta), $\nabla \cdot (-\rho u_{\mathrm{s}} \boldsymbol{v}_{\mathrm{s}}^{\mathrm{str}})$ (solid blue) split into the relative contribution of $\nabla \cdot (-\rho u_{\mathrm{un}} \boldsymbol{v}_{\mathrm{s}}^{\mathrm{str}})$ (dash-dotted blue) and $\nabla \cdot (-\rho u_{\mathrm{s}}^{\mathrm{str}} \boldsymbol{v}_{\mathrm{s}}^{\mathrm{str}})$ (dotted blue) as expressed in (4.6), local sum of terms of (4.9) (dashed black). (*c*) A_i^{E} (orange) and A_i^{D} (red) along x/h.

of (negative) streamwise-momentum streaks. Attention must be paid to the fact that (4.9) does not give direct information on the trend followed by A_i in x, on the topology of the excess lobes and the central low-momentum dip, or on the distribution of streamwise-momentum streaks within Ω^{E} and Ω^{D}. These are other relevant features, which ought to be addressed by analysing (4.7) locally in the flow field and/or by other tools. The terms (4.9) are evaluated numerically; we choose x_i to be the streamwise coordinates of the nodes of the computational mesh. The results of the numerical integration and the trend followed by A_i^{E} and A_i^{D} along the streamwise direction are presented in figure 4.13.

At first glance, figure 4.13(*a*) reveals that generation of positive velocity streaks (black solid line) is first significant near the micro-ramp and, for $x/h > 10$, it experiences a noticeable decrease. Accordingly, we structure the analysis presented next in the following manner: we first focus on generation of momentum excess at and near the micro-ramp by analysing the evolution in x/h of the integral terms of (4.9) evaluated at Ω^{E} for $-4 \leq x/h \leq 10$. In

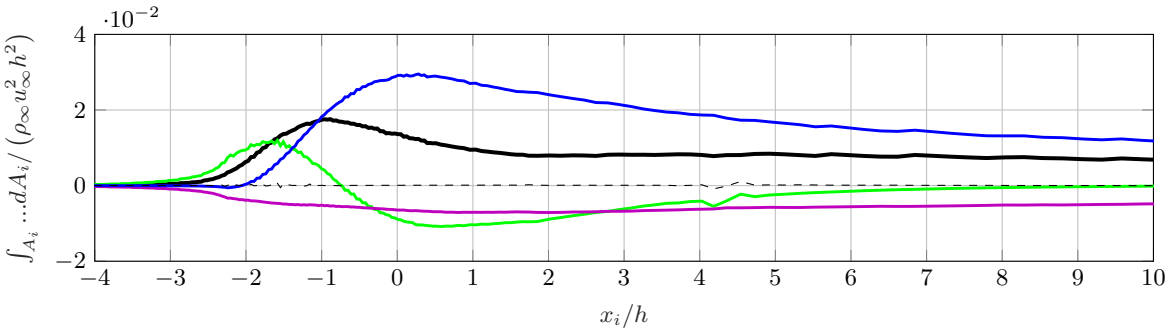

Figure 4.14: Integral terms of (4.9) as function of the streamwise coordinate evaluated in Ω^{E}. $\rho(\boldsymbol{v}_{\mathrm{un}} \cdot \nabla)u_{\mathrm{s}}^{\mathrm{str}}$ (solid black), $-\partial p_{\mathrm{s}}^{\mathrm{str}}/\partial x$ (solid green), $\mu\nabla^2 u_{\mathrm{s}}^{\mathrm{str}}$ (solid magenta), $\nabla \cdot (-\rho u_{\mathrm{s}} \boldsymbol{v}_{\mathrm{s}}^{\mathrm{str}})$ (solid blue), local sum of terms of (4.9) (dashed black).

figure 4.14, we reproduce figure 4.13(a) zooming into this x-range. Thereafter, we discuss the generation of momentum excess and deficit for $10 \leq x/h \leq 90$ by assessing the streamwise evolution of the terms of (4.9) evaluated at both Ω^{E} and Ω^{D}.

Generation of momentum excess at and near the micro-ramp ($-4 \leq x/h \leq 10$)

Results of figure 4.14 indicate that streak stresses (blue curve) act so as to generate momentum excess for all x/h in the range $-4 \leq x/h \leq 10$; the associated curve lies in the positive half-plane. Diffusion (purple curve) plays an opposite role, it is of *destructive* nature. Pressure (green curve) first contributes positively to the flux of $\rho u_{\mathrm{s}}^{\mathrm{str}}$ across $\partial\Omega^{\mathrm{E}}$ and, as x/h increases, it contributes negatively. We observe inaccuracies of the results presented in figure 4.14 around $x/h = 4.25$, as explained above, due to a too steep coarsening of the mesh in this location.

To better understand the behaviour of the pressure curve in figure 4.14, we recall figure 4.9(b) depicting the pressure distribution at a spanwise plane ($z/h = -1.2$) contained in the excess region at the micro-ramp vicinity. The boundary layer is not subjected to an external pressure gradient, so $p_{\mathrm{s}} - p_{\mathrm{s},\infty}$ represents the pressure streaks field. Pressure starts to contribute to the generation of momentum excess when $\partial p_{\mathrm{s}}/\partial x$ aside the micro-ramp becomes negative due to the influence of the vortex cores. The pressure curve in figure 4.14 peaks at $x/h \approx -1.7$; immediately upstream of this position, pressure has undergone a rapid decrease; see figure 4.9(b). From $x/h \approx -1.7$ onward, the contribution of the pressure in streak generation first decreases and thereafter ($x/h > -0.75$) becomes destructive. The latter is ascribed to the fact that pressure recovery in streamwise direction yields $\partial p_{\mathrm{s}}/\partial x > 0$. Downstream of $x/h = 0.5$, the pressure curve in figure 4.14 gradually approaches the horizontal axis from the negative half-plane. Current results show that pressure contributes significantly to the initial generation of momentum excess at the micro-ramp. As soon as the pressure introduces gradients of $\rho u_{\mathrm{s}}^{\mathrm{str}}$, diffusion starts to play a role as well. The largest productive contribution, however, comes from streak stresses. The associated curve in figure 4.14 first becomes non-zero at $x/h = -2.1$, which is approximately the position of the micro-ramp's leading edge, and peaks at $x/h = 0$, the position of the micro-ramp's trailing edge.

Through visual inspection, we first detect regions of positive $u_{\mathrm{s}}^{\mathrm{str}}$ in the flow field at $x/h = -3$, thus upstream the micro-ramp. At this streamwise coordinate, the positive contribution of

pressure to the flux of ρu_s^{str} across $\partial\Omega^E$ starts to exceed the negative contribution of diffusion. As a consequence, the curve in figure 4.14 indicating the total generation of momentum excess departs from the horizontal axis. Further downstream, although the contribution of pressure eventually decreases, the rapid streamwise growth of the streak stresses maintains the flux of momentum excess across $\partial\Omega^E$ increasingly positive in streamwise direction until it attains a maximum at $x/h = -1$.

From $x/h = -1$ onward, generation of positive streamwise-momentum streaks decreases. However, it remains significant for an initial range of x/h values downstream the micro-ramp. This shows partial disagreement with conclusions drawn by Wang et al. (2013), inasmuch as they claim that the mechanism of the micro-ramp is position alternation along the micro-ramp rather than the downstream activity of the primary vortices. Although we agree with Wang et al. (2013) in that the capability of the primary vortices to generate momentum excess downstream the micro-ramp is less than what is established by the current consensus, our results indicate that momentum excess is not uniquely generated at the micro-ramp. Furthermore, it ought to be emphasised that the current interpretations are based on the base flow results. In §4.1 we have pointed out the importance of disturbance activity in the micro-ramp functionality, an issue that is discussed later on.

Generation of momentum excess and deficit along the domain ($0 \leq x/h \leq 90$)

We have shown that pressure has a destructive effect on the momentum excess at the micro-ramp's downstream vicinity. Similar observations are made for the region of reduced momentum: downstream the micro-ramp, the pressure generates momentum deficit, i.e., contributes negatively to the flux of ρu_s^{str} across $\partial\Omega^D$; see figure 4.13(b). The core of the low-momentum dip is located at the centre plane. In this region near the micro-ramp, pressure recovery yields $\partial p_s/\partial x > 0$ (figure 4.9(a)) and thus the pressure term in (4.9) yields a negative contribution. Results of figure 4.13(a,b) indicate that for $x/h > 10$, the pressure does not add a significant contribution to the generation of momentum excess nor momentum deficit.

Diffusion has a *destructive* nature in Ω^E but also in Ω^D for all x/h, i.e., contributes negatively to the flux of ρu_s^{str} across $\partial\Omega^E$ and positively to the flux of ρu_s^{str} across $\partial\Omega^D$. This behaviour was expected, inasmuch as diffusion acts to balance the amount of streamwise-momentum streaks. Unlike pressure, its contribution is prolonged until far downstream the micro-ramp rather than exclusively at the vicinity of it. The curves associated to diffusion in figure 4.13(a,b) follow a rather constant trend in streamwise direction. The largest (absolute) values are found for small x/h. In this range, the interface of Ω^E and Ω^D features large gradients of u_s^{str}; see figure 4.11.

Streak stresses act so as to generate momentum excess and deficit along the entire streamwise extent of the domain, i.e., contribute positively to the flux of ρu_s^{str} across $\partial\Omega^E$ and negatively to the flux of ρu_s^{str} across $\partial\Omega^D$. We first focus on added momentum. Streak stresses have been shown to play the central role in the generation of momentum excess at the micro-ramp and at its immediate downstream vicinity. Results of figure 4.13(a) show that in the range $0 \leq x/h \leq 90$, the curve of streak stresses decreases monotonically. Gradually, their contribution to the flux of ρu_s^{str} across $\partial\Omega^E$ approaches that of diffusion in absolute value; eventually, streak stresses solely counter-act the effect of diffusion. As a consequence, for $x/h > 50$, the total flux of momentum excess (black line in figure 4.13(a)) approaches zero from above. Thus, at these downstream locations, the momentum excess generated upstream

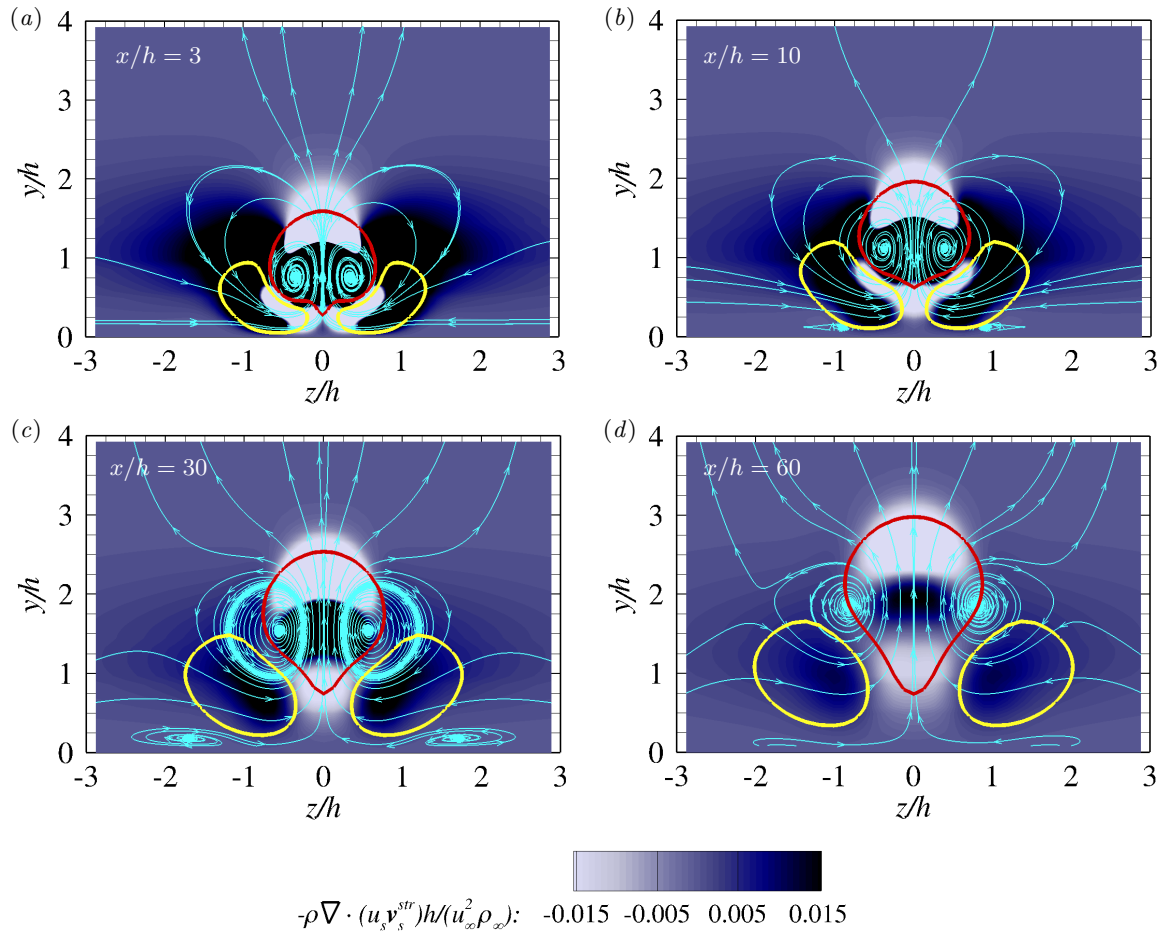

Figure 4.15: y-z planes of streak-shear-correlation with selected projected streamlines at (*a*) $x/h = 3$, (*b*) $x/h = 10$, (*c*) $x/h = 30$, (*d*) $x/h = 60$. Iso-contours of $u_s^{str}/u_\infty = -0.06$ (red line), $u_s^{str}/u_\infty = 0.06$ (yellow line).

is conserved; it is essentially transported downstream without further significant addition or subtraction. Current results thereby confirm quantitatively that the primary vortices are not capable of generating momentum excess sufficiently downstream the micro-ramp. As mentioned previously, this is hypothesised to be mainly combination of two factors: the decay of vortex-induced downwash and the fact that as the primary vortices lift up, they move into portions of the boundary layer featuring lower wall-normal gradients of streamwise velocity. With regard to the momentum deficit, the total generation of negative streamwise-momentum streaks persists for large x/h with a small productive value. This highlights the endurance of the central upwash as compared to the lateral downwash.

In figure 4.15 we reproduce figures 4.3 and 4.11 and we show y-z planes of the non-dimensionalised streak-shear-correlation field (4.7) with iso-contours of streamwise-velocity streaks. Streak stresses play the central role in the budget of ρu_s^{str} and we observe that the system of streamwise-velocity streaks evolves according to the distribution of streak-shear-correlation. Close to the micro-ramp, the lateral regions of positive streak-shear-correlation (figure 4.15(a,b)) match the regions of figure 4.3(a,b) in which fluid from mid-outer portions of

the boundary layer is actively moved downward under the action of the primary vortices. For increasing x/h, these lateral regions of positive streak-shear-correlation decrease in strength and move beneath the vortex cores; see figure 4.15(c,d). At the regions where positive streak-shear-correlation in figure 4.15(c,d) is dominant, the layers of streamwise velocity aside the centre plane display the largest downward curvature in figure 4.3(c,d).

For all x/h, we observe regions of negative streak-shear-correlation at the bottom and top parts of the momentum deficit region. The bottom part is attributed to the lift-up of low-momentum fluid near the wall under the action of vortex-induced upwash. The top part, linked as well to the action of upwash, characterises the transport of low-momentum fluid from the core of the deficit region upward and towards outer fresh portions of boundary layer. The central region of positive streak-shear-correlation is ascribed to the transport of high-momentum fluid initially entrained near the wall back towards upper positions under the self-induced motion of the primary vortices. This explains the efficient recovery of the core of the low-momentum dip in x/h; the velocity deficit is initially strong enough to persist the continuous entrainment of high-momentum fluid from the excess region. We see lateral branches of negative streak-shear-correlation at the bottom part of Ω^{D} for small x/h. They are as well attributed to redistribution of high-momentum fluid.

The action of the primary vortices causes an initial efficient large-scale transport of streamwise momentum. Thus, close to the micro-ramp, we observe the shape of the momentum excess and deficit regions to undergo rapid deformation in x/h. Far downstream the micro-ramp, decay of vortex activity together with the fact that transport by diffusion becomes relevant merely cause the diffusion of the excess and deficit regions. The rate of change in x/h of the shape of Ω^{E} and Ω^{D} is much slower than in the near-ramp field. This is in agreement with plotted trends of the areas A_i^{E} and A_i^{D} in figure 4.13(c).

4.3 Instantaneous flow

In §4.2, we have described the base flow and analysed micro-ramp flow features in absence of disturbance activity. We now turn our attention to the dynamics of perturbations naturally evolving in the flow field when SFD is not applied. As for considering a supercritical roughness Reynolds number for our analysis, we expect unsteady and transitional behaviour of the flow, as detailed in §1.1. Disturbance growth alters the structure of the primary vortex pair, modifies the topology of the base flow and introduces a new (time-dependant) flow organisation.

In the first part of the analysis presented next, we analyse the dynamics of small-amplitude perturbations, i.e., the behaviour of the field $\boldsymbol{q}'$ when it is of *infinitessimally*-small amplitude (1.3) and evolves without distorting the base flow. This is exemplified in figure 4.16, depicting iso-surfaces of u' obtained by applying the flow unleash technique merged to a plane of shear in the base flow. Assessing linear perturbation dynamics provides insight into the onset and nature of flow instabilities. In the second part of the analysis, we compute DNS without SFD and characterise the dynamics of large-amplitude perturbations and the instantaneous organisation of $\boldsymbol{q}_s + \boldsymbol{q}'$. The focus is put on the evolution of perturbation-induced vortical structures in the transitional wake of the micro-ramp. Furthermore, we quantify linear and non-linear perturbation growth along the streamwise extent of the domain. For validation purposes, the results of the DNS are compared with the results of linear stability analysis performed for the base flow presented in §4.2 and with experimental work of Ye (2017). Details regarding the approach and numerical set-up of the stability analysis are provided in §2.5 and in (Groot et al., 2016), whereas details regarding the experimental set-up can be found in (Ye, 2017).

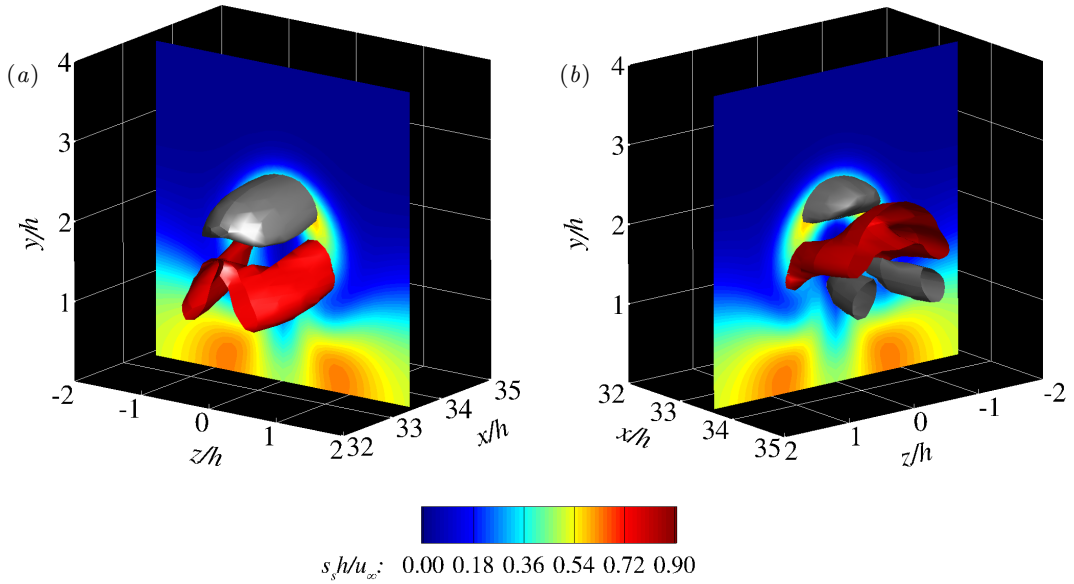

Figure 4.16: Instantaneous streamwise velocity perturbations (u'). Isosurfaces of $(u-\bar{u})/u_\infty = 9\times10^{-4}$ (red) and -6×10^{-4} (grey) from DNS when the base flow is unleashed. y-z plane of shear in the base flow. (*a*) front view, (*b*) back view.

4.3.1 Small-amplitude-perturbation dynamics

Detached shear layers in the wake of roughness elements are commonly identified as the regions of onset of flow instabilities. When unstable, disturbances growing downstream the element can ultimately cause transition if they attain a sufficiently large amplitude (Ergin and White, 2006). Many authors identify streamwise vortices originated at the roughness element giving rise to a system of streamwise velocity streaks able to sustain eigenmodes of unstable nature (Redford et al., 2010; Choudhari et al., 2010; De Tullio et al., 2013). The micro-ramp base flow described in §4.2 fits this description. As illustrated in figure 4.12, the momentum excess and deficit caused by the action of the primary vortices are accompanied by strong shear layers.

The central arch-shaped shear layer is especially critical for the stability of the system, inasmuch as the local velocity profile contains an inflection point susceptible to the K-H instability. Li and Liu (2010) and Sun et al. (2012) observe large-scale hairpin vortices induced by a flow instability of this type being shed downstream the micro-ramp. In the case of cylindrical and diamond-shaped roughness elements, Kegerise et al. (2012) and Loiseau et al. (2014) identify two types of modes supported by the unstable wake of the roughness element, of antisymmetric (sinuous) and symmetric (varicose) nature with respect to the centre plane. For a cylindrical roughness element of large aspect ratio, the latter is claimed to be responsible for inducing hairpin vortices which ultimately cause transition (Loiseau et al., 2014). Groot et al. (2016) observe the varicose instability to exhibit the shape of hairpin and to be more unstable than the sinuous instability.

Spatial spanwise BiGlobal linear stability analysis (§2.5) carried out for the current micro-ramp base flow confirms the existence of convectively unstable varicose and sinuous instabilities. For a broad range of x/h and frequencies, two branches of eigenvalues are observed to penetrate into the unstable region of eigenspectra computed at successive y-z planes in the x-direction. Upon integration of the eigenmode's spatial growth rate, per fixed frequency, along the streamwise direction, one obtains a set of curves representing the perturbation growth in this direction. The envelope of these curves yields the maximum logarithmic disturbance amplification factor, denoted by N (Van Ingen, 2008). For engineering applications, it is common to correlate this total perturbation growth N and the transition location (Schmid and Henningson, 2001). Based on it, current results from linear stability analysis indicate that the varicose eigenmode is the dominant instability kind, i.e., yields the largest growth rates. This is in agreement with conclusions drawn by Groot et al. (2016) and by Kegerise et al. (2012) from experiments performed at similar roughness Reynolds number ($\mathcal{R}e_{hh} = 470$ and $\mathcal{R}e_{hh} = 462$ respectively). In the latter case, the sinuous instability is reported to claim dominance only when $\mathcal{R}e_{hh}$ is sufficiently small ($\mathcal{R}e_{hh} = 319$ for their set-up).

We start the validation of results from DNS and from linear stability analysis by qualitatively comparing the disturbance field in the unleashed base flow (§3.3) with eigenfunctions from the spanwise BiGlobal stability analysis. For the sake of completeness, we shall highlight the following: first, for the reasons stated above, we only present stability results related to the varicose instability. Secondly, BiGlobal is a two-dimensional approach; the three-dimensional structures developing when the flow is unleashed are compared with stability eigenfunctions interpolated along x/h between sets of y-z planes over which stability analysis is applied. Thirdly, the flow unleash technique relies on slightly perturbing the unstable base flow after turning off the SFD model. Thereafter, we expect modal exponential growth of perturbations

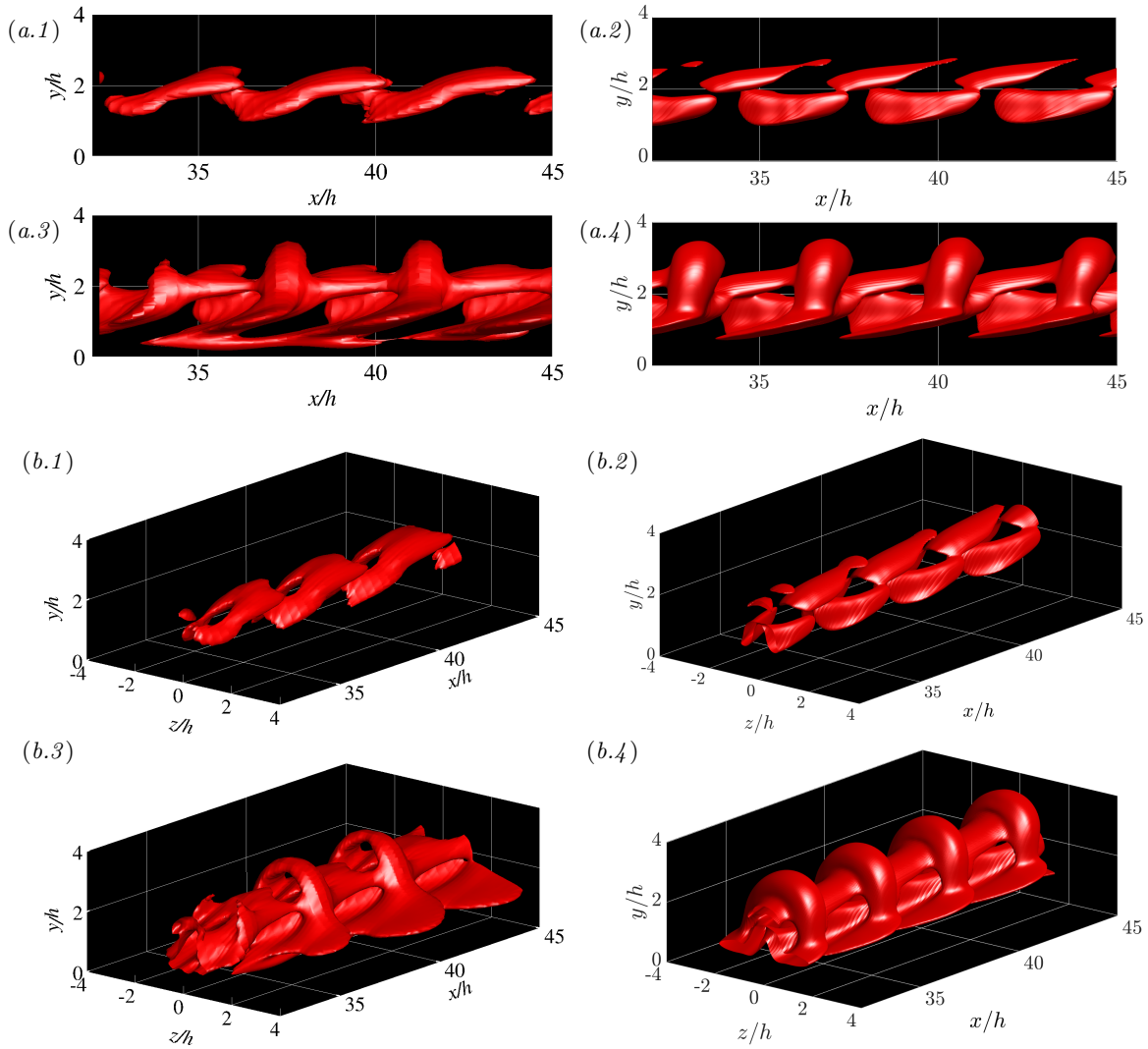

Figure 4.17: Instantaneous positive streamwise velocity perturbations (u'). Isosurfaces of $(u - \bar{u})/u_\infty = 0.0022$ (1) and 6.8×10^{-4} (3) from DNS when the base flow is unleashed. Real part of spanwise BiGlobal stability eigenfunctions (2,4), interpolated along x/h. (*a*) side view, (*b*) perspective.

downstream the micro-ramp as the first stage of their development. The initial disturbance amplitude after SFD is imposed to be sufficiently small such that we can capture the linear evolution of disturbances for a broad range of x/h. Only when these disturbances have grown sufficiently, assumption (1.3) breaks down, non-linear perturbation mechanisms may arise, and disturbances may deform the base flow. We carry out the comparison for a range of x/h values in which the latter is not the case. Finally, varicose instability has been reported to be of convective nature in the current case. Consequently, in the DNS we expect unsteady disturbances travelling in the form of a wave packet resulting from superposition of wave forms with different frequencies (Schmid and Henningson, 2001). The results from stability analysis only account for one single frequency. So, to compare the DNS results with the stability analysis results, a wave packet was selected having a large streamwise envelope, such

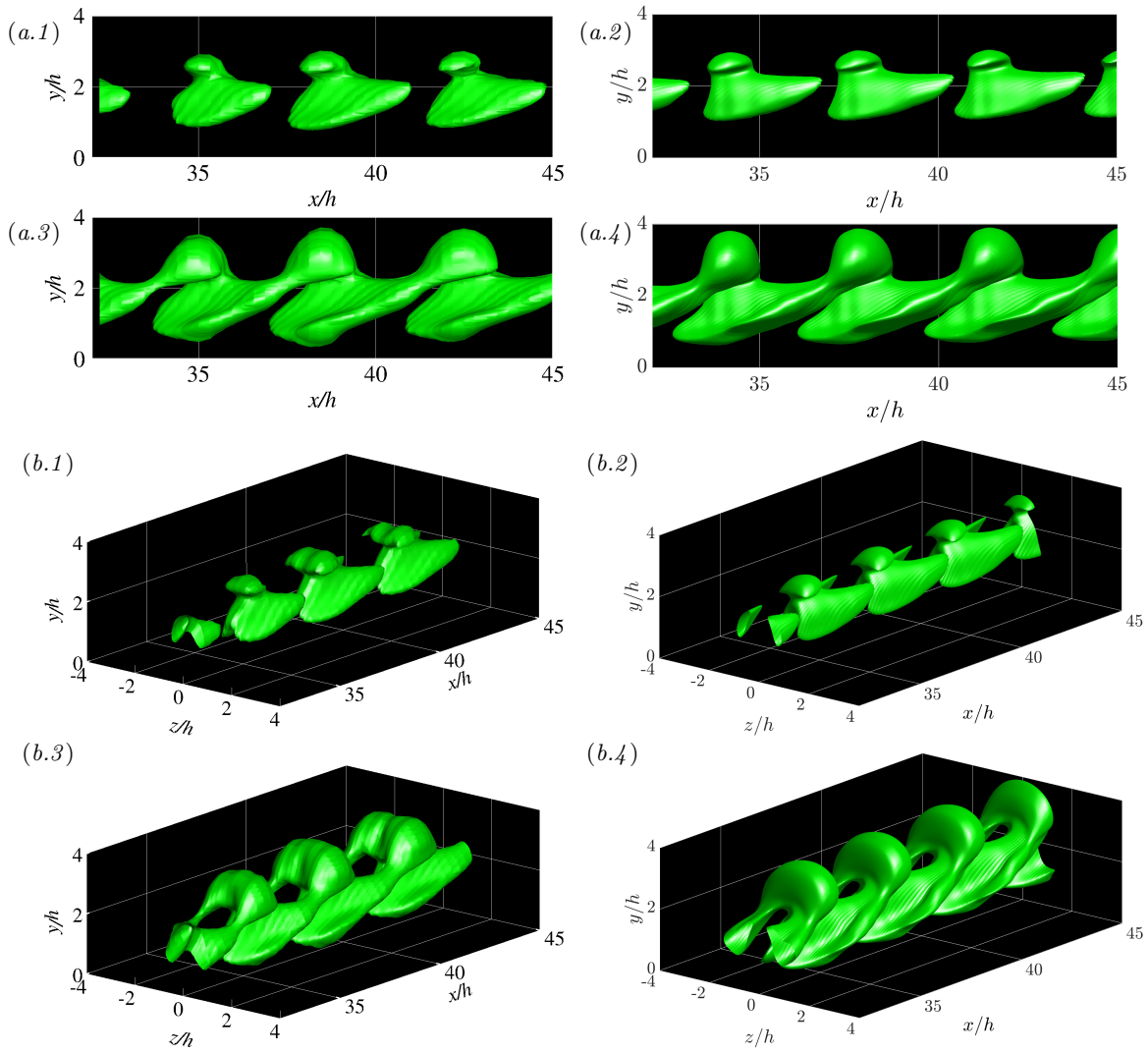

Figure 4.18: Instantaneous negative wall-normal velocity perturbations (v'). Isosurfaces of $(v - \bar{v})/u_\infty = -0.0011$ (1) and -3×10^{-4} (3) from DNS when the base flow is unleashed. Real part of spanwise BiGlobal stability eigenfunctions (2,4), interpolated along x/h. (*a*) side view, (*b*) perspective.

that it could be reasonably compared to the wavetrain. Particularly, we chose that frequency corresponding to the largest integrated growth rate (N-factor) at $x/h = 18.75$.

Results of the comparison are presented in figures 4.17, 4.18 and 4.19, characterising perturbations of streamwise velocity, wall-normal velocity and streamwise vorticity, respectively. The latter is obtained as $\omega'_x = \omega_x - \omega_{x,\mathrm{s}}$. We observe a reasonable match for v' and ω'_x. The u' field shows lower resemblance. With regard to the v' field, large iso-surface levels (figure 4.18(*a.1*,*b.1*,*a.2*,*b.2*)) are characterised as disconnected ghost-shaped structures. Minor differences are found in the head and neck regions. When the iso-level is decreased, the backward part of the body connects with the head of the backward structure. In turn, the head expands and the lower part of the body develops lobes. All structures seem to cover a

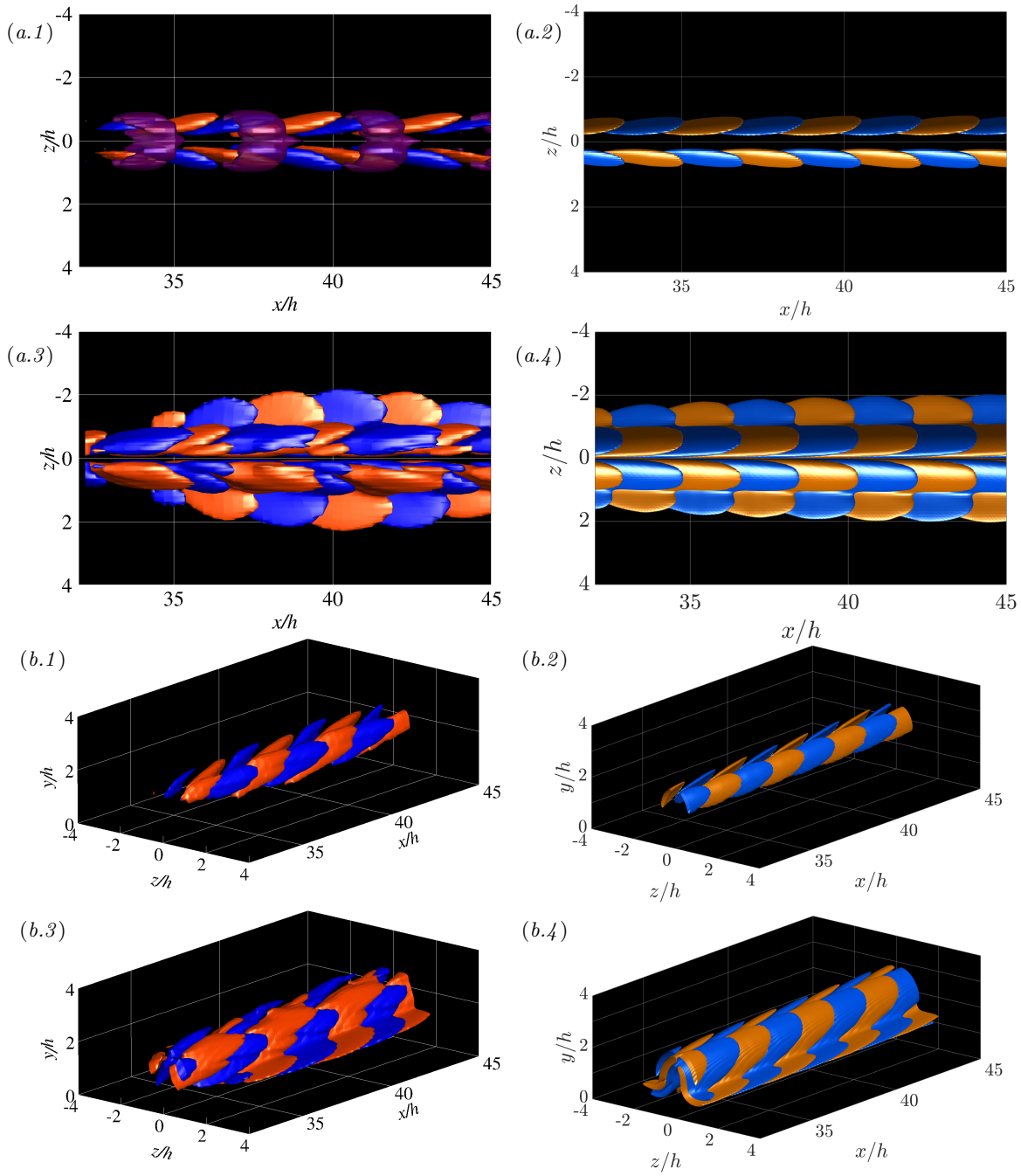

Figure 4.19: Instantaneous streamwise vorticity perturbations (ω_x'). Isosurfaces of $(\omega_x - \omega_{x,s})h/u_\infty = \pm 0.01$ (1) and ± 0.003 (3), orange for clockwise rotation and blue for anticlockwise rotation, from DNS when the base flow is unleashed. Real part of spanwise BiGlobal stability eigenfunctions (2,4), interpolated along x/h. Translucent purple isosurfaces of $\lambda_2 - \lambda_{2,s} = -2 \times 10^{-4}$, only in $(a.1)$. (*a*) top view, (*b*) perspective.

similar wall-normal extent of the domain.

Large iso-surface levels of streamwise velocity perturbations appear in the form of elongated

structures (figure 4.17(*a.1*,*b.1*,*a.2*,*b.2*)). The forward part of each structure features two legs which are connected to the forward structure from below. We observe differences between results of DNS and stability analysis in the topology of the body and leg parts, and the way structures connect to each other. As the iso-surface level is decreased, we observe the formation of a characteristic arch. In turn, this arch connects to the forward structure while lobes are being developed aside. The spanwise expansion of the lobes is one of the main differences between figure 4.17(*b.3*) and (*b.4*). We detect other significant differences, as for instance, the existence of a structure near the wall in the DNS results whose origin is unclear to us.

Figure 4.19(*a.1*,*b.1*,*a.2*,*b.2*) depicts the streamwise vorticity perturbation field as patches of opposite vorticity. These patches resemble the leg structure of a hairpin vortex. When isosurfaces of λ_2 (Jeong and Hussain, 1995) are additionally introduced, the combination of isosurfaces features an overall hairpin-like shape; see figure 4.19(*a.1*). More precisely, hairpin heads in figure 4.19(*a.1*) are characterised through isosurface of $\lambda_2' = \lambda_2(\boldsymbol{v}) - \lambda_2(\boldsymbol{v}_\mathrm{s}) = \lambda_2 - \lambda_{2,s}$. These are observed to be connected with ω_x' patches in pairs (positive ω_x' for $z > 0$, negative ω_x' for $z < 0$). In a fashion similar to the previously described perturbation fields, when the iso-level of ω_x' is decreased, we observe lateral lobes. Neither the streamwise vorticity patches in between hairpin heads nor the lobes developing aside are detected by λ_2'. We assume these structures to be regions of induced shearing motion.

The topological resemblance between perturbations developing in the unleashed base flow and varicose mode eigenfunction suggests that this instability kind rules the linear perturbation dynamics in DNS as well. Due to the existence of an inflection point in the velocity profile as well as the similarities found with literature, the instabilities in the central shear layer are of an inviscid nature. In figure 4.16, isosurfaces of unleashed u' are merged to a slice of shear in the base flow. We observe isosurfaces of opposite sign to develop around the central arch-shaped shear layer and to fit with each other. This is in line with results presented by Loiseau et al. (2014); the varicose eigenmode is recognised as an instability of the full shear layer enclosing the low-momentum dip rather than an instability of the $\partial u_\mathrm{s}/\partial y$ component as indicated by Asai et al. (2002). As expected, the central shear layer does not manifest large distortions during the first stages of the flow unleash technique despite the presence of unstable perturbations (1.3). Even though another strong shear layer is present near the wall (figure 4.12), no perturbation activity is captured in this region associated to the varicose eigenmode. Results of figure 4.19 seem to confirm the existence of a train of hairpin vortices travelling downstream the micro-ramp. The evolution of vortices of this kind is further analysed in §4.3.2. Yet, the current results point out that hairpin-shaped structures are generated through linear perturbation mechanisms associated to the varicose K-H instability. Opposite conclusions are drawn by De Tullio et al. (2013); hairpin-like vortices are claimed to be an effect of the base flow deformation due to the non-linear evolution of the varicose instability.

4.3.2 Transitional flow dynamics

The sustained growth of small-amplitude disturbances eventually triggers non-linear mode interaction and saturation if perturbations attain large enough amplitude. When the system evolves towards this state, modal perturbation growth is then solely captured for small x/h.

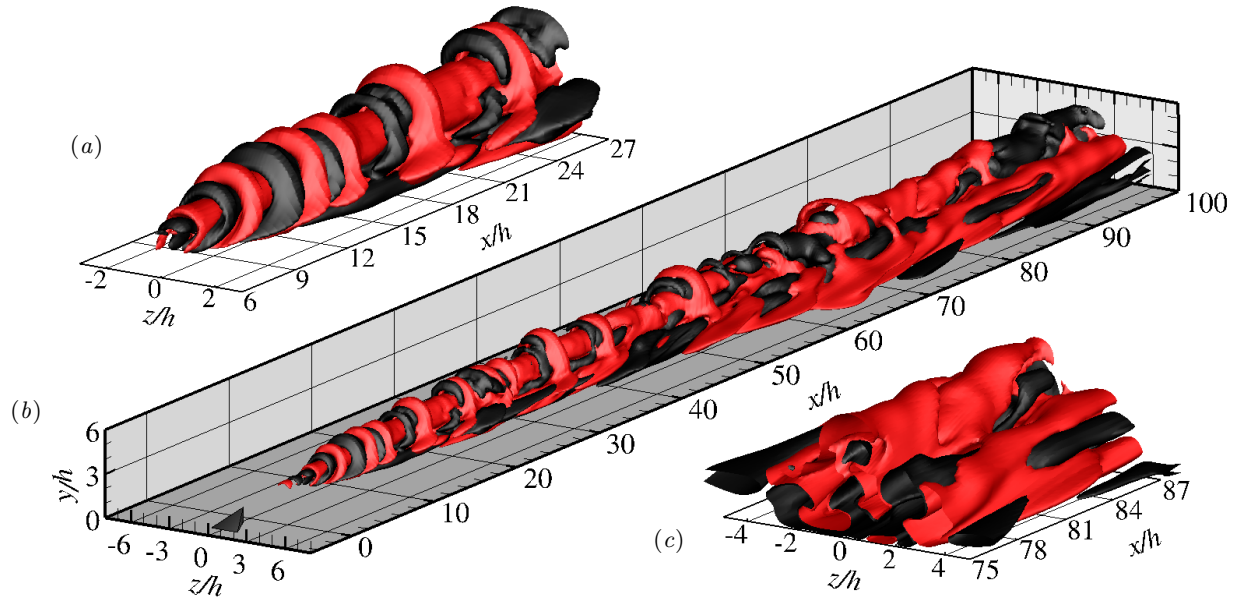

Figure 4.20: Instantaneous streamwise perturbation field (u''). (b) isosurfaces of $(u-\langle u\rangle)/u_\infty = 0.012$ (red) and -0.012 (black). Zoom (a) close to the micro-ramp, (c) far downstream the micro-ramp.

We perform DNS of the micro-ramp flow without SFD to resolve the non-linear evolution of flow instabilities.

Sufficiently downstream the micro-ramp, disturbance activity significantly deforms the base flow. The time-averaged flow configuration, $\langle \boldsymbol{q} \rangle$, then becomes a relevant entity to represent the organisation of the flow. Hence, in the current section, the dynamics of large-amplitude perturbations are characterised by measuring instantaneous disturbances with respect to mean flow quantities. This is addressed as follows: we compute DNS of $\boldsymbol{q}$ and $\langle \boldsymbol{q} \rangle$. Details on how the mean flow field is obtained are given in §4.4. We then define the perturbation field $\boldsymbol{q}''$ as the departure of the instantaneous flow field to the mean flow solution, i.e., $\boldsymbol{q}'' = \boldsymbol{q} - \langle \boldsymbol{q} \rangle$ (2.20). Figures 4.20 and 4.21 illustrate the streamwise evolution of disturbances u'' and v''.

Close to the micro-ramp, we capture the expected linear perturbation behaviour; structures in figures 4.20, 4.21 resemble those of figures 4.17, 4.18 since for small x/h, $\boldsymbol{v'} \approx \boldsymbol{v''}$ reasonably. Initially, isosurfaces of opposite sign fit with each other and show a rapid growth. Generally from $x/h \approx 14$ onward, significant differences arise between the structure of perturbations in figures 4.20, 4.21 and the real part of stability eigenfunctions. Along the approximate range of $14 \leq x/h \leq 50$, perturbations undergo distortion while maintaining elements of their original morphology. This is for instance the case of the arch exhibited by positive u'' perturbations or the expanded head part of positive v'' perturbations. In this range, we additionally detect the onset of lateral strips of streamwise velocity perturbation; see figure 4.20. For $x/h > 50$, the u'' field is dominated by elongated patches of this kind. We observe a central dominant region of positive u'' surrounded by strips of positive and negative u''. Although v'' structures also appear to be highly distorted for $x/h > 50$, they do not undergo significant elongation. We observe u'' and v'' disturbances to significantly spread in spanwise direction. As a consequence, the wake of the micro-ramp broadens and it becomes much wider

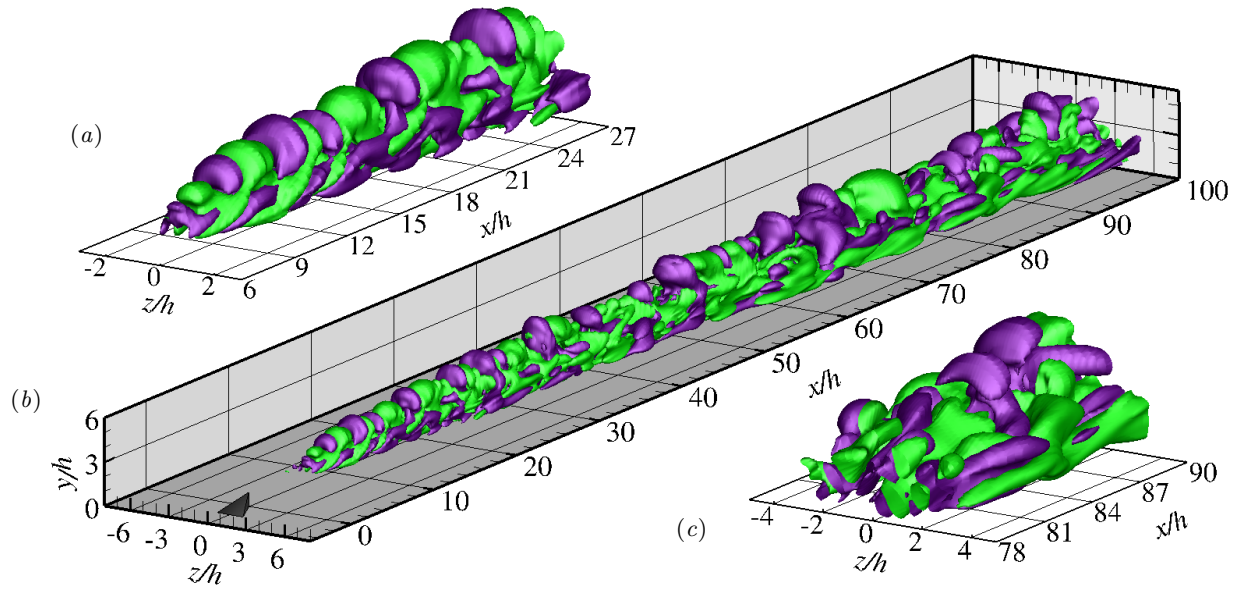

Figure 4.21: Instantaneous wall-normal perturbation field (v''). (*b*) isosurfaces of $(v-\langle v\rangle)/u_\infty = 0.012$ (purple) and -0.012 (green). Zoom (*a*) close to the micro-ramp, (*c*) far downstream the micro-ramp.

than the micro-ramp span; far downstream the micro-ramp, perturbations have contaminated a large portion of the flow field. As for being of great relevance, this issue is further analysed later on in this section.

Previously, we have confirmed the existence of hairpin vortices travelling downstream the micro-ramp in the unleashed base flow. We now examine the manifestation of this and other relevant vortical structures in the instantaneous flow field when perturbations non-linearly saturate. Figure 4.22(*a*,*b*) and (*c*,*d*) respectively depict isosurfaces of λ_2 and ω_x from DNS without SFD. For validation purposes, figure 4.22(*e*,*f*) displays isosurfaces of ω_x obtained from tomo-PIV experiments after low order POD reconstruction (Ye, 2017). Around the micro-ramp and at its downstream vicinity, isosurfaces of λ_2 and ω_x represent the primary vortex pair. These isosurfaces show a steady behaviour and a spatial development equal to that observed in the base flow configuration (figure 4.6). Hence, current results indicate that the primary vortex pair is present in the instantaneous flow solution at the micro-ramp's downstream vicinity. For increasing x/h, the structures gradually start to oscillate under the influence of perturbations, as also reported by Li and Liu (2010). At $x/h \approx 4$, the motion has become more pronounced and along $4 \leq x/h \leq 7$ we observe the onset of arch-shaped vortices on top of the structures characterising the primary vortices. As detailed in the analysis of the base flow, near the micro-ramp the primary vortex pair is bounded superiorly by the central shear layer, around which K-H instabilities develop and associated vortices are incepted. In the range $4 \leq x/h \leq 7$, based on qualitative observations, the vortex-to-vortex distance is generally determined to fluctuate between $1.7h$ and $2h$. Ye (2017) reports a value of $3.5h$.

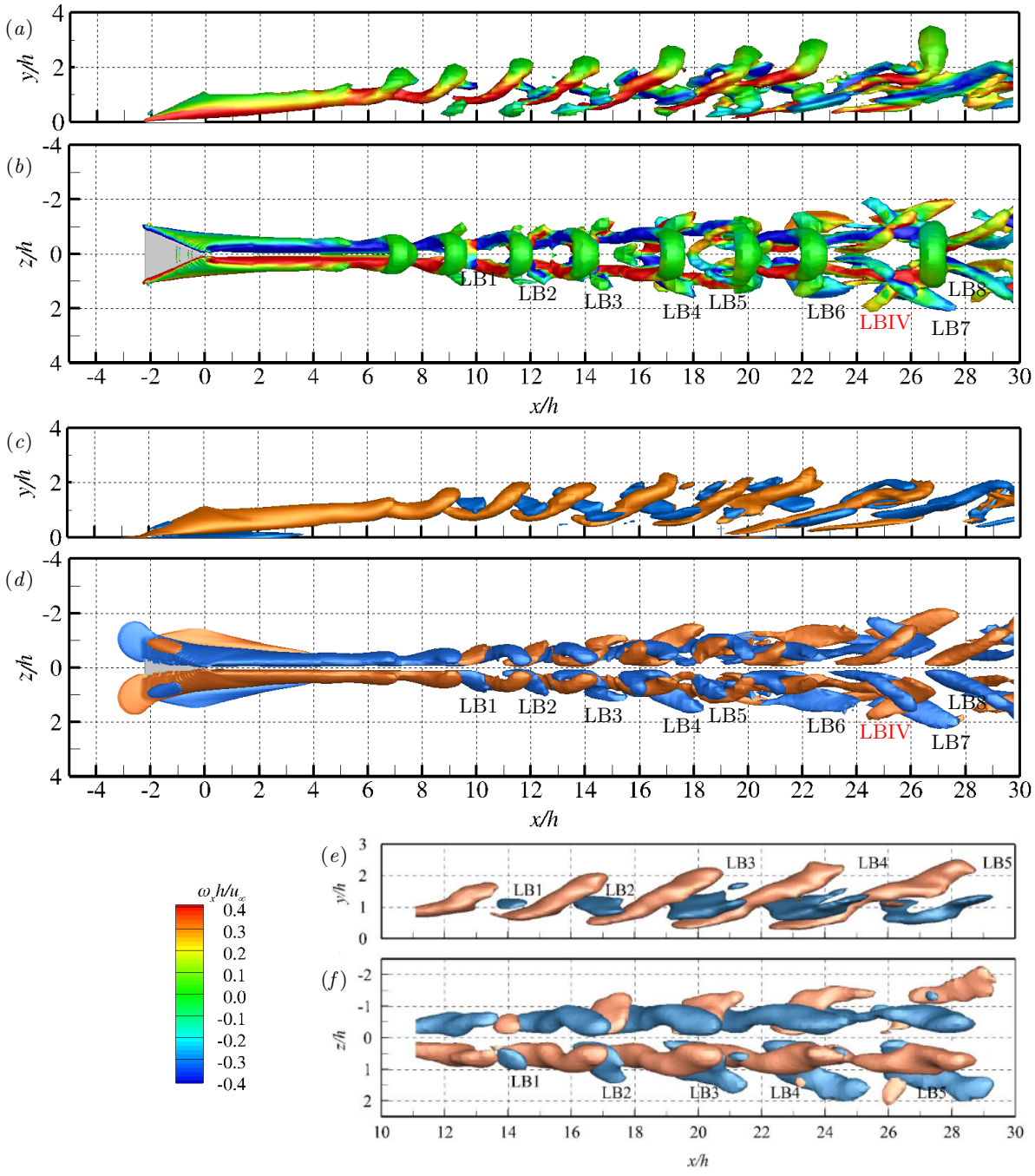

Figure 4.22: Instantaneous streamwise vorticity and λ_2. Isosurface of $\lambda_2 = -0.004$ from DNS colour-coded by streamwise vorticity, (*a*) side view, (*b*) top view. Isosurface of $\omega_x h/u_\infty = \pm 0.3$ from DNS, (*c*) side view, (*d*) top view. Isosurface of ω_x from tomo-PIV experiments (Ye, 2017)(*e*,*f*).

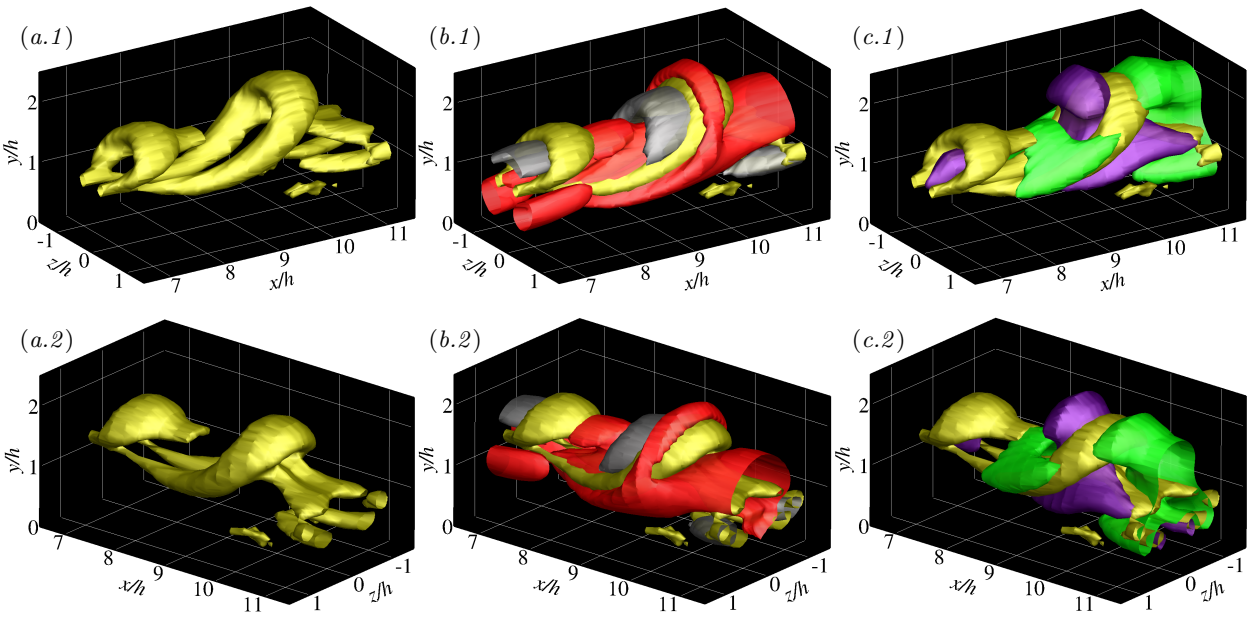

Figure 4.23: Instantaneous streamwise and wall-normal velocity and λ_2 perturbation fields (u', v', λ_2') near the micro-ramp. Isosurfaces of (*a*) $\lambda_2 - \lambda_{2,s} = -0.01$ (yellow), (*b*) -0.01 (yellow), $(u-u_s)/u_\infty = 0.03$ (red) and -0.05 (grey), (*c*) $\lambda_2 - \lambda_{2,s} = -0.01$ (yellow), $(v-v_s)/u_\infty = 0.03$ (purple) and -0.04 (green). (1) front view, (2) back view.

Along $7 \leq x/h \leq 11$, we detect vortices featuring a hairpin shape for the first time. For the current interpretation, unsteady vortical structures are isolated via subtraction of the $\lambda_{2,s}$ field to the instantaneous λ_2 field, thus yielding λ_2'. In this range, the instantaneous velocity perturbations of figures 4.20 and 4.21 resemble those developing in the unleashed base flow and are observed to fit with isosurfaces of λ_2'; see figure 4.23. In the head portion of λ_2' isosurface, we observe the combined action of positive and negative u', v' causing the central shear layer to roll-up (figure 4.23). The roll-up of the detached shear layer due to instability growth was first described by Li and Liu (2010). More specifically, events associated to $u' < 0$, $v' > 0$ (ejection) focus on the inner part of the head, whereas events associated to $u' > 0$, $v' < 0$ (sweep) are predominant on the outer part of the head. In parallel, the initially arch-shaped vortices develop an elongated streamwise leg part, hereafter referred to as "HL" (hairpin leg); see figure 4.23.

Sufficiently downstream the micro-ramp we do not find evidence of the activity of the primary vortex pair in the instantaneous flow field. Instead, the instantaneous flow organisation appears to be dominated by the dynamics of downstream-travelling large-scale hairpin vortices. Blinde et al. (2009) perform similar observations. Eventual breakdown of primary vortices is suggested by Lu et al. (2010). At $x/h \approx 10$, λ_2 structures in figure 4.22(*a*,*b*) are completely disconnected for the first time. Along $11 \leq x/h \leq 30$, the head part of hairpin vortices lifts up and straightens (Groot et al., 2016), the leg portion undergoes further elongation while shifting downward, vortex-to-vortex distance is observed to gradually increase; see figure 4.22. This behaviour matches that reported by Ye (2017).

In the aforementioned range of $7 \leq x/h \leq 11$, along which hairpin vortices are observed to

acquire their characteristic "separated" shape, we additionally capture the onset and initial evolution of a new kind of vortex. We observe a structure detected by λ_2 protruding forward from the hairpin head in a region dominated by $u' > 0$, $v' < 0$ (sweep) events (figure 4.23). The action of perturbations causes this new structure to move forward, downward and away from the centre plane, bifurcate into two parts featuring opposite streamwise vorticity, elongate, detach from the head part, and eventually interact with the forward hairpin leg. This secondary vortex structure, referred to as leg-buffer and labelled as "LB" in figure 4.22, was initially discovered by Ye (2017). It has been observed to play a critical role in the development of the wake of the micro-ramp and so we now put the focus onto its streamwise evolution. It should be noted that even though the phases of the spatial evolution of leg-buffers are similar among all captured structures, we notice differences regarding the streamwise location at which they occur when different time instants of DNS results are considered. Discrepancies are found as well when comparing the streamwise location of structures from DNS and from tomo-PIV experiments.

For the time instance represented in figure 4.23, the interaction between leg-buffer and forward hairpin leg takes place at $x/h \approx 12$. From that point onward, we distinguish two differentiated trends followed by distinct parts of the leg-buffer structure. On the one hand, the forward part, which has just interacted with the forward vortex, increases its vorticity, elongates, aligns with the forward hairpin leg and moves away from the centre plane. On the other hand, the backward part of the leg-buffer wraps around the backward hairpin leg from below and moves towards the centre plane. Both parts show a tendency to tilt around the wall-normal direction. The aforementioned behaviour is generally captured along $12 \leq x/h \leq 24$. Ye (2017) indicates $x/h = 14$ to be the onset location of a secondary vortex pair captured in the time-averaged streamwise vorticity field aside the primary vortex pair, hypothesised

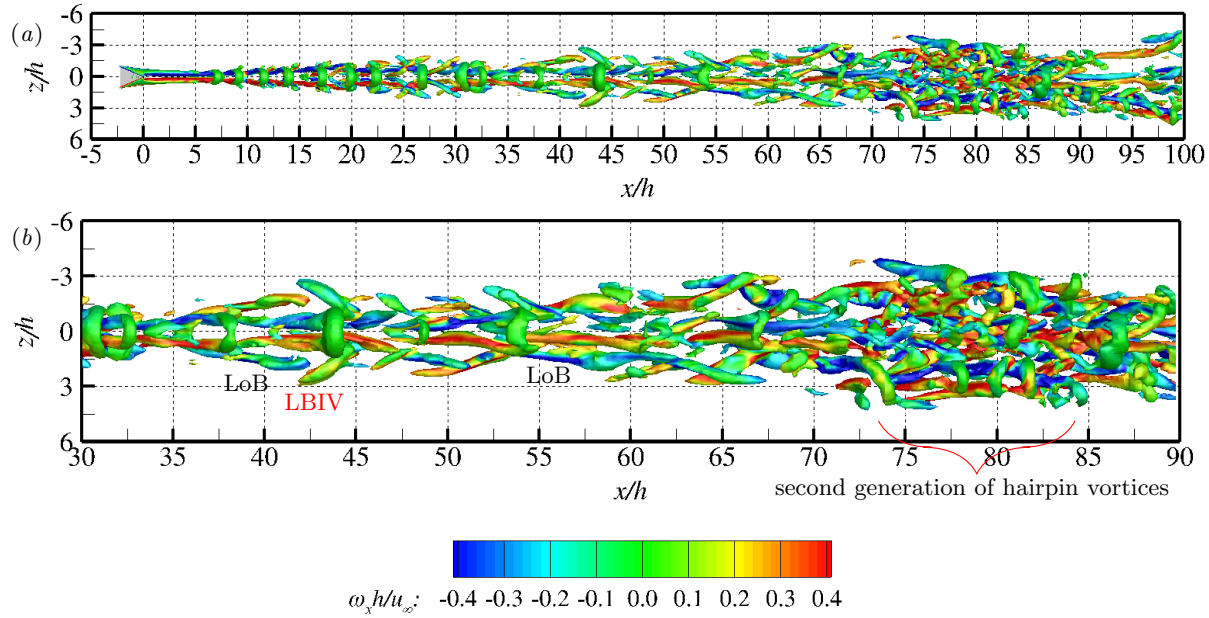

Figure 4.24: Instantaneous λ_2. Isosurface of $\lambda_2 = -0.004$ from DNS colour-coded by streamwise vorticity, (*a*) top view, (*b*) zoomed top view.

to be an artefact of averaging of leg-buffer structures. The coordinate $x/h = 14$ had been previously reported as inception location of disturbances developing aside the original perturbation train (illustrated in figures 4.20 and 4.21) and starting point of significant differences between perturbation structure characterised through linear stability analysis and obtained from instantaneous DNS. Generally for $x/h \geq 24$, the two branches in which the leg-buffer has mutated elongate, further incline towards larger $|z/h|$ and increase their vorticity intensity. The structure labelled as "LB7" in figure 4.22(d) is representative of this.

The leg-buffer is observed to induce a new vortical structure, which initially grows quasi-perpendicularly to it. The onset of this leg-buffer-induced-vortex (labelled as "LBIV" in figure 4.22(b,d)) is generally captured in the range $20 \leq x/h \leq 28$. As a consequence, for $x/h > 30$, two main vortical structures appear to significantly contribute to the broadening of the wake of the micro-ramp by introducing lateral disturbances, the LBIV, and the lower branch (LoB) of the original leg-buffer structure (figure 4.24). The latter shows to disconnect from the upper branch and to move downstream separately. The upper branch is observed to be rather weak and it is eventually destroyed. On the contrary, the lower branch persists until far downstream the micro-ramp.

A common characteristic between LoBs and LBIVs is the fact that further downstream they undergo significant elongation. These structures first penetrate deep into the flow region aside the perturbation core and as they move downstream tend to align in the streamwise direction. In this range, distance between hairpin heads shows a noticeable increase. The leg portion has acquired large dimensions in x/h as it has continuously undergone elongation due to the shearing motion of the flow since early stages. Due to the fact that HLs remain attached to the wall whereas hairpin heads gradually lift up, far downstream the micro-ramp hairpin legs cover a large extension in x/h and also in y/h. Around $x/h = 70$, we capture a second generation of large-scale hairpin vortices; see figure 4.24(b). This is as well reported by Ye (2017). In this region, we furthermore identify hairpin vortices originally induced near the micro-ramp which persist far downstream and the elongated lower branches of leg-buffers.

Ye (2017) captures a tertiary vortex pair aside the secondary vortex pair in the time-averaged streamwise vorticity field arising at $x/h = 45$. The secondary vortex pair is assumed to be an artefact of time-averaging of the leg-buffer structure. In a similar fashion, the tertiary vortex pair detected in the time-average flow field (Ye, 2017) is now hypothesised to be linked to the activity of LBIVs. Furthermore, based on our results, we conjecture that iso-surfaces of time-averaged streamwise vorticity presented by Ye (2017) in figure 5.1(b) identified as the primary vortex pair may only represent this structure close to the micro-ramp. Sufficiently downstream, the mean representation of the streamwise vorticity field at the centre plane location would characterise hairpin-vortex structures. This is supported by the following reasoning: in the base flow analysis, we have used iso-surfaces of $\omega_{x,\mathrm{s}}h/u_\infty = \pm 0.04$ to represent the structure of the primary vortices (figure 4.1 of this work). This is the same iso-surface level used by Ye (2017) in figure 5.1(b) to characterise streamwise vortices in the time-averaged configuration. In figure 4.1 of this work, we observe the iso-surfaces to gradually decrease their cross-sectional area and to terminate at $x/h = 50$; the vortices are maintained active but reduce their strength in x/h. In figure 5.1(b) of (Ye, 2017), the iso-surfaces of streamwise vorticity at the centre plane maintain a rather constant structure in the streamwise direction and show to persist until (at least) $x/h = 70$.

Moreover, as mentioned above, we find no sign of the primary vortices sufficiently downstream

the micro-ramp in the instantaneous flow organisation. This is in line with observations performed by Blinde et al. (2009), Lu et al. (2010) and Bo et al. (2012). Blinde et al. (2009) indicate the presence of instantaneous individual pairs of counter-rotating vortices in the wake of the micro-ramp. These are hypothesised to be linked to the presence of hairpin vortices. Bo et al. (2012) suggest that, sufficiently downstream the micro-ramp, the hairpin vortices become the dominant vortical structure in place of the primary vortex pair. Results of figures 4.22 and 4.24 and the aforementioned description of the instantaneous vortical field are in agreement with these descriptions and seem to support the aforementioned speculation regarding the micro-ramp mean flow representation. Sun et al. (2012), on the other hand, indicate that the primary vortex pair persist in the instantaneous flow field although it interacts with K-H vortices induced at the shear layer. They report that the latter do not manifest in the mean flow field. Sun et al. (2012) study the micro-ramp wake in the range $8.75 \leq x/h \leq 15$, considering a turbulent $M = 2$ boundary layer. At these streamwise positions, we capture the

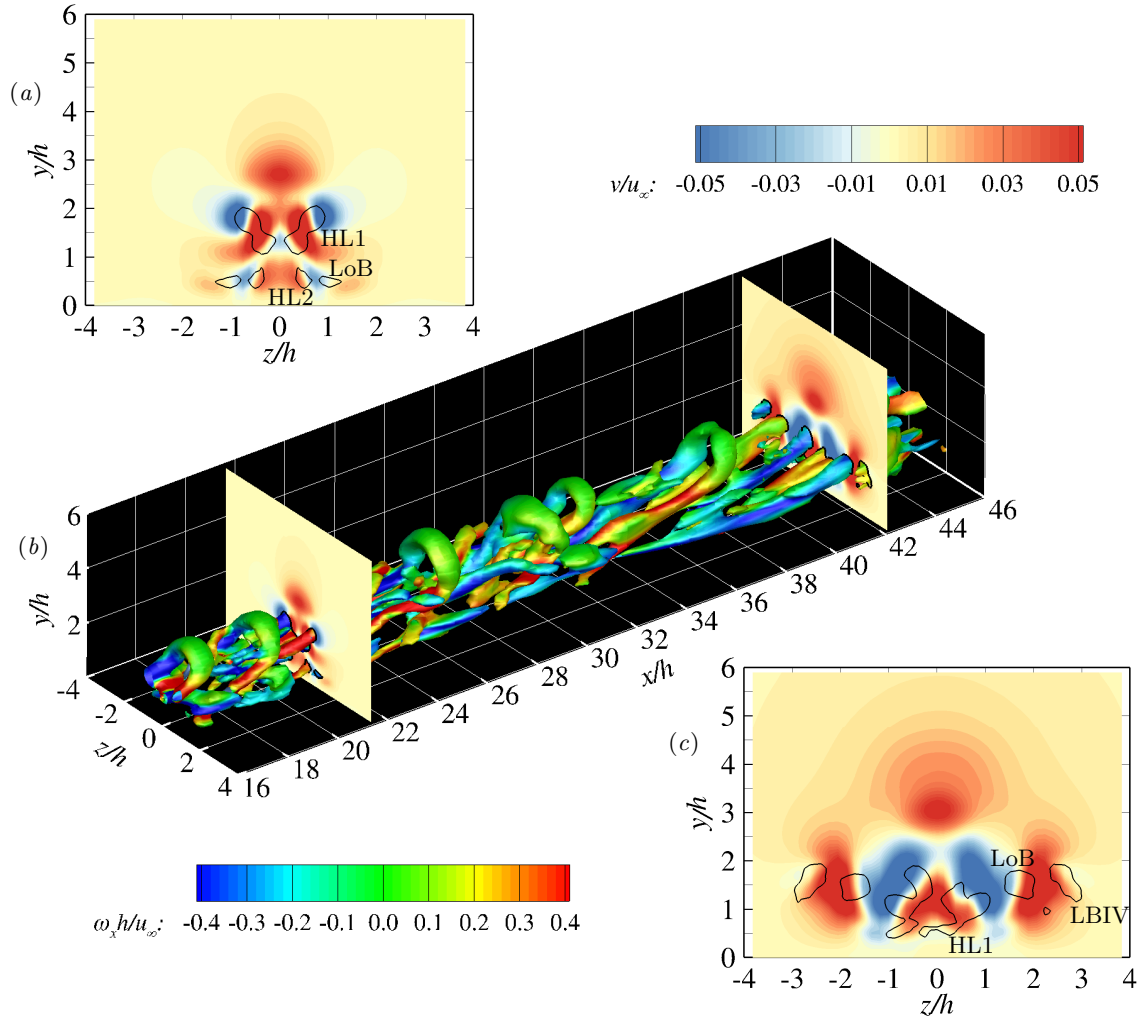

Figure 4.25: Instantaneous λ_2 and wall-normal velocity. (*b*) isosurface of $\lambda_2 = -0.004$ colour-coded by streamwise vorticity. y-z planes of v at (*a*,*b*) $x/h = 21.5$, (*b*,*c*) $x/h = 42.2$ with iso-contour of $\lambda_2 = -0.003$ (black line).

first stages of the development of the large-scale hairpin vortices; the perturbation activity is less intense, as compared to more downstream positions. In figure A.6(a.2), in the appendix, we show a y-z plane of the mean wall-normal velocity at $x/h = 10$. At this streamwise position, the structure of the upwash and downwash only shows a small distortion with respect to that observed in the base flow (figure A.6(a.1)).

The characterisation of unsteady vortical activity downstream the micro-ramp is paramount to understand the instantaneous evolution of flow quantities of interest. In particular, to better understand how perturbation development enhances the transport of momentum which carries the increase of wall shear illustrated in figure 4.2, it appears relevant to inquire on how are upwash and downwash initially induced by the primary vortex pair altered by the presence of unsteady hairpin vortices. Figure 4.25 portrays instantaneous vortices captured by λ_2. It is combined with y-z planes of instantaneous wall-normal velocity at two streamwise stations which, based on the previous discussion, aim to be representative of two distinct phases of hairpin vortex development. For the sake of consistency, both planes characterise flow events taking place at the upstream vicinity of a hairpin head.

Figure 4.25(a) shows the cross-sectional contour of relevant vortex kinds at $x/h \approx 20$, namely leg portions of the current hairpin vortex (HL1), leg portions of the forward hairpin vortex (HL2) and lower branches of the leg-buffer (LoB). At this stage, the lower and upper branches of the leg-buffer are still connected. The latter, which wraps around the current hairpin leg, is captured as well and its contour appears attached to the lower part of the HL1 structure. Sufficiently downstream the micro-ramp, the development of this system of vortices introduces a new dominant pattern of instantaneous wall-normal fluid motion. In figure 4.25(a) we observe local upwash and downwash generated at the sides of HL1, HL2, and LoB, and upwash induced by the motion of the hairpin head at the top. At its downstream vicinity, the hairpin head causes a strong downwash instead (not shown). The hairpin leg portions rotate in the same sense as the primary vortex pair; they induce upwash close to the centre plane and lateral downwash. The lower branches of leg-buffers rotate in an opposite sense as the hairpin legs and thus act to enhance the hairpin-leg-induced downwash near the wall while generating upwash aside. Even though the magnitude and relative position of induced wall-normal velocity fluctuations is dependant on the location of the vortical structures in space, the large streamwise extension of elongated HLs and thereafter LoBs makes this pattern of instantaneous wall-normal velocity recurrent in x/h. When moving downstream, hairpin head portions increase their spatial separation. In figure 4.25(c), we only identify the cross-sectional contour of one pair of hairpin legs. They remain at a rather constant spanwise position. The LoB structures have evolved and seem to contribute more significantly to the enhancement of wall-normal velocity fluctuations. At these streamwise positions we additionally capture weak activity of LBIVs which, in turn, reinforce lateral upwash and introduce negative wall-normal velocity perturbations aside.

Overall, far downstream the micro-ramp, the instantaneous wall-normal velocity field features a spanwise-alternating pattern of upwash and downwash. On the contrary, upwash and especially downwash in the base flow reduce their strength when moving downstream the micro-ramp. These results indicate further evidence in support of the hypothesis that sufficiently downstream the micro-ramp the primary vortex pair does not coexist with hairpin vortices or, at least, that induced upwash and downwash is solely attributed to hairpin vortex dynamics.

4.3.3 Quantification of perturbation growth

Until now, we have qualitatively assessed the instantaneous development of velocity perturbations and vortical structures in the wake of the micro-ramp. We now aim to condense and quantitatively characterise previous findings by analysing the evolution in x/h of disturbance growth. For that purpose, following the approach of Ergin and White (2006) and Ye (2017), we evaluate

$$\epsilon_{rms} = \int_{S_{\text{wake}}} \frac{\langle u''u'' \rangle}{u_\infty^2} d\left(\frac{y}{h}\right) d\left(\frac{z}{h}\right), \tag{4.10}$$

the integrated streamwise velocity perturbation energy. S_{wake} is the local area of the micro-ramp wake. Ye (2017) defines it as the region in which $\langle u'' \rangle / \langle u'' \rangle_{\max} \geq 0.3$; for consistency, we follow this definition when comparing the results from the DNS and from the PIV experiments of Ye (2017). On the other hand, to compare the perturbation growth in the DNS with that obtained from the linear stability analysis, ϵ_{rms} is evaluated using full y-z planes. The results of the comparison are presented in figure 4.26: it contains the N-factor curve obtained through linear stability analysis with (4.10) computed from DNS and tomo-PIV experiments. It should be noted that, since we measure the streamwise evolution of perturbation *energy*, we include a factor 2 to the N-factor curve.

Close to the micro-ramp, we observe that ϵ_{rms} computed from DNS follows a plateau. It is ascribed to the numerical contamination near the micro-ramp, which sets an initial perturbation amplitude. At $x/h = 3$, DNS perturbations start to grow exponentially at the same rate as the N-factor curve. Inherent to the e^N method is the fact that it characterises amplitude growth rather than total amplitude (Van Ingen, 2008). Therefore, we use the DNS data to assign linear perturbations an initial amplitude based on the best visual match between the N-factor curve and the integrated DNS perturbation energy. Exponential growth of K-H disturbances is captured until $x/h \approx 9$; at this streamwise location, a difference arises between the trend followed by the N-factor curve and integrated DNS disturbance energy. From the results of figure 4.26(b), we obtain that $\epsilon_{rms}(3) = 1.6 \times 10^{-5}$ and $\epsilon_{rms}(9) = 7.3 \times 10^{-3}$. Thereby, $N(9) - N(3) = 3.1$.

At $x/h = 9$, the DNS distribution bends and starts a plateau due to non-linear perturbation saturation. The plateau settles at $x/h = 13$. Nonetheless, at $x/h = 14.5$, disturbance energy is observed to grow again; see figure 4.26(a)). This streamwise station has been previously reported in the current analysis as starting point of lateral perturbation development due to leg-buffer activity. From this point onward, we observe exponential perturbation growth at a relatively constant rate, much lower than in the micro-ramp vicinity. The disturbance energy measured from tomo-PIV experiments grows at the same rate.

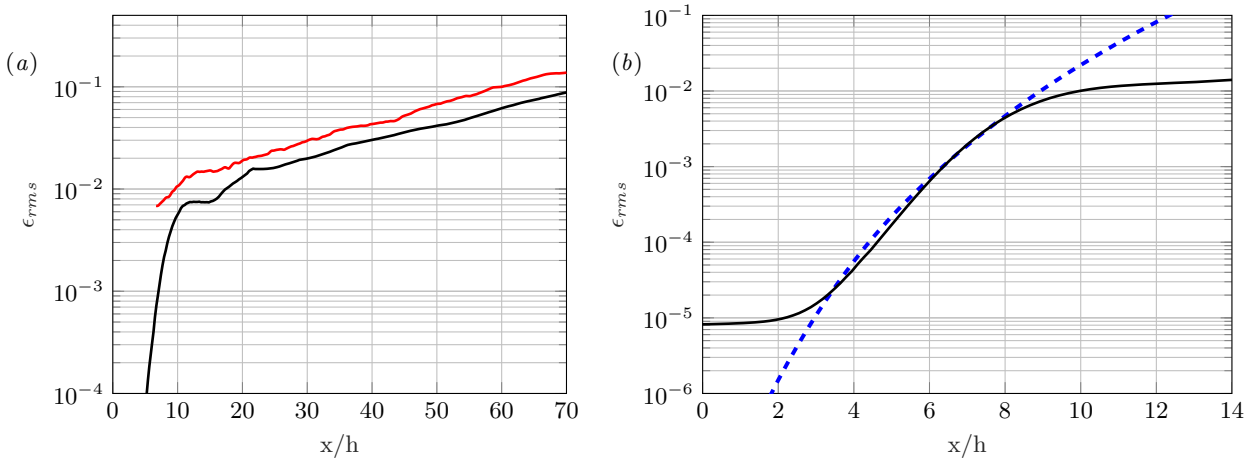

Figure 4.26: Integrated streamwise velocity perturbation energy as function of x/h from DNS (solid black) and (*a*) from tomo-PIV (solid red), (*b*) combined with the e^{2N} curve (dashed blue).

4.4 Mean flow

In §4.3, we have analysed the instantaneous evolution of perturbations in the unstable wake of the micro-ramp. As explained, when disturbances acquire sufficiently large amplitude, (1.3) is rendered invalid, and perturbation activity deforms the base flow. Under these circumstances, the time-averaged flow field characterises the flow organisation more accurately. Accordingly, in the current section we describe the mean flow organisation and highlight the major differences with the base flow organisation. Comparison between base and mean flow results allows us to segregate mechanisms attributed to disturbance growth from those purely contained in the system's base state. In figure 4.2, the importance of perturbation development in the micro-ramp functionality was highlighted: wall shear in $\langle \boldsymbol{q} \rangle$ is significantly larger than in $\boldsymbol{q}_s$. In the current analysis, we deepen into this matter by examining the role of perturbations in the improvement of the "health" of the boundary layer; we ultimately show how the evolution of transitional disturbances downstream the micro-ramp is key to the device performance.

At the micro-ramp tip, ϵ_{rms} (4.10) has an order of magnitude of $\mathcal{O}\left(10^{-5}\right)$. This low level of perturbation energy, as compared to base flow quantities, ought to imply $\boldsymbol{q}_s = \langle \boldsymbol{q} \rangle$ around the micro-ramp and at its downstream vicinity. We, however, observe differences between mean and base streamwise velocity at $x/h = 0$ to be of order $\mathcal{O}\left(10^{-2}\right)$, mainly at the location the primary vortex pair. This could lead to misleading interpretations with regard to the role of perturbations in the way the base flow becomes distorted. Accordingly, differences between base and mean flow are highlighted sufficiently downstream the micro-ramp, when base flow distortion is observed to be the consequence of perturbation growth primarily.

The mean flow configuration presented in this work has been obtained by time-averaging the instantaneous flow field of a simulation performed without SFD over approximately 5 flow-through-cycles (FTC). The period of an FTC is the time required for a fluid particle to travel across the entire streamwise extent of the domain. In each FTC, we generate approximately 400 samples, which roughly represent 7 samples per cycle of hairpin shedding. Far downstream the micro-ramp, this does not seem to yield a sufficiently well-converged mean flow, inasmuch as we capture a slight asymmetry of the flow field —see for instance figure 4.2(*b*). The

instantaneous wake of the micro-ramp has been shown to contain an intricate system of unsteady vortical structures. Larger averaging times would be required to very accurately represent their mean activity at the end of the computational domain. For the current DNS simulations, this would represent a high computational cost, whereas it is beyond the scope of this work to thoroughly assess the flow behaviour in this range.

4.4.1 Base flow *vs* mean flow topology

Four main fields previously used to characterise the base flow over the micro-ramp are next compared with their mean representation, namely streamwise and wall-normal velocity, shear and streamwise-velocity streaks. To pinpoint diverging patterns, we additionally present the mean-flow distortion (2.19). This field, denoted by $\langle \boldsymbol{q} \rangle^{\mathrm{d}}$, is obtained as subtraction of the base flow to the mean flow, i.e., $\langle \boldsymbol{q} \rangle^{\mathrm{d}} = \langle \boldsymbol{q} \rangle - \boldsymbol{q}_{\mathrm{s}}$. Thus, when considering the streamwise velocity and shear fields, regions with $\langle \boldsymbol{q} \rangle^{\mathrm{d}} > 0$ express that mean flow values are larger in magnitude than base flow values and vice-versa. This may not be the case for the wall-normal velocity and streamwise-velocity-streak fields due to the importance of the sign in these quantities. To maintain this consistency with respect to the interpretation of the sign in the comparison between base and mean representations, differences in the wall-normal velocity and streak fields are respectively highlighted by computing $|\langle v \rangle| - |v_{\mathrm{s}}|$ and the distorted streamwise-velocity-streak energy, i.e., $\langle e^{\mathrm{str}} \rangle^{\mathrm{d}} = 1/2(\langle u^{\mathrm{str}} \rangle^2 - (u_{\mathrm{s}}^{\mathrm{str}})^2)$. Accordingly, regions of positive values of these variables express as well that the mean flow quantities are larger in magnitude and vice-versa. An extended list of y-z planes of the aforementioned flow variables at different streamwise locations can be found in §A.4, in the appendix.

Streamwise and wall-normal velocity fields

Through visual inspection, differences between base and mean streamwise and wall-normal velocity fields are observed to become significant for $x/h \geq 10$. This streamwise location has as well been reported as the point of divergence between the N-factor curve and the integrated DNS disturbance energy (figure 4.26). Furthermore, as for being the region of onset of flow instabilities, differences are first detected at the central shear layer. At $x/h = 10$, the streamwise mean-flow distortion captures the imprint of K-H instability in this region; see figure A.5(a) of the appendix.

As discussed previously in this work, the wall-normal velocity field in the base flow undergoes a strong decrease in magnitude along x/h. In the mean flow field, however, upwash and downwash regions maintain their strength and expand upward and sideward; see figure A.6 of the appendix. The activity of hairpin vortices and leg-buffers has shown to introduce a spanwise-alternating pattern of upwash and downwash in the instantaneous flow field (figure 4.25). This is as well captured in the mean flow configuration. The organisation of $\langle v \rangle$ in figure 4.27(c,d) is consistent with the organisation of v in figure 4.25(a,b) and the analysis presented in §4.3.2. The increased wall-normal activity of the instantaneous flow enhances the redistribution of streamwise momentum within the boundary layer.

Close to the micro-ramp, perturbation-induced upwash and downwash gradually start exchanging momentum between the deficit region and central outer portions of the boundary layer. Due to the fact that for increasing x/h hairpin legs move downward and remain close to the surface, wall-normal perturbation activity gradually intensifies near the wall as well.

This carries a strong implication, because the perturbation-induced downwash maintains an effective entrainment of high-momentum fluid near the wall. In the mean flow field, the lower portion of the boundary layer aside the centre plane progressively becomes fuller, while it undergoes a rapid recovery in the base flow. At $x/h \approx 14$, two symmetric regions of positive streamwise mean-flow distortion arise at $|z/h| = 1$, the spanwise location of enhanced downwash (figure 4.27)(a,c). On the other hand, a hairpin-induced central upwash moves low-momentum fluid upward, which causes a downward expansion of the momentum deficit. In the laminar base flow, the persistent central upwash has shown to produce a similar effect. Hence, for a broad range of x/h, streamwise mean-flow distortion yields near-zero values at the centre plane near the wall; see figure A.5 of the appendix.

Further downstream, the activity of LoBs enhances the downwash around $|z/h| = 1$; at $x/h = 40$, all regions of positive streamwise mean-flow distortion have become similar in magnitude, as illustrated in figure A.5($d.3$) of the appendix. In the near-wall region along the micro-ramp span, the downwash gradually fills up the boundary layer at the centre plane since it starts to dominates over central upwash. In parallel, LoBs exert as well upwash at their outermost side; this upwash lifts low-momentum fluid up and empties the boundary layer around $|z/h| = 2$. Regions of negative $\langle u \rangle^{\mathrm{d}}$ thus arise at these spanwise positions. Ye et al. (2016) point out that sideward regions of low-speed fluid yield conditions for a second generation of hairpin vortices to grow far downstream the micro-ramp. These vortices have been previously identified in the instantaneous vortical field depicted in figure 4.24. LBIVs further contribute to subtract momentum from the boundary layer at $|z/h| = 2$ since they rotate in a sense opposite to LoBs. In turn, the rotational motion associated to LBIVs introduces new regions of positive streamwise mean-flow distortion away from the centre plane (figure 4.27(b)). High and low-momentum fluid moved under the action of LoBs and LBIVs is recognised as the first and second generations of lateral perturbations in figure 4.20.

As a consequence of the aforementioned, we observe major differences between base and mean flow organisations far downstream the micro-ramp. For the latter case, at $x/h = 80$, the spanwise-alternating pattern of wall-normal velocity extends to approximately $0 \leq y/h \leq 5$, $|z/h| \leq 5$, as illustrated in figure 4.27(d). The mean streamwise velocity field features a wavy pattern, which is assumed to be consequence of the fact that the system of elongated quasi-streamwise vortices has taken the dominant role in redistributing momentum within the boundary layer. The location of peaks and valleys along z/h in figure 4.27($b.2$) is coherent with the spanwise organisation of upwash and downwash in figure 4.27($d.2$). From approximately $x/h = 50$ onward, the largest difference between the base and mean streamwise velocity fields is captured near the wall aside the centre plane, as mentioned, due to the sustained perturbation-induced entrainment of high-momentum fluid in this region. The spanwise spreading of the wake, however, has also caused the region of positive mean-flow distortion to expand along approximately $|z/h| = 6$. On the other hand, the central-upper region of positive streamwise mean-flow distortion, initially much stronger than its near-wall counterpart, has significantly decreased in magnitude. This is the consequence of the sustained upwash in the base flow that shapes part of the central velocity profile (§4.2.1) in a manner similar to hairpin vortices.

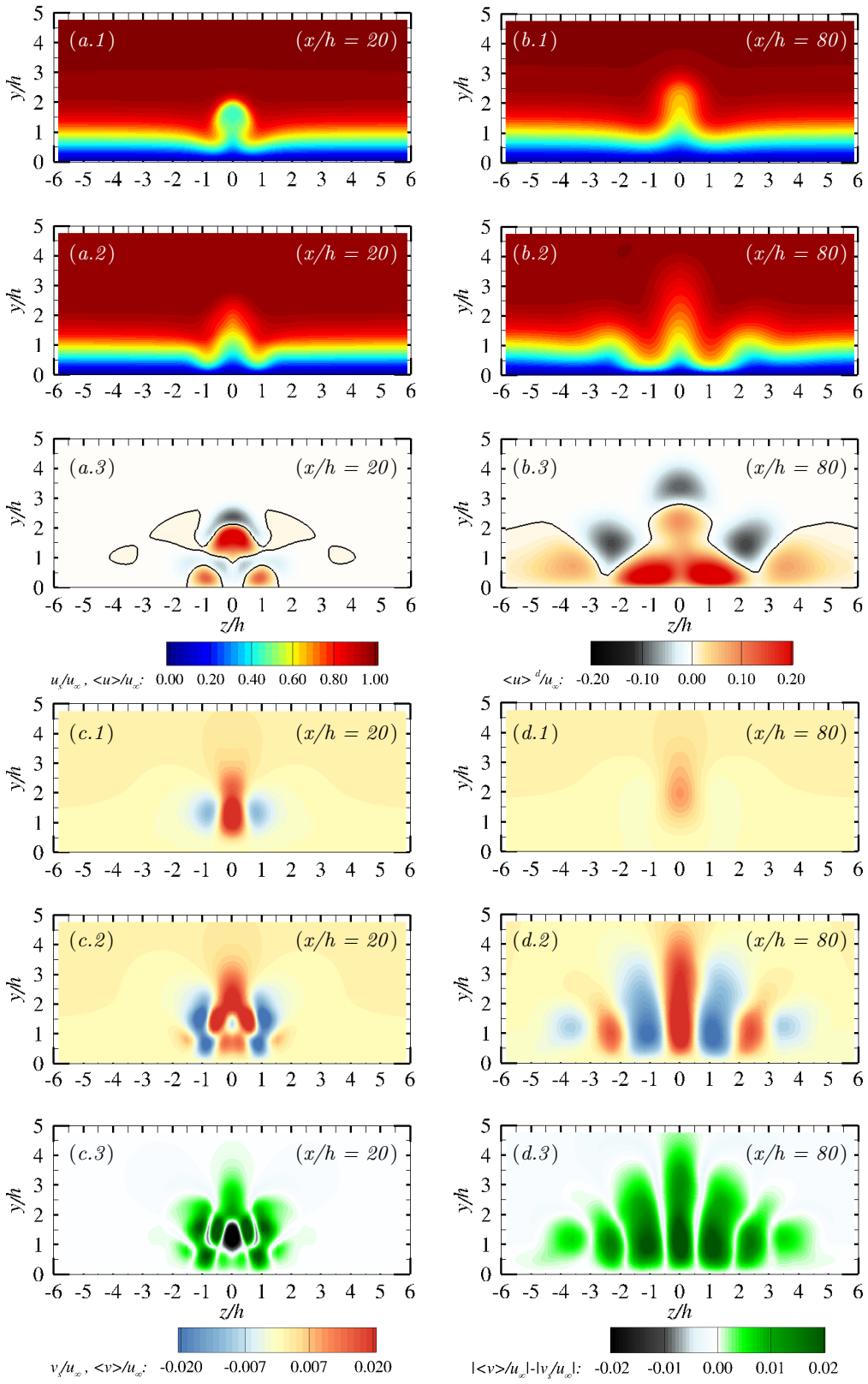

Figure 4.27: y-z planes of (a,b) streamwise and (c,d) wall-normal velocity in (1) base flow, (2) mean flow at (a,c) $x/h = 20$; (b,d) $x/h = 80$. $\langle u \rangle^{\mathrm{d}}$ at (a.3) $x/h = 20$; (b.3) $x/h = 80$. $|\langle v \rangle| - |v_{\mathrm{s}}|$ at (c.3) $x/h = 20$; (d.3) $x/h = 80$. Iso-contour of $\langle u \rangle^{\mathrm{d}} = 0$ (black line).

Streamwise-velocity-streak and shear fields

The wake of the micro-ramp develops a system of streamwise-velocity streaks different to that observed in the base flow. The differences are consistent with the topology of the streamwise mean-flow distortion field. Already at $x/h = 20$, the cores of the momentum excess regions in the mean flow have become stronger and remain close to the surface; see figure 4.28(c.2). The largest values of $\langle u_s^{str} \rangle$ are observed at $|z/h| = 1$, the spanwise location of downwash in the mean flow and positive streamwise mean-flow distortion near the wall. On the other hand, the core of the momentum deficit in the mean flow has recovered more rapidly than in the base flow and the whole region of reduced momentum has grown upward; see figure 4.28(c). As explained, this is consequence of alternate upwash and downwash in x/h at the central shear layer induced by hairpin vortices.

Far downstream the micro-ramp, velocity deficit at the central outer portion of the boundary layer maintains its initial characteristics: it is less strong that the base flow deficit and reaches larger wall-normal positions; see figure 4.28(d). On either side, above the wall, we capture further regions of reduced velocity produced by the activity of LoBs and LBIVs. Momentum excess is dominant near the wall and much stronger than in the base flow. Aside the centre plane, we detect patches of added momentum attached to the wall; these feature the largest values of $\langle u_s^{str} \rangle$. Sufficiently downstream the micro-ramp, the streamwise-momentum streak field becomes positive at $z/h = 0$. This is not the case in the base flow. Moreover, the action of LBIVs introduces positive streaks much aside the centre plane, which coincide with the lateral regions of positive mean-flow distortion. As a consequence, the momentum excess close to the surface covers a spanwise extent much broader than the micro-ramp span. Only in the range $2 \leq |z/h| \leq 3$ —the exact position depends on x/h— less momentum excess is generated, as compared to its spanwise vicinity. This is ascribed to the fact that LoBs and LBIVs lift upward the lowest level fluid at this spanwise position.

Added momentum near the wall yields an enhanced wall shear. The behaviour of the mean shear field in figures 4.28(a,b) and A.7 of the appendix is in agreement with the trend initially presented in figure 4.2(b). Sufficiently close to the micro-ramp, the distribution of wall shear in $\boldsymbol{q}_s$ and in $\langle \boldsymbol{q} \rangle$ resemble each other qualitatively. At $x/h \approx 14$, wall shear in the mean flow experiences an increase. The leg portions of hairpin vortices move towards the surface, suggesting that they enhance the momentum transport close to the wall and introduce the positive mean-flow distortion in this region. The change of role in the re-energisation of the near-wall fluid from the primary vortices to hairpin vortices would be additionally supported by the fact that in figure 4.2(b), we detect a sudden spanwise expansion of the high wall-shear strips at the position at which these increase in magnitude. As illustrated in figure 4.22(b), hairpin legs cover a larger spanwise extent than the primary vortices at this location.

When moving downstream, hairpin legs are maintained at a rather constant spanwise position, and so do the regions of enhanced wall shear. Like the situation in the base flow, we detect a less "healthy" boundary layer at the centre plane for a broad range of x/h, as a consequence of the lift-up of low momentum fluid under the action of the hairpins, but at the outer part of the wake as well, due to negative streamwise velocity streaks introduced by LoBs. The action of LBIVs manifests as well; when moving downstream, wall shear is observed to gradually expand in the spanwise direction. Away from the surface, the action of perturbation has introduced a spanwise-alternating patter of low and high shear and has destroyed the upper part of the central arch-shaped shear layer; see figure 4.28(b.2).

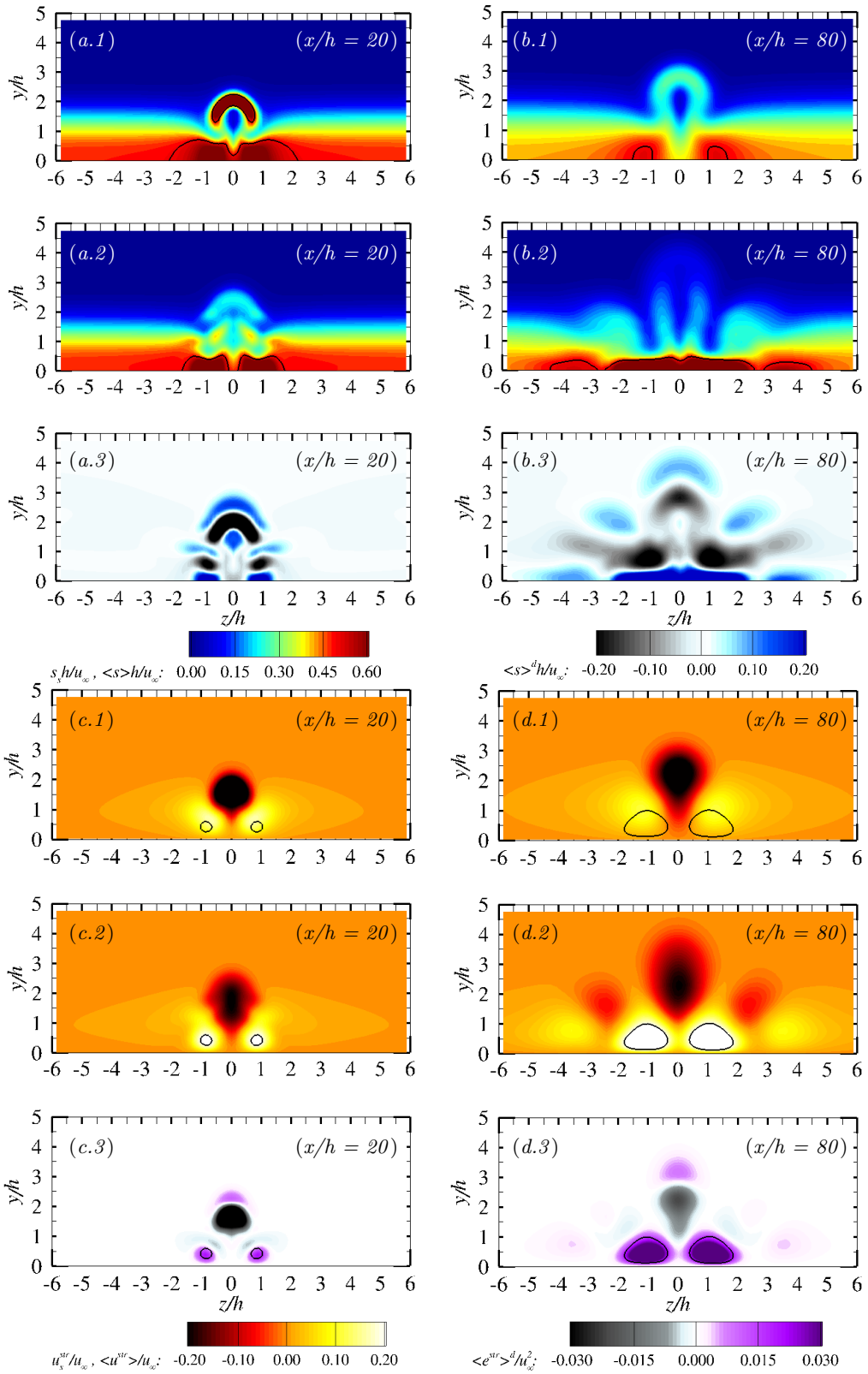

Figure 4.28: y-z planes of (*a*,*b*) shear and (*c*,*d*) streamwise velocity streaks in (1) base flow, (2) mean flow at (*a*,*c*) $x/h = 20$; (*b*,*d*) $x/h = 80$. $\langle s \rangle^{\mathrm{d}}$ at (*a*.3) $x/h = 20$; (*b*.3) $x/h = 80$. $\langle e^{\mathrm{str}} \rangle^{\mathrm{d}}$ at (*c*.3) $x/h = 20$; (*d*.3) $x/h = 80$. Iso-contours of (*a.1*,*b.1*) $s_{\mathrm{s}} h/u_\infty = 1/2$, (*a.2*,*b.2*) $\langle s \rangle^{\mathrm{d}} h/u_\infty = 1/2$, (*c*,*d*) $\langle u^{\mathrm{str}} \rangle /u_\infty = 0.2$ (black line).

4.4.2 Derivation and evaluation of a streamwise-momentum-streak transport equation for incompressible mean flow fields

Results of figure 4.28(c,d) show visual evidence that perturbation activity enhances the generation of momentum excess. Like in the base flow analysis, we intend to assess these observations quantitatively. For that purpose, we next reproduce figure 4.13 and the streak budget analysis presented in §4.2.4 for the mean flow field. So, we first address the derivation of a streamwise-momentum-streak transport equation for incompressible mean flow fields analogous to (4.7).

We assume incompressible flow with constant viscosity. In the unperturbed region (2.16), $w_{\mathrm{un}} = 0$, $\partial u_{\mathrm{un}}/\partial z = 0$, $\partial v_{\mathrm{un}}/\partial z = 0$. Moreover, we consider the mean flow field to be a time-independent solution, i.e., $\partial \langle \boldsymbol{q} \rangle / \partial t = 0$. Due to the lack of mean flow convergence near the outlet, we consider this assumption valid for $0 \leq x/h \leq 70$, a range in which we do not observe significant asymmetries in the mean flow organisation. Following the RANS decomposition (White, 2006), we express the instantaneous velocity field as (2.20)

$$\boldsymbol{v} = \langle \boldsymbol{v} \rangle + \boldsymbol{v}''. \tag{4.11}$$

Under the definition of the instantaneous streaks field (2.17), the time-averaged velocity-streak field reads

$$\left\langle \boldsymbol{v}^{\mathrm{str}} \right\rangle = \langle \boldsymbol{v} \rangle - \boldsymbol{v}_{\mathrm{un}}. \tag{4.12}$$

We now propose to re-express (4.11) as

$$\boldsymbol{v} = \boldsymbol{v}_{\mathrm{un}} + \left\langle \boldsymbol{v}^{\mathrm{str}} \right\rangle + \boldsymbol{v}''. \tag{4.13}$$

A similar decomposition is performed for the pressure. First, introducing (4.13) into the mass conservation equation (2.3) yields

$$\nabla \cdot \left\langle \boldsymbol{v}^{\mathrm{str}} \right\rangle + \nabla \cdot \boldsymbol{v}'' = 0,$$

inasmuch as $\nabla \cdot \boldsymbol{v}_{\mathrm{un}}$. By time-averaging the equation above, and since $\langle \boldsymbol{q}'' \rangle = 0$, it follows that

$$\nabla \cdot \boldsymbol{v}'' = 0 \tag{4.14}$$

and

$$\nabla \cdot \left\langle \boldsymbol{v}^{\mathrm{str}} \right\rangle = 0. \tag{4.15}$$

Secondly, by introducing the velocity and pressure decompositions into the streamwise component of the momentum conservation equation (2.4), we obtain

$$\begin{aligned} &\rho \frac{\partial \boldsymbol{v}}{\partial t} + \rho \boldsymbol{v}_{\mathrm{un}} \cdot \left(\nabla \left\langle u^{\mathrm{str}} \right\rangle + \nabla u'' \right) + \rho \left(\left\langle \boldsymbol{v}^{\mathrm{str}} \right\rangle + \boldsymbol{v}'' \right) \cdot \left(\nabla u_{\mathrm{un}} + \nabla \left\langle u^{\mathrm{str}} \right\rangle + \nabla u'' \right) + \\ &\underbrace{\rho \boldsymbol{v}_{\mathrm{un}} \cdot \nabla u_{\mathrm{un}} + \frac{\partial p_{\mathrm{un}}}{\partial x} - \mu \nabla^2 u_{\mathrm{un}}}_{= 0 \ (4.5)} = -\frac{\partial \left\langle p^{\mathrm{str}} \right\rangle}{\partial x} - \frac{\partial p''}{\partial x} + \mu \nabla^2 \left\langle u^{\mathrm{str}} \right\rangle + \mu \nabla^2 u''. \end{aligned} \tag{4.16}$$

Finally, by time-averaging equation (4.16) and since $\boldsymbol{v}_{\mathrm{un}}$, $\langle \boldsymbol{v}^{\mathrm{str}} \rangle$, and $\boldsymbol{v}''$ are solenoidal fields, it follows that

$$\begin{aligned} \rho(\boldsymbol{v}_{\mathrm{un}} \cdot \nabla) \langle u^{\mathrm{str}} \rangle = &- \frac{\partial \langle p^{\mathrm{str}} \rangle}{\partial x} + \mu \nabla^2 \langle u^{\mathrm{str}} \rangle + \nabla \cdot \left(-\rho u_{\mathrm{un}} \langle \boldsymbol{v}^{\mathrm{str}} \rangle \right) \\ &+ \nabla \cdot \left(-\rho \langle u^{\mathrm{str}} \rangle \langle \boldsymbol{v}^{\mathrm{str}} \rangle \right) + \nabla \cdot \left(-\rho \langle u'' \boldsymbol{v}'' \rangle \right) \end{aligned} \tag{4.17}$$

or

$$\underbrace{\rho(\boldsymbol{v}_{\mathrm{un}} \cdot \nabla) \langle u^{\mathrm{str}} \rangle}_{\textbf{streak advection}} = \underbrace{- \frac{\partial \langle p^{\mathrm{str}} \rangle}{\partial x}}_{\textbf{pressure}} + \underbrace{\mu \nabla^2 \langle u^{\mathrm{str}} \rangle}_{\textbf{diffusion}} + \underbrace{\nabla \cdot \overbrace{(-\rho \langle u \rangle \langle \boldsymbol{v}^{\mathrm{str}} \rangle)}^{\textbf{streak stress}}}_{\textbf{streak-shear-correlation}} + \nabla \cdot \overbrace{(-\rho \langle u'' \boldsymbol{v}'' \rangle)}^{\textbf{Reynolds stress}} . \tag{4.18}$$

Equation (4.18) as a whole, and its terms independently, show a structure similar to the transport equation of streamwise-momentum streaks for steady flow fields (4.7). In particular, the streak stress term, which is the primary generator of the streaks in the base flow, presents the same form as in (4.7). Here, an extra term on the RHS of (4.18) is obtained, the well-known Reynolds stress term of the RANS equations. It represents a new streak transport mechanism since it does not have a counterpart in (4.7). Congruence between terms in equations (4.18) and (4.7) allows us to compare their relative contribution in the generation and destruction of streamwise-momentum streaks in the base and mean configurations of the micro-ramp wake. Differences will be attributed to the effect of perturbation development.

Following the approach of the base flow analysis, we evaluate the transport equation (4.18) using a control volume approach. Expression (4.18) is integrated over the excess and deficit regions: Ω^{E} and Ω^{D}, which are now defined based on the mean quantities. In a fashion similar to the base flow analysis, positive or negative flux of $\rho(\boldsymbol{v}_{\mathrm{un}} \cdot \nabla) \langle u^{\mathrm{str}} \rangle$ across $\partial\Omega^{\mathrm{E}}$ respectively express local generation or destruction of momentum excess. In Ω^{D}, positive or negative flux of $\rho(\boldsymbol{v}_{\mathrm{un}} \cdot \nabla) \langle u^{\mathrm{str}} \rangle$ across $\partial\Omega^{\mathrm{D}}$ respectively indicate whether momentum deficit is locally destructed or generated. The results of the integration are presented in figure 4.29(a,b). It contains two curves that are not present in the base flow analysis, namely the contribution of Reynolds stresses and $\int \left(\rho(\boldsymbol{v}_{\mathrm{un}} \cdot \nabla) \langle u^{\mathrm{str}} \rangle - \rho(\boldsymbol{v}_{\mathrm{un}} \cdot \nabla) u_{\mathrm{s}}^{\mathrm{str}} \right) dA_i^{\mathrm{E}}$. The latter is additionally incorporated to highlight differences between generation or destruction of momentum streaks in the base and mean flows. In figure 4.29(c), the distribution of A_i^{E} and A_i^{D} along x/h is additionally presented. Upon first glance, figure 4.29(a) gives a quantitative confirmation that the generation of momentum excess in the mean flow far downstream the micro-ramp is positive and much larger than that in the base flow.

First, we focus on the streak generation in Ω^{E}. Like in the base flow, in the micro-ramp vicinity, the primary vortex pair plays the dominant role in introducing positive streamwise-velocity streaks into the flow field. In absence of significant perturbation activity, the contribution of the Reynolds stresses (red curve in figure 4.29(a)) to the flux of $\rho \langle u^{\mathrm{str}} \rangle$ across $\partial\Omega^{\mathrm{E}}$ is virtually zero close to the micro-ramp, conform with small-perturbation amplitude. All other terms in (4.18) follow a trend similar to that presented in figure 4.13(a). As perturbations grow gradually, the Reynolds stress term departs from the horizontal axis, becomes negative, and so it yields a destructive contribution, i.e., contributes negatively to the flux of $\rho \langle u^{\mathrm{str}} \rangle$ across $\partial\Omega^{\mathrm{E}}$. The effect of disturbance activity in the transport of momentum

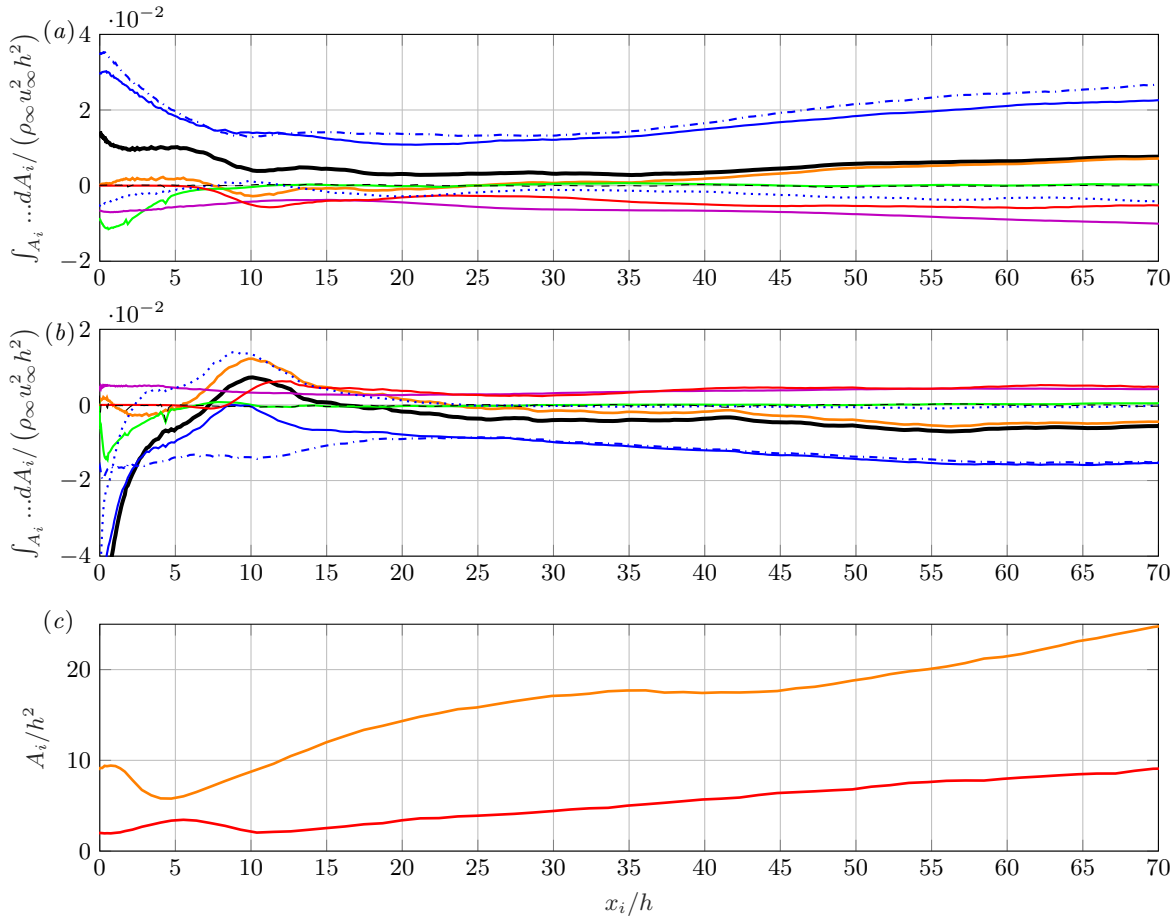

Figure 4.29: Terms of (4.18) integrated over (*a*) Ω^{E}, (*b*) Ω^{D} in the mean flow as function of the streamwise coordinate: $\rho(\boldsymbol{v}_{\mathrm{un}} \cdot \nabla) \langle u^{\mathrm{str}} \rangle$ (solid black), $-\partial \langle p^{\mathrm{str}} \rangle / \partial x$ (solid green), $\mu \nabla^2 \langle u^{\mathrm{str}} \rangle$ (solid magenta), $\nabla \cdot (-\rho \langle u'' \boldsymbol{v}'' \rangle)$ (solid red), $\nabla \cdot (-\rho \langle u \rangle \langle \boldsymbol{v}^{\mathrm{str}} \rangle)$ (solid blue) split into the relative contribution of $\nabla \cdot (-\rho u_{\mathrm{un}} \langle \boldsymbol{v}^{\mathrm{str}} \rangle)$ (dash-dotted blue) and $\nabla \cdot (-\rho \langle u^{\mathrm{str}} \rangle \langle \boldsymbol{v}^{\mathrm{str}} \rangle)$ (dotted blue) as expressed in (4.17), $\rho(\boldsymbol{v}_{\mathrm{un}} \cdot \nabla) \langle u^{\mathrm{str}} \rangle - \rho(\boldsymbol{v}_{\mathrm{un}} \cdot \nabla) u_{\mathrm{s}}^{\mathrm{str}}$ (solid orange), local sum of terms of (4.18) (dashed black). (*c*) A_i^{E} (orange) and A_i^{D} (red) in the mean flow along x/h.

streaks is, however, not completely characterised by the Reynolds stress term. It also manifests itself through the adaptation of the streak stresses (blue curve) and diffusion (purple curve) in that perturbation development deforms the mean flow with respect to the base flow. The pressure (green curve) exhibits a behaviour that is very similar to that in the steady-state configuration, i.e., does not add a significant contribution for $x/h > 10$, neither in Ω^{E} nor in Ω^{D}. At $x/h = 11.5$ the curve characterising Reynolds stresses reaches a local minimum; the K-H instability has given rise to the first generation of hairpin vortices. The term $\int \left(\rho(\boldsymbol{v}_{\mathrm{un}} \cdot \nabla) \langle u^{\mathrm{str}} \rangle - \rho(\boldsymbol{v}_{\mathrm{un}} \cdot \nabla) u_{\mathrm{s}}^{\mathrm{str}}\right) dA_i^{\mathrm{E}}$ (orange curve in figure 4.29(*a*)) is negative around this position mainly as a consequence of the destructive contribution of the Reynolds stresses. It implies that generation of momentum excess momentarily becomes larger in the base flow.

The decrease of the streak stress curve along x/h in the base flow highlights that the primary vortices gradually lose their capability to generate momentum excess. In the mean flow, how-

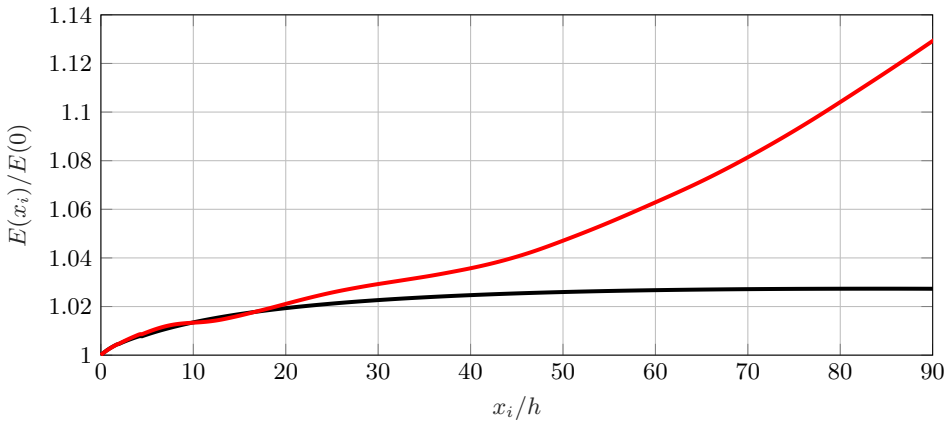

Figure 4.30: Streamwise evolution of the normalised (4.19), the added momentum in the base flow, E_{B} (black), and in the mean flow, E_{M} (red).

ever, the curve of the streak stresses —which adds the largest productive contribution as well— reaches a global minimum at $x/h = 21$. As mentioned previously, the downwash induced by the hairpins starts to reinforce the core of the excess region. This manifests through the streak stress term, whose decreasing trend is first stabilised and thereafter reverted. Perturbation motion takes over the role of the primary vortex pair in redistributing momentum within the boundary layer, in agreement with observations of Bo et al. (2012), and starts to enhance it. At $x/h = 25$, the contribution of the Reynolds stresses has decreased in absolute value, while that of diffusion is maintained rather constant; the $\int \left(\rho(\boldsymbol{v}_{\mathrm{un}} \cdot \nabla) \left\langle u^{\mathrm{str}} \right\rangle - \rho(\boldsymbol{v}_{\mathrm{un}} \cdot \nabla) u_{\mathrm{s}}^{\mathrm{str}}\right) dA_i^{\mathrm{E}}$ becomes zero at this streamwise position. From that point onward, until $x/h = 70$, this difference becomes positive and gradually increases due to the intensification of streak stresses. The action of the streak stresses grows sufficiently to counteract the effect of diffusion and the Reynolds stresses, which remain of destructive nature, and generates the momentum excess with increasing x/h. At the end of the domain, the flux of $\rho \left\langle u^{\mathrm{str}} \right\rangle$ across $\partial\Omega^{\mathrm{E}}$ becomes as large as at $x/h = 8$.

With regard to the momentum deficit, the previously reported initial effective exchange of momentum between the deficit region and the outer part of the boundary layer due to K-H activity is mathematically expressed as positive flux of $\rho \left\langle u^{\mathrm{str}} \right\rangle$ across $\partial\Omega^{\mathrm{D}}$ for $7.2 \leq x/h \leq 16$ in figure 4.29(b). Momentum deficit is destroyed in this range, which is conform with the initial rapid recovery of the low-momentum dip, much faster than in the base flow. It is illustrated in figure A.8 of the appendix. Further downstream, the system of fluxes across $\partial\Omega^{\mathrm{D}}$ shows similarities to that across $\partial\Omega^{\mathrm{E}}$. Diffusion and Reynolds stresses remain of a destructive nature, i.e., contribute positively to the flux of $\rho \left\langle u^{\mathrm{str}} \right\rangle$ across $\partial\Omega^{\mathrm{D}}$. The contribution of streak stresses gradually grows in x/h and carries an increase of the total momentum deficit. For $x/h > 25$, the curve characterising the total flux of negative momentum streaks (solid black curve) follows a trend analogous to that of the positive streaks; it first stabilises and thereafter experiences an increase. At $x/h = 70$, the streak stresses, the Reynolds stresses and diffusion evolve in absolute value at a rather similar rate in x/h, which balances the generation of momentum streaks in Ω^{D} and in Ω^{E}.

We finalise the analysis by condensing previous findings with regard to the momentum excess

generated in the base flow and in the mean flow. We evaluate the streamwise evolution of the amount of momentum excess contained in the boundary layer at a particular streamwise position, relative to the amount of momentum excess at $x/h = 0$. For that purpose, we define

$$E_{\mathrm{B}}(x_i) = \int_{A_i^{\mathrm{E}}} \frac{\rho u_{\mathrm{s}}^{\mathrm{str}}}{\rho_\infty u_\infty}\, d\left(\frac{A_i}{h^2}\right) \quad \text{and} \quad E_{\mathrm{M}}(x_i) = \int_{A_i^{\mathrm{E}}} \frac{\rho \left\langle u^{\mathrm{str}} \right\rangle}{\rho_\infty u_\infty}\, d\left(\frac{A_i}{h^2}\right), \tag{4.19}$$

i.e., the non-dimensional added momentum in the base flow (E_{B}) and in the mean flow (E_{M}) at x_i. The terms in (4.19) are respectively integrated over the regions of momentum excess defined using the base flow and the mean flow quantities. Expressions (4.19) evaluated in the range $0 \leq x/h \leq 90$ are presented in figure 4.30. The trend followed by the curves of figure 4.30 is consistent with the analysis presented above. In the base flow, the generation of momentum excess is not limited to the micro-ramp location, but the amount of momentum excess in the boundary layer eventually stabilises in the streamwise direction. In the mean flow, we observe that around $x/h = 12$, the amount of momentum excess is slightly lower than in the base flow. This is in agreement with the result of figure 4.29(a) and the previous analysis with regard to the role played by the Reynolds stresses for small x/h. The curves of figure 4.30 diverge at $x/h \approx 20$, slightly upstream the x-position at which we reported that the generation of momentum excess in the mean flow equals to that in the base flow. From that point onward, the amount of added momentum in the mean flow becomes increasingly larger than in the base flow for increasing x/h. At approximately $x/h = 50$, the curve representing the productive flux of momentum excess in the mean flow in figure 4.29(a) acquires a relatively constant trend, and the curve of E_{M} in figure 4.30 grows in x/h quasi-linearly. At $x/h = 90$, the amount of added momentum in the mean flow is significantly larger than in the base flow.

Chapter 5

Conclusions and Recommendations

In the introduction, we raised four main research questions and stated several objectives. We now aim to summarise and condense the major achievements and findings of our investigations based on these, as well as to provide recommendations for possible future work.

5.1 Conclusions

5.1.1 SFD functionality

Selective Frequency Damping (SFD) is a method for the computation of steady-state solutions of globally unstable dynamical systems. Our interest in SFD was driven by the necessity to numerically stabilise the unstable wake of a micro-ramp vortex generator operating at supercritial roughness Reynolds number ($\mathcal{R}e_{hh}$) conditions. In this flow regime, the classical numerical time-marching methods generally fail to converge towards a steady solution of the Navier-Stokes equations, because the instantaneous flow field, denoted by $\boldsymbol{q}$, naturally diverges from the laminar steady (base) flow field, denoted by $\boldsymbol{q}_s$. SFD is widely used nowadays and the preferred approach for aerospace applications. However, it has two model parameters, χ and Δ, which are key to the method's effectiveness and efficiency and whose selection remains a common predicament in the literature. In the first part of this work, we examined in detail the effect of χ and Δ to the functionality of SFD.

Upon relation of the eigenvalues, μ, of an uncontrolled Navier-Stokes system with the eigenvalues, λ, of its controlled SFD version, we found simplified algebraic expressions which describe the dynamics of SFD systems. Useful properties were derived based on these: we found that the SFD equations are self-similar to the ratio of the growth rate over the frequency of the most unstable eigenvalue, μ^{c}, of the system and we proved that SFD is not capable of stabilising systems unstable to steady eigenmodes, as suggested by some authors in the literature.

Two different, but interconnected, behaviours of the λ eigenvalues of the controlled system were identified. When $\chi \to 0$, one solution tends to μ^{c} and the other to $-\mathrm{i}/\Delta$. When $\chi \to \infty$, one solution tends to 0 and the other to μ_r^{c} in its real part and to $-\infty$ in its imaginary part. We showed that the λ solution which approaches the origin when $\chi \to \infty$ does that from the

positive semi-plane (unstable region). Consequently, we indicated that choosing too large χ yields unstable behaviour of the controlled system and SFD may fail to converge. This is opposed to what is claimed by Åkervik et al. (2006), the accepted consensus in the literature, and recently questioned by Jordi et al. (2014). We proved that SFD is always able to stabilise systems that are unstable to one mode with a non-zero eigenfrequency. Upon examination of the λ solution branches, we found that there exists a combination of model parameters, denoted by $\chi^\star$ and $\Delta^\star$, which maps both λ solutions towards the same point in the complex plane ($\lambda^\star$). Since $\lambda^\star$ is always located in the negative semi-plane (stable region), choosing $\chi = \chi^\star(\mu^c)$ and $\Delta = \Delta^\star(\mu^c)$ virtually always stabilises the flow problem.

Although $\chi^\star$ and $\Delta^\star$ are simple analytical expressions, their computation requires a previous knowledge of μ^c, in turn requiring the base flow. We proposed the flow unleash technique for characterising the stability properties of the unstable eigenmode associated to the discretised system without having to perform an independent stability analysis. The technique relies on letting the small perturbation eigenmodes of the system develop on a sufficiently time-converged SFD base flow. From the controlled and flow unleash SFD simulations, the eigenvalues μ^s and μ^c respectively ruling the dynamics of the stabilised and uncontrolled systems can be inferred. In this regard, the accuracy of the estimate of μ^c is key to the success of $\chi^\star$ and $\Delta^\star$ to yield convergence; we found that the non-dimensional parameter μ_i^c/μ_r^c rules the numerical feasibility of SFD. The larger μ_i^c/μ_r^c, the larger is the required relative accuracy of $\chi^\star$ and $\Delta^\star$. Accordingly, depending on the digital precision of the numerical tools used to compute the base state, a threshold can be set for which the application of SFD is practically infeasible.

The stabilisation of systems unstable to more than one mode is challenging and can even be impossible depending on the dynamical characteristics of the system. Difficulties arise when unstable eigenvalues with large μ_i/μ_r are located close to the origin of the complex plane. We derived an analytical expression that can be used to determine whether SFD is capable of driving the system, unstable to multiple modes, towards the base solution. Under these conditions, a technique is introduced to select adequate χ and Δ yielding global stabilisation of the system.

We implemented SFD into INCA, a TU Delft's in-house code. We tested the SFD method and the aforementioned theoretical developments by computing the steady state of an incompressible cylinder flow at $\mathcal{R}e = 100$. The usage of $\chi^\star$ and $\Delta^\star$ yielded a well-converged base flow under the conditions predicted by our mathematical model. Furthermore, by applying the flow unleash technique to the cylinder case, we obtained matching eigenmode dynamics with the results of an independent stability analysis.

The choice of $\chi^\star$ and $\Delta^\star$ generally yields suboptimal performance in terms of convergence rate. Based on the dynamics of the controlled eigenvalues λ, we proposed a new hypothetical optimal configuration: the highest convergence rate of an SFD simulation is obtained when the most critical stable steady or low-frequency eigenvalue intersects $\max\left\{\lambda_{1,i}^c, \lambda_{2,i}^c\right\}$ in the imaginary coordinate at the furthest distance from $\lambda_i = 0$. This represents a new contribution that leads to more efficient parameters than the current consensus established by Jordi et al. (2015); the existence of such parameters for the cylinder flow case was already demonstrated by Cunha et al. (2015). The optimisation analysis was based on the fact that the time-asymptotic SFD dynamics are governed by the least stable controlled eigenvalue λ^s; in the linear perturbation regime the spectral radius of the simulation is determined by λ_i^s. Given the

hypotheses that the base state is unstable to an unsteady discrete mode and the convergence of the stabilised dynamics is ruled by a stable steady mode, we presented analytical expressions for the SFD parameters, χ_{opt} and Δ_{opt}, that minimise the spectral radius of the simulation.

The proposed optimal configuration was tested to the cylinder flow case. We ran simulations with different model parameters and compared the computational time required to reach a convergence bound of 10^{-7}. The application of χ_{opt} and Δ_{opt} yielded a reduction in time by 35% with respect to the parameters presented by Jordi et al. (2015), which coincided with the application of $\chi^\star$ and $\Delta^\star$. A reduction by 75% of the time was achieved when comparing the usage of χ_{opt} and Δ_{opt} and standard model parameters, $\chi = 1$ and $\Delta = 5$.

5.1.2 Micro-ramp flow dynamics

In the second part of this work, we studied the wake of a micro-ramp vortex generator immersed in a quasi-incompressible ($M = 0.2$) boundary layer at low supercritical $\mathcal{R}e_{hh}$ conditions. The micro-ramp is a passive flow control device which has become popular due to its structural robustness and reduced drag. It induces a pair of counter-rotating streamwise vortices, the so-called primary vortex pair, which alters the structure of the boundary layer. Ye et al. (2016) and Ye (2017) recently assessed the potential of this device to trigger laminar-turbulent transition. By means of Direct Numerical Simulations (DNS), we numerically reproduced the Particle Image Velocimetry (PIV) experiments performed by Ye (2017) and analysed the transitional flow dynamics behind the micro-ramp. The DNS results were additionally compared with the results from linear stability analysis performed for the micro-ramp base flow. Furthermore, our analysis intends to contribute to the discussion on the micro-ramp working principle. Some authors suggest the micro-ramp to behave differently from conventional vortex generators and question the current consensus with regard to the role played by the primary vortex pair in making the boundary layer more robust.

We computed with DNS and SFD the base flow over the micro-ramp. SFD successfully quenched the unstable frequencies developing in the micro-ramp wake. Nonetheless, large computational efforts were required to obtain a sufficiently well-converged representation of the three-dimensional base flow because SFD relies on asymptotic eigenmode decay in time. The interest in obtaining the micro-ramp base state was driven, first, because it is an entity required to perform linear stability analysis. Secondly, the primary vortex pair is a flow feature contained in the base solution. Upon computation of $\boldsymbol{q}_s$, we isolated the structure of the primary vortex pair and examined its momentum-transport capabilities when transitional perturbation structures do not develop. We observed that the laminar primary vortices only produce a significant entrainment of high-momentum fluid towards the wall at the micro-ramp location and for an initial limited range of streamwise positions downstream from it. The lower portion of the boundary layer aside the centre plane in the base flow undergoes a rapid recovery in the streamwise direction, which is conform with the observed large decrease of the wall shear far downstream the micro-ramp as compared to the near-ramp field. This was hypothesised to be consequence of the rapid upward shift of the primary vortices together with the steep decay of the lateral vortex-induced downwash in streamwise direction. At the centre plane, a sustained upwash lifts the lowest-level fluid and empties the boundary layer in this region. We detected secondary vortices in the base flow, much weaker than the primary ones. These were assumed to not contribute significantly to redistribute momentum.

We captured flow separation at the leading and trailing edges of the micro-ramp and our results reproduced the mechanism of position alternation described by Wang et al. (2013). According to this mechanism, low- and high-momentum fluid from the incoming boundary layer at the micro-ramp span are respectively moved upward and downward along the micro-ramp chord, which generates significant momentum excess and deficit already at the streamwise position of the micro-ramp tip. However, contrarily to what is claimed by Wang et al. (2013), we found that the momentum excess —both in the base flow and in the mean flow configurations— is not uniquely generated at the micro-ramp. Lifted low-momentum fluid under the action of the primary vortices (Li and Liu, 2011; Wang et al., 2013) and rear separation at the micro-ramp would give rise to the characteristic low-momentum dip in micro-ramp flows.

The results of spanwise BiGlobal stability analysis applied to the SFD-computed base flow indicated that the wake of the micro-ramp sustains two convective instabilities. We qualitatively compared the real part of the stability eigenfunction of the dominant mode with the structure of disturbances developing in the unleashed flow and we found high topological resemblance with regard to the wall-normal-velocity and streamwise-vorticity perturbation fields. The onset location of small-amplitude disturbances was found to be the detached shear layer featuring an inflection point; the instability in this shear layer was hypothesised to be of Kelvin-Helmholtz (K-H) type. Close to the micro-ramp, we obtained a good match between the N-factor curve computed from the results of the linear stability analysis and the integrated streamwise velocity perturbation energy obtained from the DNS. Significant differences between the trend followed by these curves in streamwise direction were observed to arise at nine micro-ramp heights downstream from the micro-ramp tip.

We computed with DNS the instantaneous organisation of the transitional micro-ramp wake. Hairpin vortices induced at the detached shear layer were found to be a major structure contributing to the unsteady behaviour of the wake. We detected hairpin-shaped vortices developing in the unleashed flow, which suggested that these structures may be generated through linear perturbation mechanisms. In agreement with the results presented by Ye (2017), we captured a secondary vortical structure initially developing in between hairpin vortices, the so-called leg-buffer. In turn, it induces another secondary vortical structure; together, they play the central role in expanding the wake of the micro-ramp in spanwise direction. We found a good topological match between the instantaneous iso-surfaces of streamwise vorticity from DNS and those presented by Ye (2017) from PIV experiments after low-order Proper Orthogonal Decomposition (POD) reconstruction. We detected the primary vortices in the instantaneous flow field close to the micro-ramp. Sufficiently downstream, however, we did not find evidence of their activity; the dominant pattern of upwash and downwash in the instantaneous flow field was attributed to the dynamics of transitional perturbations. We conjectured that the iso-surfaces of time-averaged streamwise vorticity identified by Ye (2017) as the primary vortex pair would represent the mean activity of the hairpin vortices sufficiently downstream the micro-ramp. In the streamwise range of ten to seventy micro-ramp heights downstream from the micro-ramp tip, the curves of the integrated streamwise velocity perturbation energy presented by Ye (2017) and computed from the DNS results grow in streamwise direction at a similar rate.

We compared the topology of the $\boldsymbol{q}_s$ and the time-averaged $\boldsymbol{q}$ fields. The differences were attributed to the effect of perturbation development. Far downstream the micro-ramp, whereas the central upwash and the lateral downwash in the base flow have significantly decreased

their strength, the mean wall-normal velocity field displays a spanwise-alternating pattern of upwash and downwash of larger magnitude. A major difference between the base and the mean streamwise velocity fields was found near the wall aside the centre plane; the boundary layer in the mean flow becomes fuller than the base flow boundary layer in this region. Sufficiently far from the micro-ramp in the streamwise direction, perturbation activity takes a central role in redistributing momentum in place of the primary vortices, and produces a sustained entrainment of high-momentum fluid towards the surface close to the centre plane. As a consequence of the spanwise spread of the perturbations under the action of the secondary vortices, the near-wall momentum at larger spanwise coordinates increases as well and regions of reduced momentum are introduced away from the wall and from the centre plane; the boundary layer in the mean flow is modulated in the spanwise direction. We observed a significant increase in the wall shear in the mean flow as compared to the base flow, which is conform with the aforementioned description. Furthermore, we showed that, whereas the amount of momentum excess in the base flow boundary layer is stabilised in the streamwise direction, the generation of momentum excess in the mean flow is kept significant far downstream the micro-ramp. The primary vortex pair in the base flow eventually becomes unable to increase the near-wall momentum, but the instantaneous transitional perturbations are capable of doing so in the mean flow.

All in all, our results question the current consensus with regard to the working principle of the micro-ramp. We have shown the importance of the perturbation development in improving the functionality of the micro-ramp for flow control applications when it is immersed in a laminar boundary layer under the flow conditions considered in this work.

5.2 Recommendations and future work

On the efficiency of SFD

The SFD method succeeded to provide a well-converged base flow for both the cylinder and the micro-ramp problems. However, even though we propose an optimal configuration in terms of convergence rate, large computational efforts may be required to stabilise large discretised systems because the nature of the method relies on eigenmode decay, asymptotically in time. SFD is a very robust method and it is easy to implement, but it is not an efficient method, especially when compared to the class of Newton iteration methods (Knoll and Keyes, 2004). In §A.1, in the appendix, we test a coupled approach between SFD and a Newton method to combine their strong points which shows promising results. It is applied to a test case, the Lorenz system; see §A.1. On the one hand, when the coupled approach is compared to the pure SFD method, the coupled approach reduces in two orders of magnitude the number of iterations required to stabilise the system. On the other hand, when compared to a pure Newton method, a similar number of iterations is needed, but the coupled approach does not show sensitivity to the initial conditions, a major drawback in Newton methods. Accordingly, we propose to test this idea of coupling SFD and the Newton iteration methods on Navier-Stokes systems.

On the effectivity of SFD

We have shown that SFD is virtually always capable to stabilise systems that are unstable to one unsteady eigenmode. At the same time, however, we have reported that SFD may

not be able to stabilise systems supporting multiple modes. In the latter case, even though the most unstable eigenmodes are quenched after applying SFD, less unstable modes, and especially those with an associated small frequency, may remain unstable. At this point, we would like to propose the following: one could think of the SFD-stabilised configuration as a *new* system, $F(\boldsymbol{q}, \bar{\boldsymbol{q}})$, to which SFD (or a different stabilising method) could be applied. Since we have proved that a property of the SFD equations is that stable eigenmodes do not become unstable after applying SFD, with a *stabilising iterative* approach, one could focus on the most critical eigenmodes over and over until all of them have become stable, without risk of destabilising the initially stable ones. We found that Massa (2014) proposes a similar approach, by studying the effect of adding multiple control and filter terms to the original system. Massa (2014) shows, through a parametric study, that for a particular flow problem (initially posing difficulty to be stabilised with SFD), it is possible to reach a steady state if a large enough number of extra terms is introduced.

A starting point of our proposed approach would be, for instance, to initially apply $\chi^\star$ and $\Delta^\star$ evaluated for μ^c and, at each SFD iteration, apply $\chi^\star$ and $\Delta^\star$ computed using the least stable λ of the previous iteration. Accordingly, it could be guaranteed that, at each SFD iteration, the most unstable eigenmode is stabilised and hence, the maximum required number of SFD iterations would be equal to the number of unstable eigenmodes supported by the original system. Furthermore, considering the encapsulated formulation introduced by Jordi et al. (2014), this method might be developed in such a way that it is only required to concatenate multiple matrices containing the information of the parameters χ and Δ at each iteration, without altering the original discretised system. However, we have shown that too large χ values move the unstable solutions towards the origin. After some iterations, the eigenvalues associated to certain eigenmodes might have significantly increased their argument, eventually leading to an infeasible application of this approach in reality.

On the micro-ramp functionality

The results presented in this work suggest a revision of the working principle of the micro-ramp. We analyse the performance of this device when it is immersed in a laminar and incompressible boundary layer. However, other authors which study micro-ramps operating at supersonic and turbulent flow conditions point in a similar direction with regard to the role played by the hairpin vortices. This is for instance the case of Bo et al. (2012) for a turbulent $M = 2.7$ boundary layer. Based on the results of our analysis, we suggest to examine the role played by the primary vortices and the large-scale hairpin vortices in different flow environments as well. Sun et al. (2012) study the interaction between the primary vortex pair and K-H vortices in a turbulent $M = 2$ boundary layer, but only for a limited range of streamwise positions. We have observed a strong dependence of the development and the role played by the primary vortices and the hairpin vortices with regard to the spatial coordinates. We expect our analysis to serve for future studies of the design of micro-ramp set-ups, both isolated and in an array configuration. Important features would be the strength of the primary vortices, but also the stability properties of the detached shear layer and thus the characteristics of the low-momentum dip.

When considering the usage of micro-ramps for laminar flow control applications, our results highlight the relevance of the parameter $\mathcal{R}e_{hh}$. If the roughness Reynolds number is small enough, the boundary layer remains laminar despite the presence of the micro-ramp, thus yielding a possibly reduced performance. This is observed in the analysis presented in §A.5,

in the appendix, considering a micro-ramp operating at $M = 0.7$. The stabilising effect of compressibility weakens the perturbation growth, which affects negatively the micro-ramp performance with respect to the $M = 0.2$ case.

A main reason for the eventual incapability of the base flow primary vortices to increase the near-wall momentum is their rapid upward shift downstream the micro-ramp. An improved design of a laminar passive flow control device would combine an enhanced momentum-transport capability of the induced streamwise vortices with the promotion of laminar-turbulent transition. For instance, a surface roughness element which would generate a strong pair of streamwise counter-rotating vortices rotating in a sense opposite to that of the primary vortices. Downstream-travelling vortex filament might then be kept attached to the wall, thus possibly maintaining a more effective entrainment of high-momentum fluid towards the wall. At the same time, the device would ideally introduce a strong instability into the flow field. A hypothetical associated detached shear layer would give rise to transitional perturbation structures initially closer to the surface.

Bibliography

E. Åkervik, L. Brandth, D. S. Henningson, J. Hœpffner, O. Marxen, and P. Schlatter. Steady solutions of the Navier-Stokes equations by selective frequency damping. *Phys. Fluids*, 18: 357–397, 2006. [8, 9, 16, 17, 26, 27, 28, 36, 90]

E. Åkervik, J. Hœpffner, U. Ehrenstein, and D. S. Henningson. Optimal growth, model reduction and control in a separated boundary-layer flow using global eigenmodes. *J. Fluid Mech.*, 579:305–314, 2007. [9]

M. S. Acarlar and C. R. Smith. A study of hairpin vortices in a laminar boundary layer. part 1. hairpin vortices generated by a hemisphere protuberance. *J. Fluid Mech.*, 175:1–54, 1986. [4]

J. Aholt and F. Finaish. Active flow control stategy of laminar separation bubbles developed over subsonic airfoils at low reynolds numbers. 49th AIAA Aerospace Sciences Meeting Including the New Horizons Forum and Aerospace Exposition, 2011. AIAA 2011-733. [2]

B. H. Anderson, H. Tinapple, and L. Surber. Optimal control of shock wave turbulent boundary layer interactions using micro-array actuation, 2006. AIAA Paper 2006-3197. [6, 22, 41]

M. Asai, M. Minagawa, and M. Nishioka. The instability and breakdown of a near-wall low-speed streak. *J. Fluid Mech.*, 455:289–314, 2002. [68]

H. Babinsky, Y. Li, and C. W. Pitt Ford. Microramp Control of Supersonic Oblique Shock-Wave/Boundary-Layer Interactions. *AIAA J.*, 47(3), 2009. [xv, 5, 6, 41, 45, 50, 51]

S. Bagheri, P. Schlatter, P. J. Schmid, and D. S. Henningson. Global stability of a jet in crossflow. *J. Fluid Mech.*, 624:33–44, 2009. [9]

D. Barkley. Linear analysis of the cylinder wake mean flow. *Europhys. Lett.*, 75:750–756, 2006. [xxi, 19, 34]

M. Bernardini, S. Pirozzoli, and P. Orlandi. Compressibility effects on roughness-induced boundary layer transition. *International Journal of Heat and Fluid Flow*, 35:45–51, 2012. [3, 23, 125]

S. A. Berry and A. H. Auslender. Hypersonic boundary-layer trip development for Hyper-X. *J. Spacecr. Rockets*, 38(6), 2001. [6]

P. L. Blinde, R. A. Humbre, B. W. van Oudheusden, and F. Scarano. Effects of micro-ramps on a shock wave/turbulent boundary layer interaction. *Shock Waves*, 19:507–520, 2009. [6, 7, 41, 72, 75]

R. Blockley, R. Agarwal, F. Collier, A. Schaefer, and A. Seabridge. *Green aviation*. Wiley, New Jersey, United States, 2016. [2]

W. Bo, L. Weidong, Z. Yuxin, F. Xiaoqiang, and W. Chao. Experimental investigation of the micro-ramp based shock wave and turbulent boundary layer interaction control. *Phys. Fluids*, 24, 2012. [7, 41, 75, 87, 94]

A. V. Boiko, A. V. Dovgal, G. R Grek, and V. V. Kozlov. *Physics of transitional shear flows*. Springer, 2012. [3]

A. Braslow and E. Horton. Effects of surface roughness on transition. NACA, Conference on High-Speed Aerodynamics, Washington DC, 1958. [3]

M. Choudhari, F. Li, and J. Edwards. Stability Analysis of Roughness Array Wake in a High-Speed Boundary Layer. 47th AIAA Aerospace Sciences Meeting Including The New Horizons Forum and Aerospace Exposition, 2009. AIAA 2009-170. [3, 4]

M. Choudhari, F. Li, M. Wu, C. Chang, J. Edwards, M. Kegerise, and R. King. Laminar-Turbulent Transition behind Discrete Roughness Elements in a High-Speed Boundary Layer. AIAA Paper 2010-1575, January 2010. [4, 64]

V. Citro, P. Luchini, F. Giannetti, and F. Auteri. Efficient stabilization and acceleration of numerical simulation of fluid flows by residual recombination. *J. Comput. Phys.*, 344: 234–246, 2017. [35]

G. Cunha, P.-Y. Passaggia, and M. Lazareff. Optimization of the selective frequency damping parameters using model redution. *Phys. Fluids*, 27:094103, 2015. [8, 9, 18, 27, 38, 90]

C. de Boor. B-form basics. In G. E. Farin, editor, *Geometric modeling: algorithms and new trends*, pages 131–148. SIAM, Philadelphia, 1987. [24]

N. De Tullio, P. Paredes, N. D. Sandham, and V. Theofilis. Laminar-turbulent transition induced by a discrete roughness element in a supersonic boundary layer. *J. Fluid Mech.*, 735:613–646, 2013. [4, 64, 68]

J. S. Delnero, J. Marañon Di Leo, M. Martinez, F. A. Bacchi, J. Colman, A. Scarabino, and U. Boldes. Effects of turbulators on an airfoil at low reynolds number in turbulent flow. 45th AIAA Aerospace Science Meeting and Exhibit, 2007. AIAA 2007-1273. [2]

G. E. Elsinga and J. Westerweel. Tomographic-PIV measurement of the flow around a zigzag boundary layer trip. *Exp. in Fluids*, 52:865–876, 2012. [2]

F. G. Ergin and E. B. White. Unsteady and transitional flows behind roughness elements. *AIAA Journal*, 44(11):2504–2514, 2006. [2, 4, 64, 77]

A. Fani, S. Camarri, and M. V. Salvetti. Unsteady asymmetric engulfment regime in a T-mixer. *Phys. Fluids*, 26:074101, 2014. [9]

J. H. M. Fransson, A. Talamelli, L. Brandt, and C. Cossu. Delaying transition to turbulence by a passive mechanism. *Annu. Rev. Fluid Mech*, 96:1–4, 2006. [2]

X. Garnaud, L. Lesshafft, P. J. Schmid, and J.-M. Chomaz. A relaxation method for large eigenvalue problems, with an application to flow stability analysis. *J. Comput. Phys.*, 231: 3912–3927, 2012. [16]

S. Ghosh, J. Choi, and J. R. Edwards. Numerical simulations of effects of micro vortex generators using immersed-boundary methods. *AIAA J.*, 48(1), 2010. [6, 41, 46, 48, 51]

R. H. M. Giepman, F. F. J. Schrijer, and B. W. van Oudheusden. Flow control of an oblique shock wave reflection with micro-ramp vortex generators: effect of location and size. *Phys. Fluids*, 26:1–16, 2014. [6, 22]

S. Gottlieb, C.-W. Shu, and E. Tadmor. Strong stability-preserving hihg-order time discretization methods. *Siam Review*, 43(1):89–112, 2001. [20]

K. J. Groot. Derivation of and simulations with biglobal stability equations. Master's thesis, Technische Universiteit Delft, The Netherlands, 2013. [3, 24]

K. J. Groot, Q. Ye, and B. W. van Oudheusden. BiGlobal stability analysis of a micro-ramp wake using PIV base flows. 46th AIAA Fluid Dynamics Conference, 2016. AIAA AVIATION Forum 2016. [24, 45, 63, 64, 72]

G. Haller. An objective definition of a vortex. *J. Fluid Mech.*, 525:1–26, 2004. [50]

S. Hickel, C. P. Egerer, and J. Larsson. Subgrid-scale modeling for implicit large eddy simulation of compressible flows and shock-turbulence interaction. *Phys. Fluids*, 26:106–101, 2014. [19]

D. Jackson and B. Launder. Osborne Rreynolds and the publication of his papers on turbulent flow. *Annu. Rev. Fluid Mech.*, 39:19–35, 2007. [1]

M. Jahanmiri. Aircraft drag reduction: an overview. Research report 2011:02, 2011. [2]

J. Jeong and F. Hussain. On the identification of a vortex. *J. Fluid Mech.*, 285:69–94, 1995. [68]

L. E. Jones and R. D. Sandberg. Numerical analysis of tonal airfoil self-noise and acoustic feedback-loops. *J. Sound Vib.*, 330:6137–6152, 2011. [9]

B. E. Jordi. *Steady-state solvers for stability analysis of vortex dominated flows*. PhD thesis, Imperial College London, 2015. [19]

B. E. Jordi, C. J. Cotter, and S. J. Sherwin. Encapsulated formulation of the selective frequency damping method. *Phys. Fluids*, 26:034101, 2014. [9, 17, 27, 90, 94]

B. E. Jordi, C. J. Cotter, and S. J. Sherwin. An adaptive selective frequency damping method. *Phys. Fluids*, 27:094104, 2015. [xvi, 9, 35, 38, 39, 90, 91]

M. Kegerise, R. King, L. Owens, M. Choudhari, A. Norris, F. Li, and C.-L. Chang. An experimental and numerical study of roughness-induced instabilities in a Mach 3.5 boundary layer. NATO Unclassified, May 2012. [4, 64]

P. Klebanoff, G. Schubauer, and K. Tidstrom. Measurements of the effect of two-dimensional and three-dimensional roughness elements on boundary-layer transition. *AIAA J.*, 2:803–804, 1955. [3, 22]

D. A. Knoll and D. E. Keyes. Jacobian-free Newton-Krylov methods: a survey of approaches and applications. *J. Comput. Phys.*, 193:357–397, 2004. [8, 93, 104]

H. B. E. Kurz and M. J. Kloker. Mechanisms of flow tripping by discrete roughness elements in a swept-wing boundary layer. *J. Fluid Mech.*, 796:158–194, 2016. [9]

M. J. Lai and L. L. Schumaker. *Spline functions on triangulations*, volume 110 of *Encyclopedia of Mathematics and Its Applications*. Cambridge University Press, Cambridge, UK, 2007. [24]

M. T. Landhal. A note on an algebraic instability of inviscid parallel shear flows. *J. Fluid Mech.*, 98:243–251, 1980. [3]

S. Lee, M. K. Goetteke, E. Loth, J. Tinapple, and J. Benek. Microramps upstream of an oblique-shock/boundary-layer interaction. *AIAA J.*, 48(1):104–118, 2010. [6, 41, 45]

Q. Li and C. Liu. LES for supersonic ramp control flow using MVG at $M = 2.5$ and $Re_\theta = 1440$. 4-7 January 2010. AIAA Paper 2010-592. [6, 45, 46, 64, 70, 72]

Q. Li and C. Liu. Implicit LES for supersonic microramp vortex generator: new discoveries and new mechanisms. *Model. Simul. Eng.*, 2011, 2011. [6, 7, 41, 45, 48, 51, 92]

Q. Li, Y. Yan, P. Lu, A. Pierce, C. Liu, and F. Lu. Numerical and experimental studies on the separation topology of the MVG controlled flow at Mach 2.5. 49th AIAA Aerospace Sciences Meeting Including the New Horizons Forum and Aerospace Exposition, 2011. AIAA 2011-72. [50]

J. C. Lin. Review of research on low-profile vortex generators to control boundary-layer separation. *Prog. Aerosp. Sci.*, 38:389–420, 2002. [2, 5, 41]

X.-D. Liu, S. Osher, and T. Chan. Weighted essentially non-oscillatory schemes. *J. Comput. Phys.*, 115(1), 1994. [23]

J.-Ch. Loiseau, J.-Ch. Robinet, S. Cherubini, and E. Leriche. Investigations of the roughness-induced transition: Global stability analyses and direct numerical simulations. *J. Fluid Mech.*, 760:175–211, 2014. [2, 4, 9, 64, 68]

F. K. Lu, A. J. Pierce, and Y. Shih. Experimental study of near wake of micro vortex generators in supersonic flow. 40th Fluid Dynamics Conference and Exhibit, 2010. AIAA Paper 2010-4623. [41, 72, 75]

M. Malik, W. Liao, and M. Choudhari. DRE-enhanced swept-wing natural laminar flow at high reynolds numbers. 51st AIAA Aerospace Sciences Meeting Including the New Horizons Forum and Aerospace Exposition, 2013. AIAA 2013-0412. [2]

L. Massa. Mach number effects on the global mixing modes induced by ramp injectors in supersonic flows. *J. Fluid Mech.*, 757:403–431, 2014. [10, 32, 94]

M. Meyer, A. Devesa, S. Hickel, X.Y. Hu, and N. A. Adams. A conservative immersed interface method for Large-Eddy Simulation of incompressible flows. *J. Comput. Phys.*, 229(18):6300–6317, 2010. [19]

B. Pier. Local and global instabilities in the wake of a sphere. *J. Fluid Mech.*, 603:39–61, 2008. [9]

F. Pinna. *Numerical study of stability of flows from low to high Mach number.* PhD thesis, von Karman Institute for Fluid Dynamics, Chaussee de Waterloo 72,1640 Rhode-Saint-Genese,Belgium, 2012. [1, 3]

L. Popelka, M. Matejka, D. Simurda, and N. Souckova. Boundary layer transition, separation and flow control on airfoils, wings and bodies in numerical, wind-tunnel and in-flight studies. XXX OSTIV Congress, 28 July - 4 August 2010, Szeged Hungary, 2010. [2]

J. A. Redford, N. D. Sandham, and G. T. Roberts. Compressibility Effects on Boundary-Layer Transition Induced by an Isolated Roughness Element. *AIAA Journal*, 48, 2010. [3, 4, 23, 64, 125]

H. L. Reed, W. S. Saric, and D. Arnal. Linear stability theory applied to boundary layers. *Annu. Rev. Fluid. Mech.*, 28:389–428, 1996. [3]

E. Reshotko. Paths to transition in wall layers. In RTO-EN-AVT-151 - Advances in laminar-turbulent transition modelling, 2008. NATO Science and Technology Organization. [4]

F. Richez, M. Leguille, and O. Marquet. Selective frequency damping method for steady RANS solutions of turbulent separated flows around an airfoil at stall. *Comput. Fluids*, 132:51–61, 2016. [8, 9, 34]

D. P. Rizzeta and M. R. Visbal. Direct numerical simulations of flow past an array of distributed roughness elements. *AIAA J.*, 45:1967–1976, 2007. [4]

P. J. Schmid. Global modes and control in a square cavity. *AIAA Paper 2008-4229 in: 5th Theoretical Fluid Mechanics Conference.*, pages 1–7, June 2008. [9]

P. J. Schmid and D. S. Henningson. *Stability and transition in shear flows.* Springer, 2001. [3, 16, 24, 64, 65]

S. P. Schneider. Effects of roughness on hypersonic boundary-layer transition. *J. Spacecr Rockets*, 45(2), 2008. [3]

R. Sedney. A survey of the effect of small protuberances on boundary-layer flows. *AIAA J.*, 11(6):782–792, 1973. [3]

Z. Sun, F. F. J. Schrijer, F. Scarano, and B. W. van Oudheusden. The three-dimensional flow organization past a micro-ramp in a supersonic boundary layer. *Phys. Fluids*, 24, 2012. [6, 45, 51, 64, 75, 94]

I. Tani. Boundary-layer transition. *Annu. Rev. Fluid. Mech.*, pages 169–196, 1969. [3]

R. S. Teixeira and L. S. B. Alves. Minimal gain marching schemes: searching for unstable steady-states with unsteady solvers. *Theor. Comput. Fluid Dyn.*, pages 1–15 (to appear), 2017. [8, 10]

V. Theofilis. Advances in global linear instability analysis of nonparallel and three-dimensional flows. *Prog. Aerosp. Sci.*, 39:249–315, 2003. [3, 16]

V. Theofilis. Global linear instability. *Annu. Rev. Fluid. Mech.*, 43:319–352, 2011. [24]

J. J. Thibert, J. Reneaux, and V. Schmitt. Onera activities on drag reduction. Office National d'Études et de Recherches Aérospatiales, 1990. [2]

S. C. Tirtey, O. Chazot, and L. Walpot. Characterization of hypersonic roughness-induced boundary-layer flow. *Exp. Fluids*, 50:407–418, 2011. [6, 7, 45]

H. J. Tol, M. Kotsonis, and C. C. de Visser. Localised estimation and control of linear instabilities in 2-D wall-bounded shear flows. *J. Fluid Mech.*, 824:818–865, 2016. [24]

E. F. Toro, M. Spruce, and W. Speares. Restoration of the contact surface in the hll-riemann solver. *Shock Waves*, 4:25–34, 1994. [23]

J. L. Van Ingen. The e^{n} method for transition prediction. Historical review of work at TU Delft. AIAA 2008-3830, June 2008. [64, 77]

S. B. Verma and A. Hadjadj. Supersonic flow control. *Shock Waves*, 25:443–449, 2015. [41]

A. E. von Doenhoff and A. L. Braslow. *The effect of distributed surface roughness on laminar flow. In boundary layer and flow control.* G.V. Lachmann, Pergamon, 1961. [3, 22, 125]

E. Vyazmina. *Bifurcations in a swirling flow.* PhD thesis, École Polytechnique X, 2010. [9, 27]

X. Wang, Y. Yan, Z. Sun, and C. Liu. LES investigation into the generation of momentum deficits in the supersonic wake of a micro-ramp. *J. Mech. Sci. Technol.*, 28, 2013. [7, 41, 44, 45, 50, 51, 60, 92]

X. Wang, Y. Yan, and Z. Sun. The vortical structures in the rear separation and wake produced by a supersonic micro-ramp. *Flow Turbul. Combust.*, 93:25–36, 2014. [50]

A. Washburn. Drag reduction status and plans-laminar flow and AFC. Oral Presentation at AIAA Aero Sciences Meeting, Orlando, FL, January 4-7, 2011. [2]

F. White. *Viscous Fluid Flow.* New York: McGraw-Hill, 3rd ed. edition, 2006. [1, 21, 57, 84]

Y. Yan, L. Chen, Q. Li, and C. Liu. Numerical study of micro-ramp vortex generator for supersonic ramp flow control at mach 2.5. *SHOCK WAVES*, 25:443–449, 2016. [52]

Q. Ye. *Mechanisms of boundary layer transition induced by isolated roughness.* PhD thesis, Technische Universiteit Delft, 2017. [xviii, xxi, 6, 20, 21, 22, 41, 42, 48, 63, 70, 71, 72, 73, 74, 77, 91, 92]

Q. Ye, F. F. J. Schrijer, and F. Scarano. Boundary layer transition mechanisms behind a micro-ramp. *J. Fluid Mech.*, 793:132–161, 2016. [xv, 4, 6, 7, 45, 51, 80, 91]

D. Zuck. Osborne Reynolds, 1842-1912, and the flow of fluids through tubes. *Brit. J. Anaesth.*, 43:1175–1182, 1971. [1]

Appendix A

Appendix

A.1 Selective Frequency Damping and Jacobian-free Newton-Krylov methods to stabilise a Lorenz attractor

The first section of the Appendix includes an initial test case which served to investigate the functionality of SFD. Besides testing SFD, its performance was compared to that of Newton iteration methods. The latter were finally discarded for the final cylinder and micro-ramp applications.

A.1.1 Jacobian-free Newton-Krylov (JFNK) methods

As stated previously, the non-linear Navier-Stokes equations are expressed as $\dot{\boldsymbol{q}} = f(\boldsymbol{q})$. Since we aim to drive this system towards a solution such that $\dot{\boldsymbol{q}} = 0$, the goal of the approach is to find the roots of $f(\boldsymbol{q})$. The Newton iteration for $\dot{\boldsymbol{q}} = f(\boldsymbol{q})$ relies on applying a Taylor expansion of $f(\boldsymbol{q})$ around a *past* state $\boldsymbol{q}^n$, such that $f(\boldsymbol{q})$ evaluated at a *future* state $\boldsymbol{q}^{n+1}$ reads

$$f(\boldsymbol{q}^{n+1}) = f(\boldsymbol{q}^n) + \left.\frac{\partial f(\boldsymbol{q})}{\partial \boldsymbol{q}}\right|_{\boldsymbol{q}^n} (\boldsymbol{q}^{n+1} - \boldsymbol{q}^n) + \text{h.o.t.}$$

By neglecting high-order terms and setting $f(\boldsymbol{q}^{n+1}) = 0$, the Newton algorithm is expressed as

$$\boldsymbol{J}(\boldsymbol{q}^n)\delta\boldsymbol{q}^n = -f(\boldsymbol{q}^n), \qquad \boldsymbol{q}^{n+1} = \boldsymbol{q}^n + \delta\boldsymbol{q}^n, \qquad n = 0, 1, ..., \tag{A.1}$$

where $\boldsymbol{J}(\boldsymbol{q}^n)$ is the Jacobian matrix of $f(\boldsymbol{q})$ evaluated at $\boldsymbol{q} = \boldsymbol{q}^n$; $\delta\boldsymbol{q}^n$ represents an increment of $\boldsymbol{q}$ between states n and $n+1$.

Now we have to solve linear system defined by (A.1) at every nth step. For that purpose we use a Krylov sub-space method. It is based on defining an initial linear residual, $\boldsymbol{r}_0$, for a given initial guess of $\delta\boldsymbol{q}_0$,

$$\boldsymbol{r}_0 = -f(\boldsymbol{q}^n) - \boldsymbol{J}(\boldsymbol{q}^n)\delta\boldsymbol{q}_0. \tag{A.2}$$

The method aims to minimize $\boldsymbol{r}_0$. Since it must be accomplished at every nth state, $\boldsymbol{r}$ and $\delta\boldsymbol{q}$ are named with a different index (j). From all existing Krylov methods, we particularly choose the Biconjugate Gradient Stabilized Method (BiCGSTAB).

In (A.1) we see that one of the terms of the expression is the product of $\boldsymbol{J}(\boldsymbol{q}^n)$ with the increment of $\boldsymbol{q}$ between states n and $n+1$. The storage of the Jacobian matrix at every time step for the current flow case described by the Navier-Stokes equations is not feasible due to memory requirements. Therefore, a Jacobian-free approach is considered. This technique relies on approximating the product of $\boldsymbol{J}(\boldsymbol{q}^n)$ with vector $\delta\boldsymbol{q}_j$ as follows:

$$\boldsymbol{J}(\boldsymbol{q}^n)\delta\boldsymbol{q}^j \approx \frac{f(\boldsymbol{q}^n + \epsilon\delta\boldsymbol{q}^j) - f(\boldsymbol{q}^n)}{\epsilon}, \tag{A.3}$$

with ϵ representing a *small* quantity. We take $\epsilon = 10^{-6}$ for the current analysis.

A.1.2 Coupled approach between SFD and JFNK

A new proposed method which couples SFD and JFNK with the aim of combining their strong points is presented next. Major considerations are:

A. **Initialization:** due to the fact that the JFNK method is very sensitive to the initialisation parameters, the coupled approach first applies a pure SFD method. After some initial iterations, and once the solution has started to *point* towards the steady-state, the method is switched and then pure JFNK takes the role. Generally, the JFNK method converges very fast once a correct iteration direction has been taken. On the contrary, the SFD method needs a few iterations to bring the solution near the steady state but then it shows a low convergence rate until the problem is stabilized.

B. **Modified line search method:** we test a common globalisation approach combined with the class of Newton iteration methods based on the line search method (Knoll and Keyes, 2004). It relies on applying a relaxation factor (s) to the calculated $\delta\boldsymbol{q}^n$ parameter, based on the idea that although $\delta\boldsymbol{q}^n$ may point towards a correct direction, its magnitude might not be adequate to ensure convergence. Therefore, at every iteration, the new state is obtained as

$$\boldsymbol{q}^{n+1} = \boldsymbol{q}^n + s\ \delta\boldsymbol{q}^n. \tag{A.4}$$

Then the question that arises is what value to assign to the parameter s. We propose to gradually decrease it (from $s = 1$ to $s = 0.2$) and choose a value such that $||f(\boldsymbol{q}^{n+1})|| < ||f(\boldsymbol{q}^n)||$, since the aim of the Newton iteration method is to drive $f(\boldsymbol{q})$ towards a $\boldsymbol{q}$ solution such that $f(\boldsymbol{q}) \to 0$.

The implementation of the coupled SFD/JFNK approach considers the following steps:

1. Compute the multivariate function $f(\boldsymbol{q}^n)$ at the original state n
2. Evaluate $f(\boldsymbol{q})$ at the new state, based on $\boldsymbol{q}^{n+1} = \boldsymbol{q}^n + \delta\boldsymbol{q}^n$
3. Define a tolerance (normcond), set $s = 1$ and $logical = false$

4. **if** $(||f(\boldsymbol{q}^{n+1})|| > \text{normcond} \times ||\text{f}(\text{q}^{\text{n}})||)$
5. **while** $(s > 0.2)$ **and** $(logical == false)$
6. $s = s - 0.1$
7. Compute a new update of $||f(\boldsymbol{q}^{n+1})||$ but now based on $\boldsymbol{q}^{n+1} = \boldsymbol{q}^n + s\ \delta\boldsymbol{q}^n$
8. **if** $(||f(\boldsymbol{q}^{n+1})|| < ||f(\boldsymbol{q}^n)||)$
9. $lock = true$
10. **end**
11. **end**
12. **if** $(||f(\boldsymbol{q}^{n+1})|| > \text{normcond} \times ||\text{f}(\text{q}^{\text{n}})||)$
13. $\boldsymbol{q}^{n+1} = \boldsymbol{q}^{n+1}_{\text{SFD}}$
14. **else**
15. $\boldsymbol{q}^{n+1} = \boldsymbol{q}^n + s\ \delta\boldsymbol{q}^n$
16. **end**
17. **else**
18. $\boldsymbol{q}^{n+1} = \boldsymbol{q}^n + \delta\boldsymbol{q}^n$
19. **end**

A.1.3 Application to the Lorenz attractor

The Lorenz attractor is a set of three-dimensional non-linear time-dependant ordinary differential equations well-known for having chaotic solutions for a certain combinations of system parameters. The equations defining the system read

$$\begin{aligned} \frac{dx}{dt} &= \sigma(x - y), \\ \frac{dy}{dt} &= x(\rho - z) - y, \\ \frac{dz}{dt} &= xy - \beta z, \end{aligned} \tag{A.5}$$

where $x = x(t)$, $y = y(t)$, $z = z(t)$. The parameters of the system are $\sigma, \rho, \beta \in \mathbb{R}$, which are generally assumed to be positive. The Lorenz system is a simplified model describing atmospheric flows under the effect of convection.

For $\rho < 1$, there is only one steady-state point, corresponding to $(0, 0, 0)$ and hence all trajectories are attracted to the origin regardless of the initial conditions. For $\rho > 1$, two additional

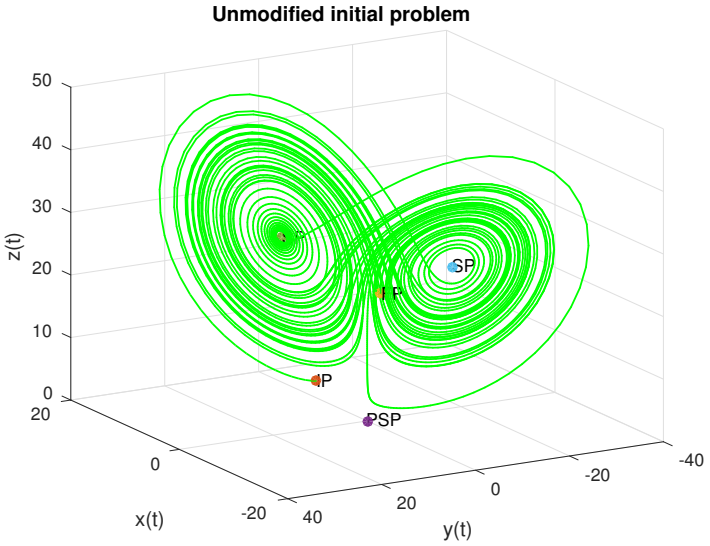

Figure A.1: Trajectory $r(t) = (x(t), y(t), z(t))$ of the Lorenz system in an unstable situation with $\sigma = 10$, $\rho = 28$, and $\beta = 8/3$

steady-state points arise, whose coordinates are $\left(\pm\sqrt{\beta(\rho-1)}, \pm\sqrt{\beta(\rho-1)}, \rho-1\right)$. These points are stable if

$$\rho < \sigma\frac{\sigma+\beta+3}{\sigma-\beta-1}. \tag{A.6}$$

When the system parameters are chosen such that the equilibrium points are unstable, the solution orbits infinitely around these. Figure A.1 is representative of this, and shows the trajectory of $r(t) = (x(t), y(t), z(t))$ considering $\sigma = 10$, $\rho = 28$ and $\beta = 8/3$, for which the Lorenz attractor has chaotic solutions. To indicate the location in space of different relevant solution point, in all figures we include the following notation: "IP" stands for *initial point* (of the simulation), "FP" for *final point* (of the simulation), "'SP" for *steady point* and "PSP" for *permanent steady point*, which corresponds to $(0, 0, 0)$. Now the aim is to apply different stabilisation methods to drive the solution of the Lorenz attractor towards a steady state for system parameters which make it unstable.

Based on the aforementioned specifications, the spatial evolution of $r(t)$ when considering $\sigma = 10$, $\rho = 28$ and $\beta = 8/3$ (corresponding to the same parameters of the unmodified problem shown in figure A.1) is presented next for each of the stabilising methods (figure A.2). Although it corresponds to an unstable configuration, it is *moderately unstable*. Thus, we test as well more unstable configurations of the Lorenz system by increasing ρ for fixed σ and β. For all simulations, the time step is set to $\tau = 0.01$, $\chi = 1$, $\Delta = 5$, the initial condition is $(5, 5, 5)$ and normcond $= 2$ for the coupled approach. To compare the performance of the methods in terms of convergence velocity, the number of iterations until the steady-state point is reached ($||q^{n+1} - q^n|| = 10^{-4}$) for each approach is computed and summarised in table A.1. In the coupled ESFD/JFNK approach, the total number of iterations includes those of the base algorithm plus the ones associated to the line search method.

	SFD	ESFD	JFNK	Coupled ESFD/JFNK
$\rho = 25$	1217	1221	43	24
$\rho = 30$	2179	2351	14	22
$\rho = 40$	3204	3162	7	17
$\rho = 50$	-	-	7	17
$\rho = 90$	-	-	66	19
$\rho = 150$	-	-	76	27

Table A.1: Number of iterations required to reach the steady-state of the Lorenz system for each of the tested methods and for different values of the ρ parameter

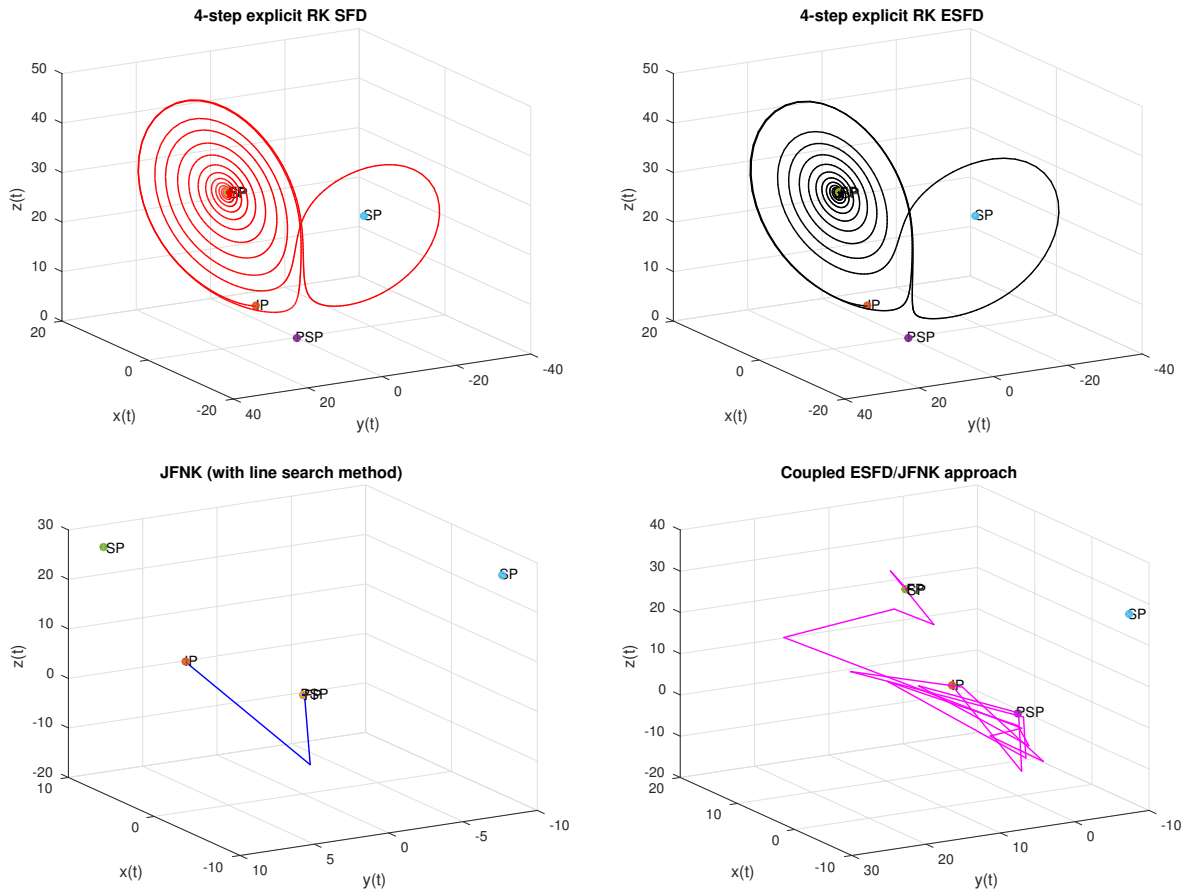

Figure A.2: Trajectory $r(t)$ of the Lorenz system when it is artificially driven towards steady-state points by using four different methods (SFD, ESFD, JFNK and coupled ESFD/JFNK). The parameters of the system are $\sigma = 10$, $\rho = 28$ and $\beta = 8/3$

A.2 List of y-z planes of base flow variables in the near-ramp region

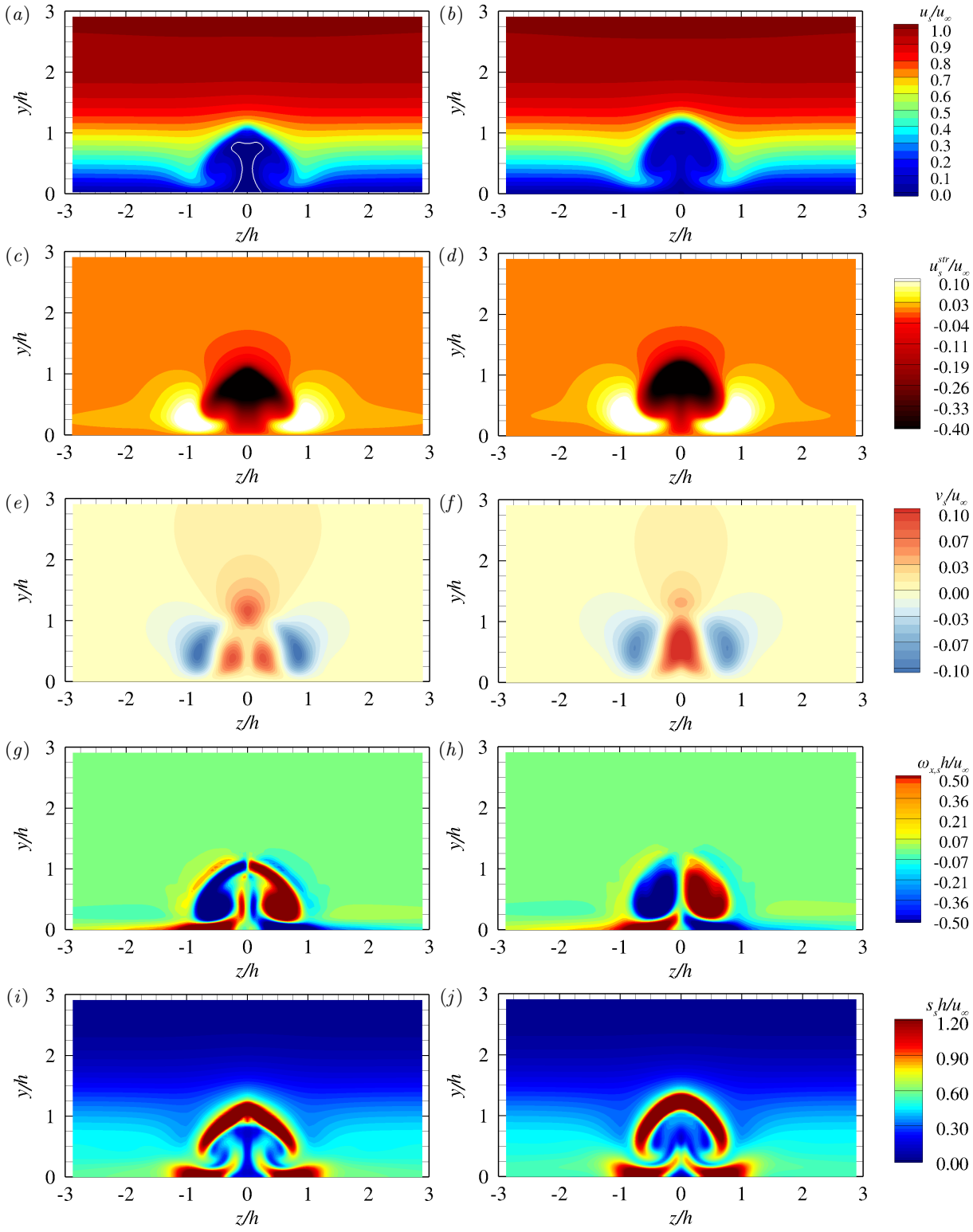

Figure A.3: y-z planes. Streamwise velocity, $x/h = 0$ (*a*), $x/h = 1$ (*b*); iso-contour of $u_s/u_\infty = 0$ (white line). Streamwise velocity streaks, $x/h = 0$ (*c*), $x/h = 1$ (*d*). Wall-normal velocity, $x/h = 0$ (*e*), $x/h = 1$ (*f*). Streamwise vorticity, $x/h = 0$ (*g*), $x/h = 1$ (*h*). Shear, $x/h = 0$ (*i*), $x/h = 1$ (*j*).

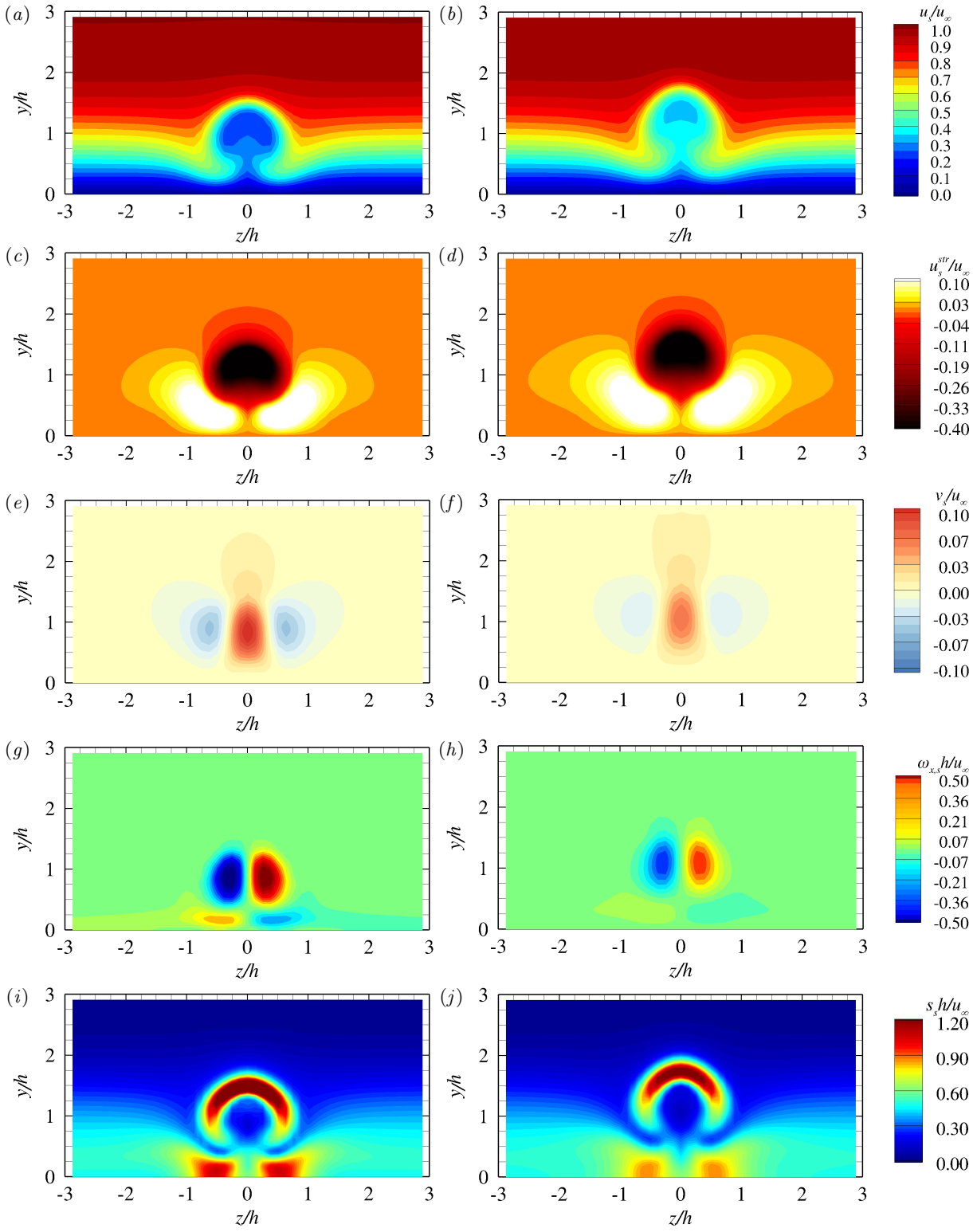

Figure A.4: y-z planes. Streamwise velocity, $x/h = 5$ (*a*), $x/h = 10$ (*b*). Streamwise velocity streaks, $x/h = 5$ (*c*), $x/h = 10$ (*d*). Wall-normal velocity, $x/h = 5$ (*e*), $x/h = 10$ (*f*). Streamwise vorticity, $x/h = 5$ (*g*), $x/h = 10$ (*h*). Shear, $x/h = 5$ (*i*), $x/h = 10$ (*j*).

A.3 List of y-z planes of base and mean flow variables

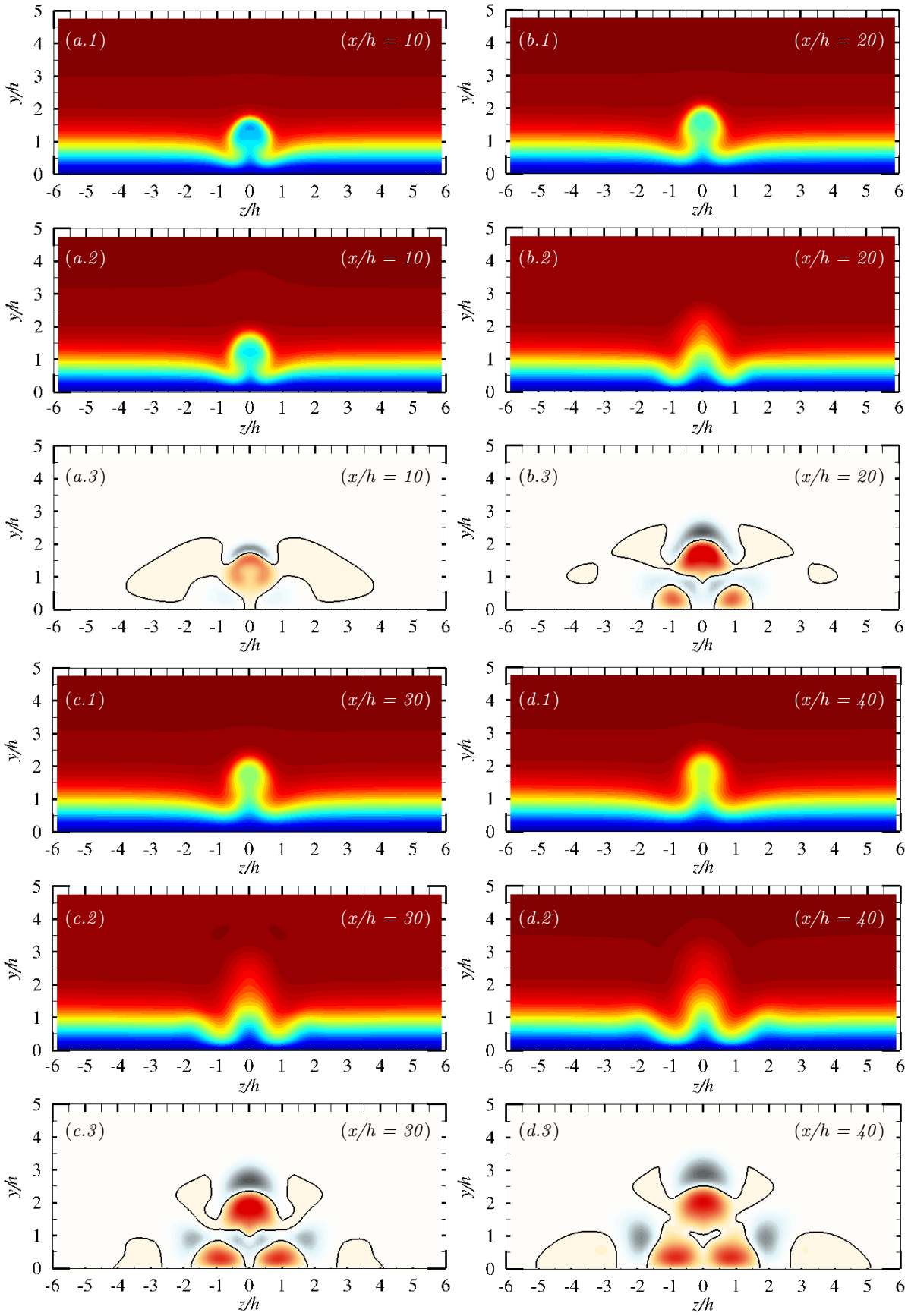
(a.1) (x/h = 10)
(b.1) (x/h = 20)
(a.2) (x/h = 10)
(b.2) (x/h = 20)
(a.3) (x/h = 10)
(b.3) (x/h = 20)
(c.1) (x/h = 30)
(d.1) (x/h = 40)
(c.2) (x/h = 30)
(d.2) (x/h = 40)
(c.3) (x/h = 30)
(d.3) (x/h = 40)
y/h
z/h

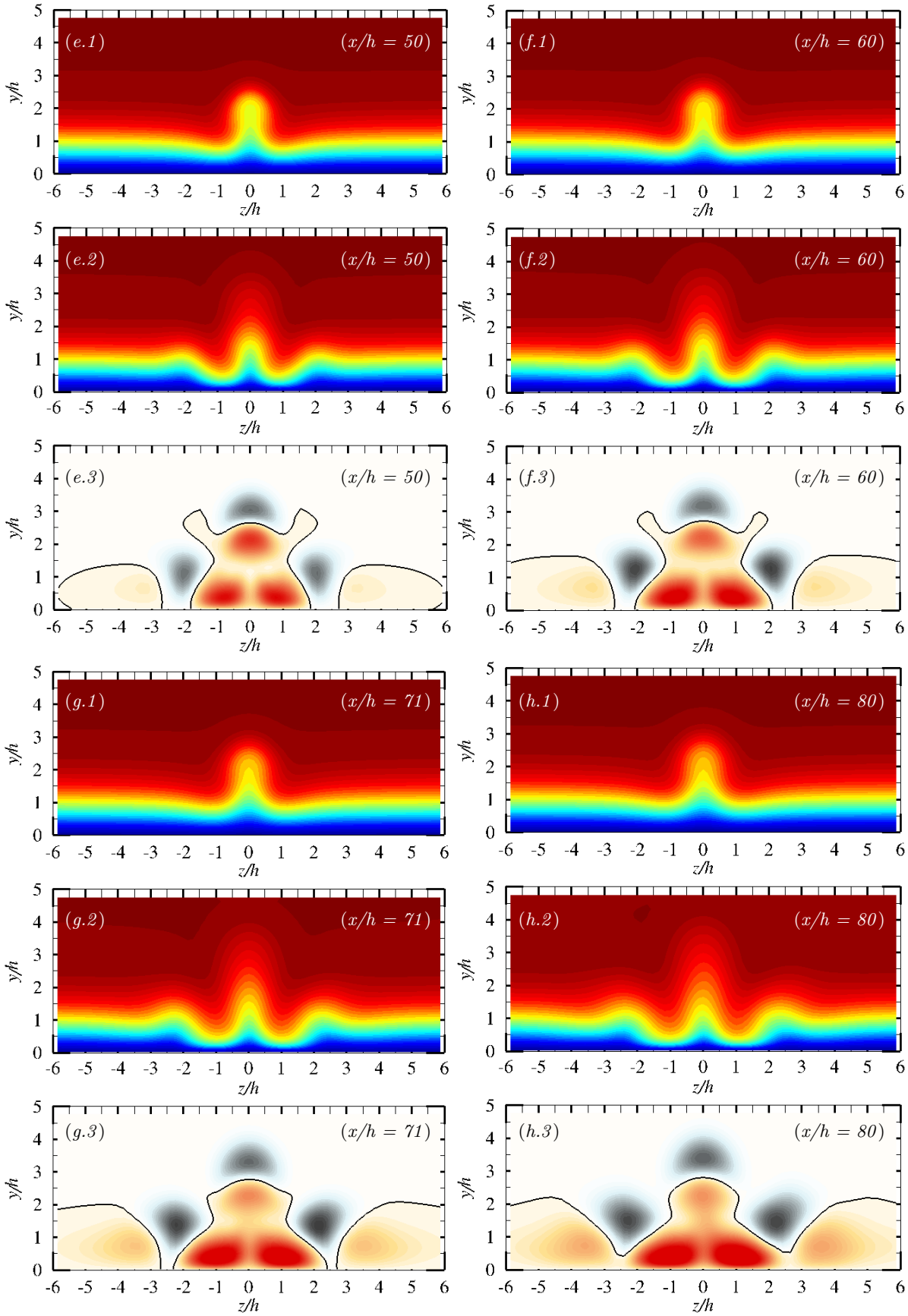
(e.1) (x/h = 50)
(f.1) (x/h = 60)
(e.2) (x/h = 50)
(f.2) (x/h = 60)
(e.3) (x/h = 50)
(f.3) (x/h = 60)
(g.1) (x/h = 71)
(h.1) (x/h = 80)
(g.2) (x/h = 71)
(h.2) (x/h = 80)
(g.3) (x/h = 71)
(h.3) (x/h = 80)
y/h
z/h

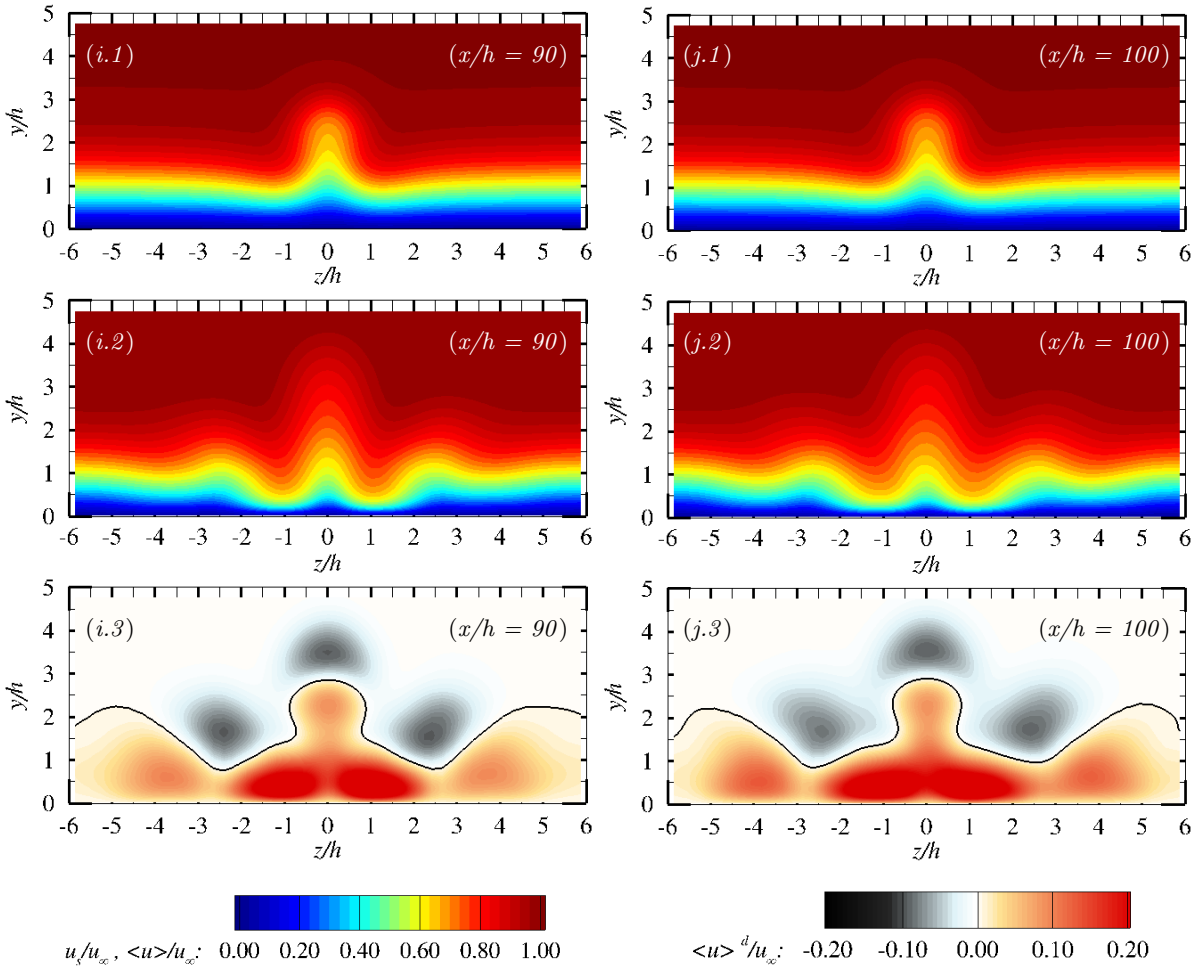

Figure A.5: Streamwise velocity in the base flow (1), mean flow (2), and $\langle u \rangle^{\mathrm{d}}/u_\infty$ (3). y-z planes at $x/h = 10$ (*a*), $x/h = 20$ (*b*), $x/h = 30$ (*c*), $x/h = 40$ (*d*), $x/h = 50$ (*e*), $x/h = 60$ (*f*), $x/h = 71$ (*g*), $x/h = 80$ (*h*), $x/h = 90$ (*i*), $x/h = 100$ (*j*). Iso-contour of $\langle u \rangle^{\mathrm{d}}/u_\infty = 0$ (solid black line).

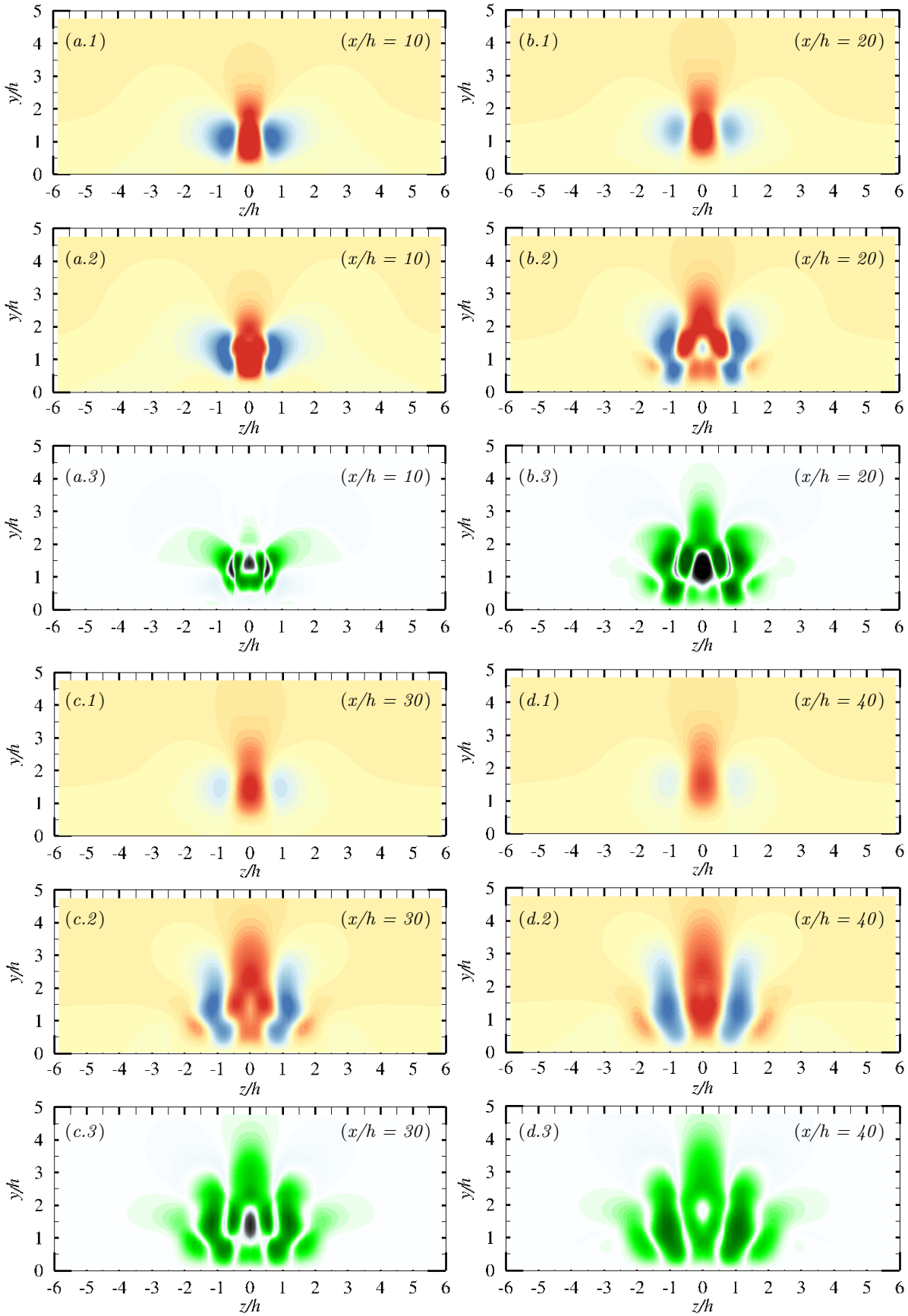
(a.1) (x/h = 10)
(b.1) (x/h = 20)
(a.2) (x/h = 10)
(b.2) (x/h = 20)
(a.3) (x/h = 10)
(b.3) (x/h = 20)
(c.1) (x/h = 30)
(d.1) (x/h = 40)
(c.2) (x/h = 30)
(d.2) (x/h = 40)
(c.3) (x/h = 30)
(d.3) (x/h = 40)
y/h
z/h

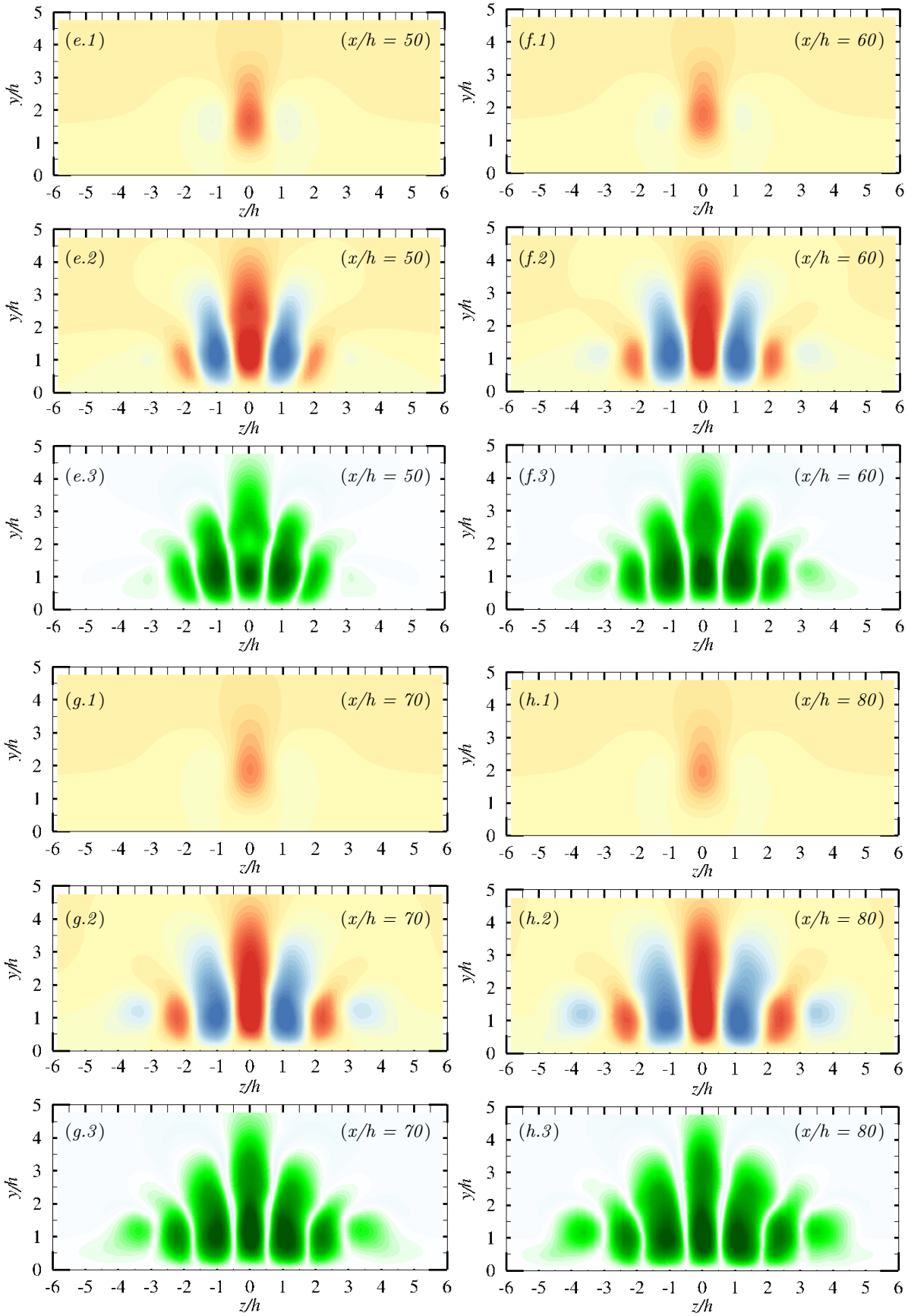
(e.1) (x/h = 50)
(f.1) (x/h = 60)
(e.2) (x/h = 50)
(f.2) (x/h = 60)
(e.3) (x/h = 50)
(f.3) (x/h = 60)
(g.1) (x/h = 70)
(h.1) (x/h = 80)
(g.2) (x/h = 70)
(h.2) (x/h = 80)
(g.3) (x/h = 70)
(h.3) (x/h = 80)
y/h
z/h

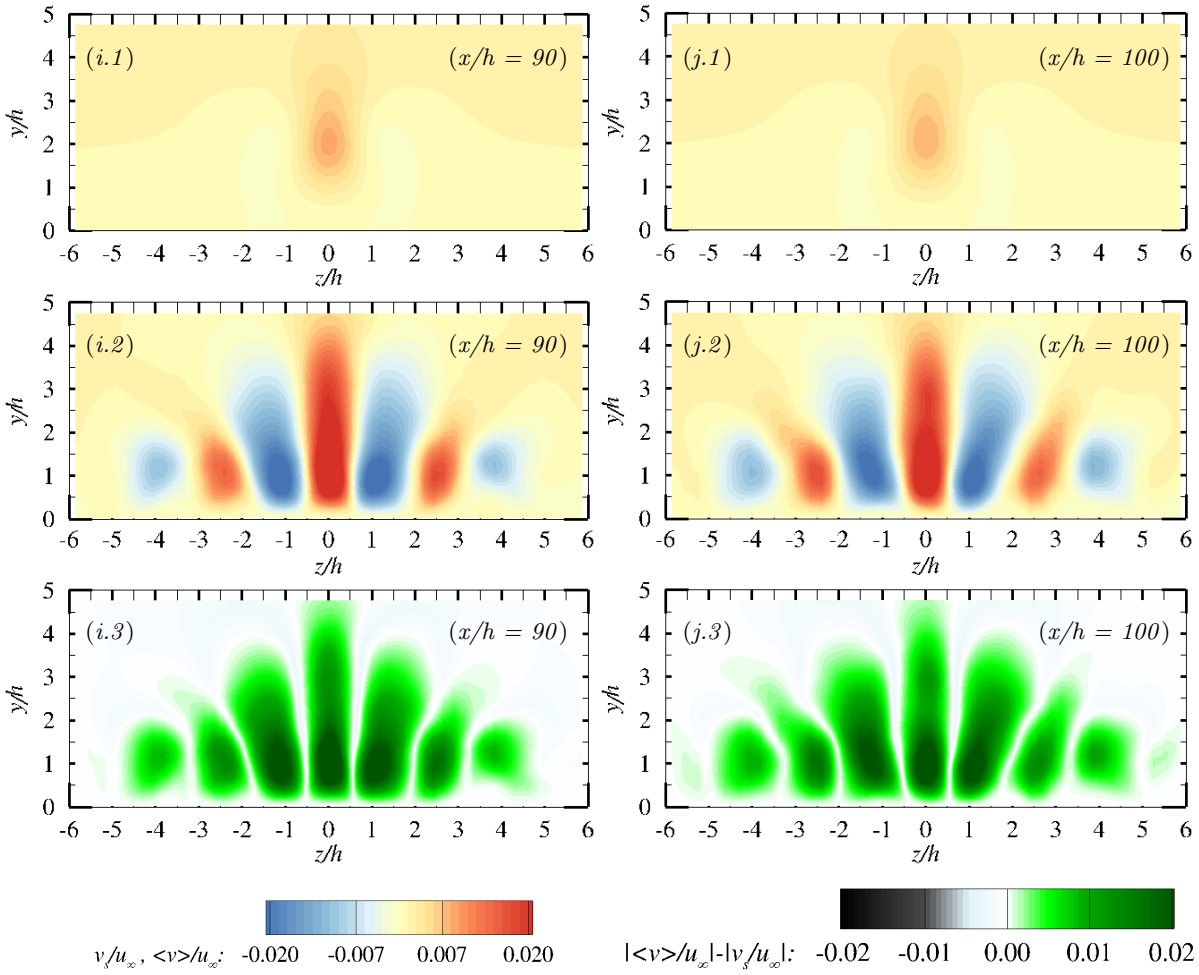

Figure A.6: Wall-normal velocity in the base flow (1), mean flow (2), and $|\langle v \rangle / u_\infty| - |v_s/u_\infty|$ (3). y-z planes at $x/h = 10$ (*a*), $x/h = 20$ (*b*), $x/h = 30$ (*c*), $x/h = 40$ (*d*), $x/h = 50$ (*e*), $x/h = 60$ (*f*), $x/h = 70$ (*g*), $x/h = 80$ (*h*), $x/h = 90$ (*i*), $x/h = 100$ (*j*).

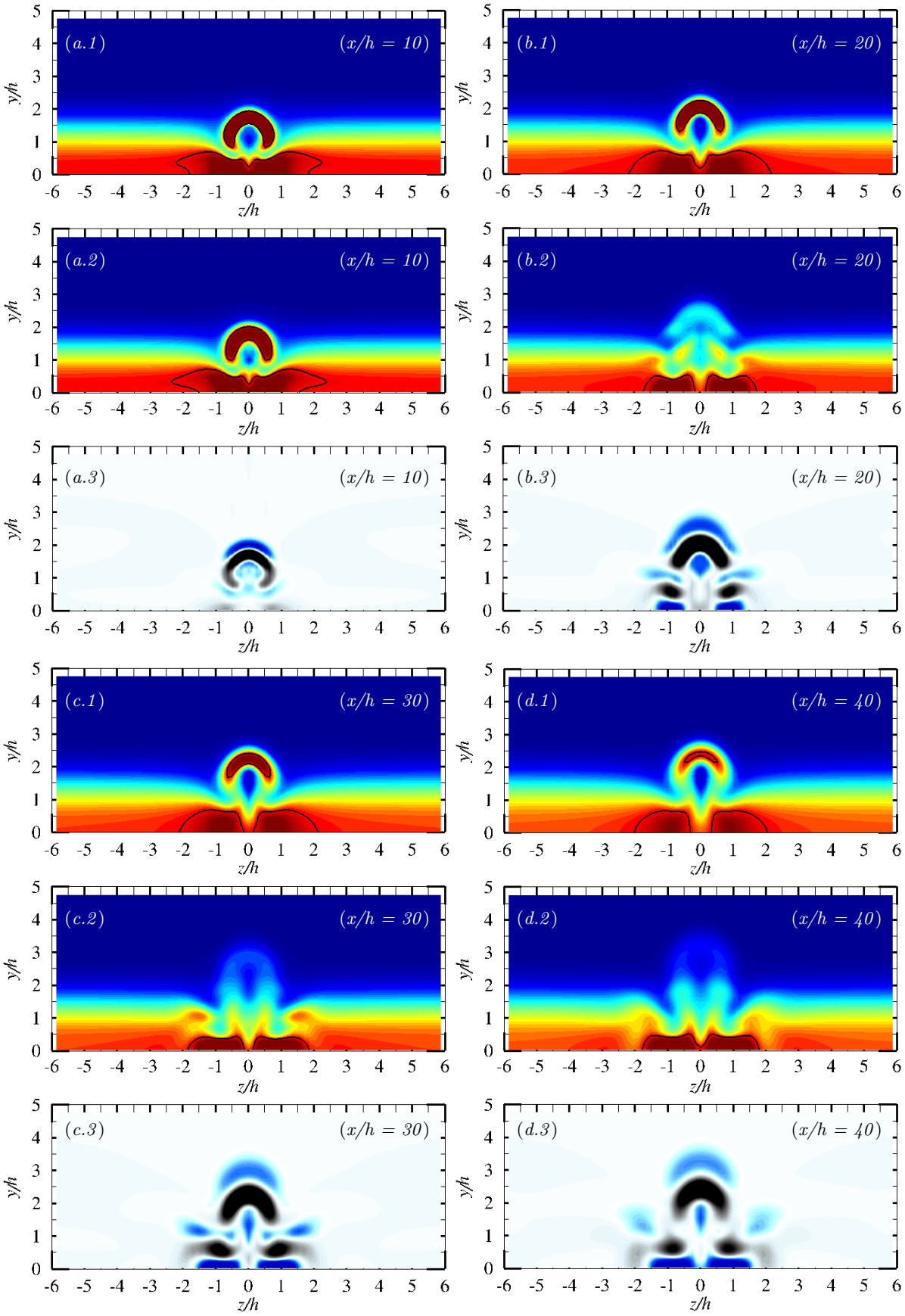
(a.1) (x/h = 10)
(b.1) (x/h = 20)
(a.2) (x/h = 10)
(b.2) (x/h = 20)
(a.3) (x/h = 10)
(b.3) (x/h = 20)
(c.1) (x/h = 30)
(d.1) (x/h = 40)
(c.2) (x/h = 30)
(d.2) (x/h = 40)
(c.3) (x/h = 30)
(d.3) (x/h = 40)
y/h
z/h

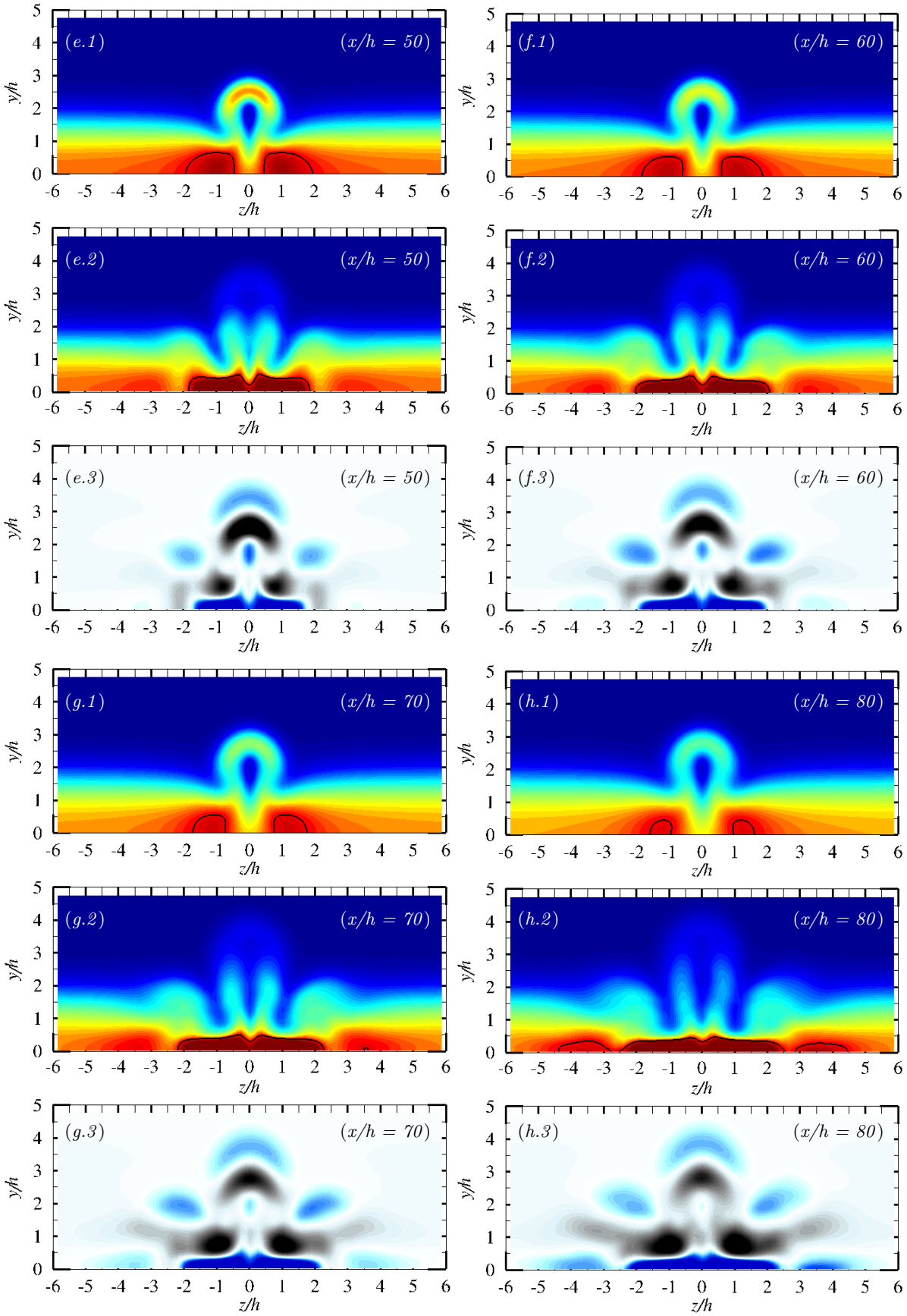
(e.1) (x/h = 50)
(f.1) (x/h = 60)
(e.2) (x/h = 50)
(f.2) (x/h = 60)
(e.3) (x/h = 50)
(f.3) (x/h = 60)
(g.1) (x/h = 70)
(h.1) (x/h = 80)
(g.2) (x/h = 70)
(h.2) (x/h = 80)
(g.3) (x/h = 70)
(h.3) (x/h = 80)
y/h
z/h

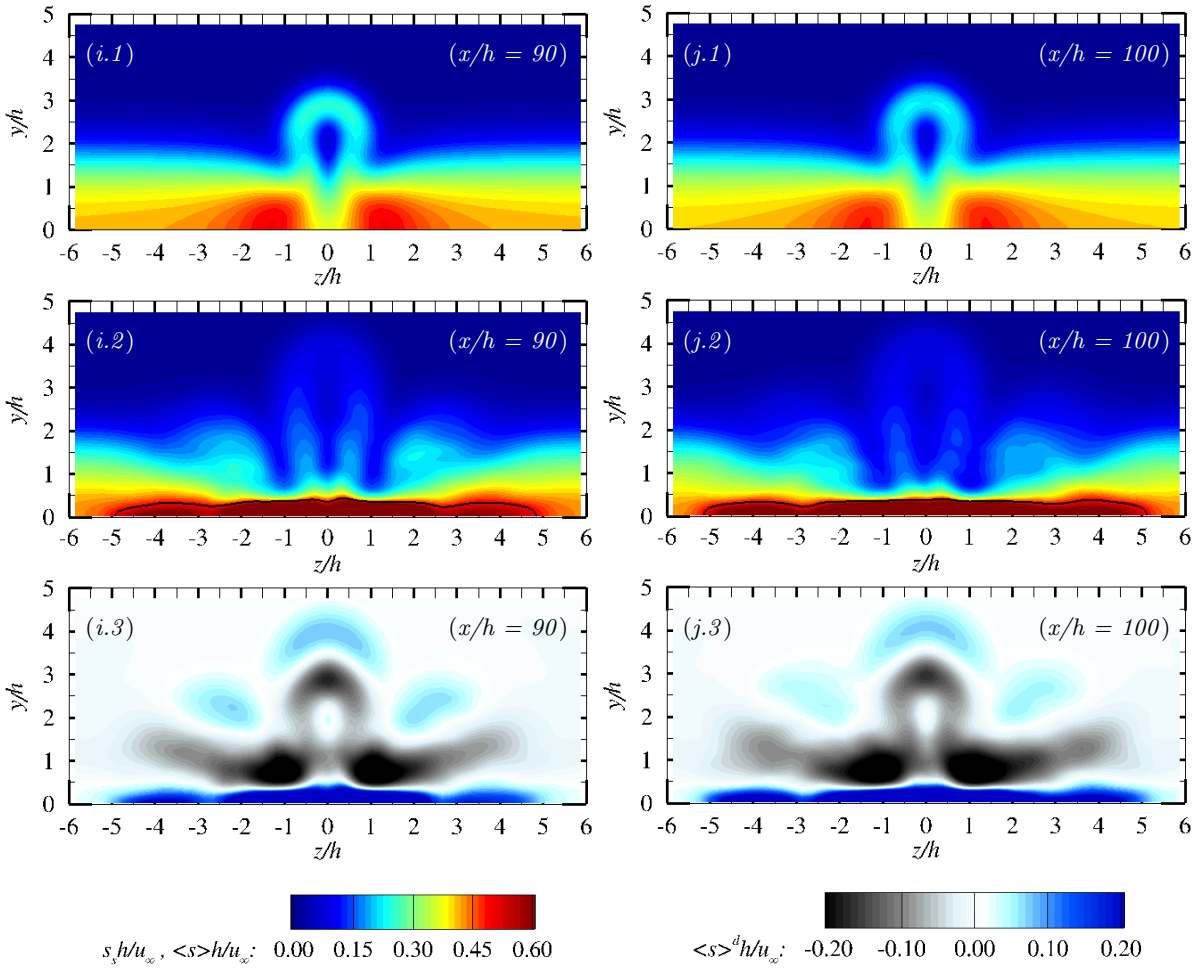

Figure A.7: Shear in the base flow (1), mean flow (2), and $\langle s \rangle^{\mathrm{d}} h/u_\infty$ (3). y-z planes at $x/h = 10$ (*a*), $x/h = 20$ (*b*), $x/h = 30$ (*c*), $x/h = 40$ (*d*), $x/h = 50$ (*e*), $x/h = 60$ (*f*), $x/h = 70$ (*g*), $x/h = 80$ (*h*), $x/h = 90$ (*i*), $x/h = 100$ (*j*). Iso-contours of $s_{\mathrm{s}} h/u_\infty = 1/2$, $\langle s \rangle^{\mathrm{d}} h/u_\infty = 1/2$ (solid black line).

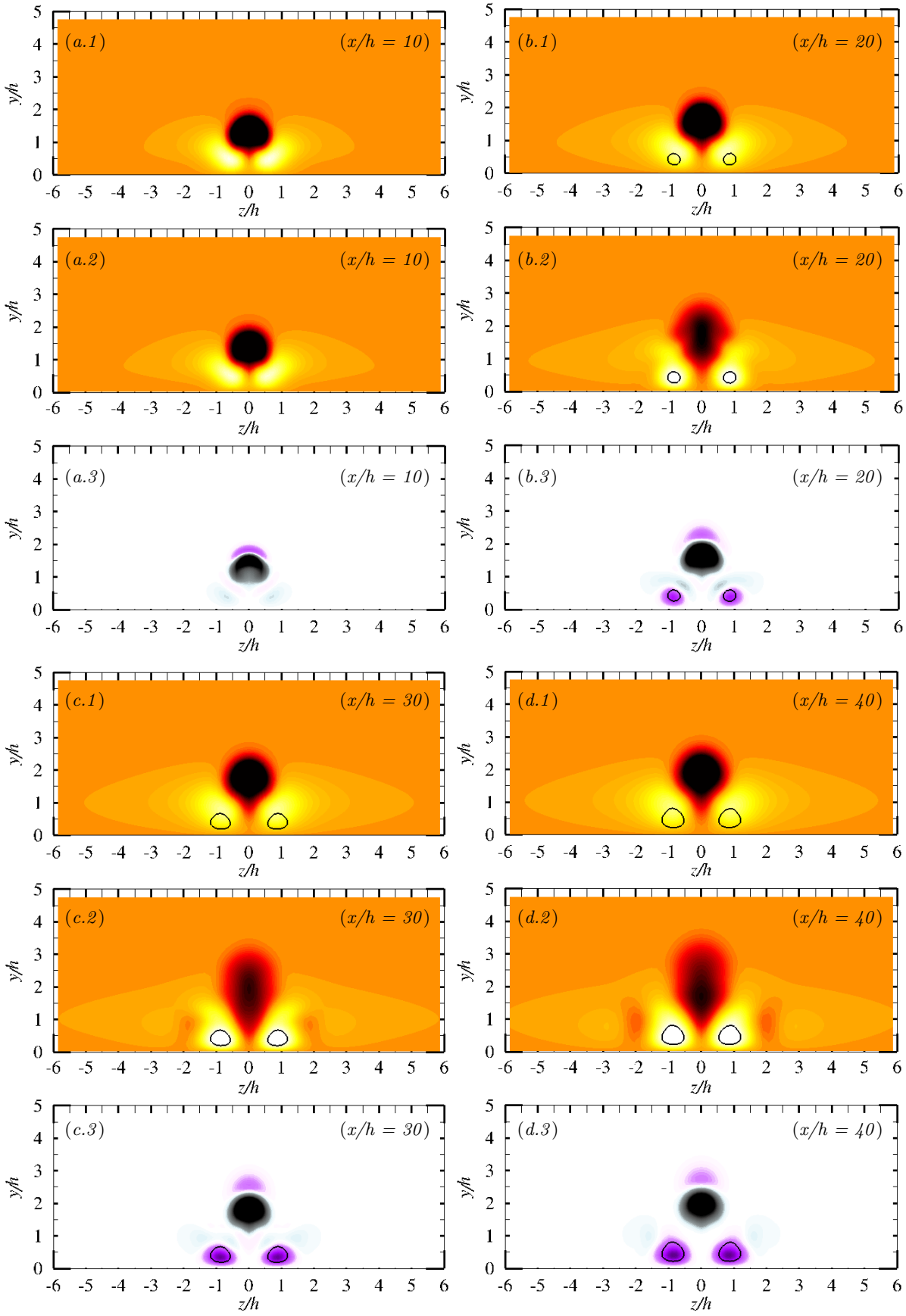
(a.1) (x/h = 10)
(b.1) (x/h = 20)
(a.2) (x/h = 10)
(b.2) (x/h = 20)
(a.3) (x/h = 10)
(b.3) (x/h = 20)
(c.1) (x/h = 30)
(d.1) (x/h = 40)
(c.2) (x/h = 30)
(d.2) (x/h = 40)
(c.3) (x/h = 30)
(d.3) (x/h = 40)
y/h
z/h

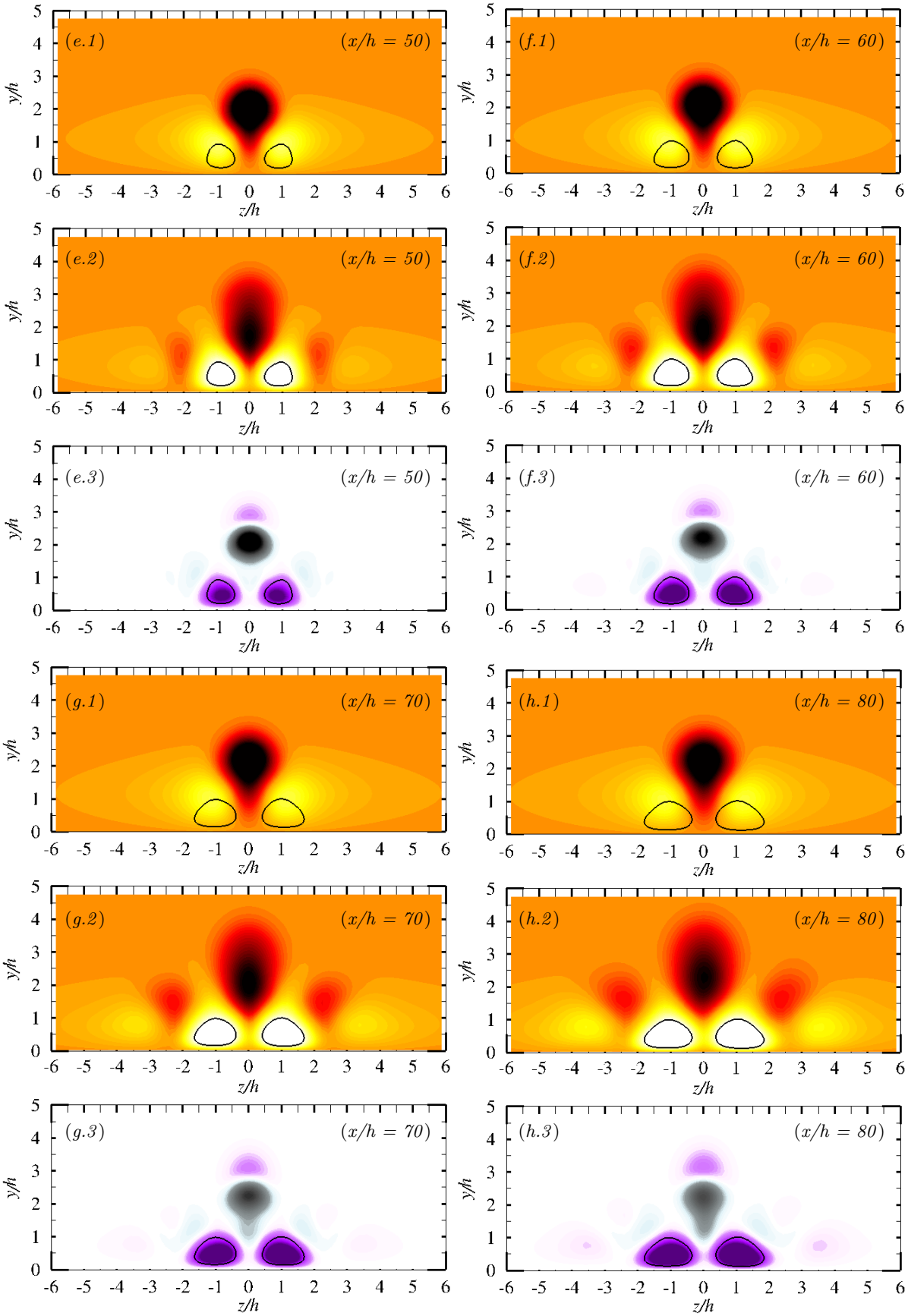
(e.1) (x/h = 50)
(f.1) (x/h = 60)
(e.2) (x/h = 50)
(f.2) (x/h = 60)
(e.3) (x/h = 50)
(f.3) (x/h = 60)
(g.1) (x/h = 70)
(h.1) (x/h = 80)
(g.2) (x/h = 70)
(h.2) (x/h = 80)
(g.3) (x/h = 70)
(h.3) (x/h = 80)
y/h
z/h

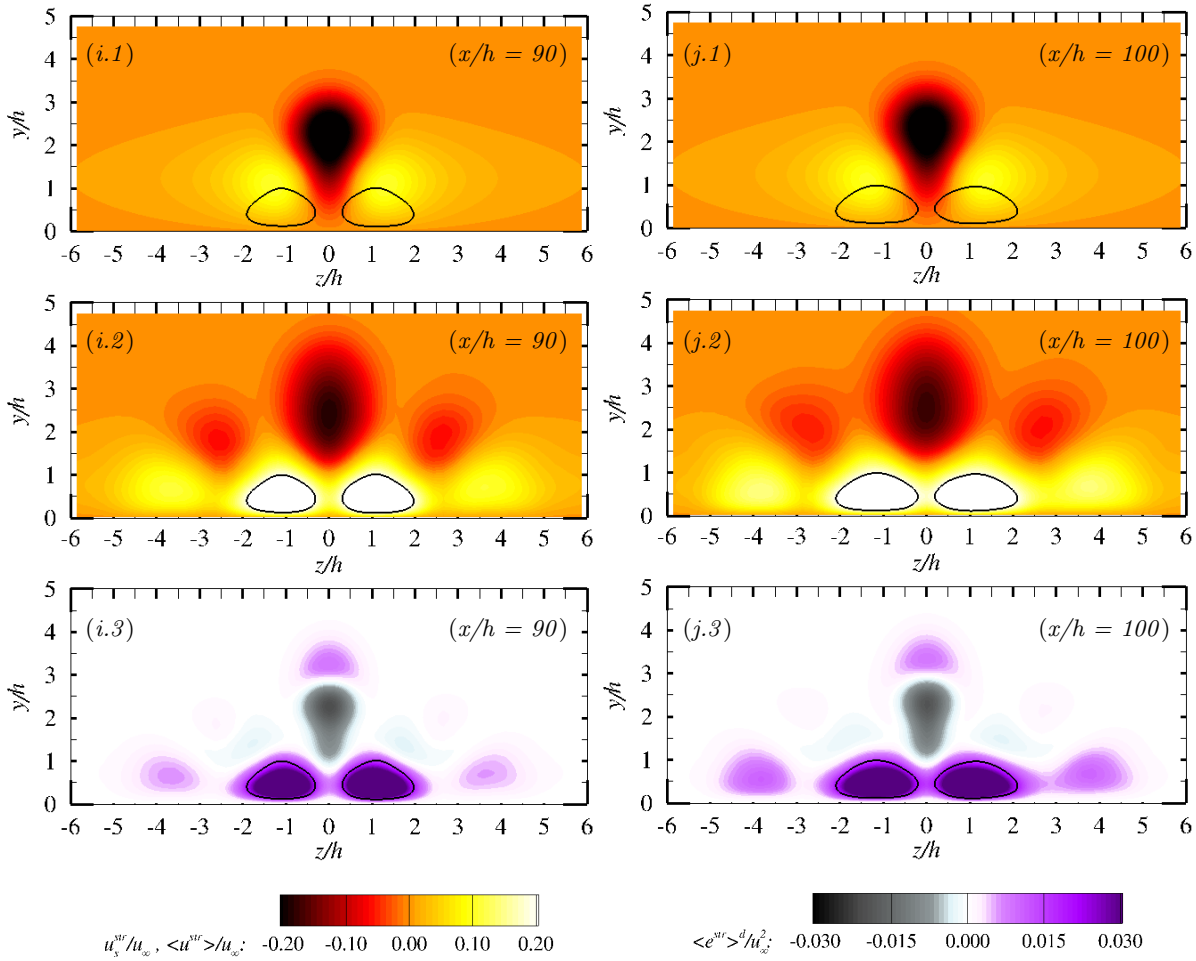

Figure A.8: Streamwise streaks in the base flow (1), mean flow (2), and $\langle e^{\mathrm{str}} \rangle^{\mathrm{d}} / u_\infty^2$ (3). y-z planes at $x/h = 10$ (*a*), $x/h = 20$ (*b*), $x/h = 30$ (*c*), $x/h = 40$ (*d*), $x/h = 50$ (*e*), $x/h = 60$ (*f*), $x/h = 70$ (*g*), $x/h = 80$ (*h*), $x/h = 90$ (*i*), $x/h = 100$ (*j*). Iso-contour of $\langle u^{\mathrm{str}} \rangle / u_\infty = 0.2$ (solid black line).

A.4 Boundary layer shape factor in the base and mean flow fields

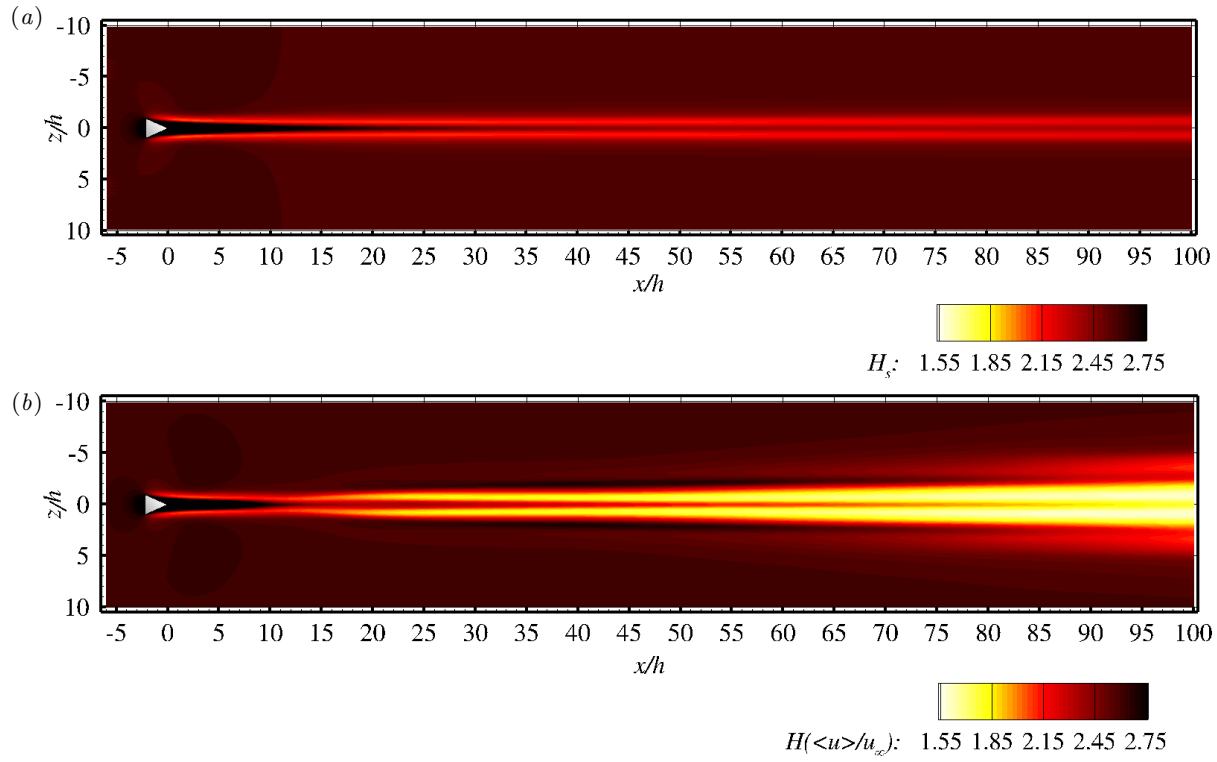

Figure A.9: Shape factor of the boundary layer in (*a*) the base and (*b*) the time-averaged flow fields, depicted at $y = 0$.

A.5 Compressibility effects

In this last section of the Appendix, we extend and describe some of the results of the $M = 0.2$ micro-ramp flow analysis to a $M = 0.7$ boundary layer case. The base flow is computed via ESFD using $\chi = 0.96$ and $\Delta = 1.86$, the same SFD parameters used to stabilise the $M = 0.2$ case. The convergence bound of the simulation is $\epsilon_R = 10^{-8}$. We use the $M = 0.2$ base flow solution as initial condition.

A first main observation is the strong stabilising effect of compressibility, as suggested by the literature (von Doenhoff and Braslow, 1961; Redford et al., 2010; Bernardini et al., 2012). In the $M = 0.7$ instantaneous flow field, for small-to-moderate x/h, we do not capture a significant perturbation activity and the structure of the primary vortex pair resembles that of the $M = 0.7$ base flow configuration. Only for large x/h, the primary vortices start to become distorted under the action of disturbances; see figure A.10. Although it is critical for the system's stability, the effect of the Mach number increase does not seem to significantly alter the organisation of the base flow.

In the $M = 0.7$ instantaneous flow field, the primary vortex pair rapidly lifts off from the surface; at $x/h \approx 30$, its lifting motion has become less pronounced. This trend is analogous to that reported in the $M = 0.2$ base flow analysis (§4.2.1). Gradually, the primary vortices start to oscillate due to the fact that a (rather weak) perturbation train develops at the spanwise upper shear layer. Differently from the $M = 0.2$ case, perturbation-induced vortical structures do not become arch-shaped and feature significantly lower streamwise vorticity values. As a consequence of the decreased disturbance activity, transitional perturbations are not capable to significantly enhance the transport of momentum within the boundary layer, even for large x/h. The primary vortices remain as the dominant structure in the instantaneous flow field. This is supported by the results of figure A.11. Qualitatively, the trend followed by the wall shear in the $M = 0.7$ base and mean flow fields appears to be almost identical. Furthermore, the evolution in x/h of the regions of enhanced wall shear is similar to that exhibited in the $M = 0.2$ base flow. Since secondary vortical structures do not develop, the micro-ramp wake does not show to significantly expand in $|z/h|$.

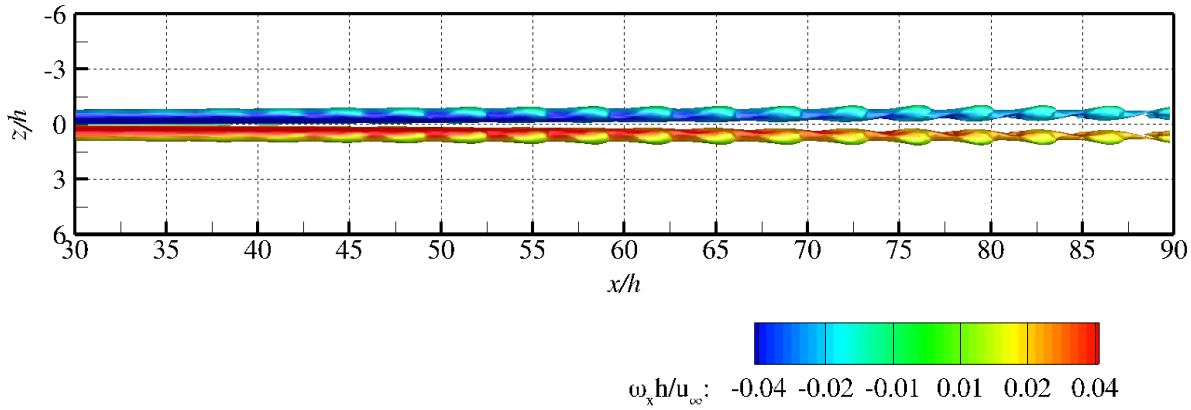

Figure A.10: Instantaneous λ_2 in the $M = 0.7$ case. Isosurface of $\lambda_2 = -4 \times 10^{-5}$ colour-coded by streamwise vorticity.

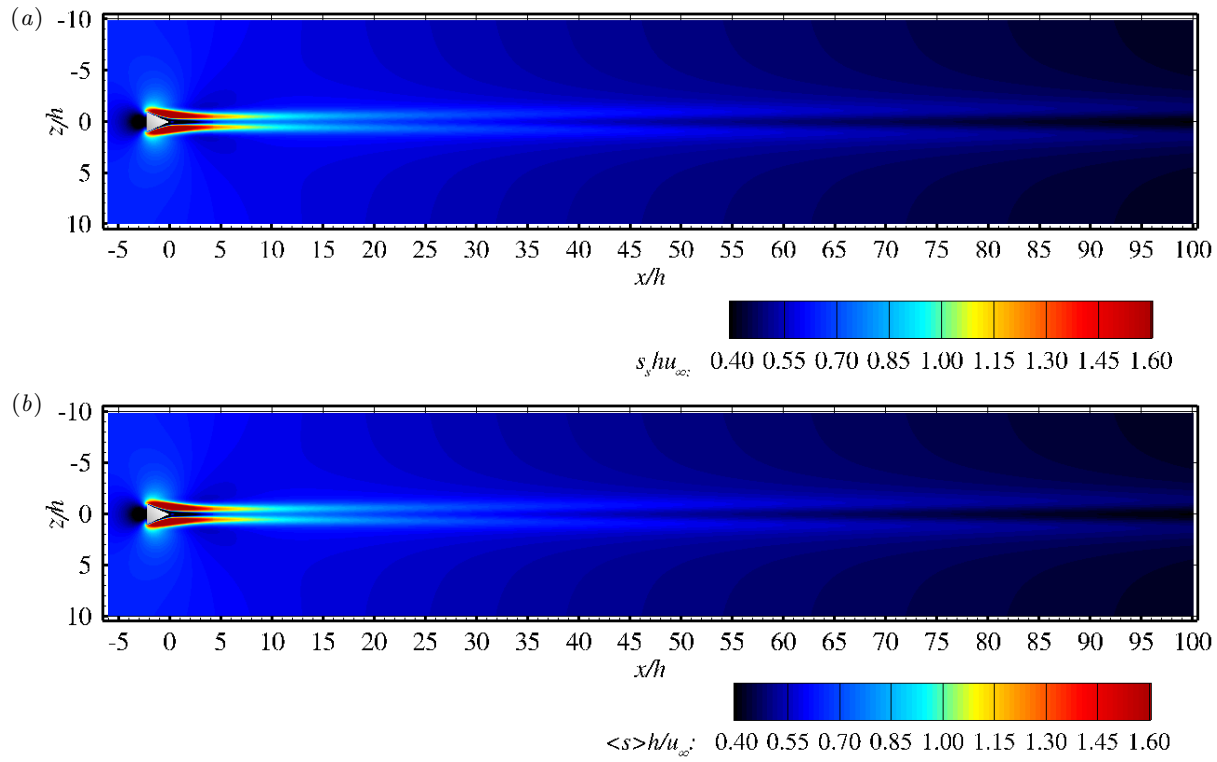

Figure A.11: Wall shear in the $M = 0.7$ case for (*a*) the base and (*b*) the time-averaged flow fields.

Thus, when it is immersed in a $M = 0.7$ boundary layer, the micro-ramp investigated in this work shows a similar performance with and without disturbance development because compressibility strongly weakens the perturbation activity. Since for this configuration the primary vortices play the central role in the re-energisation of the lowest-level fluid, the boundary layer is less "healthy" than in the $M = 0.2$ case sufficiently downstream the micro-ramp.